Continuum Modeling of Liquid-Solid Suspensions for Nonviscometric Flows

A Thesis
Presented to
The Academic Faculty

by

Ryan M. Miller

In Partial Fulfillment
of the Requirements for the Degree
Doctor of Philosophy

School of Chemical & Biomolecular Engineering
Georgia Institute of Technology
September 2004

Continuum Modeling of Liquid-Solid Suspensions for Nonviscometric Flows

Approved by:

Dr. Jeffrey F. Morris, Advisor
School of Chemical & Biomolecular Engineering

Dr. Minami Yoda
School of Mechanical Engineering

Dr. Larry Forney
School of Chemical & Biomolecular Engineering

Dr. Sotira Z. Yiacoumi
School of Civil & Environmental Engineering

Dr. Timothy M. Wick
School of Chemical & Biomolecular Engineering

Dr. Wallace W. Carr
School of Polymer, Textile & Fiber Engineering

Dr. William J. Koros
School of Chemical & Biomolecular Engineering

Date Approved: September 24, 2004

To my wife,

Kate,

who has helped me through this journey.

ACKNOWLEDGEMENTS

I would like to acknowledge my advisor, Dr. Jeff Morris, for sticking with me throughout this process and helping me see it to the end. I appreciate the time and guidance he has given me. I would also like to acknowledge Dr. Lisa Mondy and Dr. Rekha Rao from Sandia National Laboratories for collaborating with us on the modeling efforts.

I would like to thank my research group members, Brian Timberlake and Roy Furbank, for their support and always being there to lend me an ear when I needed it. I also would like to thank them for answering my frequent phone calls, near the end, with yet another request to restart the computers. Furthermore, I would like to thank Duane Mikulencak for helping me settle into things when I started, which now seems so long ago.

Finally I would like to thank my family for their support and guidance. I thank my parents, Madeline and Terry, for giving me the foundation and support to get to where I am. I thank my brother Jake for being there when I have needed him. I especially thank my in-laws Rob and Sue for this past year, and even Lauren and Jennie too. But especially I would like to thank my wife, Kate, who has walked through this process with me every step of the way, and even found some time to give us two wonderful sons. I could not have done it without you.

TABLE OF CONTENTS

DEDICATION . . . . . **iii**

ACKNOWLEDGEMENTS . . . . . **iv**

LIST OF TABLES . . . . . **viii**

LIST OF FIGURES . . . . . **ix**

SUMMARY . . . . . **xiii**

CHAPTER 1 INTRODUCTION AND BACKGROUND **1**

1.1 Suspension forces 2

1.2 Shear induced particle migration 5

1.3 Modeling efforts 6

CHAPTER 2 COMPUTATIONAL TOOL: SOLVER-EVOLVER **8**

2.1 Governing Equations 9

2.1.1 Suspension balances 9

2.1.2 Suspension stress law 11

2.2 Numerical Implementation 14

2.2.1 Discretization of the transport equations 16

2.2.2 Solution method 18

2.3 Numerical Verification 20

2.3.1 Flow of a Newtonian fluid through a planar $\beta = 4$ contraction . . . 22

2.3.2 Flow of a Newtonian fluid through an axisymmetric $\beta = 2$ contraction 24

2.3.3 Particle migration in a channel flow 24

CHAPTER 3 SIMPLE GEOMETRY: AXIALLY DEVELOPING FLOWS **31**

3.1 Governing Equations 32

3.1.1 Nonlocal stress contributions 34

3.1.2 Scaling and unidirectional flow 36

3.2 Pressure-driven Flow of a Concentrated Suspension Through a Long Conduit 37

3.2.1 Experimental comparisons 38

3.3 Numerical Implementation 39

3.3.1 Full two-dimensional solution: the solver-evolver tool 39
3.3.2 Marching method solution 40
3.4 Results and Discussion 42
3.5 Conclusions 60

CHAPTER 4 SIMPLE GEOMETRY: SUSPENDING FLUID EFFECTS 64

4.1 Governing Equations 64
4.2 Wide-gap Circular Couette Flow of a Suspension with a Shear-thinning Suspending Fluid 66
4.3 Model Equations for a Wide-gap Circular Couette Flow 68
4.3.1 Flow field equations 68
4.3.2 Particle migration equations 69
4.3.3 Numerical solution equations 70
4.4 Results and Discussion 72
4.4.1 Comparison with experiments 72
4.4.2 Approach to steady-state 77
4.5 Conclusions 81

CHAPTER 5 COMPLEX GEOMETRY: FRAME INVARIANT RHEOLOGY 85

5.1 Frame Invariant Rheology 87
5.1.1 Kinematic ratio 88
5.1.2 Compression-tension coordinates 89
5.1.3 Three-dimensional kinematics 90
5.2 Particle Stress Constitutive Model 91
5.2.1 Weighted-isotropic constitutive model 91
5.2.2 Anisotropic constitutive model 93
5.3 Suspension Flow Modeling with an Isotropic Constitutive Law 94
5.3.1 Piston-driven flow of a suspension in a 4:1:4 contraction/expansion 96
5.3.2 Effect of contraction ratio on predicted results 101
5.3.3 Effect of flow direction on predicted results 108
5.4 Effects of the Constitutive Law on Model Predictions 111
5.4.1 Weighted-isotropic constitutive model predictions 111

5.4.2 Anisotropic constitutive model predictions 113
5.5 Conclusions 127
CHAPTER 6 COMPLEX GEOMETRY: APPLICATIONS 130
6.1 Piston-driven suspension flow in a closed rectangular channel 131
6.1.1 Results and discussion 132
6.2 Pressure-driven suspension flow in a rectangular channel with an obstruction near the entrance 139
6.2.1 Results and discussion 140
6.3 Conclusions 148
CHAPTER 7 FUTURE DIRECTIONS 150
7.1 Experiment, Simulation and Rheology 151
7.2 Using the Solver-Evolver 153
7.3 Extending the Particle Stress Constitutive Model 153
7.4 Conclusions 156
APPENDIX A Solver-Evolver Code: MATLAB m-files 158
REFERENCES 159

LIST OF TABLES

Table 1 Predicted entrance lengths of the ϕ profile and pressure drop for axially-developing conduit flows. 47

Table 2 Comparison of experimentally observed ϕ profile entrance lengths with model predictions for conduit flows. 48

Table 3 Quantitative comparison of experimental results and model predictions for a wide-gap circular Couette suspension flow with a shear-thinning suspending fluid. 75

Table 4 Comparison of the time predicted to achieve steady state in a wide-gap circular Couette flow with Newtonian and shear-thinning suspending fluids. 82

Table 5 Constitutive models for the particle stress. 91

Table 6 Predictions of the inlet pressure before and after migration has occurred in a sharp-edged, $\beta = 4$ contraction flow. 108

Table 7 Predictions of the inlet pressure before and after particle migration for an axially-developing channel flow with an obstruction near the entrance. . . 148

LIST OF FIGURES

Figure 1 Imposed flow field effects on a fluid element versus a rigid, suspended particle. 4

Figure 2 Plots of the shear viscosity models and sedimentation hindrance function. 12

Figure 3 Fully-staggered computational grid arrangement. 15

Figure 4 Illustration of control volume elements. 15

Figure 5 Sketch of a of sharp-edged contraction geometry. 21

Figure 6 Typical computational grid for a contraction flow geometry. 22

Figure 7 The velocity streamlines and values for a rectangular $\beta = 4$ contraction flow. 23

Figure 8 The velocity streamlines and values for a axisymmetric $\beta = 2$ contraction flow. 25

Figure 9 Comparison of $\beta = 2$, axisymmetric contraction flow predictions with literature data. 26

Figure 10 Comparison of numerical and analytical ϕ and velocity predictions for a rectangular channel flow. 29

Figure 11 Illustration of the nonlocal stress. 35

Figure 12 Sketch of the channel flow geometry and imposed boundary conditions. . 38

Figure 13 Computational grid used for the channel flow. 40

Figure 14 Calculated and curve-fitted values of E_p for the ϕ profile 43

Figure 15 Comparison of axially-developing channel flow predictions to the experimental results of Lyon and Leal (1998a). 44

Figure 16 Comparison of axially-developing pipe flow predictions with the experimental data of Hampton *et al* (1997), $R/a = 16$. 45

Figure 17 Comparison of axially-developing pipe flow predictions with the experimental data of Hampton *et al* (1997), $R/a = 40$. 46

Figure 18 Comparison of axial-velocity predictions with experimental results for a channel and pipe flow. 50

Figure 19 Comparison of the effect of α, particle size, and the viscosity model on the channel flow predictions. 51

Figure 20 Comparison of the effect of α, particle size, and the viscosity model on pipe flow predictions. 52

Figure 21 Comparison of the full two-dimensional model predictions with the marching method for an axially-developing channel flow. 54

Figure 22 Comparison of the full two-dimensional model predictions with the marching method for an axially-developing pipe flow. 55

Figure 23 Variation of the pressure drop with axial position for a suspension flow through a channel or pipe. 56

Figure 24 Variation of the cross-stream averaged particle phase concentration with axial position for a suspension flow through a channel or pipe. 57

Figure 25 The effect of geometry and N_2 on the predicted fully-developed ϕ profile. 59

Figure 26 Velocity streamlines and ϕ contours for a channel flow with a 2:1 contraction at the exit. 61

Figure 27 Sketch of the wide-gap Couette flow geometry. 67

Figure 28 Carreau viscosity fit to the experimental rheometry data of Rao *et al* (2002). 68

Figure 29 Comparison of the effect of suspended particle size on model predictions and experimental results for a wide-gap circular Couette flow with a shear-thinning suspending fluid. 73

Figure 30 Comparison of the effect of inner cylinder rotation rate on model predictions and experimental results for a wide-gap circular Couette flow with a shear-thinning suspending fluid. 74

Figure 31 Comparison of the ϕ profile for model predictions and experimental results for a wide-gap circular Couette flow with a shear-thinning suspending fluid. 76

Figure 32 Comparison of the ϕ profile for model predictions with a Newtonian suspending fluid and the experimental results with a shear-thinning suspending fluid. 78

Figure 33 Steady-state velocity and shear-rate profiles for suspension flow in a wide-gap circular Couette. 79

Figure 34 Plots of the evolution of the ϕ profile for suspension flow in a wide-gap circular Couette with Newtonian and shear-thinning suspending fluids. . 80

Figure 35 Plots of the evolution of the ϕ profile to steady state for a wide-gap circular Couette flow with a shear-thinning suspending fluid. 82

Figure 36 Polymer coils in shearing and extending flows. (taken from J. Rheol, Schunk and Scriven (1990), Figure 1) 86

Figure 37 Plot of the kinematic weighting factor, $B(\hat{\rho}_k)$. 92

Figure 38 Sketch of the flow streamlines for a pure-extensional flow and a simple-shear flow relative to the compression-tension coordinate axes. 93

Figure 39 Plot of the normal-stress difference in compression-tension coordinates as function of $\hat{\rho}_k$. 95

Figure 40 A sketch of the experimental flow apparatus used in Altobelli *et al* (1997) for an axisymmetric contraction/expansion geometry. 98

Figure 41 A sketch of the computational domain used to approximate the conditions of the Altobelli *et al* (1997) experiments. 98

Figure 42 Comparison between model predictions and experimental results for the expansion section of an axisymmetric contraction/expansion geometry. . . 99

Figure 43 Comparison of model predictions and experimental observations in the neck region of a contraction/expansion geometry. 100

Figure 44 Comparison of the effect of the contraction ratio on isotropic model predictions. 102

Figure 45 Isotropic model predictions of the flow streamlines and pressure field in a $\beta = 2$ contraction. 103

Figure 46 Isotropic model predictions of the flow streamlines and pressure field in a $\beta = 4$ contraction. 104

Figure 47 Comparison of the direction of the particle migration flux vectors for a $\beta = 2$ contraction, $\beta = 4$ contraction, and $\beta = 4$ expansion. 106

Figure 48 Comparison of the magnitude of the particle migration flux vectors for a $\beta = 2$ contraction, $\beta = 4$ contraction, and $\beta = 4$ expansion. 107

Figure 49 Comparison of the effect of the flow direction (contraction/expansion) on isotropic model predictions. 109

Figure 50 Isotropic model predictions of the flow streamlines and pressure field in a $\beta = 4$ expansion. 110

Figure 51 Surface plots of the normalized kinematic ratio, magnitude of the rate of strain, and magnitude of the relative rotation in a $\beta = 4$ contraction. . . 112

Figure 52 Plot of the kinematic weighting function, $B(\hat{\rho}_k)$, of the particle pressure for the weighted-isotropic particle stress model in a $\beta = 4$ contraction. . . 114

Figure 53 Plot of the product of the kinematic weighting function $B(\hat{\rho}_k)$ with the nonlocal shear rate at initial conditions in a $\beta = 4$ contraction. 115

Figure 54 Model predictions of the ϕ profile in a $\beta = 4$ contraction flow using an isotropic-weighted particle stress constitutive model. 116

Figure 55 Sketch of the orientation of the local compression-tension coordinates in a $\beta = 4$ contraction flow. 117

Figure 56 Plot of the extensional eigenvectors and the angle that these vectors make with the x-axis. 118

Figure 57 Plot of the geometric normal-stress difference, N_{xy}, in a $\beta = 4$ contraction flow. 120

Figure 58 Comparison of the effect of the particle normal stress on the streamlines in a rectangular $\beta = 4$ contraction. 121

Figure 59 Vector plots of the pressure gradient and particle normal stress divergence predicted with an anisotropic particle stress constitutive model, $N_{ct} = 0$. 122

Figure 60 Vector plots of the pressure gradient and particle normal stress divergence predicted with an anisotropic particle stress constitutive model, $N_{ct} = 0.2$. 123

Figure 61 Close up of the corner region for vector plots of the Newtonian pressure gradient and particle normal-stress divergence with an anisotropic model. 124

Figure 62 Predicted ϕ profiles in a $\beta = 4$ contraction using an anisotropic particle stress constitutive model. 125

Figure 63 Comparison of ϕ profile predictions with an isotropic and anisotropic particle stress constitutive model. 126

Figure 64 Sketch of the piston flow geometry. 131

Figure 65 Computation grid used for the piston-flow geometry. 133

Figure 66 Initial flow solution (unform particle concentration) for a rectangular piston-driven flow. 134

Figure 67 Plots of the evolution of the ϕ field in a piston-driven suspension flow. . . 135

Figure 68 Comparison of model predictions and experimental observations for the area averaged ϕ value along the axial length of a rectangular piston flow. 136

Figure 69 Comparison of the direction of the particle migration flux and velocity vectors for a piston-driven suspension flow. 137

Figure 70 The predicted nonlocal shear rate at the initial, uniform bulk concentration in a piston-driven suspension flow. 138

Figure 71 Sketch of a channel with an obstruction. 141

Figure 72 Computational grid for a two-dimensional, rectangular channel with an obstruction, $b_1/b_2 = 1/3$. 141

Figure 73 Streamline plots for a channel flow with an obstruction. 142

Figure 74 The predicted nonlocal shear rate for a channel flow with an obstruction. 143

Figure 75 The ϕ field results for an obstructed channel flow near the obstruction. . 144

Figure 76 Contour plots of the ϕ field for a channel with and without an obstruction. 145

Figure 77 Comparison of the axial evolution of the ϕ profile in a channel flow with and without an obstruction. 146

Figure 78 Comparison of the cross-stream ϕ profile far away from the obstruction with that of an un-obstructed channel flow. 147

SUMMARY

A suspension flow model based on the "suspension balance" approach (Nott and Brady, 1994, Morris and Boulay 1999) has been developed. This work modifies the model to allow the solution of suspension flows under general flow conditions. This requires the development of a frame-invariant constitutive model for the particle stress which can take into account the spatially-varying local kinematic conditions. The mass and momentum balances for the bulk suspension and particle phase are solved numerically using a finite volume method. The method is termed the "solver-evolver" because of the form of the update algorithm: first, the flow equations are "solved" for a given particle concentration field, $\phi(\mathbf{x})$, and then the flow information is used to update, or "evolve," this $\phi(\mathbf{x})$ field. The particle stress is based upon the computed rate of strain and the local kinematic conditions, which impact primarily the potentially anisotropic normal stress. A nonlocal stress contribution corrects the continuum approximation of the particle phase for finite particle size effects. Local kinematic conditions are accounted through the local ratio of rotation to extension in the flow field. The coordinates for the stress definition are the local principal axes of the rate of strain field.

The developed model is applied to a range of problems. (*i*) Axially-developing conduit flows are computed and model predictions compared to experimental results for cross-stream particle concentration profiles and axial development lengths. Good agreement is found in comparison between the full two-dimensional solution and the more computationally efficient "marching" method which takes advantage of the small axial gradients of these flows. (*ii*) Model predictions are compared to experiments for wide-gap circular Couette flow of a concentrated suspension in a shear-thinning liquid. With minor modification, the suspension flow model predicts the major trends and results observed in this flow. (*iii*) As an example of a complex-geometry suspension flow, a sharp-edged contraction

flow is studied. Comparisons are made to experiments for an axisymmetric contraction-expansion. The influence of model formulation on the two-dimensional planar contraction flow is explored. Model predictions are obtained for variations of the magnitude of an isotropic particle normal stress with local kinematic conditions, and allowing anisotropy in the in-plane normal stresses. The formulation of the particle phase stress is found to have significant effects on the solid fraction and velocity. (*iv*) Finally, for two other complex flow fields, a rectangular piston-driven flow and an obstructed channel flow, a "computational suspension dynamics" study explores the effect of particle migration on the bulk flow field, system pressure drop and particle phase composition.

CHAPTER 1

INTRODUCTION AND BACKGROUND

Many important and practical applications contain solid-liquid suspensions flows. Ceramic injection molding involves the flow of a highly concentrated particulate suspension into a mold. The process objective is to pack as much ceramic powder as possible into the suspension while maintaining the necessary fluidity. For these suspensions, some rheology measurements have been taken but very little attention has been given to predicting flow behavior through the use of models (Mutsuddy and Ford, 1995). Textile inkjet printing can involve two-phase dyes, consisting of pigment molecules encapsulated into hydrophilic carrier particles. These particles can jam print heads or distribute unevenly on the deposited surface if experimental conditions are not right. Other practical applications include proppant transport in petroleum and natural gas wells, solid rocket propellant processing (Husband, 1989), paper coating, paper manufacturing, electro-rheological and magneto-rheological fluids (von Pfeil *et al*, 2003) or any number of other solid-liquid slurry flows. All these applications would benefit from the addition of a general, rigorous suspension flow model.

Current methods of study include experimental investigation, particle tracking simulations (Brady *et al*, 1988; Dratler and Schowalter, 1996; Phung, Brady and Bossis, 1996; Singh and Nott, 2000) based on methods such as Stokesian dynamics (Brady and Bossis, 1988) and continuum based modeling approaches (Nott and Brady, 1994; Mills and Snabre, 1995; Phillips *et al*, 1992; Morris and Boulay, 1999). Both experimental studies and particle tracking simulations provide valuable insight into specific systems, but are time consuming and the results are not easily generalized. Continuum based modeling approaches approximate the particle phase as a pseudo-continuum. By representing the particle phase concentration as a field variable governed by an additional conservation equation, the continuum based approaches are in a format readily adaptable to coupling with current computational

fluid dynamics (CFD) solvers. This makes them a powerful tool for the modeling of solid-liquid suspension flows and can provide insight into a broad number of problems.

The objective of this work is to develop a frame-invariant normal stress based rheological model for concentrated particulate suspensions and to use this model to predict suspension flow in general geometries. The modeling approach is based on the suspension balance model of Nott and Brady (1994) with the fundamental modifications made by Morris and Boulay (1999). The basic development of this modeling approach is presented in Chapter 2 along with the method used to discretize the transport equations, which is a finite volume method. This results in a working computational tool, which we call the "solver-evolver" approach. It is called this because each time step is broken up into two pieces. First, the flow equations are "solved" for a given particle concentration field and then the flow information is used to update, or "evolve," the particle volume fraction field. Chapter 3 presents a study of particle migration in axially developing flows, specifically rectangular and circular conduits. The entrance lengths and steady-state particle concentration profiles are predicted for a number of different experimental and model conditions. In Chapter 4, a circular wide-gap Couette flow with a non-Newtonian suspending fluid is examined. Chapter 5 illustrates the formulation of the particle phase constitutive model in a frame invariant manner for general flow conditions. Various formulations of the particle phase constitutive law are explored and what effect these variations have on the flow through a sudden contraction or expansion is examined. Chapter 6 probes various general flow problems utilizing "computational suspension dynamics" to study a rectangular piston-driven channel flow and a rectangular channel flow with an obstruction. Finally, Chapter 7 puts this work into context with the current state of suspension flow research and illustrates research directions for the future.

1.1 Suspension forces

We divide the forces significant in a two-phase particulate suspension into two categories: non-hydrodynamic forces and hydrodynamic forces. The non-hydrodynamic forces are present at all times and include Brownian motion, interparticle interactions, and external field effects such as gravity or imposed electrical and magnetic fields. Brownian motion

results from the random thermal fluctuations of the particles and is significant when the particle length scale is less than 1 μm. Interparticle interactions include short-range forces such as hard-sphere repulsion or van der Waals forces. The influence of gravity is significant if the densities of the two phases do not match and electric/magnetic fields are important if the particulate phase carries a charge or has significant polarization (Russel, Saville and Schowalter, 1989). The balance between these forces determines the equilibrium particle phase structure or configuration. Hydrodynamic forces present themselves only in an imposed flow field and include particle inertia and viscous interactions between the particulate phase transmitted through the fluid.

We limit our focus to non-colloidal ($Pe = \dot{\gamma}a^2/D_o \rightarrow \infty$), non-inertial ($Re_p = \dot{\gamma}a^2\rho_p/\eta_o \rightarrow 0$) particles with no external field effects except gravity. The particle Reynolds number, Re_p, represents the balance between the particle inertia and the viscous forces of the fluid where $\dot{\gamma}$ is the shear rate of the flow field, a is the radius of a particle, ρ_p is the density of a particle and η_o is the viscosity of the fluid phase. The Peclét number, Pe, represents the balance between shear and Brownian forces in the suspension flow, where D_o is the Brownian diffusion coefficient for an isolated particle. In addition, we focus on rigid, spherical bodies which eliminates the need to account for particle orientation or deformation. The only interparticle interactions considered are short range ($\sim O(a)$) repulsive forces or roughness, which can account for certain observed non-Newtonian suspension behavior (Brady and Morris, 1997), as noted below. This leaves hydrodynamic interactions as the dominant influence on the particle phase.

Hydrodynamic forces result from the continuum nature of a fluid. A discrete fluid element deforms with the stress induced by a flow field. A rigid particle, taking the place of this fluid element, reacts differently. As shown in Figure 1, it resists deformation and pushes back on the fluid. This causes a local stress field around the particle which affects the local velocity field. If particles are close enough together, like in a concentrated suspension, they feel the influence of the particles around them. This leads to hydrodynamic interactions between the particles and can effect the bulk flow field.

The work of Batchelor and Green (1972) found that for a dilute suspension of spheres

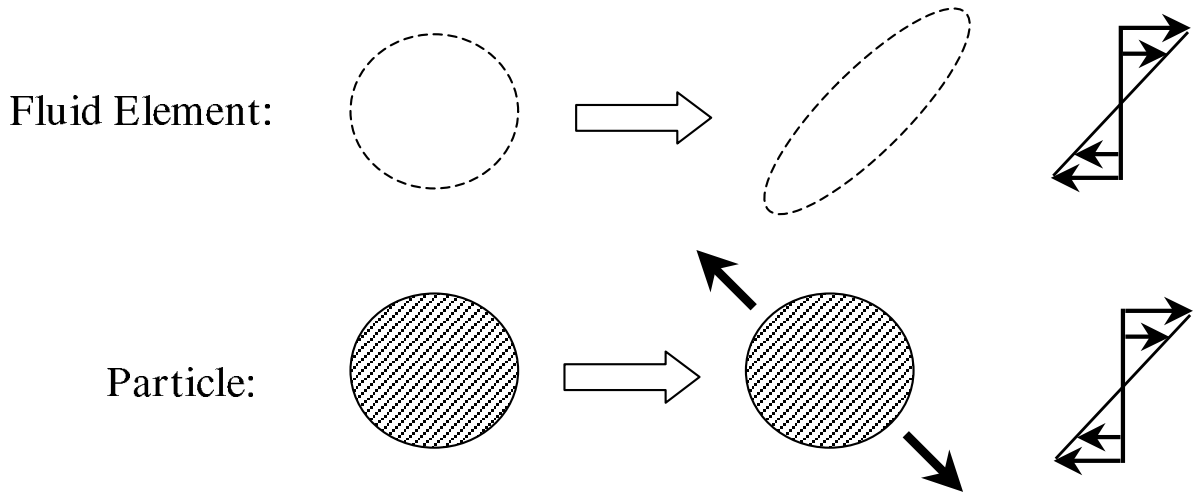

Figure 1: Imposed flow field effects on a fluid element versus a rigid, suspended particle.

with hydrodynamic interactions only ($Pe \to \infty$), the predicted microstructure of the suspension from analytical relationships maintains spherical symmetry. This implies that such suspensions behave in a Newtonian fashion. For a weakly sheared suspension ($Pe \ll 1$), Batchelor (1977) found the microstructure to be asymmetric with a build up of particles in the extensional quadrant of a shear flow. An asymmetric microstructure can account for the non-Newtonian behavior and normal stresses observed in the suspension flows discussed in the next section. However, these flows occur in a flow regime where the Peclét number is large, such as in the experimental findings of Parsi and Gadala-Maria (1987) where $Pe = 3 \times 10^5$ or the simulation results of Phung *et al* (1996) where $Pe \leq 10^4$. The work of Brady and Morris (1997) addresses this issue through the analytical prediction of an $O(aPe^{-1})$ boundary layer surrounding each particle. In this boundary layer, the hydrodynamic advection of particles toward one another is balanced by weak Brownian diffusion or interparticle forces. The effect of this boundary layer leads to the asymmetric particle microstructure and non-Newtonian behavior. They further show that the interparticle forces can result from surface discontinuities or particle "roughness." This leads to the conclusion that to observe the behavior predicted by Batchelor and Green (1972), infinitesimally

smooth particles must be used.

1.2 Shear induced particle migration

Leighton and Acrivos (1987) first recognized and described shear-induced particle migration as a way to explain anomalies observed in a Couette viscometer. Since then, shear-induced migration has been observed in a number of other two-phase flow experiments and simulations. Koh, Hookham and Leal (1994) and Lyon and Leal (1998a) observed the migration of monodisperse spherical particles in pressure driven channel flow experiments while Nott and Brady (1994) observed such behavior in particle tracking simulations of channel flow. Hampton *et al* (1997) experimentally observed particle migration in pressure driven pipe flow. In these cases, particles migrate from regions of high shear (near the walls) to regions of low shear (the centerline). In addition, a number of curvilinear flows have been studied including wide-gap circular Couette flow, parallel-plate torsional flow and small angle cone-and-plate torsional flow. In wide-gap Couette flow, Abbott *et al* (1991) and Phillips *et al* (1992) observed particles migrating away from the rotating inner cylinder, a region of high shear. Chapman (1990) and Chow *et al* (1994) observed little to no particle migration in a parallel-plate torsional flow while Chow *et al* (1995) observed migration radially outward from the cone apex in a torsional cone-and-plate flow. The last two results do not follow the assumption of migration from regions of high to low shear. If this held, the particles would have migrated radially inward from the higher shear experienced on the outer edges of the plate in the parallel-plate torsional flow and there would have been no migration in the cone-and-plate torsional flow where the shear rate remains constant throughout the domain, leaving no shear rate gradients to drive particle migration. This suggests that some other "forces" in the suspension must be driving particle migration.

Morris and Boulay (1999) suggest that normal stresses generated by the interaction of the particles drive particle migration in suspension flows. Gadala-Maria (1979), Laun (1994), Zarraga, Hill and Leighton (2000) and Singh and Nott (2003) have experimentally observed normal stresses in particulate suspensions. In addition, simulations by Phung *et al* (1996) and Singh and Nott (2000) have revealed the existence of normal stresses over a

broad range of experimental parameters in both bounded and unbounded shear flow. The experimental results of Zarraga *et al* (2000), utilizing multiple experimental techniques to fully characterize the normal stress state of a particulate suspension in shear flow, observe similar values for the normal stress differences as those proposed in the modeling efforts of Morris and Boulay (1999).

1.3 Modeling efforts

There are two main types of continuum based modeling approaches in use. One is the phenomenological approach which utilizes experimentally observed behavior and scaling arguments to form an expression for particle migration. Based on the scaling arguments of Leighton and Acrivos (1987), the diffusive flux model of Phillips *et al* (1992) assumes that particle migration is driven by local particle-particle interaction frequency and viscosity variation. This leads to a particle migration flux, $j_\perp$, which is proportional to the local shear rate gradient, $j_\perp \sim \nabla\dot{\gamma}$. The particle migration flux represents the movement of the particle phase relative to the motion of the bulk suspension. The diffusive flux method captures basic particle migration phenomena but breaks down in its initial unaltered state for flows with curved streamlines, such as cone-and-plate and parallel plate torsional flows. A number of studies have worked to extend the diffusive flux model to more generalized applications (Zhang and Acrivos, 1994; Subia *et al*, 1998; Rao *et al*, 2002; Fang *et al*, 2002), but none of these extensions are based on solid physical principles. Instead, they represent attempts to "fit" the model to general conditions.

Another approach is the suspension balance model, based on averaging the mass and momentum conservation equations over the particle phase to form a particle phase transport equation. This approach, presented in Nott and Brady (1994), requires a constitutive model for the particle phase stress, $\mathbf{\Sigma}_\mathrm{P}$, which drives migration through the particle migration flux, $j_\perp \sim \nabla \cdot \mathbf{\Sigma}_\mathrm{P}$. The form of the constitutive model is based on rheological theory and experiment and contains experimentally accessible quantities such as stress and shear rate. Nott and Brady (1994) propose a form of $\mathbf{\Sigma}_\mathrm{P}$ with an isotropic particle phase pressure while Morris and Boulay (1999) illustrated the importance of anisotropy and normal stress

difference effects for predictions of migration in curvilinear flows.

For our work here, we choose to build on the suspension balance approach of Nott and Brady (1994) with the anisotropic particle stress law introduced in Morris and Boulay (1999). This places our key focus on the proper formulation of the particle stress constitutive model. In this study, we generalize the particle stress model of Morris and Boulay (1999) for application to general geometries. This involves careful consideration of the frame of reference used to define the model parameters. In addition, local kinematic effects on the particle stress relationship need to be addressed. The consideration of kinematic effects in a constitutive definition has been shown to work for polymer solutions (Schunk and Scriven, 1990; Ryssel and Brunn, 1999a,b), but has not been completely considered for suspension flows, even in the few cases where it has been addressed (Fang *et al*, 2002). We illustrate through our work here a method to account for general flow conditions in the particle stress model and use this constitutive relationship to model suspension flow for a number of general geometries, including a sharp-edged contraction flow, an expansion flow, a rectangular piston-driven flow and a channel flow with an obstruction near the entrance.

CHAPTER 2

COMPUTATIONAL TOOL: SOLVER-EVOLVER

This section explains the development of a computational tool used to solve the suspension flow problems presented here. We base the work on the suspension balance model of Nott and Brady (1994) with the fundamental modifications made by Morris and Boulay (1999). These studies both illustrate particle volume fraction, ϕ, dependent stress leading to particle phase migration. Morris and Boulay (1999) further this by highlighting the importance of normal stress differences in predicting particle migration in curvilinear flows. The objective of our work is to further the development of this modeling approach into flows of a general nature. In Chapter 5, we extend the application of the model to general flow geometries through modification of the particle stress constitutive model.

The model is implemented for two-dimensional, Cartesian geometries (x,y) as well as for two-dimensional, axisymmetric flows (z,r). The finite volume method (FVM) is utilized for the spatial discretization of the transport equations. The resulting computer code is built of a series of MATLAB script files run in a PC environment. This allows flexibility in the implementation and provides adequate computational speed for the two-dimensional geometries considered.

The method is called the "solver-evolver" approach due to the way the flow field and particle migration equations are coupled. In one computational step, the flow field, $\mathbf{u}(\mathbf{x})$, is determined for a given particle volume fraction, $\phi(\mathbf{x})$. This flow field solution then provides the necessary stress information to determine the change in the ϕ field over a single explicit time step. This sequence of steps is repeated to provide the solution of the $\mathbf{u}$ and ϕ fields as they evolve over time. In addition, this approach allows for the use of alternate flow solvers, such as commercial CFD packages, as long as they can handle a spatially varying viscosity and user defined source terms.

The goal of this chapter is to provide a general overview of the suspension flow model

and numerical implementation. In Section 2.1, we present the development of the model, leaving detailed explanation of the extension of the constitutive model to general geometries for later chapters. In Section 2.2, a summary of the finite volume method approach is provided, along with details for the implementation of the suspension flow model utilizing the FVM. In Section 2.3, we verify the flow field solution of the FVM code for the flow of a Newtonian fluid through a complex geometry, specifically a sharp-edged contraction. In addition, we compare numerical and analytical solutions of particle migration in a channel flow.

2.1 Governing Equations

The governing equations are established for the flow of suspensions of rigid, spherical particles in a Newtonian fluid. We assume viscous conditions and non-Brownian particles with no external field effects except gravity. This results in hydrodynamics as the dominant interaction between the particles.

For the flows considered, it is assumed that the Reynolds number is sufficiently small that bulk inertia has little influence, $Re = \langle\rho\rangle U_s L_s/\eta_o \ll 1$ where $\langle\rho\rangle$ is the mixture density, U_s and L_s are the velocity and length scales of the bulk flow, and η_o is the suspending fluid viscosity. For the suspended particle phase, the particle radius, a, is represented through the ratio, $\epsilon = a/L_s$. We assume ϵ is small enough to allow the continuum description of the particle phase to remain valid, a point which is explored in more detail in Chapter 3 through the discussion of a nonlocal stress correction in Section 3.1.1. The particle Reynolds number, given by $Re_p = \epsilon^2 Re$, is assumed to be vanishingly small. Note that the assumption of an inertia free bulk flow can be relaxed while still maintaining $Re_p \ll 1$, although we do not address finite-Re flows here.

2.1.1 Suspension balances

Description of the flow for a two-phase suspension requires mass and momentum balances for either the bulk suspension and one of the components, or alternatively for each component. We choose to consider balances for the bulk mixture and particle phase, an approach motivated by the work of Nott and Brady (1994). The equations are developed by assuming

that the particle phase can be approximated as a continuum, as noted above. An ensemble average, as explained in Drew and Lahey (1993), is taken of the mass and momentum equations over the bulk suspension (fluid and particle phases) and over the particle phase only. This development (Nott and Brady, 1994; Morris and Boulay, 1999) leads (with $Re \ll 1$ eliminating unsteady and inertial terms) to the suspension mass and momentum balances, respectively given by

$$\nabla \cdot \mathbf{u} = 0, \tag{1}$$

$$\nabla \cdot \mathbf{\Sigma} + \langle \rho \rangle \mathbf{g} = 0, \tag{2}$$

where $\mathbf{u}$ is the bulk suspension velocity, $\mathbf{\Sigma}$ is the bulk suspension stress, and $\langle \rho \rangle \mathbf{g}$ is the mean gravity force. For neutrally-buoyant particles, the gravitational body force may be absorbed into the hydrostatic pressure and this term will thus not appear. The particle-phase mass balance is

$$\frac{\partial \phi}{\partial t} + \nabla \cdot (\phi \mathbf{u_p}) = 0, \tag{3}$$

which may be expressed by virtue of the incompressibility of the bulk flow as

$$\frac{\partial \phi}{\partial t} + \mathbf{u} \cdot \nabla \phi = -\nabla \cdot \mathbf{j}_\perp. \tag{4}$$

In this expression, the term $\mathbf{j}_\perp = \phi(\mathbf{u_p} - \mathbf{u})$ is the particle migration flux which is the particle flux relative to the bulk motion. The term $\mathbf{u_p}$ is the particle phase average velocity and ϕ is the particle phase volume fraction. The subscript $\perp$ is used to emphasize the usual focus on the cross-stream migration. The migration flux may be obtained from the particle momentum balance, given by

$$0 = \nabla \cdot \mathbf{\Sigma}_{\mathrm{P}} + n < \mathbf{F}^H > + \phi \Delta \rho \mathbf{g}, \tag{5}$$

where $n = 3\phi/4\pi a^3$ is the number density of particles, $\Delta\rho = \rho_p - \rho_f$ is the excess density of the particles, and $\mathbf{\Sigma}_{\mathrm{P}}$ the particle contribution to the bulk stress. By noting that for Stokes flow the mean drag force, $< \mathbf{F}^H >$, may be modeled as analogous to the drag in sedimentation, we set

$$< \mathbf{F}^H > = -6\pi\eta a f^{-1}(\phi)(\mathbf{u_p} - \mathbf{u}). \tag{6}$$

The sedimentation hindrance function, $f(\phi)$, represents the mean mobility of the particle phase, and thus f^{-1} is the mean resistance. Substituting Eq. (6) into Eq. (5), we obtain

$$\mathbf{j}_\perp = \phi(\mathbf{u_p} - \mathbf{u}) = \frac{2a^2}{9\eta_o} f(\phi)[\nabla \cdot \mathbf{\Sigma}_\mathrm{P} + \phi \Delta\rho \mathbf{g}]. \tag{7}$$

Since we will consider only neutrally-buoyant particles, $\Delta\rho = 0$.

2.1.2 Suspension stress law

We take $\mathbf{\Sigma} = \mathbf{\Sigma}_f + \mathbf{\Sigma}_\mathrm{P}$ as the form for the bulk suspension stress, where $\mathbf{\Sigma}_f$ is the fluid phase contribution and $\mathbf{\Sigma}_\mathrm{P}$ is the particle phase contribution. The fluid phase stress is assumed to be

$$\mathbf{\Sigma}_f = -\langle P \rangle_f \underline{\underline{\delta}} + 2\eta_o \mathbf{E}, \tag{8}$$

where $\langle P \rangle_f$ is the fluid phase averaged pressure which will be referred to as simply P, $\underline{\underline{\delta}}$ is the identity tensor, $\mathbf{E}$ is the local rate of strain defined as $\mathbf{E} = \frac{1}{2}[\nabla \mathbf{u} + (\nabla \mathbf{u})^T]$, and η_o is the viscosity of the suspending liquid. The constitutive law for the particle stress is that suggested by Morris and Boulay (1999) for shear flows,

$$\mathbf{\Sigma}_\mathrm{P} = -\eta_o \eta_n(\phi) \dot{\gamma} \mathbf{Q} + 2\eta_o \eta_p(\phi) \mathbf{E}, \tag{9}$$

and contains both shear and normal stress portions.

The particle contribution to the shear stress, $\mathbf{\Sigma}_\mathrm{P}^{SH} = 2\eta_o \eta_p \mathbf{E}$, combines with $2\eta_o \mathbf{E}$ from the fluid stress and can be represented using a ϕ-dependent shear viscosity in the bulk stress, $\bar{\eta}_s = \eta_o \eta_s(\phi) = \eta_o(1 + \eta_p)$. This viscosity can be modeled using a number of different forms, including

$$\begin{aligned} \text{Morris and Boulay (1999)}^1 \quad &: \quad \eta_s(\phi) = 1 + 2.5\phi_m \frac{(\phi/\phi_m)}{(1 - \phi/\phi_m)} + \frac{K_s(\phi/\phi_m)^2}{(1 - \phi/\phi_m)^2}, \\ \text{Krieger (1972)} \quad &: \quad \eta_s(\phi) = (1 - \phi/\phi_m)^{-m}, \end{aligned}$$

where ϕ_m is the maximum packing particle volume fraction and K_s and m are rheological fitting parameters (see Figure 2a); we use $\phi_m = 0.68$, $m = 2$, $K_s = 0.1$ here.

The normal stress is given by $\mathbf{\Sigma}_\mathrm{P}^{NS} = -\bar{\eta}_n \dot{\gamma} \mathbf{Q}$ where $\bar{\eta}_n = \eta_o \eta_n(\phi)$. The "normal stress viscosity," $\eta_n(\phi) = K_n(\phi/\phi_m)^2(1 - \phi/\phi_m)^{-2}$ captures the ϕ dependence of the magnitude

[1] This form corrects a typographical error in Morris and Boulay (1999).

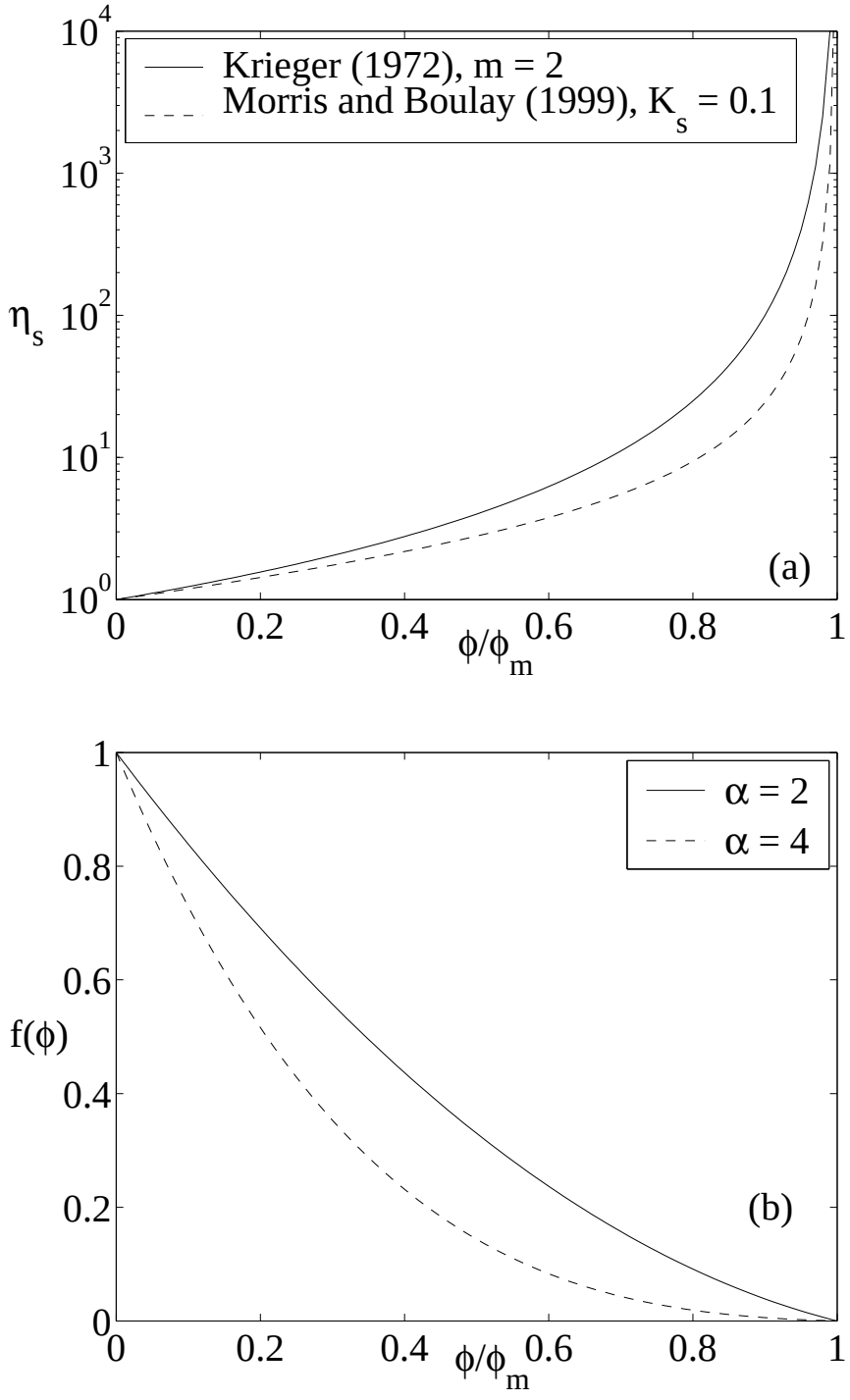

Figure 2: (a) Shear viscosity models, η_s; (b) modified sedimentation hindrance function, $f(\phi) = (1 - \phi/\phi_m)(1 - \phi)^{\alpha-1}$, where $\phi_m = 0.68$ is the assumed maximum packing fraction.

of this stress and takes its form from Morris and Boulay (1999) with $K_n = 0.75$ to match experimental data (Phillips *et al*, 1992). The shear rate, $\dot{\gamma} = \sqrt{2\mathbf{E} : \mathbf{E}}$, gives the stress its dependence on the strength of the local flow. The tensor parameter $\mathbf{Q}$ captures the anisotropy of the normal stress with the form

$$\mathbf{Q} = \begin{pmatrix} 1 & 0 & 0 \\ 0 & \lambda_2 & 0 \\ 0 & 0 & \lambda_3 \end{pmatrix}, \tag{10}$$

where $\lambda_2 \approx 0.8$ and $\lambda_3 \approx 0.5$ provide reasonably good agreement with concentrated suspension rheology (Zarraga, Hill and Leighton, 2000) and with observed migration behavior in viscometric flows (Phillips *et al*, 1992; Chow *et al*, 1994). The directions of $\mathbf{Q}$ correspond to the principal directions of a viscometric shear flow with 1, 2 and 3 denoting flow, gradient, and vorticity, respectively.

In general flow conditions, the determination of the local principal directions for the flow becomes less obvious. Local kinematics can vary spatially within the flow which leads to a non-uniform environment for the particle phase. These local kinematics define the particle stress which in turn drives the particle migration. In Chapter 5, the formulation of a constitutive model for the particle stress under spatially varying kinematic conditions is discussed.

The combination of the above definitions for fluid and particle phase stress results in a bulk stress definition of

$$\mathbf{\Sigma} = -P\underline{\underline{\delta}} + 2\eta_o\eta_s\mathbf{E} + \mathbf{\Sigma}_{\mathrm{P}}^{NS}, \tag{11}$$

where $\mathbf{\Sigma}_{\mathrm{P}}^{NS}$ is the particle-phase normal stress, *i.e.* the first term on the right hand side of Eq. (9).

We set $f(\phi)$ to a form similar to the sedimentation hindrance function described in Richardson and Zaki (1954),

$$f(\phi) = (1 - \phi/\phi_m)(1 - \phi)^{\alpha - 1}, \tag{12}$$

but alter the original form for the bounded flows studied here. This is done to ensure that particle migration ceases when the particle concentration approaches maximum packing,

ϕ_m. The parameter, α, is given by Richardson & Zaki (1954) as α = 2-5, and we have used values in the range $2 \leq \alpha \leq 4$ (see Figure 2b).

2.2 Numerical Implementation

We utilized the finite volume method (FVM) as illustrated in Patankar (1980) and Ferziger and Peric (2002) for the spatial discretization of Eq. (1), Eq. (2), and Eq. (4). This method proves advantageous due to the conservative nature of its construction which enforces mass and momentum conservation over each computational element or control volume (CV) by balancing the fluxes between one CV and its neighbors. In addition, its relative ease of implementation allows more flexibility in the numerical set-up and solution than a finite element implementation or commercial software package.

In the FVM, the solution domain is divided up into a finite number of elements, which we will call cells. The cell arrangement utilizes a structured, Cartesian grid with the capability of refinement in regions of interest. Each cell contains nodes at the center, wall mid-points and corners as illustrated in Figure 3. The dependent variables are stored in a fully-staggered arrangement, which means P and ϕ are solved at the central node of each cell and the velocity components (u, v) are solved at the wall node normal to the velocity direction. We integrate Eq. (1) and Eq. (4) over a CV centered on the central node and integrate Eq. (2) over a CV centered on the appropriate wall node as shown in Figure 4.

The fully-staggered variable arrangement provides strong coupling of the velocity and pressure field solutions which avoids oscillations and convergence problems that can arise in a collocated variable arrangement, where all of the dependent variables are stored at the central node of the cell, as noted in Ferziger and Peric (2002). In addition, the fully-staggered arrangement eliminates some of the need for variable interpolation that a collocated arrangement requires and provides straightforward flux definitions at the various CV walls, both of which will be illustrated in the section below. The only major drawbacks include the necessity for added indexing and variable storage in the program and the possibility of complications if we move to non-orthogonal grids.

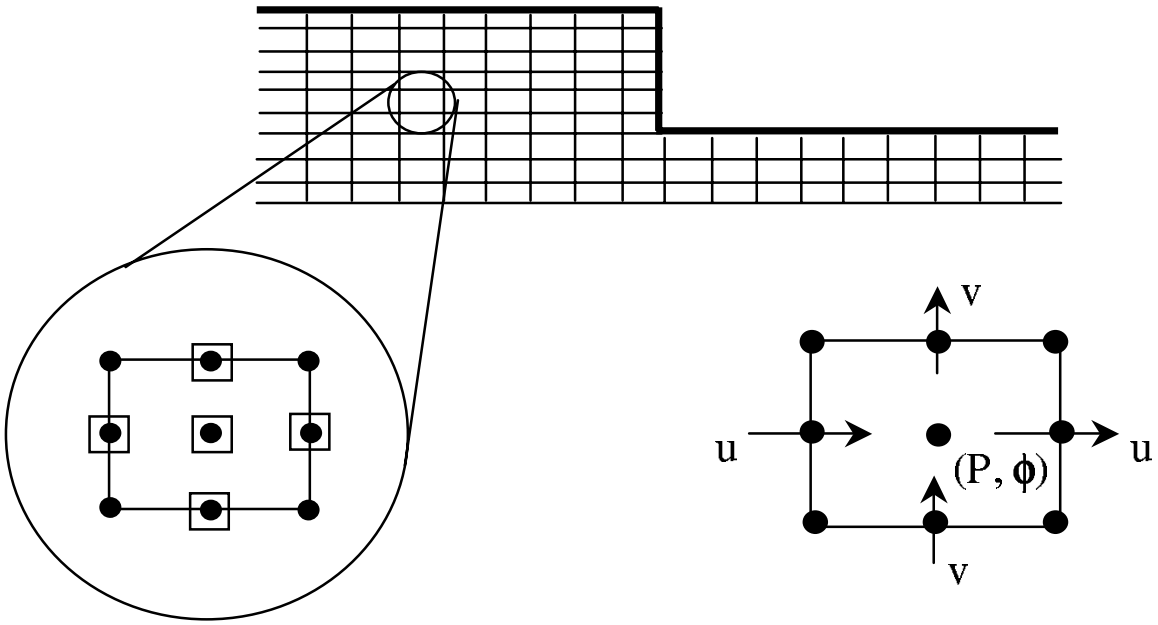

Figure 3: Fully-staggered computational grid arrangement.

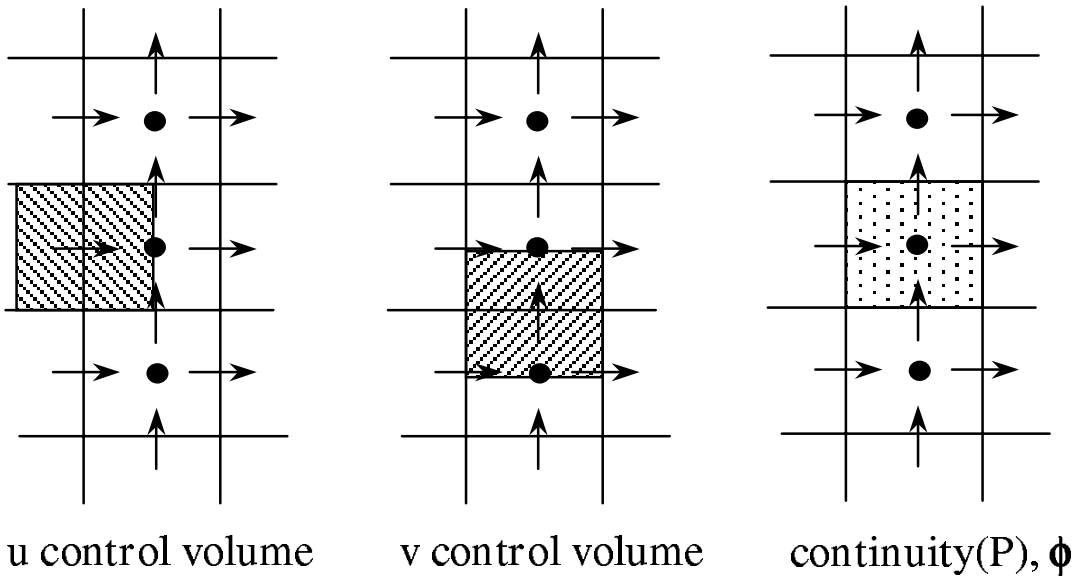

Figure 4: Illustration of control volume elements for each dependent solution variable.

2.2.1 Discretization of the transport equations

For the spatial discretization, we consider the bulk continuity (mass conservation) and momentum conservation equations, Eq. (1) and Eq. (2), and the right-hand side (RHS) of the particle phase migration equation, Eq. (4), after the following adjustment. The convection term on the left-hand side (LHS) of the equation is combined with the particle migration flux on the RHS to form an overall particle flux, $\mathbf{j}$,

$$\frac{\partial \phi}{\partial t} = -\nabla \cdot \mathbf{j} = -\nabla \cdot (\phi \mathbf{u} + \mathbf{j}_{\perp}). \tag{13}$$

The treatment of the time dependence of the migration equation is discussed in Section 2.2.2.

We begin by integrating each equation over the appropriate control volume as given in Figure 4. The Gauss theorem is applied to the divergence terms ($\nabla \cdot \mathbf{u}$, $\nabla \cdot \mathbf{\Sigma}$, $\nabla \cdot \mathbf{j}$) which converts the volume integral to an integration over the CV surface, $\int \nabla \cdot [*] \, \mathrm{d}V \rightarrow \int [*] \cdot \mathbf{n} \, \mathrm{d}A$ where $\mathbf{n}$ is the outward normal. We divide the surface integration into a sum of integrals over each CV face and approximate these using a quadrature formula that assumes the midpoint value prevails over the entire area of the face. Volume integrals not converted are approximated by assuming the integrand to be constant. This approximation results in

$$0 = \sum_{fc} [\mathbf{u} \cdot \mathbf{n}]_{fc} A_{fc}, \tag{14}$$

$$0 = \sum_{fw} [\mathbf{\Sigma} \cdot \mathbf{n}]_{fw} A_{fw}, \tag{15}$$

$$\frac{\partial \phi}{\partial t} = \sum_{fw} [\mathbf{j} \cdot \mathbf{n}]_{fw} A_{fw}, \tag{16}$$

where A_{fc} is the area of a face for a CV centered on the computational cell, A_{fw} is the area of a face for a CV centered on a wall node of the computational cell and fc, fw represent a summation over the faces of the respective CV's.

The next step is to determine the stress and flux values at the CV walls utilizing nodal data. Looking first at the bulk stress, after the substitution of the appropriate velocity gradients for the rate of strain,

$$\mathbf{\Sigma} = -P\underline{\underline{\delta}} + \bar{\eta}_s \nabla \mathbf{u} + \bar{\eta}_s (\nabla \mathbf{u})^T + \mathbf{\Sigma}_{\mathrm{P}}^{NS}, \tag{17}$$

we see there are four terms to consider. The first term represents the pressure force at the CV walls normal to the velocity direction, the second and third terms are the velocity diffusion at the CV wall, and the fourth is the influence of the particle phase normal stress at the CV wall. The third term represents an "extra" diffusion term which only has influence when $\bar{\eta}_s$ varies spatially and is eliminated by the continuity constraint when $\bar{\eta}_s$ is constant. In the staggered arrangement, the CV walls normal to the velocity direction conveniently align with the central node of the computation cells, allowing direct substitution for the pressure value at these locations. The gradients for the velocity diffusion are approximated by assuming a linear variation between the velocity values at the nodes bracketing the face, which is termed a central difference scheme (CDS). When the bulk stress of Eq. (17) is summed over the CV faces as in Eq. (15), the main diffusion term is fashioned into an expression for the velocity at the central node of the CV. We include the extra-diffusion and particle normal stress as source terms, calculating them with information from previous iterations or time steps. In a two-dimensional, axisymmetric flow, an additional curvature based source term results from the expansion of the velocity gradients and is handled in the same manner. The extra-diffusion term, calculated using CDS, is only included when variations in the $\phi(\mathbf{x})$ field cause the viscosity to vary spatially and the particle normal stress term is only included when an anisotropic stress model is used. Under isotropic conditions, the particle stress term can be lumped in with the pressure. When the normal stress is anisotropic, care must be taken to determine the effect that this term has on the flow field solution.

The resulting algebraic equations for the solution of the bulk momentum conservation are

$$a_P \mathbf{u}_P = \sum_{nb} a_{nb} \mathbf{u}_{nb} + S_u^P + S_u^D + S_u^{NS}, \tag{18}$$

where nb represents the neighboring velocity nodes, $a_{nb} = [\bar{\eta}_s A/\Delta]_{fw}$ and $a_P = \sum_{nb} a_{nb}$ with Δ corresponding to the distance between the two nodes bracketing CV face, fw. The source terms correspond to the pressure source, extra-diffusive source and normal stress source associated with velocity, $\mathbf{u}_P$.

The particle flux,

$$\mathbf{j} = \phi\mathbf{u} + \frac{2a^2}{9\eta_o} f(\phi)\nabla \cdot \mathbf{\Sigma}_{\mathrm{P}}, \tag{19}$$

consists of two terms. The first is the convective flux and the second represents the stress-induced migration flux, both calculated at the CV wall. The convective term is approximated using an upwind difference scheme (UDS) to determine the value of ϕ at the CV wall. Despite the possibility of false diffusion effects from this method (which we did not observe in our work), it avoids convergence problems due to oscillations in the ϕ field which result from taking a simple linear interpolated value (i.e. CDS) of ϕ at the CV wall. Instead the ϕ value is set equal to the node "upwind" of the velocity vector. The particle diffusion term consists of $\nabla \cdot \mathbf{\Sigma}_{\mathrm{P}}$, which we approximate with a CDS. This requires the calculation of $\Sigma_{\mathrm{P}ii}$ (where i corresponds to the direction of the particle flux) at the central nodes and $\Sigma_{\mathrm{P}ij}$ (where $i \neq j$) at the corner nodes of each cell . These terms are readily available, if we interpolate ϕ values as needed and utilize the CDS to calculate the velocity gradients in order to formulate $\mathbf{E}$ and $\dot{\gamma}$ which are required to solve for $\mathbf{\Sigma}_{\mathrm{P}}$.

2.2.2 Solution method

The spatial discretization of the conservation equations leads to algebraic expressions over each CV. Summing these expressions over all the CV's in the solution domain leads to a global system of equations. Focusing initially on just the continuity and momentum equations, we assume a constant $\phi(\mathbf{x})$ field.

The resulting system of equations for the bulk flow field presents two main issues. First, there is no independent equation for the pressure field. Second, in an incompressible flow the continuity equation contains no dominant variables to affect the momentum equations and therefore acts as a passive constraint on the flow field. To address these issues, we utilize a pressure-correction based projection method as illustrated in Ferziger and Peric (2002). Projection methods consist of constructing an approximate velocity field, which does not necessarily satisfy continuity, and then correcting this velocity field to satisfy continuity. The particular algorithm used, called the SIMPLE method presented in Patankar (1980), involves calculating the initial velocity field from an assumed pressure field solution. The

approximate velocity and pressure solutions are then corrected by calculating a pressure-correction which satisfies the continuity equation. These steps are iterated, taking the corrected pressure field as the new "guess", until the velocity field adequately satisfies continuity. To achieve convergence, under-relaxation is applied to the correction factors, with an extreme under-relaxation on the pressure field solution used here. In addition, special consideration and care is taken to achieve convergence in the case of axisymmetric flows due to the decrease in CV volume and surface area near the center or line of symmetry. The relaxation factors were set on a problem-by-problem basis, with typical values of 0.8 for the velocity relaxation and 0.005 - 0.0025 for the pressure relaxation.

In the case of an axisymmetric flow, an ad-hoc correction method was used to "push" the numerical solution toward convergence. The LHS of the velocity estimation and pressure correction, given below in Eq. (20), were multiplied by a factor which was greater than one. This was done to counter the effects of the vanishing CV volumes and surface areas near the centerline. Typical values for this factor were 100 for the velocity equations and 10 for the pressure equations. This correction, while on the surface may not seem mathematically sound, is eliminated through the pressure-correction iterations. Since the factor is applied to estimation and correction equations, it cancels itself out through the solution scheme. In the end, it serves to control the pressure correction near the center so that is does not catastrophically overshoot the solution value and lead to divergence of the numerical iterations. The algorithm used ensures that the velocity field must satisfy continuity for convergence and it produces valid results which match literature solutions for an complex, axisymmetric flow in Section 2.3.2.

This method requires two sets of linear equations to be solved for in each iteration. These equations are

$$\begin{aligned} \mathbf{A}^U\mathbf{U} &= \mathbf{S}^U, \\ \mathbf{A}^P\mathbf{P} &= \mathbf{S}^P, \end{aligned} \tag{20}$$

where $\mathbf{A}^U$, $\mathbf{A}^P$ are the global coefficient matrices for the velocity estimation and pressure correction solutions, $\mathbf{U}$ is the global velocity solution, $\mathbf{P}$ is the global pressure correction,

and $\mathbf{S}^U$, $\mathbf{S}^P$ are the global source terms. The global velocity source consists of the terms given in Eq. (18). The term, $\mathbf{S}^P$, is know as the mass source and is a measure of how close the current velocity estimate is to satisfying continuity. This term is used as the convergence criteria for the SIMPLE iterations ($\mathbf{S}^P \rightarrow 0$).

The coefficient matrices are set-up utilizing the sparse matrix capabilities in MATLAB and solved with the built in direct solver. The MATLAB direct solver tests the coefficient matrix, $\mathbf{A}$, to determine the best solution method. The algorithm involves first testing to see if $\mathbf{A}$ is triangular or a permutation of a triangular matrix. If not, it attempts to convert the matrix solution to series of triangular solutions through Cholesky or LU factorization (MathWorks, 2002).

After the flow field solution is determined, we solve for a new ϕ field using Eq. (16) and Eq. (19). The LHS of Eq. (16) is integrated over the appropriate CV and approximated as an explicit time step. This allows calculation of the RHS with information from the flow field solution and previous ϕ time step. While this formulation leads to some stability issues and requires the use of small time steps when fine spatial resolution is needed, it provides great flexibility in the implementation of complex constitutive models for $\mathbf{\Sigma}_\mathrm{P}$. Without the necessity of an implicit ϕ field solution, changes to the model can be readily made without the necessity to alter the solution algorithm.

2.3 Numerical Verification

To verify the FVM flow solver in a general geometry, we solved for the Newtonian flow solution in a sharp-edged contraction flow for both the two-dimensional planar and axisymmetric cases. A sketch of the conditions for the contraction flow is given in Figure 5. The inlet is set to a unidirectional, parabolic profile while at the outlet the velocity gradients normal to the outlet plane are set equal to zero. In addition, the pressure is set equal to zero at the outlet to provide a frame of reference for the pressure field solution. The walls are assumed to be no-slip (u = v = 0) and the centerline is set to a symmetric boundary which means that the velocity normal to the centerline is set equal to zero and the velocity gradients tangent to the centerline are set equal to zero. These boundary conditions are

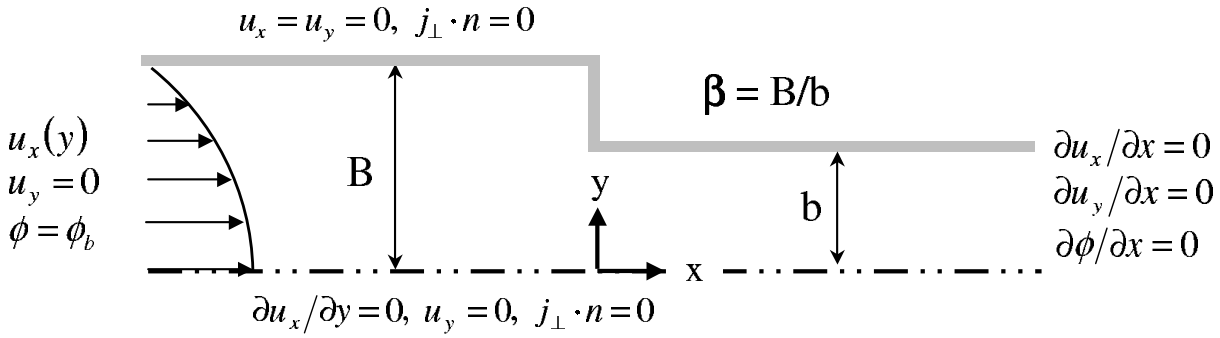

Figure 5: Sketch of a of sharp-edged contraction geometry.

the same for the axisymmetric case (which is essentially the planar solution equations with curvature terms) except that the coordinate directions are changed from (x, y) to (z, r).

The half-width/radius of the upstream section is labelled B while the downstream dimension is labelled b. We define the term β as the contraction ratio, which is the ratio of the upstream dimension to the downstream dimension ($\beta = B/b$). For verification purposes, we solved a $\beta = 4$ planar contraction to compare to the numerical data of Mompean (2002) and Bao (2002). For the axisymmetric contraction, we solved a $\beta = 2$ geometry to compare to the numerical data of Christiansen, Kelsey and Carter (1972) and Kelsey (1971).

The computation grid used for the contraction flow solutions is shown in Figure 6. This grid is for a $\beta = 4$ rectangular contraction, but is similar to the one used for the $\beta = 2$ axisymmetric contraction. The grid is refined in the y-direction around the corner and through the neck region ($y < 0.5$) to a value of $dy = 0.025$ with $dy = 0.05$ away from the corner. This is the same mesh as for the axisymmetric contraction (with dr replacing dy) except that the entire neck region is not refined. Instead only the region by the corner, $r_{cnr} \pm 0.25$ where $r_{cnr} = 0.5$, is refined to $dr = 0.0025$ with the rest of the domain at $dr = 0.05$. In the axial direction, the grid refinement is the same for both the planar (dx) and axisymmetric (dz) cases. The immediate vicinity of the corner, $x_{cnr} \pm 0.1$, is refined to a value of $dx = 0.025$, which is equal to that of the cross-stream direction. This sets

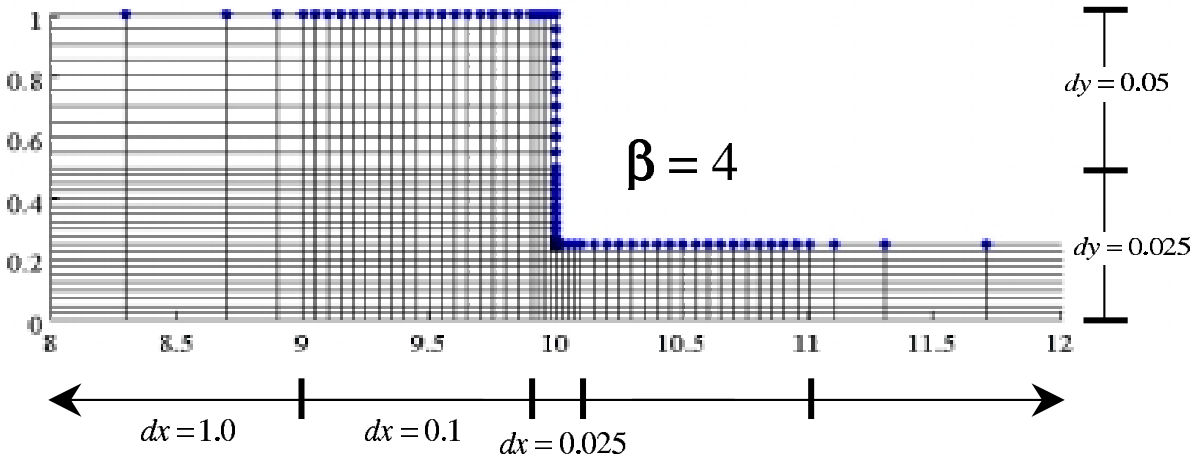

Figure 6: Typical computational grid for a contraction flow geometry.

the cell immediately next to the contraction corner to be square in shape. In the range, $x_{cnr} \pm 0.1$ to $x_{cnr} \pm 1.0$, the axial spacing is equal to $dx = 0.1$ and finally expands to a value of $dx = 1.0$ for the rest of the upstream/downstream domain. The figure only shows a portion of the computational grid, whereas the full domain goes from $x_{cnr} \pm 10$.

2.3.1 Flow of a Newtonian fluid through a planar $\beta = 4$ contraction

The flow solution for a rectangular, $\beta = 4$ contraction is presented in Figure 7. It can be seen that the maximum axial velocity increases from $u_{max} = 1$ to the expected $u_{max} = 4$ in the transition from the larger to smaller channel section. In addition, a corner vortex forms in the region upstream of the contraction. The size of this vortex is $x_{vort} = 0.354$, $y_{vort} = 0.488$ as illustrated on the streamline plot in Figure 7.

Both Bao (2002) and Mompean (2002) solved the two-dimensional mass and momentum balance equations for a low-Reynolds-number flow of a Newtonian fluid into sharp-edged, planar contraction at the ratio $\beta = 4$. Bao utilized a finite element approach while Mompean used a finite volume approach, as was done here. Bao predicts $x_{vort} = 0.334$. In addition from streamline plots in the paper, it is evident that $y_{vort} > x_{vort}$ was predicted in their results as well with $y_{vort} \approx 0.5$. Mompean predicts an $x_{vort} = 0.36$ which is very close to the value predicted here. In both cases, the literature data matches our predicted vortex size relatively well and provides an independent verification of the code for a 2-D planar

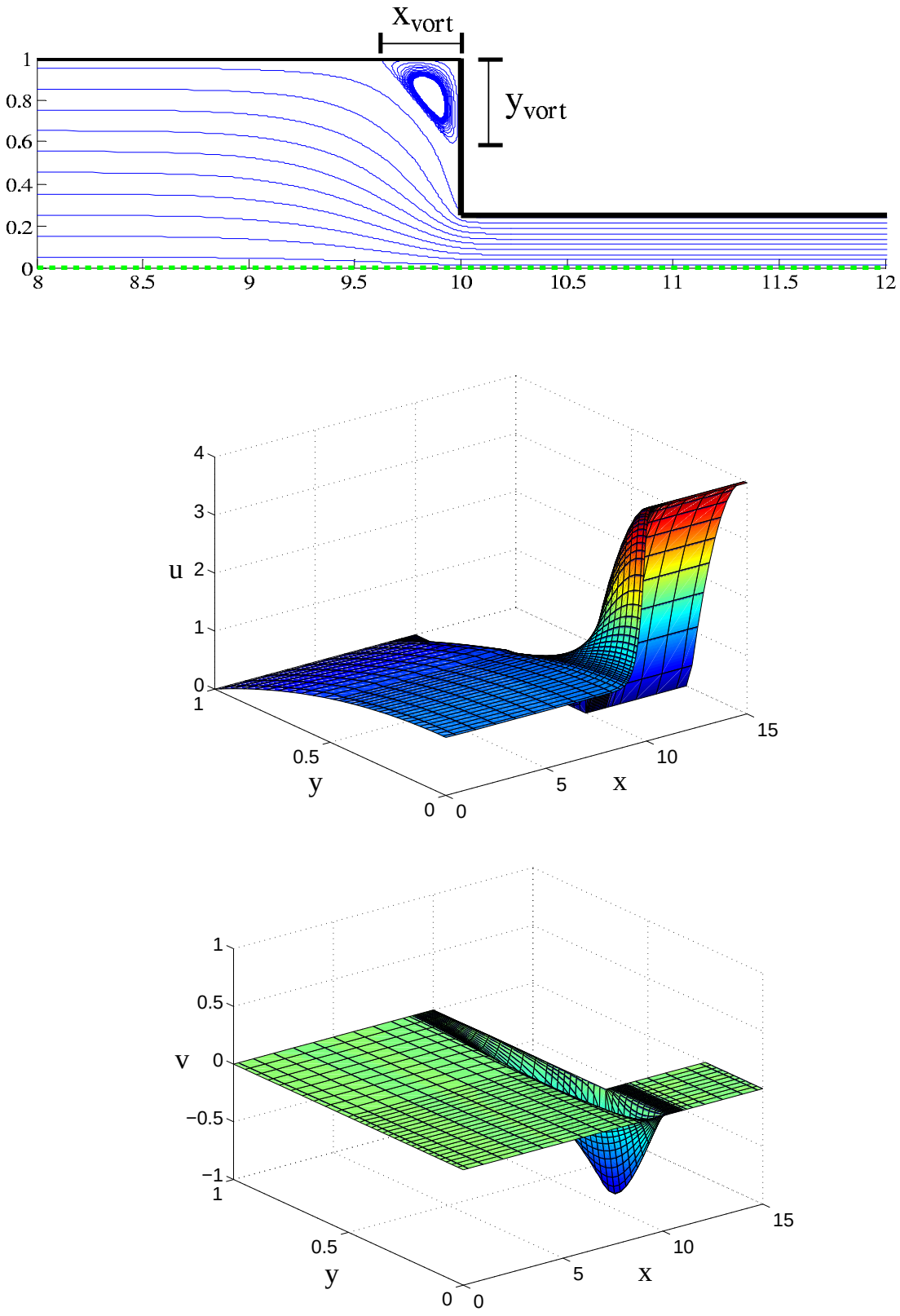

Figure 7: Plot of the velocity streamlines and x, y velocity components for a rectangular $\beta = 4$ contraction flow.

contraction.

2.3.2 Flow of a Newtonian fluid through an axisymmetric $\beta = 2$ contraction

The flow solution for a $\beta = 2$, axisymmetric contraction flow is shown in Figure 8. Again the model predicts the correct factor of 4 increase in the maximum velocity for the transition from the larger to smaller contraction sections. In addition, the presence of a corner vortex is predicted. Figure 9 shows a quantitative comparison with the numerical solution data from Christiansen *et al* (1972) and Kelsey (1971). For their work, the authors solved the vorticity-transport equations by quasilinearization and the method of lines (QL-ML method) or they used an alternate approach where they solved the fourth-order stream function equation by relaxation (SF-R method). Their data was obtained at $Re = 0.01$, where they also predicted the presence of a corner vortex. The experimental velocity data of Iwamiya, Chow and Sinton (1994), taken using an NMR technique, displayed a corner vortex in an axisymmetric $\beta = 2$ contraction, as well.

The quantitative comparison in Figure 9 shows excellent agreement between the FVM solution here and the solutions of Christiansen *et al* (1972) and Kelsey (1971). In the plots, the open circles represent the literature data and the solid lines the data generated in this work. Velocity values were normalized by the average axial velocity in the downstream section of the contraction. Length measurements were normalized by the radius of the upstream tube and the position of the contraction opening was set to $z = 0$. Figure 9(a) shows the normalized axial velocity (U_x) versus z along the centerline ($r = 0$) and Figure 9(b) shows the normalized axial velocity as a function of r at the contraction opening ($z = 0$). Figure 9(c,d) are of the normalized radial velocity (again normalized by the average downstream axial velocity). Figure 9(c) is of $U_r(z)$ at $r = 0.4$ (the downstream tube wall is at $r = 0.5$) and Figure 9(d) is $U_r(r)$ at $z = 0$.

2.3.3 Particle migration in a channel flow

To verify the "evolver" portion of the code, we compare the converged particle concentration and velocity profiles for a two-dimensional, Cartesian solution of an axially-evolving channel flow with the one-dimensional, analytic solution. The details of the two-dimensional,

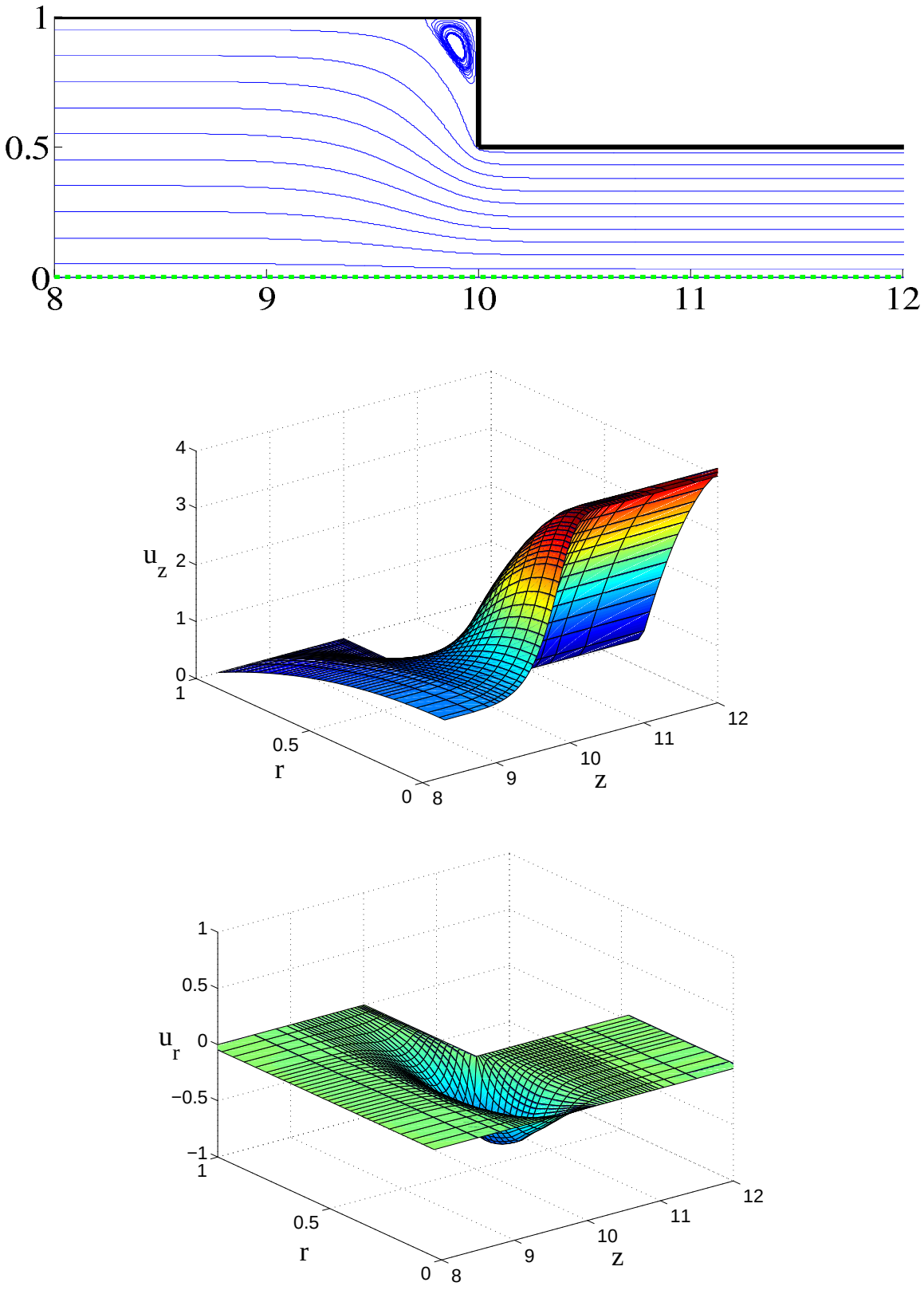

Figure 8: Plot of the velocity streamlines and z, r velocity components for a axisymmetric $\beta = 2$ contraction flow.

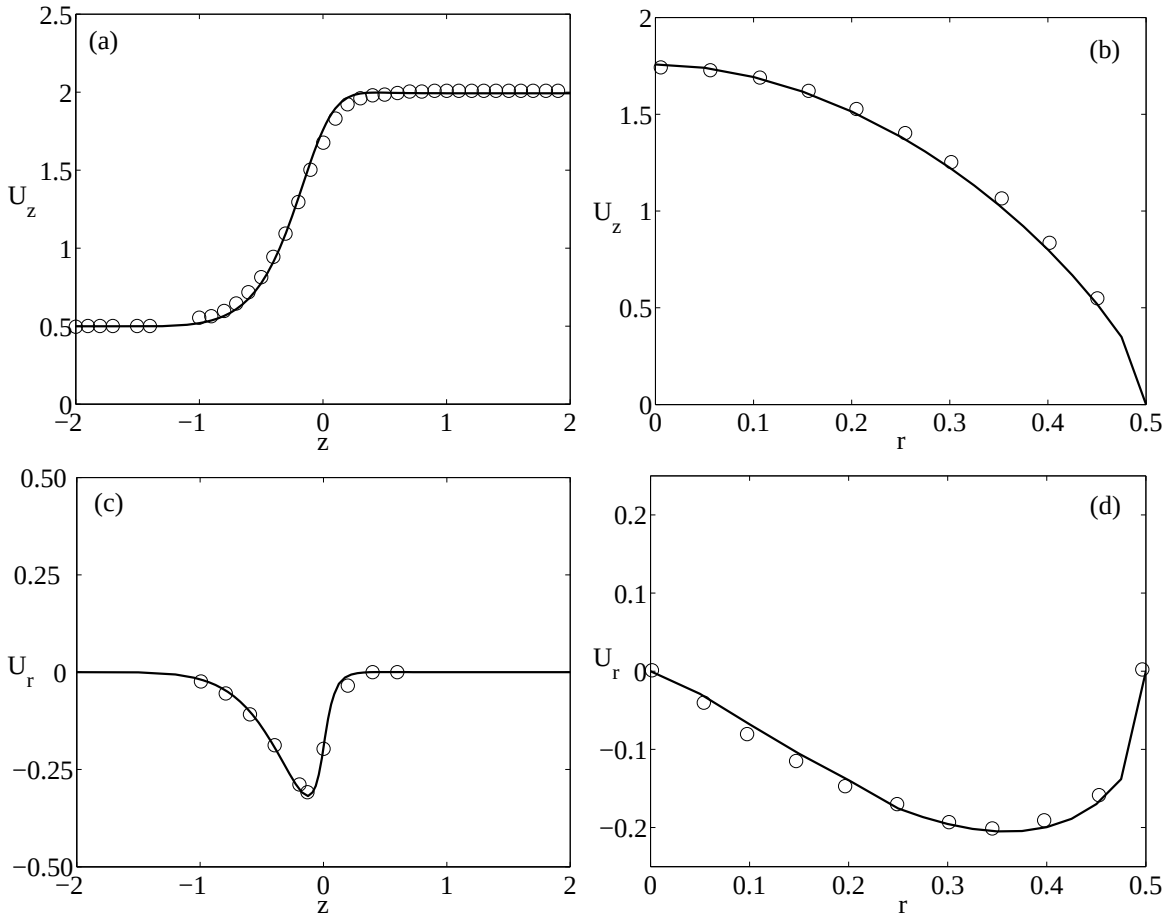

Figure 9: Comparison of the FVM velocity solution [solid line] of an axisymmetric, Newtonian contraction flow ($\beta = 2$) to literature solutions [open circles] (Christiansen *et al*, 1972; Kelsey, 1971). Lengths have been scaled to the radius of the larger section, $z = 0$ has been set to the entrance of the contraction and velocities have been scaled to the average velocity in the smaller section ($U_z = u_z / < u_z >_{sm}$, $U_r = u_r / < u_z >_{sm}$) (a) $U_z(z)$ at $r = 0$; (b) $U_z(r)$ at $z = 0$; (c) $U_r(z)$ at $r = 0.4$; (d) $U_r(r)$ at $z = 0$.

Cartesian solution are provided in Chapter 3 and use the same set of boundary conditions as explained above for the sharp-edged contraction flows in Figure 5. The inlet is set to a unidirectional, parabolic flow, while the particle volume fraction is held at the initial bulk concentration. The gradients normal to the outlet are set equal to zero, which now includes the ϕ gradient. Wall boundaries are set to no-slip conditions and the particle migration flux normal to the wall is set equal to zero, $j_\perp \cdot \mathbf{n} = 0$. The centerline is set to a symmetry boundary condition with the normal velocity and tangential velocity gradient set to zero with the particle migration flux normal to the line of symmetry set equal to zero. We look at the case where the initial bulk particle concentration is $\phi_\mathrm{B} = 0.4$ and assume model parameters of $\alpha = 2$, $\phi_\mathrm{m} = 0.68$ and set the particle size to $B/a = 18$. The viscosity model of Krieger (1972) with $m = 2$ is used for $\eta_s(\phi)$. In the steady-state solution, it will be shown below that for the one-dimensional prediction the values of α and a do not effect the final particle concentration profile.

The one-dimensional, analytic solution is determined from Eq. (2) and Eq. (4). With the x- and y-directions defined as in Figure 5, we assume there is no variation of parameters in the x-direction and that the cross-stream velocity can be set to zero, $\mathrm{u}_y = 0$. Under these assumptions, the continuity relation given in Eq. (1) provides no further information and we assume a constant axial pressure drop, dP/dx. Substituting the expression for the bulk stress ($\mathbf{\Sigma}$) from Eq. (11) into the bulk momentum equation, Eq. (2), and applying the assumptions, we get

$$2\bar{\eta}_s E_{xy} = (\frac{\mathrm{d}P}{\mathrm{d}x})y. \tag{21}$$

The shear-rate can be expressed, $\dot{\gamma} = \sqrt{2}E_{xy}$, which when substituted into Eq. (21) results in the following expression for the shear rate which can be integrated to determine the velocity field,

$$\dot{\gamma} = \frac{\sqrt{2}}{2}\frac{\partial \mathrm{u}_x}{\partial y} = \frac{\sqrt{2}}{2}(\frac{\mathrm{d}P}{\mathrm{d}x})\frac{y}{\bar{\eta}_s}. \tag{22}$$

The particle field solution is determined by simplifying Eq. (4) with the above assumptions, along with the assumption of a steady-state where $\frac{\partial \phi}{\partial t} = 0$. That leaves $\frac{\partial j_{\perp,y}}{\partial y} = 0$, which implies $j_{\perp,y} =$ constant. From the boundary conditions, this constant is determined to be equal to zero. Substituting in the expression from Eq. (7) for $j_{\perp,y}$ and simplifying, results

in

$$\frac{2a^2}{9\eta_o} f(\phi) \frac{\partial \mathbf{\Sigma}_{\mathrm{P},yy}}{\partial y} = 0. \tag{23}$$

Integrating this expression and substituting in for the particle stress with Eq. (9), we get

$$-\bar{\eta}_n(\phi)\dot{\gamma}\lambda_2 = A_{const}. \tag{24}$$

Now we substitute in for $\dot{\gamma}$ with Eq. (22) and absorb the constants, $-\frac{\sqrt{2}}{2}(\frac{\mathrm{d}P}{\mathrm{d}x})\lambda_2$, into the RHS.

$$\frac{\eta_n}{\eta_s} y = A^{\phi}. \tag{25}$$

The solution for this equation is determined by setting the value of ϕ at the wall and solving for A^{ϕ}. This value of A^{ϕ} is then used to determine the rest of the ϕ profile. At the centerline ($y = 0$), since $\dot{\gamma} \rightarrow 0$, we assume $\phi/\phi_{\mathrm{m}} = 1.0$. This assumption is necessary for the one-dimensional solution, but is not necessary for the two-dimensional numerical solution where the centerline boundary condition is enforced through the vanishing particle migration flux. The proper value of ϕ_{wall} is determined by enforcing that the particle phase mass flux, $\rho < \phi \mathrm{u}_x >$, remains equal to that at the inlet, $\rho\phi_{\mathrm{B}} < \mathrm{u}_{x,parb} >$. For the velocity field solution, the proper pressure drop is determined by enforcing that the overall mass flux, $\rho < \mathrm{u}_x >$, remains equal to that at the inlet. For our calculations, it is assumed that the density of the particle phase and fluid phase are equal and therefore remain constant throughout the suspension.

The results in Figure 10 show good agreement between the two-dimensional solver-evolver solution and the one-dimensional analytic solution. There is some discrepancy, mainly due to the way the centerline boundary condition is handled. In the analytic solution, the centerline value of ϕ is assumed to be at maximum packing since the shear rate vanishes. In the numerical code, the value is calculated at a node off of the centerline boundary (as illustrated in Figure 4) utilizing the fact that the particle flux vanishes at the symmetry boundary. Despite the slight difference, this comparison illustrates that the solver-evolver code can produce a stable solution for the particle concentration for a simple two-dimensional flow. The velocity solution for both cases shows a flattening in the center compared to the inlet parabolic profile. The numerical and analytical predictions vary

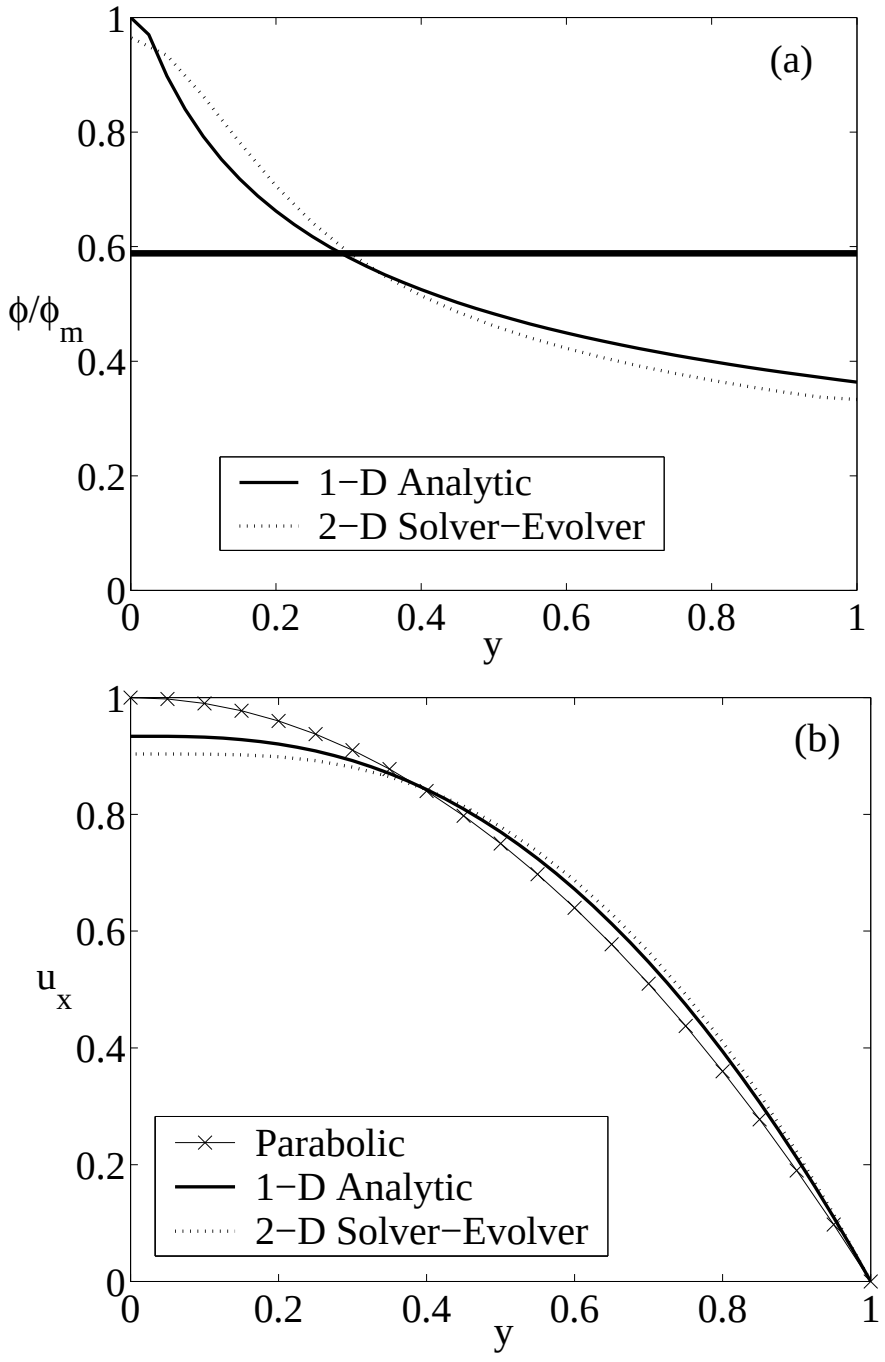

Figure 10: Comparison of the converged (a) $\phi(y)/\phi_{\rm m}$, (b) $u_x(y)$ solutions from the two-dimensional, finite volume, solver-evolver code for a rectangular channel flow with the one-dimensional analytic solution when $\phi_{\rm B} = 0.4$. ($\phi_{\rm m} = 0.68$, $\alpha = 2$, $B/a = 18$)

slightly in this flattening, most likely due to the difference in the predicted ϕ profile near the centerline.

In conclusion, this illustrates that the explicit particle solution procedure is able to correctly calculate the ϕ profile without producing major instabilities. As for the issue of the vanishing shear rate at the centerline, this is addressed in the discussion of a non-local shear rate correction in Chapter 3, Section 3.1.1.

CHAPTER 3

SIMPLE GEOMETRY: AXIALLY DEVELOPING FLOWS

In this chapter, we focus on the case of modeling axially-developing pressure-driven suspension flows in rectangular and circular conduits. For the rectangular conduit, we assume that the depth of the channel cross-section is much greater than the width ($2B$) allowing us to model the flow as two-dimensional. For the circular conduit, we assume an axisymmetric non-swirling flow, which allows us to use a two-dimensional domain as well.

Pressure-driven flow of suspensions is relevant to a range of applications. Wherever transfer from one vessel to another is required, the suspension must undergo a pressure-driven flow through some form of conduit. The impact of bulk migration of the solid particles on the system pressure drop or particle distribution can have significant effect on the design parameters. The particle volume fraction, ϕ, and velocity profiles resulting from flow through rectangular and circular conduits have been considered experimentally for what is assumed to be the fully-developed state (Koh, Hookham and Leal, 1994; Hampton *et al*, 1997; Lyon and Leal, 1998a, Han *et al*, 1999; Frank *et al*, 2003). Simulation (Nott and Brady, 1998; Morris and Brady, 1998) has also been used to examine this problem and provides rate information but has been performed in a periodic system and thus is not directly in correspondence with the experiments. The study by Hampton *et al* (1997) is, to our knowledge, the only work to provide experimental data on the axial development. While scaling arguments have been offered to describe the development length, little attention has been given to modeling the development of the ϕ profile and the associated changes to the velocity field and axial pressure variation.

We study predictions based on the suspension flow model presented in Chapter 2, with one specific modification. We take into account nonlocal effects on the stress. By nonlocal, we are referring to the concept that the "continuum point" for the material, by which we mean the minimum scale on which a continuum approach may validly be applied, is of finite

size. This issue has already been shown to be significant for a channel flow application in the evolver verification solutions presented in Chapter 2, Section 2.3.3. To account for this, a simple averaging of the computed strain-rate field over a finite volume is performed. This is explained in more detain in Section 3.1.1.

Our primary objective in this chapter is to explore suspension behavior in axially-developing flows, where certain simplifications based upon the nearly unidirectional nature of the flow appear justified. We develop a "marching" method which is derived from scaling arguments in the spirit of the lubrication approximation. When compared with the solution of the complete two-dimensional governing equations used in the solver-evolver code, the marching method approximated the results from the full model extremely well with a substantial decrease in the size of the computational domain and required computational time. The need for the full model still does arise in regions where the two velocity components are comparable, and this is illustrated by the flow of a suspension through an abrupt contraction.

We begin in the following section by reviewing the suspension flow model, explaining the concept of a nonlocal stress and how it is implemented, and illustrating the unidirectional simplification for conduit flows to form a marching method solution. Section 3.3 states the problems to be solved, Section 3.3 presents an overview of the numerical methods used in each solution method, Section 3.4 states the results with some discussion, and Section 3.5 presents concluding comments. Comparisons are made between model predictions and experimental results as well as between the two solution methods.

3.1 Governing Equations

For the solution of a suspension flow through a rectangular or circular conduit, we utilize the suspension flow equations developed in Chapter 2. These equations are established for the flow of suspensions of rigid, spherical particles in a Newtonian fluid. We assume viscous conditions and non-Brownian, neutrally buoyant particles. For the flows considered, it is assumed that the bulk and particle Reynolds numbers are sufficiently small that bulk and individual particle inertia have little influence.

The bulk mass and momentum conservation equations and particle phase conservation equations result in

$$\nabla \cdot \mathbf{u} = 0, \tag{26}$$

$$-\nabla P + \nabla \cdot (2\bar{\eta}_s \mathbf{E}) + \nabla \cdot \mathbf{\Sigma}_{\mathrm{P}}^{NS} = 0, \tag{27}$$

$$\frac{\partial \phi}{\partial t} + \mathbf{u} \cdot \nabla \phi = -\nabla \cdot \mathbf{j}_{\perp}, \tag{28}$$

where $\mathbf{u}$ is the bulk suspension velocity, P is the suspension pressure, $\bar{\eta}_s$ is the shear viscosity, $\mathbf{E}$ is the rate of strain, $\mathbf{\Sigma}_{\mathrm{P}}^{NS}$ is the particle phase normal stress, ϕ is the particle volume fraction and $\mathbf{j}_{\perp}$ is the particle migration flux. The shear viscosity is a function of ϕ and defined in Chapter 2, according to the forms suggested by Morris and Boulay (1999) or Krieger (1972). The bulk rate of strain is defined as $\mathbf{E} = \frac{1}{2}[\nabla \mathbf{u} + (\nabla \mathbf{u})^T]$ and the form of the particle normal stress, $\mathbf{\Sigma}_{\mathrm{P}}^{NS}$, is given below in the particle phase stress definition. The particle migration flux is determined from the particle momentum conservation equation to be

$$\mathbf{j}_{\perp} = \frac{2a^2}{9\eta_o} f(\phi) \nabla \cdot \mathbf{\Sigma}_{\mathrm{P}}. \tag{29}$$

In this expression, a is the particle radius, η_o is the Newtonian suspending fluid viscosity, $f(\phi)$ is the sedimentation hindrance function, and $\mathbf{\Sigma}_{\mathrm{P}}$ is the particle phase stress. The sedimentation hindrance function is based on the form described in Richardson and Zaki (1954) with a modification to ensure that particle migration ceases when the particle concentration approaches maximum packing, ϕ_{m},

$$f(\phi) = (1 - \phi/\phi_m)(1 - \phi)^{\alpha - 1}. \tag{30}$$

We use α values in the range $2 \leq \alpha \leq 4$. The particle stress model is taken from the form suggested by Morris and Boulay (1999) for shear flows,

$$\mathbf{\Sigma}_{\mathrm{P}} = -\bar{\eta}_n(\phi)\dot{\gamma}\mathbf{Q} + 2\bar{\eta}_p(\phi)\mathbf{E}, \tag{31}$$

and contains both a shear, $\mathbf{\Sigma}_{\mathrm{P}}^{SH} = 2\bar{\eta}_p \mathbf{E}$, and normal, $\mathbf{\Sigma}_{\mathrm{P}}^{NS} = -\bar{\eta}_n \dot{\gamma} \mathbf{Q}$, stress portion. The normal stress viscosity ($\bar{\eta}_n$), particle phase viscosity ($\bar{\eta}_p$), and anisotropic tensor ($\mathbf{Q}$) are defined in Chapter 2. The shear rate is defined, $\dot{\gamma} = \sqrt{2\mathbf{E} : \mathbf{E}}$.

3.1.1 Nonlocal stress contributions

When modeling the particle phase as a continuum, difficulties may arise at points where the shear rate approaches zero, as at the centerline of channel or pipe flow. At such points, continuum models based on the local shear rate have been shown (Phillips *et al*, 1992; Nott and Brady, 1994) to predict that the particle volume fraction must approach maximum packing. This produces an aphysical cusp in the ϕ profile.

This behavior represents a breakdown of the "local" description of the stress, by which we refer to the definition of continuum field variables at an infinitesimally small point in space. This does not take into account the finite size of the particles, and when the scale of interest approaches that of the individual particles, the continuum approximation may be expected to break down. To remedy this, it has been suggested to use a nonlocal stress correction (Nott and Brady, 1994; Morris and Brady, 1998; Mills and Snabre, 1995; Morris and Boulay, 1999). The nonlocal stress takes into account that particles sample neighboring flow regions over their own size scale or over the scale characteristic of interactions with near neighbors, a concept illustrated in Figure 11.

There have been several methods used to model nonlocal suspension stresses. In Nott and Brady (1994) and Morris and Brady (1998), the nonlocal stress is written as a function of the fluctuational motions of the particles, employing the "suspension temperature," defined as the mean square translational velocity fluctuation in the particle phase, $T^{\mathrm{susp}} \equiv < \mathrm{u}' \cdot \mathrm{u}' >_{\mathrm{P}}$. This leads to an additional field variable, T^{susp}, and thus requires development and solution of an added transport equation describing this quantity. Mills and Snabre (1995) propose that the nonlocal stress is the effect of large scale particle structures. They suggest that the nonlocal stress should consist of the local stress integrated over the length scale of these proposed structures. Morris and Boulay (1999) suggest a similar, but less mechanistic, approach of taking a spatial average of the shear rate over a finite volume in the constitutive law for the normal stresses.

Further arguments specific to the centerline of a channel/pipe flow may be applied to justify a nonlocal contribution to the mean shear rate by noting that no point in such a flow has, on average, a root-mean-square (RMS) shear rate of zero. The centerline represents

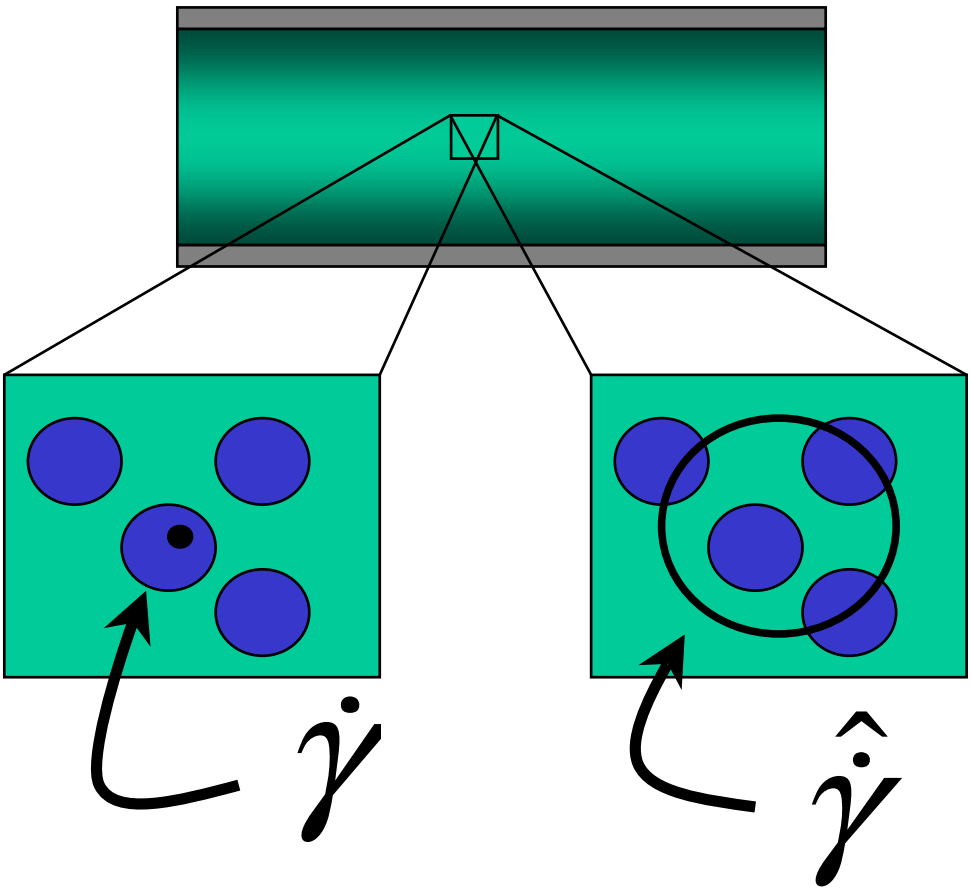

Figure 11: Illustration of the nonlocal stress. The section on the left illustrates a continuum point value and the section on the right illustrates a finite volume for the nonlocal contribution.

the maximum velocity in average only, as fluctuations in particle concentration alter the viscosity and hence the shear rate at points to either side of the centerline. Consequently, the maximum velocity may instantaneously be displaced to either side of the centerline of a channel, or radially in any direction in a tube flow. The centerline of a suspension flow thus experiences a distribution of shear rates, which will depend upon $\epsilon = a/L_s$, where L_s is the channel half width (B) or pipe radius (R). This is due to the fact that the concentration fluctuations depend upon the number of particles within a volume of scale L_s^3.

In this work, the nonlocal stress model is a simplification of the spatial averaging approach. Specifically, a small constant nonlocal contribution – depending upon the particle size – is added to the local shear rate. This reflects the fact that the RMS value of $\dot{\gamma}$ is larger than the mean shear rate, owing to fluctuations resulting from finite size of the particles. The normal stress portion of Eq. (31) is thus computed as

$$\mathbf{\Sigma}_{\mathrm{P}}^{NS} = -\eta_o \eta_n(\phi)[\dot{\gamma}(\mathbf{x}) + \dot{\gamma}_{NL}]\mathbf{Q}, \tag{32}$$

with the nonlocal contribution depending on the mean shear rate and particle size,

$$\dot{\gamma}_{NL} = a_s(\epsilon)\dot{\gamma}_s, \quad \text{where} \quad \dot{\gamma}_s = \mathrm{u}_{max}/L_s. \tag{33}$$

We examine values of $a_s(\epsilon) = 0, \epsilon$, and ϵ^2. The finite $\dot{\gamma}_{NL}$ values satisfy $\dot{\gamma}_{NL} \ll \dot{\gamma}(\mathbf{x})$ except where $\dot{\gamma} \to 0$, giving the model the desired effect of influencing results only near the centerline in the present context. In fact, for the linearly-varying shear stress of a pressure-driven flow in a conduit, this method differs little from taking an average of the shear rate (defined positive) about the point of interest, and can readily be extended to this form for the general case, which we do in Chapter 5 and Chapter 6 for general flow conditions. In these chapters, we determine the nonlocal stress by averaging the shear rate about the point of interest over a small, finite volume.

3.1.2 Scaling and unidirectional flow

We consider the flow of a neutrally-buoyant suspension in a channel or tube with steady inlet conditions. Following an initial transient as the flow is introduced to the conduit, the flow is steady and the volume fraction develops axially according to the steady form of

Eq. (28),

$$\mathbf{u} \cdot \nabla\phi = -\frac{2a^2}{9\eta_o}\nabla \cdot (f(\phi)\nabla \cdot \mathbf{\Sigma}_{\mathrm{P}})\,. \tag{34}$$

Assuming there is no average cross-stream velocity of the bulk material (a reasonable assumption given that this velocity component must vanish at both the centerline and the wall), the left-hand side becomes

$$\mathbf{u} \cdot \nabla\phi \approx \mathrm{u}_{\parallel}\frac{\partial\phi}{\partial x_{\parallel}} \tag{35}$$

where $\parallel$ represents the axial direction (x for the channel flow and z for the pipe flow).

The right-hand side of Eq. (34) can be simplified under the assumption that the development length in the channel or pipe, L, is much greater than the cross-stream length scale, $L_s \ll L$. Scaling the cross-stream direction ($x_\perp$ which is y for a channel and r for a pipe) with L_s and the axial direction ($x_\parallel$) with L leads to $\frac{\partial}{\partial x_\parallel} \sim 1/L \ll 1/L_s \sim \frac{\partial}{\partial x_\perp}$. Variations in the axial direction are much smaller than those in the cross-stream direction, and therefore may safely be neglected in computing the particle migration flux; note that it is not clear this must hold true for extremely concentrated suspensions. This reduces the particle-evolution equation to

$$\frac{\partial\phi}{\partial x} = -\frac{1}{\mathrm{u}_x}\frac{2a^2}{9\eta_o}\frac{\partial}{\partial y}\left(f(\phi)\frac{\partial\Sigma_{\mathrm{P},yy}}{\partial y}\right) \tag{36}$$

for the axial variation of ϕ in a two-dimensional channel flow and to

$$\frac{\partial\phi}{\partial z} = -\frac{1}{\mathrm{u}_z}\frac{2a^2}{9\eta_o}\frac{\partial}{\partial r}\left(f(\phi)\left[\frac{\partial\Sigma_{\mathrm{P},rr}}{\partial r} + \frac{N_2}{r}\right]\right) \tag{37}$$

for an axisymmetric tube flow, where $N_2 = \Sigma_{\mathrm{P},rr} - \Sigma_{\mathrm{P},\theta\theta}$.

3.2 Pressure-driven Flow of a Concentrated Suspension Through a Long Conduit

Pressure-driven flows in a two-dimensional channel and a circular pipe are studied. The domain for the channel flow is illustrated in Figure 12, which is similar to that of the pipe flow with axisymmetric conditions assumed. At the inlet the velocity is set to a unidirectional parabolic profile while ϕ has the imposed bulk value (ϕ_{B}). No-slip velocity conditions are imposed at the wall while the particle migration flux normal to the wall is set

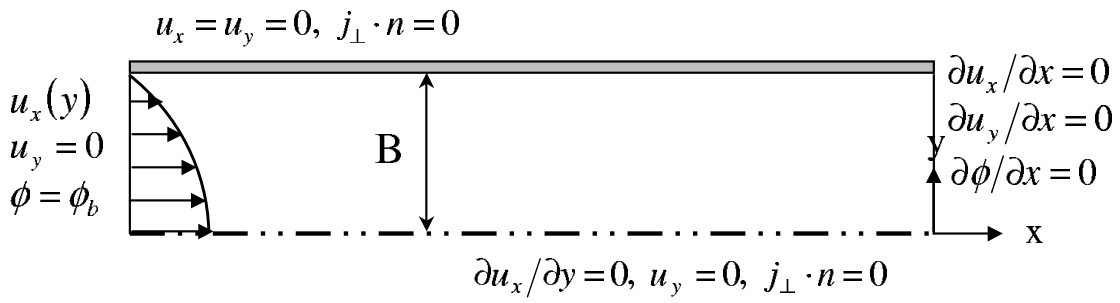

Figure 12: Sketch of the channel flow geometry and imposed boundary conditions.

equal to zero. At the centerline a symmetry boundary condition is imposed resulting in a vanishing normal velocity and particle migration flux with normal gradients of the tangential components vanishing as well. At the exit, all the normal gradients of components are set equal to zero while the pressure is set to zero to provide a reference value. In the finite volume approach, the domain is initially filled with suspension at ϕ_{B}.

3.2.1 Experimental comparisons

The numerical studies performed include conditions which match those of experiments presented in Lyon and Leal (1998a) for a rectangular conduit and in Hampton *et al* (1997) for a circular conduit. Both sets of experiments used density-matched particles sufficiently large to rule out Brownian diffusion effects (diameters $50-100\mu m$ for Lyon and Leal; $650\mu m$ and $3175\mu m$ for Hampton *et al*).

Lyon and Leal (1998a) measured ϕ and axial velocity using a laser-Doppler velocimetry (LDV) method. Data was extracted across the width of the channel at a length of $224B$ downstream of the entrance to the channel, where B is the half width of the channel. The longer dimension of the channel in their experiments was $50B$ for the results of interest, and the flow is thus well-approximated as two-dimensional. Results at $B/a = 18$ and bulk concentrations of $\phi_{\mathrm{B}} = 0.3$, 0.4, and 0.5 are considered. This value of B/a is below the

lower bound of continuum behavior, $B/a = 50$, argued by Hampton *et al* (1997) based on capillary rheometry experiments (Seshadri and Sutera, 1970; Mondy, Graham and Gottlieb, 1988), but we will apply the continuum model (with the non-local stress) nonetheless. The LDV data tends to obtain ϕ values which are systematically low near the channel walls, apparently due to a lower signal to noise ratio in the regions near the wall; this finding was confirmed by direct optical measurements in another study (Lyon and Leal, 1998b). This should be borne in mind when considering experimental results used for comparison in the near-wall region, *i.e.* outside $-0.8 \leq x \leq 0.8$.

The results of Hampton *et al* (1997) were taken at bulk concentrations of $\phi_{\mathrm{B}} = 0.20$, 0.30, and 0.45 for $R/a = 16$ and 40 where R is the inner radius of the pipe. This data was obtained using nuclear magnetic resonance (NMR) imaging which has been shown to provide accurate results in a number of flows (Altobelli, Givler and Fukushima,1991; Abbott *et al*, 1991; Subia *et al*, 1998).

3.3 Numerical Implementation

3.3.1 Full two-dimensional solution: the solver-evolver tool

The suspension flow model given by Eq. (26), Eq. (27), and Eq. (28) is solved using a tool termed the "solver-evolver," developed in Chapter 2 for the study of flow and particle migration in general geometries. The tool solves for the velocity field, $\mathbf{u}(\mathbf{x})$, for a given $\phi(\mathbf{x})$ field. This is followed by an "evolve" step which updates $\phi(\mathbf{x})$ based upon the particle stress field evaluated using $\mathbf{u}(\mathbf{x})$.

The solver-evolver code utilizes the finite volume method (FVM) as explained in Patankar (1980) and Ferziger and Peric (2002) to solve the suspension flow equations. For the conduit flow problems, the solution domain is divided into CV's, as illustrated in Figure 13 for a rectangular channel. The cross-stream direction is divided as $dy = 0.05B$ ($dy = 0.05$ in dimensionless form). Since gradients in the axial direction are smaller, a larger mesh size is utilized for the axial coordinate. For the first $10B$ of the axial direction $dx = 10dy$, which is increased to $dx = 200dy$ for $x = 10B$ to $100B$. Finally beyond $100B$, dx is increased to

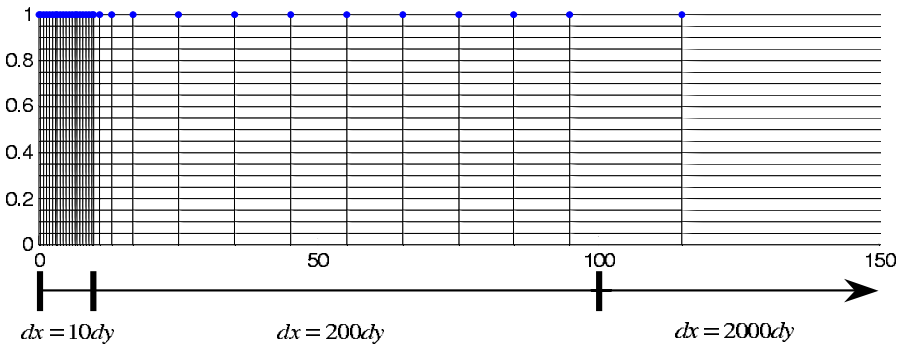

Figure 13: Computational grid used for the channel flow.

$2000dy$. This is allowable as gradients in the axial direction drop rapidly after the initial migration near the inlet, consistent with the decrease in rate of migration in the cross-stream direction beyond $100B$. The circular conduit was discretized similarly, but required a finer mesh for a longer axial distance near the inlet. For these calculations the first $10R$ in axial distance was set to $dz = 5dr$ and the region of $10R$ through $250R$ was set to $dz = 10dr$, while the region beyond $250R$ was set to $dz = 100dr$.

Even with the variable length in the axial direction, the full solution with the solver-evolver is computationally demanding. With 20 cross-stream elements, in MATLAB the method requires on a 2.5 GHz PC about 24 hours to complete the 5000 time steps required to converge a 1000B length channel and 72 hours to complete the 15000 time steps required to converge a 5000B length channel. In a pipe flow the necessary time is longer due to increased axial refinement and larger numbers of iterations for the flow field solution. Recall that the flow begins from a conduit filled with a uniform ϕ_{B} and the time is required to allow the initial volume to be displaced completely.

3.3.2 Marching method solution

The long solution times noted at the end of the previous section result from the slow axial variation and consequently large domain. We have also used the wide separation of gradients in the flow and cross-stream directions to motivate a solution technique in which the governing equation for the axial variation of ϕ, namely Eq. (36) for the two-dimensional

channel or Eq. (37) for the tube flow, is discretized with an Euler scheme for the axial coordinate ($x_\parallel$) and a one-dimensional FVM scheme in the cross-stream coordinate ($x_\perp$). This leads to a sequential solution algorithm where the velocity field at an axial cross-section is determined and used to calculate the particle volume fraction profile at the next axial step downstream. This leads to a solution which "marches" axially down the channel or pipe. The method addresses only the steady solution following the initial transient associated with the propagation through the conduit, and thus is intrinsically less complete than the first approach.

With $\phi(x_\perp)$ known at the first position, the pressure-driven velocity profile is determined subject to the constraint that the total mass flux (particles and fluid) is equal to the value at the inlet. This constraint sets the pressure drop, $\mathrm{d}P/\mathrm{d}x_\parallel$, at this axial position. Note that the cross-stream average of ϕ need not equal the inlet average or initial bulk concentration, but that global mass conservation should be maintained. To satisfy the particle flux requirement the ϕ profile is linearly rescaled to ensure that the particle phase mass flux remains at the inlet value; such an *ad hoc* approach is not needed in the full solution. Finally, the new velocity and stress information is used to determine the $\phi(x_\perp)$ profile at the next axial step, with the change given for the channel flow following from Eq. (36) as

$$\Delta\phi = -\frac{\Delta x}{u_x(y)}\frac{\partial j_y}{\partial y} = -\frac{2a^2\,\Delta x}{9\eta\,u_x(y)}\frac{\partial}{\partial y}\left(f\frac{\partial \Sigma_{yy}}{\partial y}\right), \tag{38}$$

with a similar form, but involving N_2, following from Eq. (37) for the pipe flow. This process is continued until the ϕ profile has reached its fully-developed form.

The results presented use $dx_\perp = B/100$ or $R/100$, *i.e.* 100 uniformly spaced elements in the cross-stream direction. The axial discretization varies depending upon the concentration, but is quite different from the FVM, and always such that $dx_\parallel < dx_\perp$ as suggested by the CFL stability criterion condition (Ferziger and Peric, 2002). Typically, $dx_\parallel = 0.1dx_\perp$ for $\phi_\mathrm{B} \leq 0.3$ and $dx_\parallel = 0.01dx_\perp$ for $\phi_\mathrm{B} = 0.5$. While we have made certain that the results are not substantively grid-dependent, no effort has been made to optimize the axial discretization, as the method is sufficiently rapid that it is not necessary. With 100 cross-stream elements, the method completes 1.5×10^5 axial steps per minute on a standard 1.3 GHz

PC, and thus provides results for comparison with fully-developed flows from experiments in minutes.

3.4 Results and Discussion

We begin by considering a comparison of the predictions of the full model with experimental data. This will be followed by a more limited examination of the comparison between the full model and the marching method solution, with an illustration of the limitation of the marching model.

To explore the axial evolution of the solids fraction, a scalar measure of the cross stream ϕ profile was used. We utilized the E_p term introduced in Hampton *et al* (1997),

$$E_p = \frac{1}{A}\int \frac{|\phi - \phi_{ref}|}{\phi_{avg}} \mathrm{d}A \tag{39}$$

taking ϕ_{ref} as the bulk solids fraction at the inlet (ϕ_{B}) and taking ϕ_{avg} as the local cross-sectional average solids fraction at the given axial position. This measure starts at zero and asymptotically approaches a constant value as the profile reaches its fully-developed state as illustrated in Figure 14 for a typical channel flow. A curve fit of the form suggested by Hampton *et al* (1997), namely $E_p = \alpha_1(1 - e^{\alpha_2 Z^{0.8}}) + \alpha_3$, is used to fit the data with $E_p(L^\phi) = 0.95E_p^\infty$ taken as the definition of the convergence length for the solids fraction, which corresponds to the definition used by Hampton *et al.* The terms E_p^∞ and L^ϕ are the fully-developed E_p value and convergence length for the solids fraction, respectively.

Predicted axial development of the solids fraction in a channel flow is shown in Figure 15 and for a pipe flow in Figure 16 and Figure 17. In each case, the plot at right illustrates the axial development by presenting the normalized solids fraction at the centerline and wall; the left plot in each pair provides the fully-developed cross-stream solids fraction profile. The predictions illustrate the influence of a nonlocal stress on both the fully-converged profile and the development length; it aids in considering these results to recall that $\epsilon \ll 1$. In the channel flow, a nonlocal factor of $a_s(\epsilon) = \epsilon^2$ has little more effect than no nonlocal contribution ($a_s = 0$). A nonlocal factor of $a_s = \epsilon$ results in a readily observable reduction of the predicted centerline ϕ value and reduces the predicted entrance lengths, as reported in Table 1. The fully developed profile matches the Lyon and Leal (1998a) data except

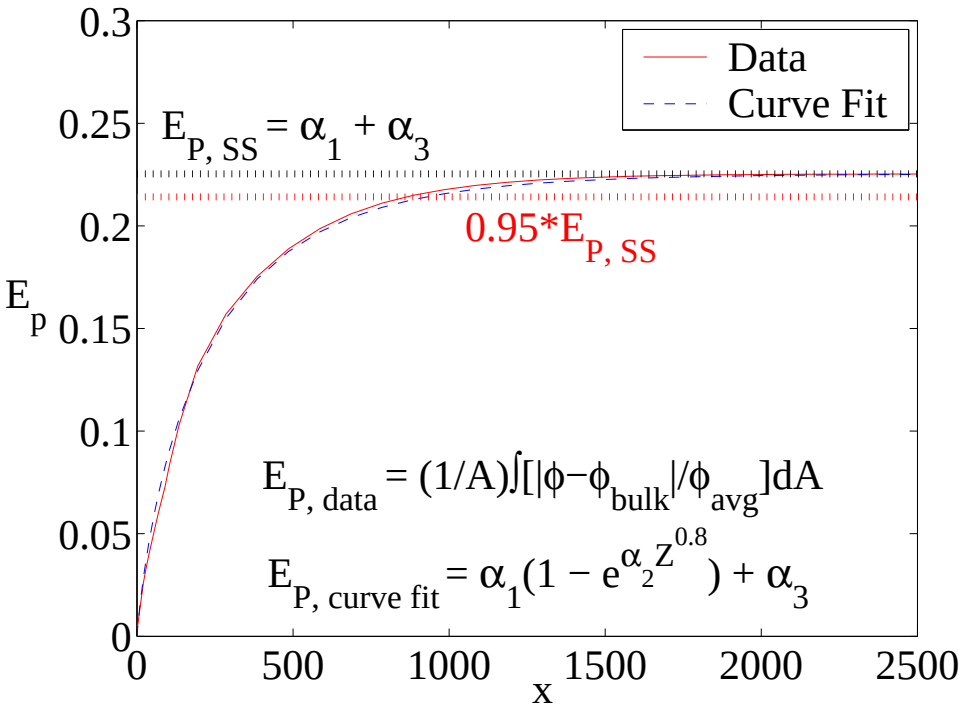

Figure 14: Calculated and curve-fitted values of E_p for the ϕ profile in a channel flow at conditions of $B/a = 18$ and $\phi_b = 0.40$, with model parameters of $\alpha = 4$, $\dot{\gamma}_{NL} = \epsilon$.

near the outer wall where the experimental data drops off at a steeper rate which, as we have discussed in Section 3.2.1, may be due to experimental artifacts. These results could, we believe, only be accounted for in the model through consideration of boundary effects. The Lyon and Leal (1998a) measurements were taken $224B$ from entry to the channel, substantially less than the L^{ϕ} computed. Note, however, that our definition of L^{ϕ} is arbitrary and also that in the referenced experiments there may be some development in the flow of the suspension in the tubing leading to the channel entry.

For the pipe flow, predictions obtained with a nonlocal factor of $a_s = \epsilon$ yield the best match to experimental data, particularly at the centerline. In the Hampton *et al* (1997) data, there again is a drop off near the wall, but less extreme than in Lyon and Leal (1998a). In Hampton *et al*, the rapid decrease in ϕ is more localized near the wall. In principle, the validity of the measured solid fraction near the wall could be assessed by examining the pressure drop (lower near-wall ϕ would be associated with a reduced rate of axial pressure drop), but such experimental data are not presently available. The predicted

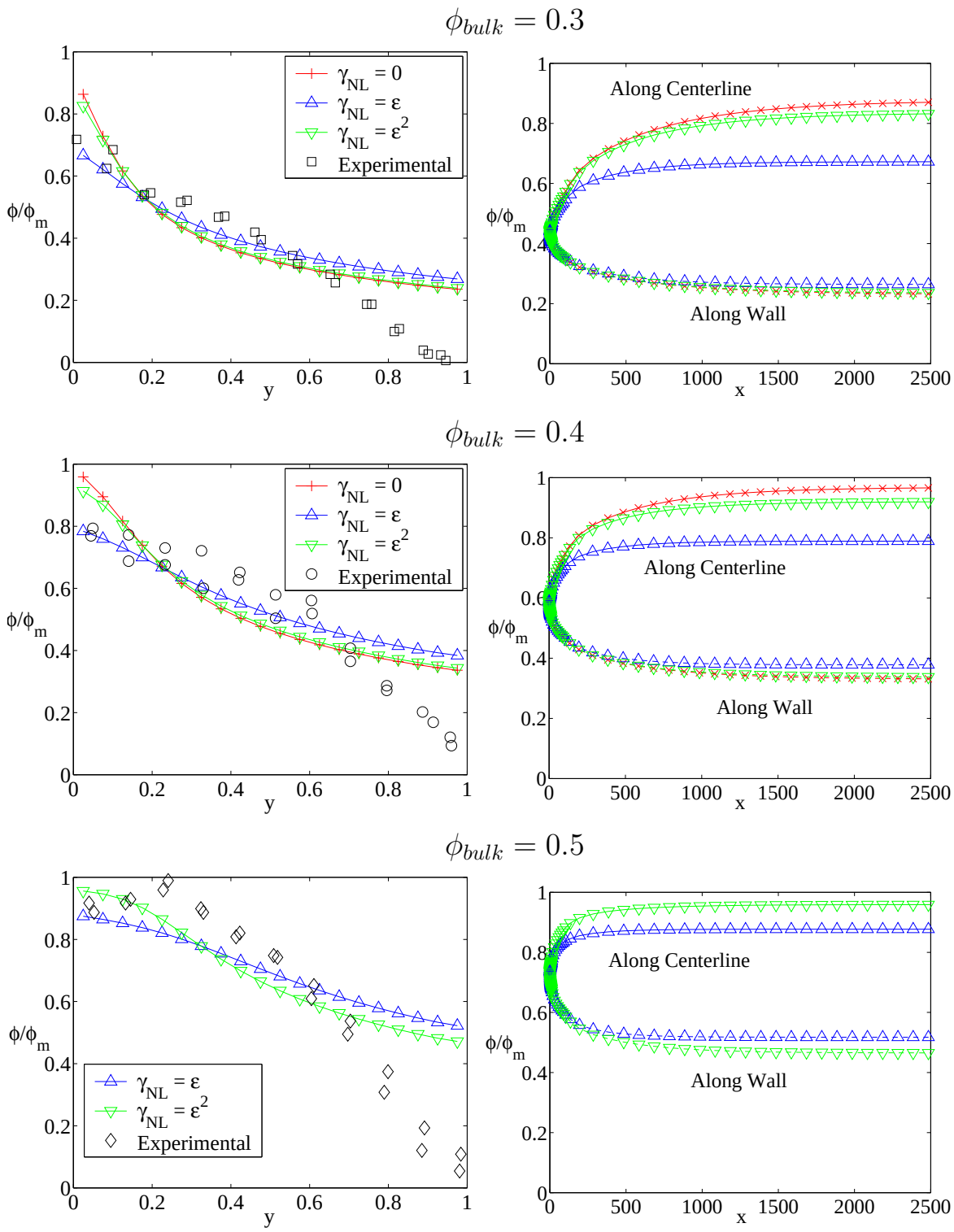

Figure 15: Fully-developed cross-stream (left) and axially-developing (right) ϕ/ϕ_m profiles, comparing the effect of nonlocal stress contributions for channel flows with $B/a = 18$ and $\alpha = 4$. Cross-stream profiles are compared to the experimental data of Lyon and Leal (1998a).

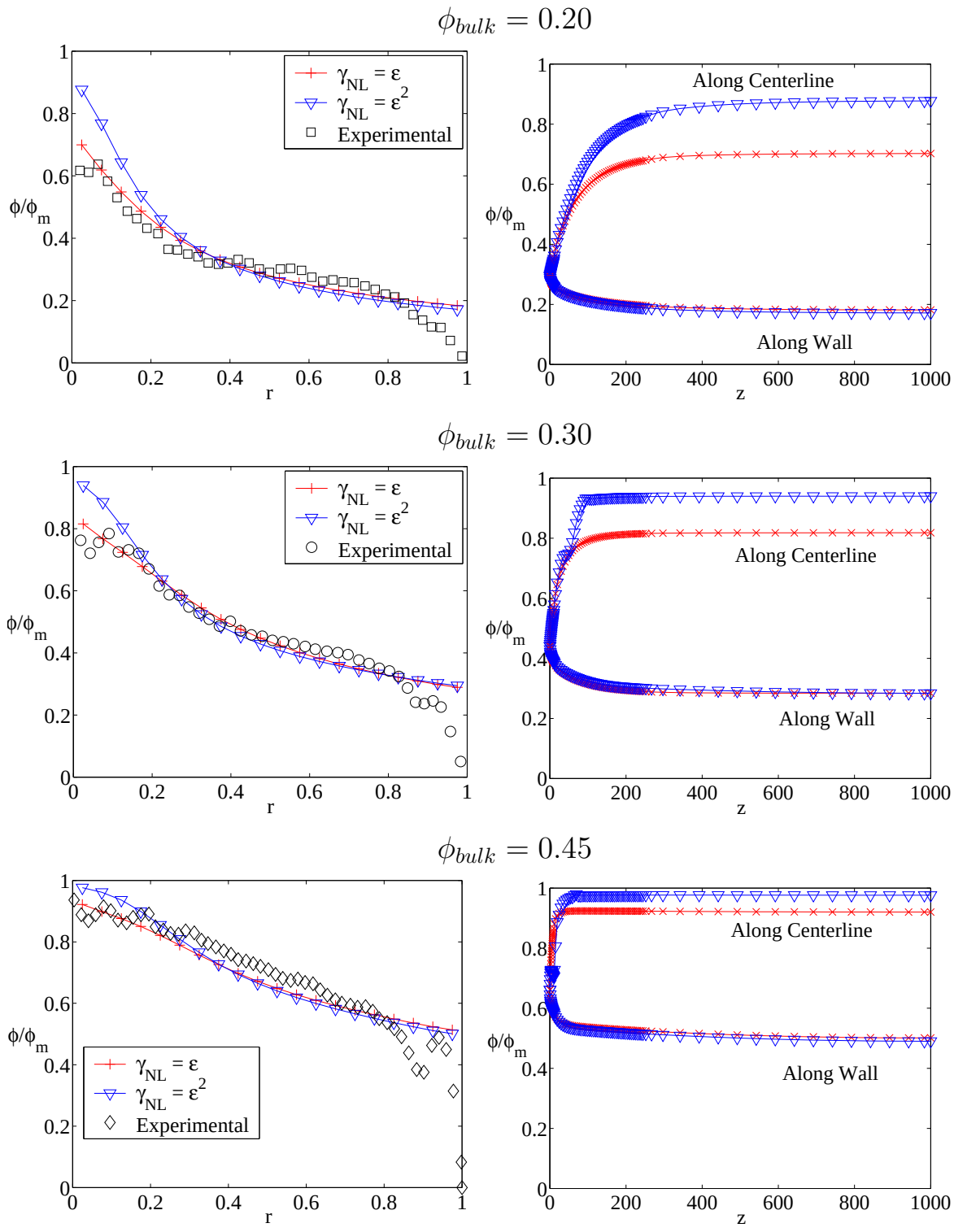

Figure 16: Fully-developed cross-stream (left) and axially-developing (right) ϕ/ϕ_m profiles comparing the effect of nonlocal stress contributions for pipe flows with $R/a = 16$ and $\alpha = 2$. Cross-stream profiles are compared to the experimental data of Hampton *et al.* (1997).

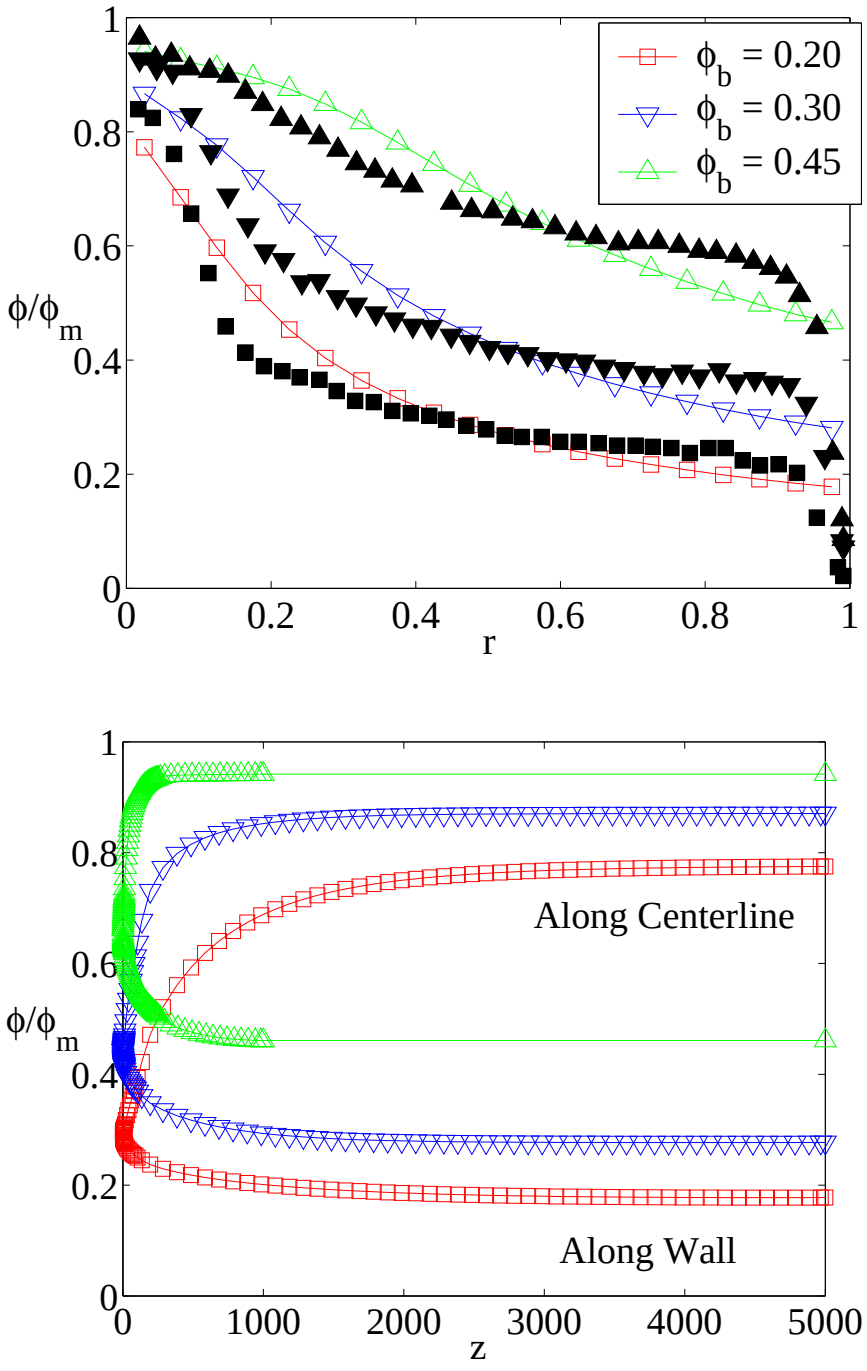

Figure 17: Fully-developed cross-stream (top) and axially-developing (bottom) ϕ/ϕ_m profiles for pipe flows with $R/a = 40$, $\dot{\gamma}_{NL} = \epsilon$, and $\alpha = 2$. Cross-stream profiles are compared to the experimental data (filled points) of Hampton *et al.* (1997).

Table 1: Predicted entrance lengths for the ϕ profile (L_ϕ) and pressure drop at the wall (L_P) for axially-developing conduit flows at various model conditions and parameters.

Geometry	ϕ_b	$a_s(\varepsilon)$	L_s/a	α	η_s-Model	L_ϕ	L_P
channel	30	0	18	4	Krieger	1,968*B	1,424*B
channel	30	ε^2	18	4	Krieger	1,806*B	1,329*B
channel	30	ε	18	4	Krieger	1,150*B	911*B
channel	40	0	18	4	Krieger	1,642*B	1,105*B
channel	40	ε^2	18	4	Krieger	1,454*B	1,000*B
channel	40	ε	18	2	Krieger	302*B	
channel	40	ε	18	4	Krieger	867*B	648*B
channel	40	ε	18	4	Morris-Boulay	685*B	
channel	40	ε	40	4	Krieger	5,531*B	
channel	50	ε^2	18	4	Krieger	1,088*B	671*B
channel	50	ε	18	4	Krieger	599*B	411*B
pipe	20	ε^2	16	2	Krieger	794*R	476*R
pipe	20	ε	16	2	Krieger	538*R	252*R
pipe	20	ε	40	2	Krieger	3,880*R	2,479*R
pipe	30	ε^2	16	2	Krieger	357*R	143*R
pipe	30	ε	16	2	Krieger	247*R	185*R
pipe	30	ε	16	2	Morris-Boulay	207*R	
pipe	30	ε	16	4	Krieger	569*R	
pipe	30	ε	40	2	Krieger	1,715*R	1,410*R
pipe	45	ε^2	16	2	Krieger	180*R	148*R
pipe	45	ε	16	2	Krieger	152*R	77*R
pipe	45	ε	40	2	Krieger	677*R	465*R

Table 2: Comparison of model predictions ($\dot{\gamma}_{NL} = \epsilon$, $\alpha = 2$) of the ϕ profile entrance length (L_ϕ) for two-dimensional channel flow and axisymmetric pipe flow at similar conditions. The experimental entrance length data of Hampton *et al.* (1997) for a pipe flow is included for further comparison. $L_s = B$ or R for channel and pipe flows, respectively.

ϕ_b	L_s/a	L_ϕ^{chan}	L_ϕ^{pipe}	$L_\phi^{pipe,exp}$
20	16		538*R	785*R
30	16,18	568*B	247*R	183*R
40	18	302*B		
45	16		152*R	42*R
50	18	131*B		
20	40		3,880*R	1,126*R
30	40	3,146*B	1,715*R	502*R
45	40	1,281*B	677*R	179*R

entrance lengths based on the L^ϕ definition data for the pipe flow are given in Table 1 and Table 2. Table 2 highlights the difference in predicted ϕ profile entrance lengths between two-dimensional, rectangular channel flow and axisymmetric pipe flow with a further comparison to experimental data from Hampton *et al* (1997) taken for a pipe flow. The predicted entrance length for a channel flow is approximately double that of the pipe flow in the cases presented. This is due to geometric differences as well as fundamental differences in the particle stress model in an axisymmetric geometry, which is explained below and illustrated in Figure 25. For a pipe flow, the predicted entrance lengths are much longer than the measured lengths in Hampton *et al* (1997) for all ϕ_B at the smaller particle size ($R/a = 40$). For the larger particle size ($R/a = 16$), the predicted values are considerably closer to the experimental measurements, and in fact under-predict the experimental value at $\phi_B = 0.2$ for this ratio of particle to tube size. The dependence on ϕ and particle size of the constitutive behavior apparently needs further consideration.

Fully-developed velocity profiles for the channel and pipe flows are given in Figure 18, and these generally match experimental data well. However, the predicted channel velocity

profile fails to fully capture the flattening observed experimentally.

Model and physical parameter influences are illustrated in Figure 19 and Figure 20. Rationalization of the effects of the various parameters is aided by noting that the predicted cross-stream migration flux has the form for the channel of

$$j_{\perp,y} \sim \frac{a^2}{\eta_o}\frac{dP}{dx}(1-\phi/\phi_m)(1-\phi)^{\alpha-1}\frac{d}{dy}(q\,y),$$

with $q = \eta_n/\eta_s$ as defined by Morris and Boulay (1999). This form follows from noting that $\dot{\gamma} \sim y\,(dP/dx)/\eta_s$ with y being the cross-stream coordinate normalized by the channel half-width B. The exponent for the sedimentation hindrance function, α, has no effect upon the fully-developed cross-stream profiles (where $j_{\perp,y}$ vanishes), but smaller α are associated with larger migration flux and thus shorter predicted lengths for axial evolution. A value of $\alpha = 2$ matches experimental observations of Hampton *et al* (1997) in the tube flow better than the $\alpha = 4$ used in Morris and Boulay (1999) for fitting of migration rate in wide-gap Couette flow evolution (and also in most channel flow predictions presented here). The ratio of particle size to flow scale alters the fully-developed cross-stream profile only near the centerline, but has strong effect upon the flux and hence upon the entrance length owing to the a^2, or in dimensionless form $(a/B)^2$, dependence of migration rate. This decreases the dimensionless convergence length for suspension of particles larger relative to the conduit cross-section. Finally, the viscosity models are observed to yield very similar results, with the Krieger (1972) form having a slightly slower migration than that proposed by Morris and Boulay (1999); the Morris and Boulay form of η_s is smaller except as $\phi \to \phi_{\rm m}$ and thus q is larger than when the Krieger form is used, resulting in a larger $|j_\perp|$.

Comparison between the predicted axial evolution of ϕ for the marching method and full two-dimensional solution are made for a channel flow in Figure 21 and for a pipe flow in Figure 22. The channel flow has $B/a = 18$ with $\alpha = 4$ and $a_s = \epsilon$; the pipe flow is at $R/a = 40$ with $\alpha = 2$ and $a_s = \epsilon$. For the channel flow, the predictions of the two methods match almost exactly. The pipe flow results match well but show some difference in the predicted centerline value, a difference attributable in part to the higher resolution in the marching method solution with 100 grid points across the radial domain where the

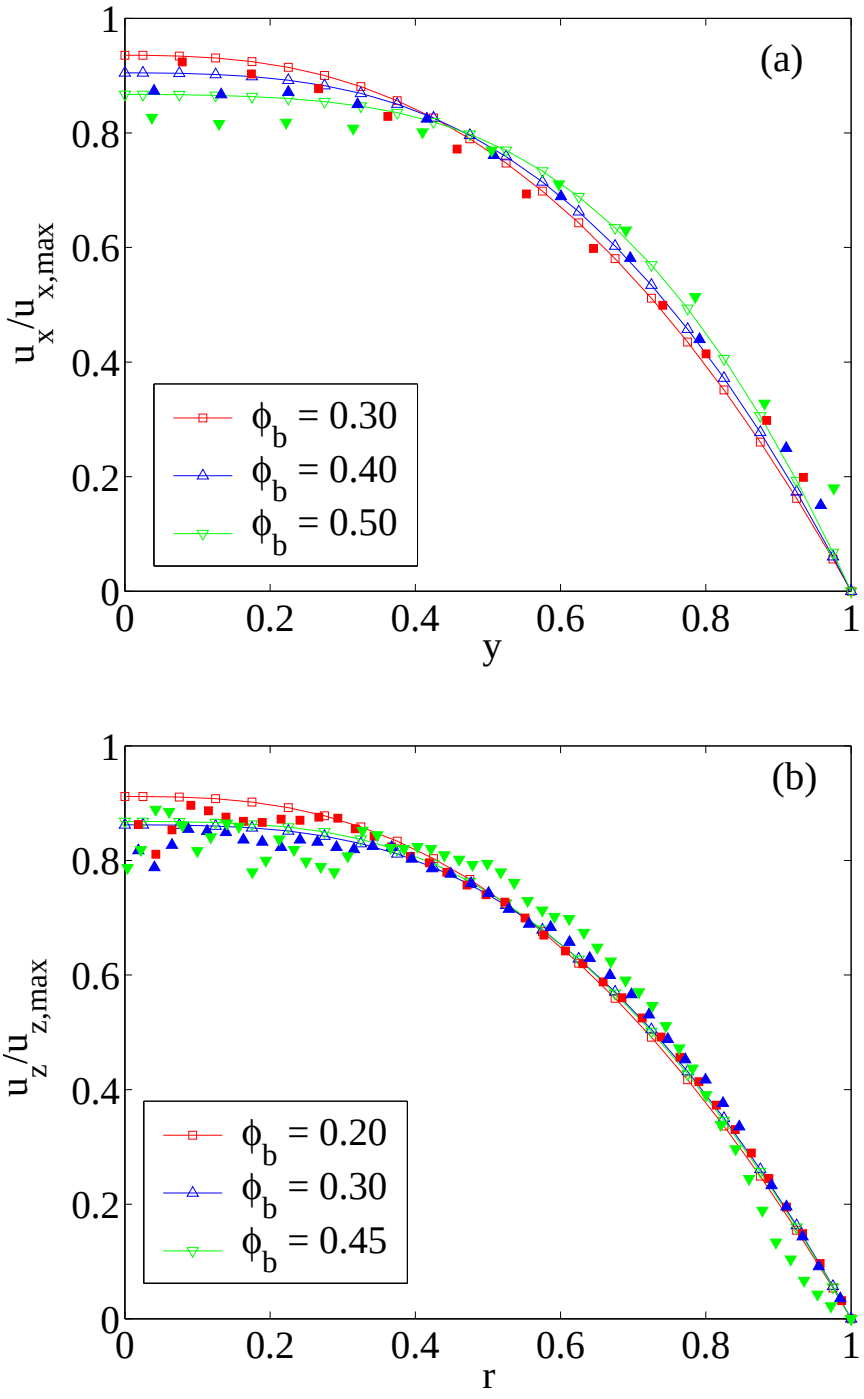

Figure 18: Fully-developed axial-velocity predictions ($\dot{\gamma}_{NL} = \epsilon$, $\alpha = 2$) and experimental results for (a) channel flow with $B/a = 18$ (Lyon and Leal, 1998a); (b) pipe flow with $R/a = 16$ (Hampton *et al*, 1997).

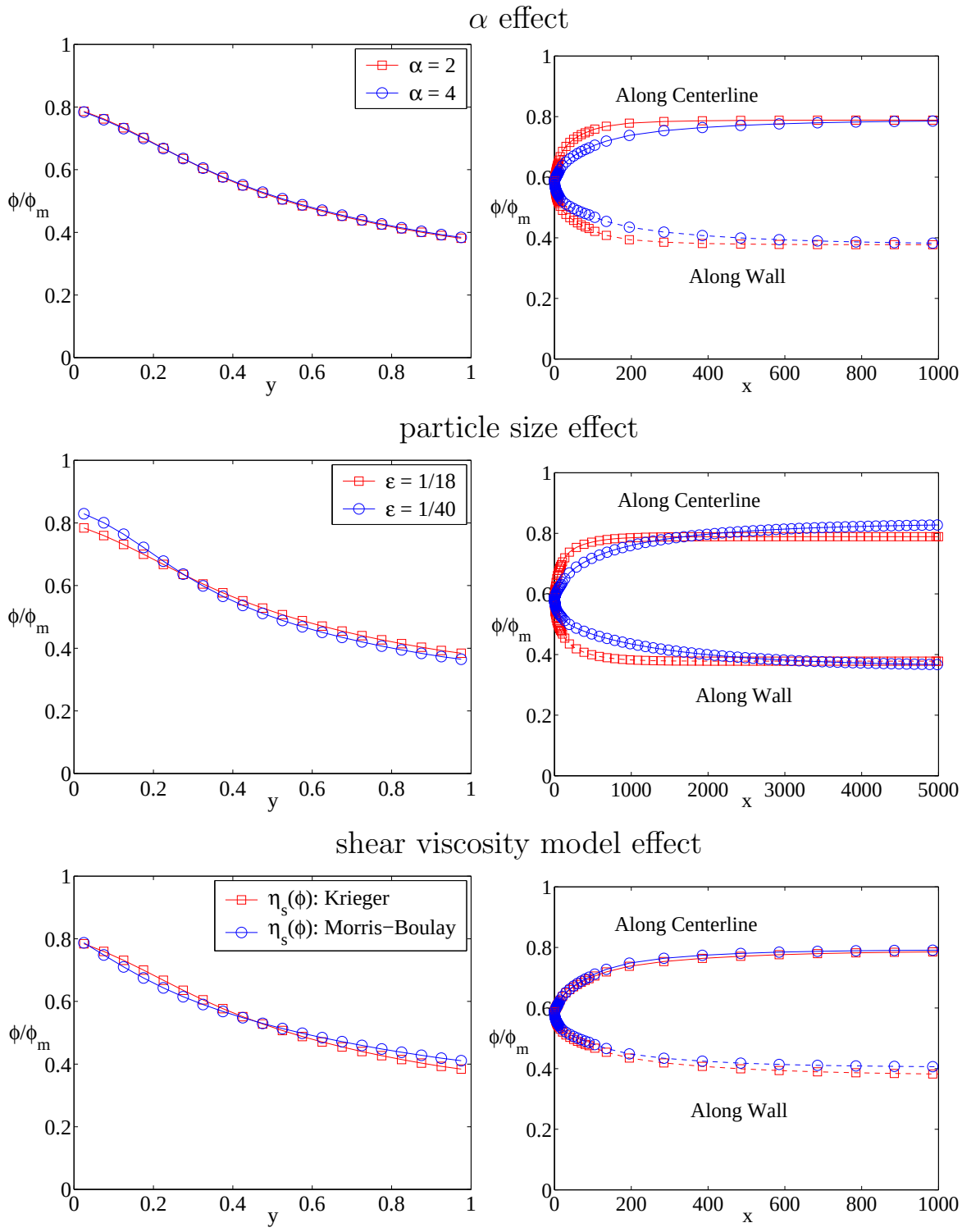

Figure 19: Comparison of the effect of model parameters on the predicted ϕ/ϕ_m profiles for channel flows when $\phi_b = 0.4$, $\dot{\gamma}_{NL} = \epsilon$.

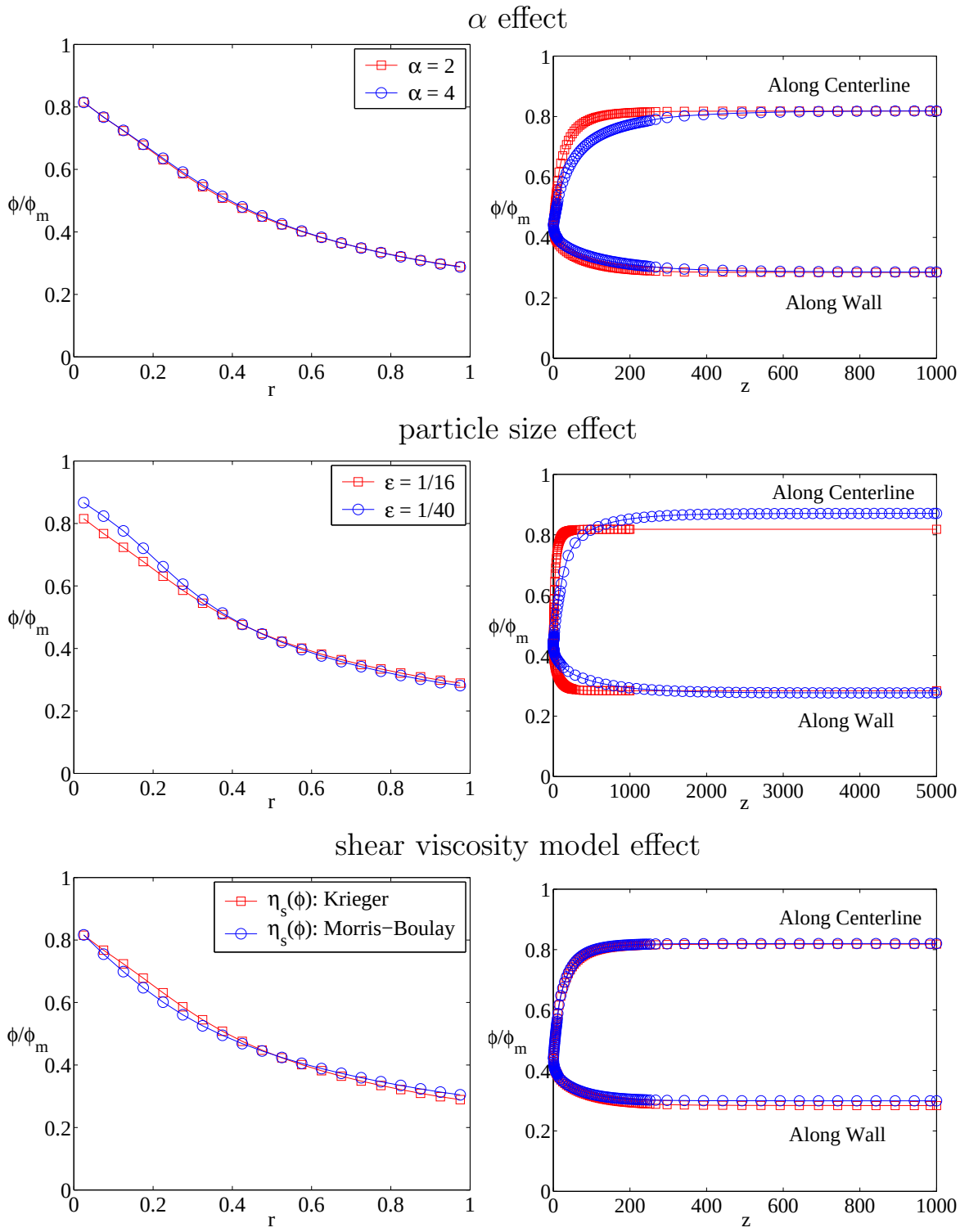

Figure 20: Comparison of the effect of model parameters on the predicted ϕ/ϕ_m profiles for pipe flows when $\phi_b = 0.3$, $\dot{\gamma}_{NL} = \epsilon$.

two-dimensional solution has 20.

Although little if any experimental measurement has appeared addressing the issue, it is found from modeling that the axial pressure variation decreases as the ϕ profile evolves in neutrally-buoyant suspension flows. A similar temporal, as opposed to axial, decrease was found in the periodic simulations of pressure-driven flow by Nott and Brady (1994). The pressure drop scales proportionally with the shear stress at the wall, which in the channel flow is of the order $\eta_o \eta_s|_{\text{wall}} U_s/B$. The migration-induced decrease in ϕ and η_s, adjacent to the wall, combined with the fixed axial flux (hence roughly fixed U_s) implies the primary variable in this scaling is the suspension viscosity. As $\eta_s|_{\text{wall}}$ decreases, the predicted axial pressure drop decreases quite significantly in moderately and highly concentrated systems, as illustrated in Figure 23 (the pressure is presented in the dimensionless form $P^* = P[L_s/\eta_o U_s]$). Consequently, a separate measure of development length, and one which may be more readily experimentally accessible than L^ϕ, is provided by the distance required for the pressure drop to complete 95% of its change in magnitude from inlet to fully-developed conditions. This length is comparable to L^ϕ but we have generally found it to be shorter in the cases presented here; see Table 1.

Noting that the particles accumulate on the high speed streamlines near the centerline, it is not surprising that a simple un-weighted average of ϕ over a cross-section decreases with axial position in either the channel or tube. This point has apparently not been addressed in work where experimental measurement of axial development has been made, but was noted by Frank *et al* (2003) as a possibility. The predicted variation of the cross-stream average of ϕ is illustrated in Figure 24 for a channel and pipe flow, with the change in mean concentration found to be slightly greater than 10% of the inlet uniform value in both cases, with the pipe flow exhibiting the greater change. This variation in the mean solids fraction may have some significance to flow systems, such as ceramics precursors, where the suspension in the conduit may subsequently be solidified and the absolute shrinkage upon loss of solvent will differ from that of the inlet material; although it is expected this will be secondary to the strong cross-stream variation.

There are strong similarities in the predicted behavior of neutrally-buoyant suspensions

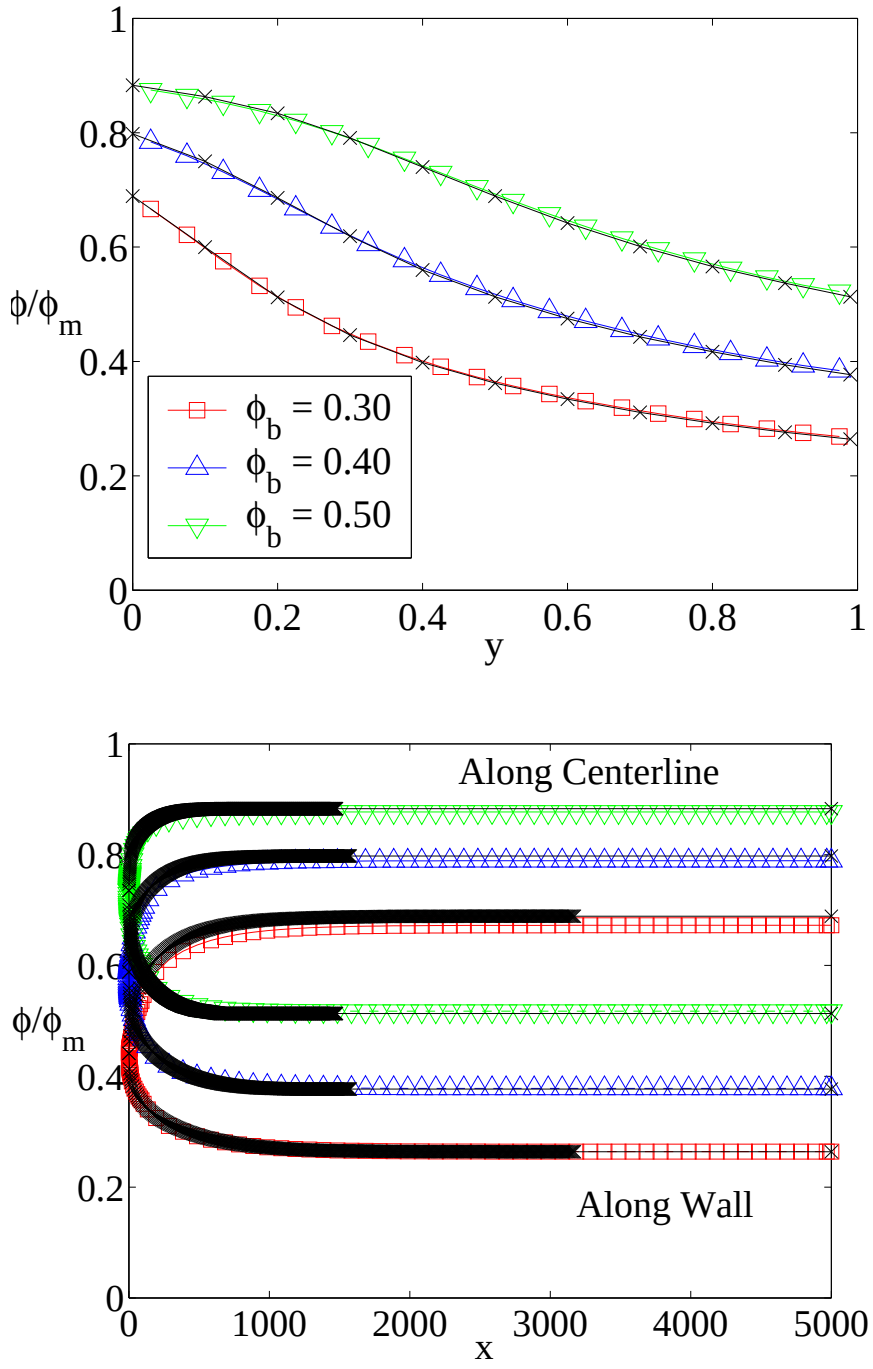

Figure 21: Predicted fully-developed cross-stream (top) and axially-developing (bottom) ϕ/ϕ_m profiles utilizing the full two dimensional numerical solution [open symbols] and a one-dimensional marching approximation [×] for channel flows with $B/a = 18$, $\dot{\gamma}_{NL} = \epsilon$, and $\alpha = 4$.

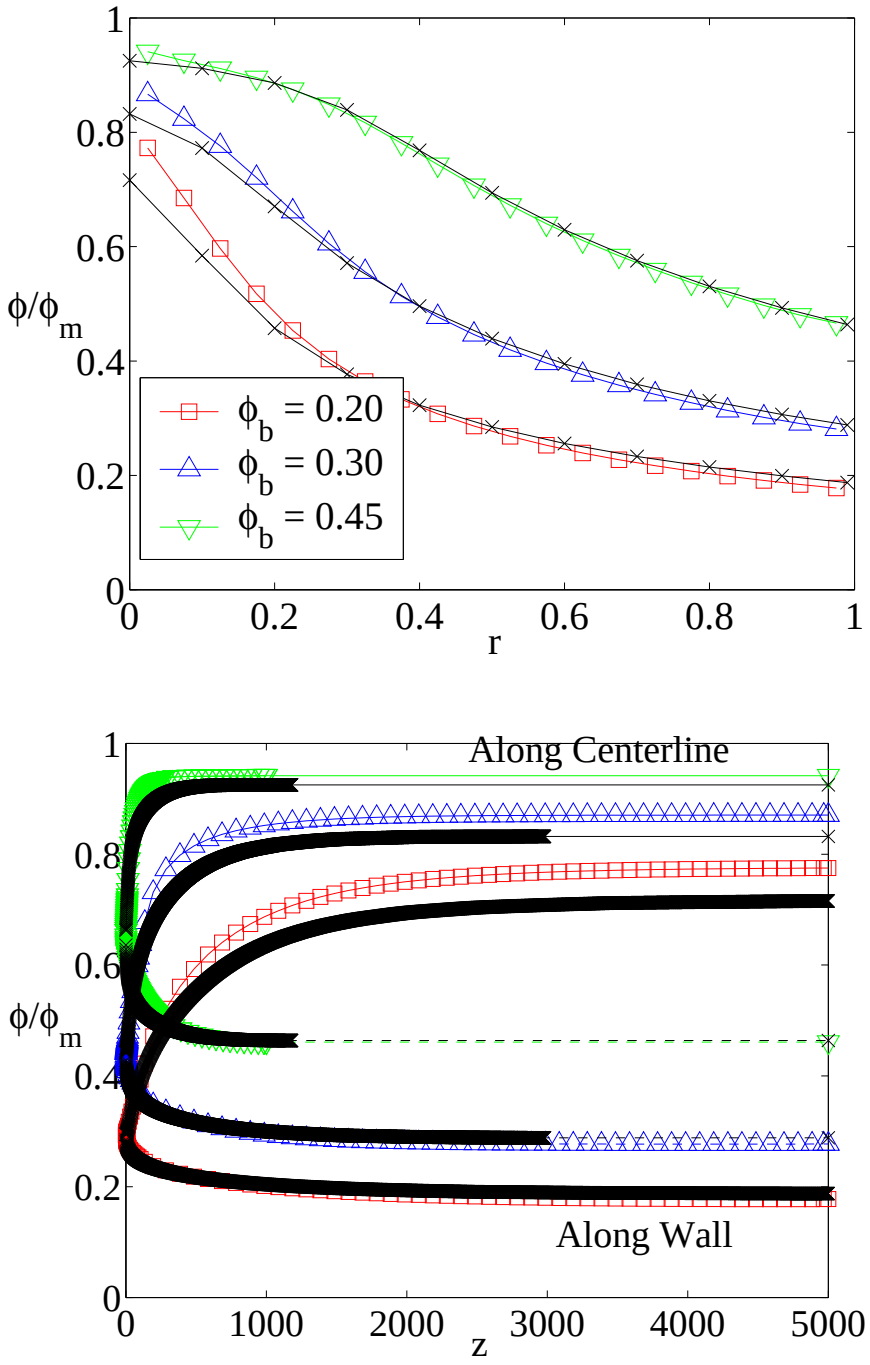

Figure 22: Predicted fully-developed cross-stream (top) and axially-developing (bottom) ϕ/ϕ_m profiles utilizing the full two dimensional numerical solution (open symbols) and a one-dimensional marching approximation [$\times$] for pipe flows with $R/a = 40$, $\dot{\gamma}_{NL} = \epsilon$, and $\alpha = 2$.

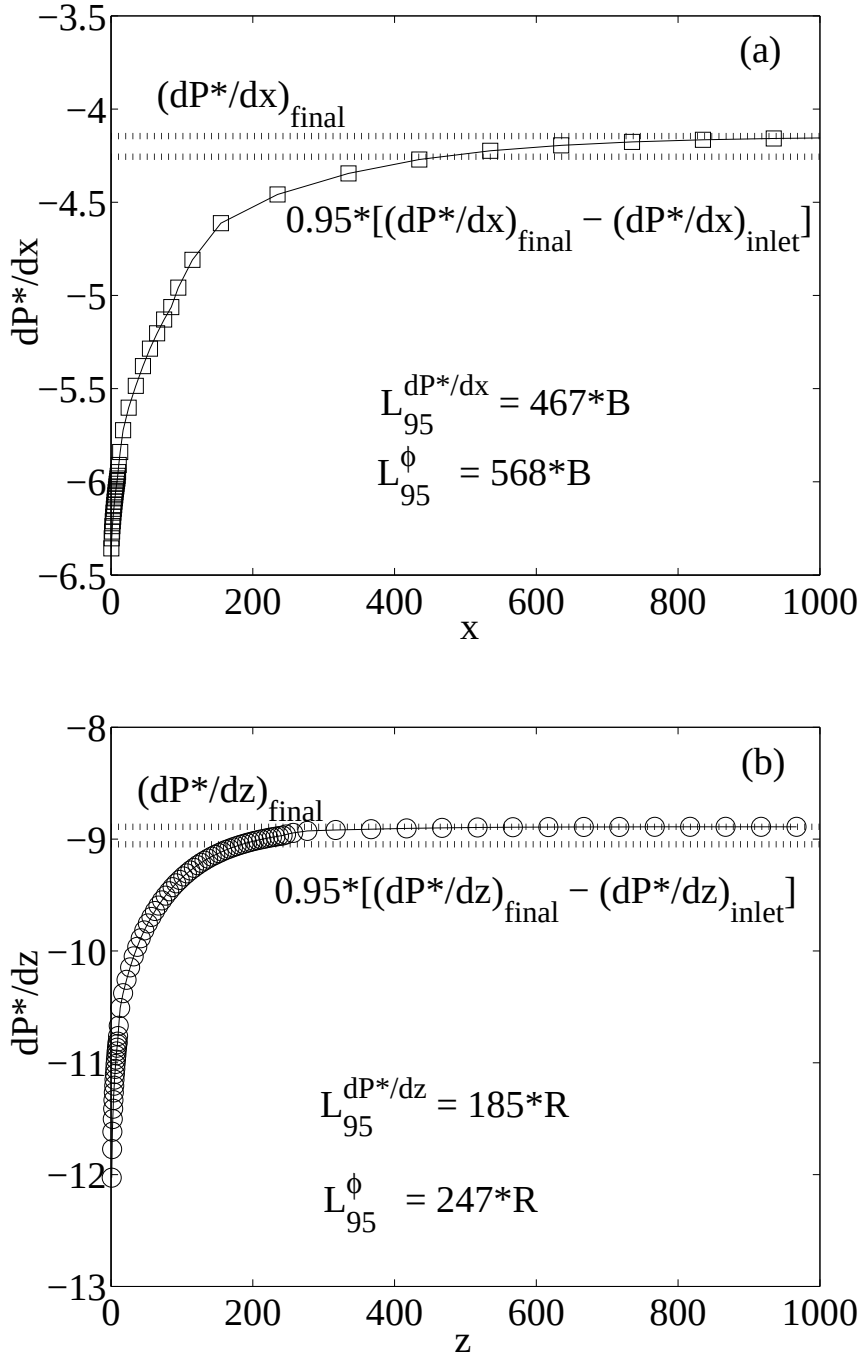

Figure 23: Predicted variation in pressure drop, with $P^* = P * (L_s/\eta_o U_s)$, as a function of axial position for (a) channel flow at $B/a = 18$ and (b) pipe flow at $R/a = 16$. ($\phi_b = 0.3$, $\alpha = 2$, $\dot{\gamma}_{NL} = \epsilon$)

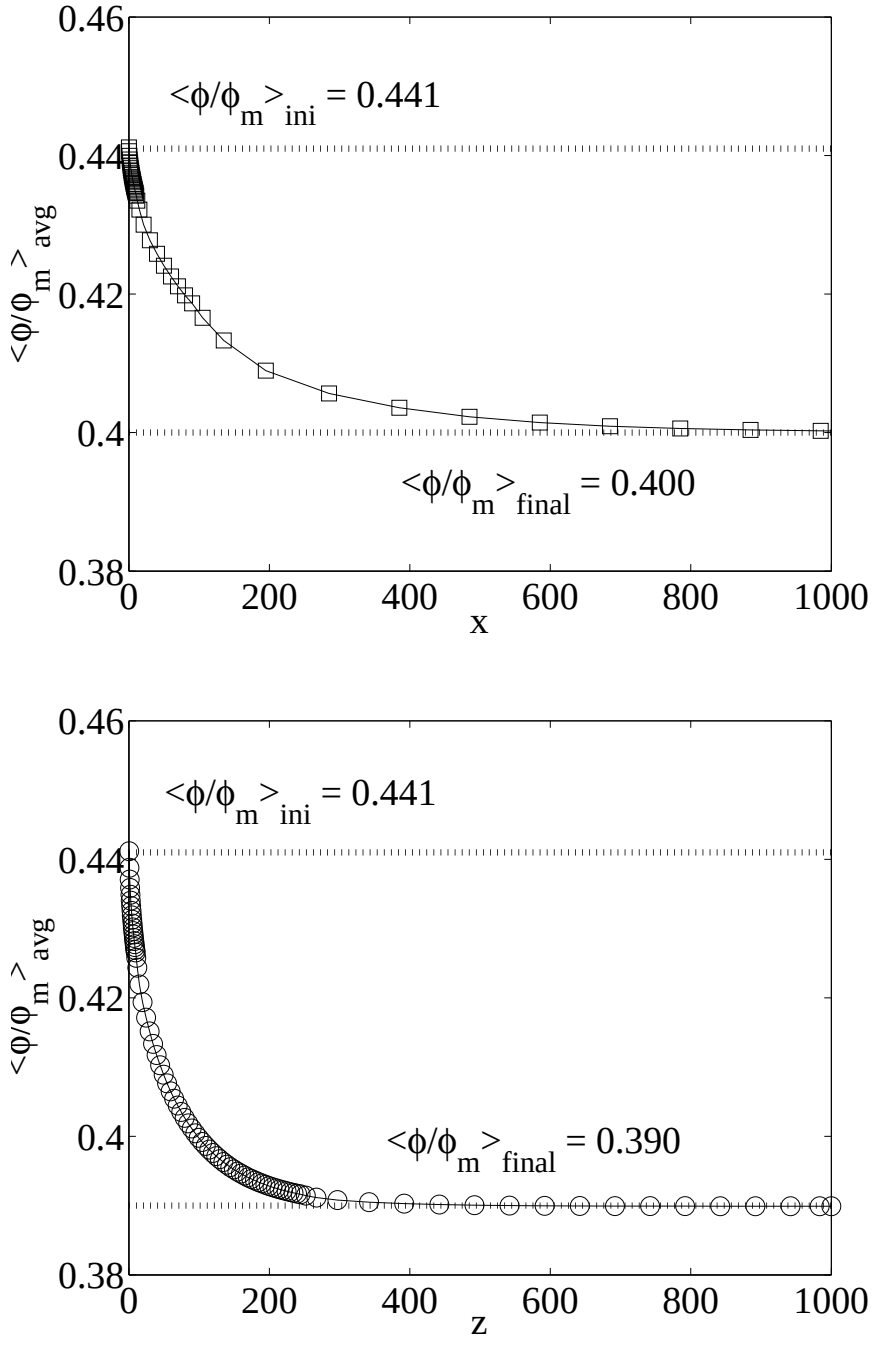

Figure 24: Predicted variation of the cross-stream averaged solids volume fraction with axial position for (a) channel flow at $B/a = 18$ and (b) pipe flow at $R/a = 16$. ($\phi_b = 0.3$, $\alpha = 2$, and $\dot{\gamma}_{NL} = \epsilon$)

for the channel and tube flows, but an important difference arises from the appearance of the second normal stress difference N_2 in the expression for the migration flux for a tube flow. This is a result of the form of the radial migration flux, which in cylindrical coordinates has the form $j_{\perp,r} \sim (\nabla \cdot \mathbf{\Sigma}_{\rm P})_r = \partial \Sigma_{{\rm P},rr}/\partial r + N_2/r$, and the relevance to the prediction of particle concentration evolution along the flow axis is illustrated by comparing the marching method approximations of the particle conservation equations for the channel, Eq. (36), and pipe, Eq. (37). While normal stress differences are known to have a role in curvilinear flows, here the relevance is seen in pipe flow. Figure 25 illustrates the role of N_2 by providing the predicted fully-developed ϕ in a channel and two separate computations of the pipe flow (using the full two-dimensional solution). The suspension conditions are $\phi_{\rm B} = 0.3$, $B/a = 18$ or $R/a = 16$ with model parameters of $\alpha = 2$, $a_s = \epsilon$. The pipe flows are run such that N_2 is set equal to zero or has the value recommended by Morris and Boulay (1999) of $N_2 \approx -0.3\eta_o\eta_n\dot{\gamma}$; the full ϕ-dependence of N_2 for a noncolloidal suspension of hard spheres is not known, but at $\phi > 0.3$ the negative value is reliable (Phung, Brady and Bossis, 1996; Morris and Katyal, 2002). The fully-developed ϕ profile satisfies $(\nabla \cdot \mathbf{\Sigma}_{\rm P})_r = 0$ or

$$\partial \Sigma_{{\rm P},rr}/\partial r + N_2/r = 0. \tag{40}$$

The inclusion of N_2 influences not only the fully-developed ϕ profile, increasing the value near the centerline and decreasing it near the wall, but also speeds the migration rate and thereby reduces the development length (see Table 2). In fact, Fang *et al* (2002) noted the role of stress anisotropy in the radial migration in tube flow, although their expression of the fully-developed radial momentum balance (their equation 69) is expressed in terms of the particle pressure rather than N_2,

$$\frac{\partial \Pi}{\partial r} + \frac{\Pi}{2r} = 0.$$

The results are nonetheless consistent with Eq. (40), given their constitutive model. To see this, note first that $\Pi = -(1/3)(\Sigma_{11} + \Sigma_{22} + \Sigma_{33})$ with 1, 2, and 3 corresponding here to axial, radial and circumferential (z, r, and θ) directions, then combine this with their modeling of the anisotropic normal stresses, $\Sigma_{11} = \Sigma_{22} = 2\Sigma_{33}$; thus $\Sigma_{11} = -6\Pi/5$ and the

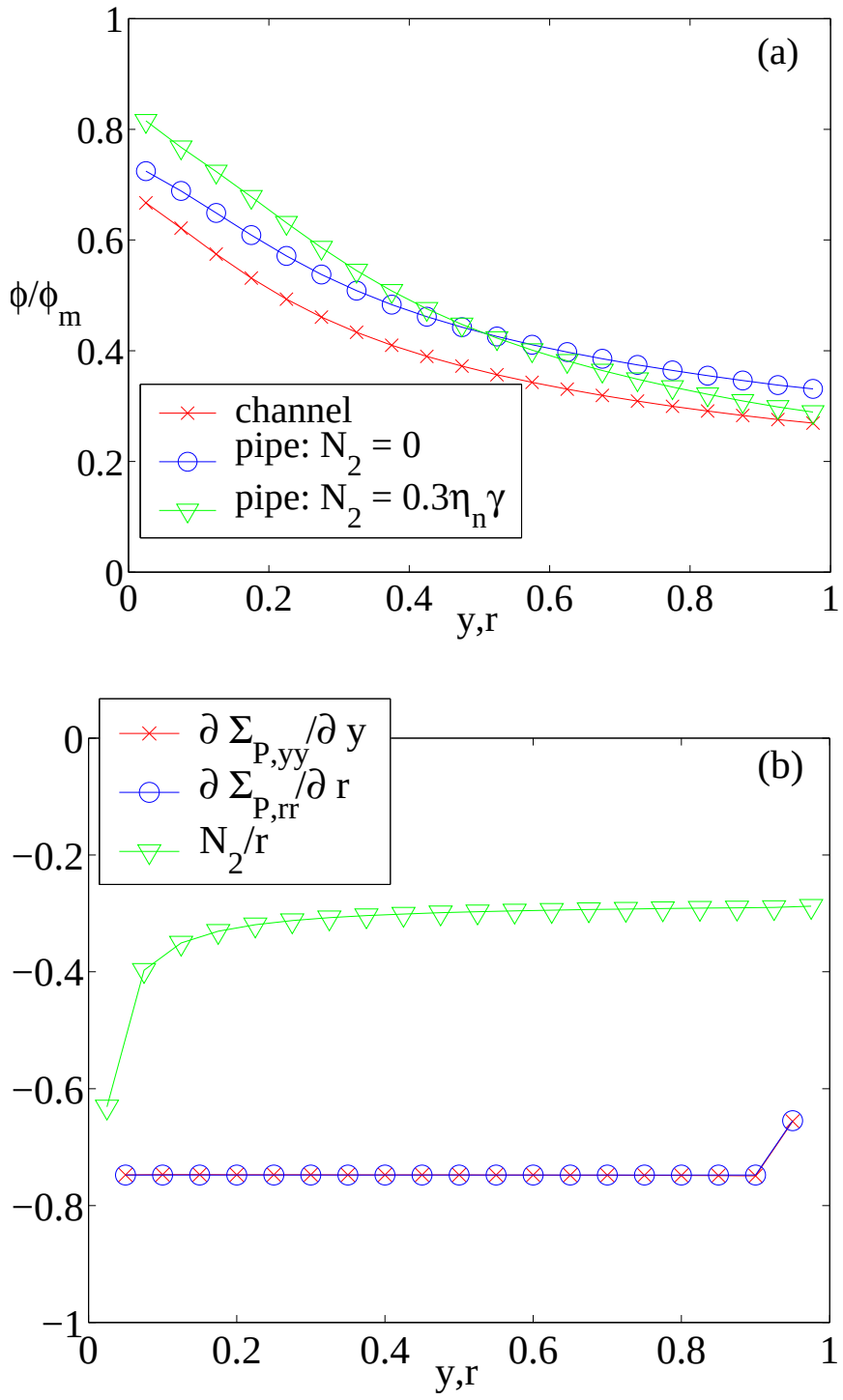

Figure 25: (a) The effect of geometry and N_2 on the predicted fully-developed cross-stream ϕ/ϕ_m profile; (b) particle stress effects at the initial bulk concentration. ($\phi_b = 0.3$, $\alpha = 2$, $\dot{\gamma}_{NL} = \epsilon$, $B/a = 18$ and $R/a = 16$)

quoted result follows by substitution.

We conclude our presentation of model predictions by pointing out a limitation to the marching method, in particular by considering pressure-driven suspension flow through a conduit with a rapidly-varying cross-section. The ability to obtain large cross-stream resolution in the marching method for little computational cost is the advantage of the approximate method where it is applicable. The marching method is not applicable to flows with rapidly changing boundary geometry, with an example of some practical relevance being a sudden contraction. This is illustrated using a channel flow with a sharp-edged contraction of ratio 2:1 (upstream half-width B, downstream $B/2$) following a straight-walled flow of $1000B$. The same particle stress constitutive model and boundary conditions are used for the contraction flow as for the previous channel flows. The solids fraction at steady fully-developed conditions and the corresponding streamlines appear in Figure 26, along with the scalar measure, E_p. While E_p does not have a readily understood meaning within the contraction, the variation of this parameter shows a localized influence upstream from the sudden contraction, as the curves with and without the contraction quickly become indistinguishable a few B upstream. While inapplicable near the contraction, the marching method may be used to determine the appropriate inlet conditions to a two-dimensional model of the domain local to the contraction. The contraction represents a flow with considerable variation of the flow type. A more thorough exploration of flow modeling in general geometries is presented in Chapter 5 and Chapter 6.

3.5 Conclusions

The axial development of pressure-driven flows of suspensions under moderate to highly concentrated conditions has been studied using the suspension flow model presented in Chapter 2, in which gradients in the particle stresses, in particular the divergence $\nabla \cdot \mathbf{\Sigma}^P$, drive particle migration. The physical basis of migration is relatively simple. In a flow in which the shear-induced stress varies, the non-Newtonian contribution to the bulk stress resulting from the presence of the particles need not be in balance, and the system may undergo a de-mixing in order to relax the imbalance.

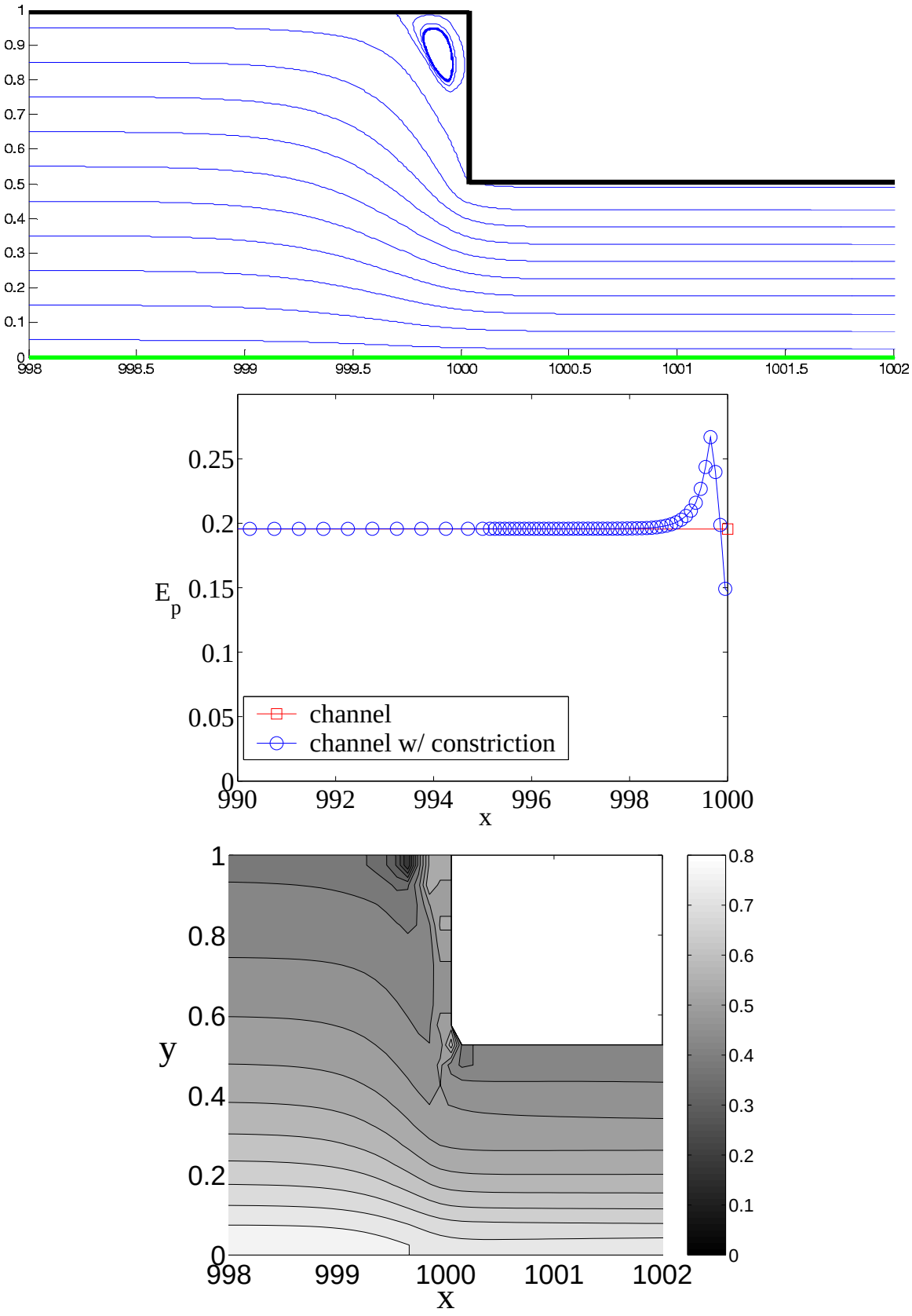

Figure 26: Velocity streamlines near the contraction for a long channel with a 2:1 contraction at the exit (top). Plots of the axial variation of E_p (middle) and contours of ϕ/ϕ_{m} (bottom) near the contraction are included.

The form of the model used here, with the develop illustrated in Chapter 2, is that presented in the work of Morris and Boulay (1999) and is similar in most features to that presented in Fang *et al* (2002). Both constitutive models include stress anisotropy. The model comparisons with experiment are generally favorable, as the salient features of behavior observed in experiments are captured by the model. The detailed form of the various quantities has not been fit by variation of parameters, but certainly could be. Hence the model provides a potentially useful tool for engineering studies of suspensions.

One parameter, the exponent in the sedimentation hindrance function representing particle mobility relative to the suspending fluid, was found to be better represented by a smaller value than the $\alpha = 4$ used in Morris and Boulay (1999), and we have used $\alpha = 2$ as this yields better agreement with the axial development data of Hampton *et al* (1997). Fang *et al* (2002) used a different form of the sedimentation function, roughly equivalent to taking $\alpha = 2.8$.

The solution of the model was determined for the conduit flows by two approaches, a finite-volume-method solution in two-dimensions and a marching method. The FVM approach was implemented in a tool which sequentially solved the flow and then updated the solids fraction field, termed the "solver-evolver." The tool was designed for study of general-geometry suspension flows and represents, in fact, a quite computationally expensive approach for the extended domains encountered in axially-evolving flows. Consequently, a marching method which uses a scaling analysis to reduce the governing equations was developed. The approximation is in the spirit of a lubrication approximation based on the strong cross-stream and weak axial gradients. Given conditions at one axial station, the variation of ϕ between this station and the next (in this approximation) along the axial direction may be expressed solely in terms of information from the upstream station. This effectively reduces the partial differential equations to a set of coupled ordinary differential equations of which one is an initial value problem readily resolved by an Euler-scheme.

Comparisons of the results of the two methods show the computationally efficient marching method is satisfactory for all straight conduit conditions studied here. We have illustrated the failure of the method in flows with rapidly varying boundary geometry, a problem

studied in detail in the following chapters and future work (Miller and Morris, 2004).

The work has illustrated that the cross-sectional mean particle volume fraction must decline in a steady state flow as the mixture moves down axis (at least for neutrally-buoyant suspensions). This is a result of the accumulation of solids on the fast moving streamlines, and the need to maintain a constant flux of particles at any axial station (equivalent to a constant cup mixing average of solid fraction). The pressure drop per unit length also decreases quite significantly from its initial value, an expected result as the effective viscosity at the wall drops with particle migration from the boundaries but one which has not been explored in experiments, to our knowledge.

While the agreement with experiment is generally good, the predicted behavior near boundaries has yet to be satisfactorily matched with data. The experiments with which comparison was made here – channel flow (Lyon and Leal, 1998a), pipe flow (Hampton *et al*, 1997) – both exhibit a drop off in ϕ near the boundaries. Although some of this may be attributed to experimental artifacts, there is some doubt as to this being a complete explanation. It may be necessary to consider wall influence upon mixture stress more carefully for concentrated systems in order to resolve the issue.

CHAPTER 4

SIMPLE GEOMETRY: SUSPENDING FLUID EFFECTS

In this chapter we model suspension flows with a non-Newtonian suspending fluid. The ability to model a suspension with a complex suspending fluid is one with a great many applications including ceramic injection molding, paper processing and even blood flow. Being able to take into account the effect of the particle migration on such flows or the effect of complex fluids on particle migration is thus relevant to many industrial and medical applications. We have chosen to do some basic work to illustrate how to go about modifying the suspension flow model to take into account a non-Newtonian suspending fluid for a very basic case — a shear-thinning suspending fluid. But by showing that this basic case is possible, we open up the avenue for the possible use of more complex non-Newtonian fluid models.

In the following section, we review the suspension flow model and illustrate how it is modified for a shear-thinning, non-Newtonian suspending fluid. In Section 4.2, we review the experimental work of Rao *et al* (2002) for a wide-gap circular Couette flow and in Section 4.3 develop the solution equations used to model this flow. In Section 4.4, we compare our model predictions with the results of Rao *et al* and show how the addition of a shear-thinning suspending fluid affects the approach of the model predictions to steady-state. In Section 4.5, we end with some conclusion and observations.

4.1 Governing Equations

As in Chapter 3, we utilize the suspension flow equations developed in Chapter 2 to model a suspension of rigid, spherical particles in a shear flow. We limit the study to non-Brownian, neutrally buoyant particles under low-Reynolds-number flow conditions where both the bulk and individual particle inertia effects are not significant. The resulting bulk mass and

momentum conservation equations and migration equation governing the particle phase are

$$\nabla \cdot \mathbf{u} = 0, \tag{41}$$

$$-\nabla P + \nabla \cdot (2\bar{\eta}_s \mathbf{E}) + \nabla \cdot \mathbf{\Sigma}_{\mathrm{P}}^{NS} = 0, \tag{42}$$

$$\frac{\partial \phi}{\partial t} + \mathbf{u} \cdot \nabla \phi = -\nabla \cdot \mathbf{j}_{\perp}, \tag{43}$$

where $\mathbf{u}$ is the bulk suspension velocity, P is the suspension pressure, $\bar{\eta}_s$ is the shear viscosity, $\mathbf{E}$ is the rate of strain, $\mathbf{\Sigma}_{\mathrm{P}}^{NS}$ is the particle phase normal stress, ϕ is the particle volume fraction and $\mathbf{j}_{\perp}$ is the particle migration flux. The bulk rate of strain is defined as $\mathbf{E} = \frac{1}{2}[\nabla \mathbf{u} + (\nabla \mathbf{u})^T]$ and the form of the particle normal stress, $\mathbf{\Sigma}_{\mathrm{P}}^{NS}$, is given below in the particle phase stress definition.

The particle migration flux is determined from the particle-phase momentum conservation to be

$$\mathbf{j}_{\perp} = \frac{2a^2}{9\eta_o} f(\phi) \nabla \cdot \mathbf{\Sigma}_{\mathrm{P}}, \tag{44}$$

where a is the particle radius, η_o is the Newtonian suspending fluid viscosity, $f(\phi)$ is the sedimentation hindrance function, and $\mathbf{\Sigma}_{\mathrm{P}}$ is the particle phase stress. We use a modified form of the sedimentation hindrance function (Richardson and Zaki, 1954), which is given in Chapter 2, Eq. (12). For our applications here, we use a value of $\alpha = 4$ for the exponent. This value was chosen for the Couette flow since it matched the value used by Morris and Boulay (1999) in their model comparisons to Couette suspension flow results (Phillips *et al*, 1992) with a Newtonian suspending fluid.

The particle stress model is of the form suggested by Morris and Boulay (1999) for shear flows

$$\mathbf{\Sigma}_{\mathrm{P}} = -\bar{\eta}_n(\phi)\dot{\gamma}\mathbf{Q} + 2\bar{\eta}_p(\phi)\mathbf{E}, \tag{45}$$

and contains both a shear, $\mathbf{\Sigma}_{\mathrm{P}}^{SH} = 2\bar{\eta}_p \mathbf{E}$, and normal, $\mathbf{\Sigma}_{\mathrm{P}}^{NS} = -\bar{\eta}_n \dot{\gamma} \mathbf{Q}$, stress portion. The local shear rate is defined, $\dot{\gamma} = \sqrt{2\mathbf{E} : \mathbf{E}}$, and we chose not to include a nonlocal correction, as explained in Chapter 3, Section 3.1.1. This is done because for a wide-gap circular Couette flow the $\dot{\gamma}$ profile across the gap is smooth with no regions where $\dot{\gamma} \to 0$. The

anisotropic tensor, $\mathbf{Q}$, follows the form given in Morris and Boulay (1999)

$$\mathbf{Q} = \begin{pmatrix} 1 & 0 & 0 \\ 0 & \lambda_2 & 0 \\ 0 & 0 & \lambda_3 \end{pmatrix}, \tag{46}$$

where $\lambda_2 \approx 0.8$ and $\lambda_3 \approx 0.5$. These were chosen to match observed migration behavior in viscometric flows (Phillips *et al*, 1992; Chow *et al*, 1994). The directions of $\mathbf{Q}$ correspond to the principal directions of a viscometric shear flow with 1, 2 and 3 denoting flow, gradient, and vorticity, respectively. For the circular Couette flow this corresponds to $(1, 2, 3) \Rightarrow (\theta, r, z)$.

The normal stress viscosity ($\bar{\eta}_n = \eta_o \eta_n(\phi)$), particle phase viscosity (η_p), and shear viscosity ($\bar{\eta}_s = \eta_o \eta_s(\phi) = \eta_o(1 + \eta_p)$) are defined in Chapter 2. We use the form suggested by Morris and Boulay (1999) for $\eta_s(\phi)$. To modify the suspension flow model for a non-Newtonian suspending fluid, we replace the suspending fluid viscosity value, η_o, in the modeling equations with a value which is a function of the local shear rate, $\eta_c(\dot{\gamma})$. This includes replacing η_o in the above viscosity equations and in Eq. (44). To match the shear-thinning nature of the suspending fluid used in Rao *et al* (2002), they chose to fit rheometric data to a Carreau viscosity law,

$$\eta_c(\dot{\gamma}) = \eta_\infty + (\eta_o - \eta_\infty)[1 - (\lambda_{TC}\dot{\gamma})^{a_c}]^{(n-1)/a_c}, \tag{47}$$

where η_∞, η_o, λ_{TC}, a_c, and n are fitting parameters which will be explained below.

4.2 Wide-gap Circular Couette Flow of a Suspension with a Shear-thinning Suspending Fluid

For the case of a circular wide-gap Couette flow with a shear-thinning suspending fluid, the model was solved at an inner cylinder rotation rate, ω, of 8.5 RPM and 82 RPM with a suspended particle size of 675 μm in diameter. Solutions were also obtained at an inner cylinder rotation rate of 8.5 RPM with a suspended particle size of 100 μm in diameter. These conditions were chosen to match the experimental data of Rao *et al* (2002). This data was taken for polymethyl methacrylate (PMMA) spheres suspended in a mixture of

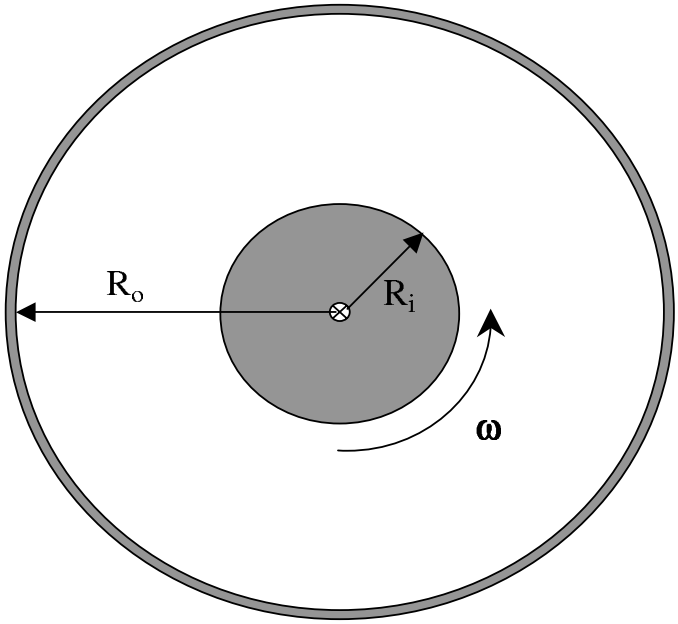

Figure 27: Sketch of the wide-gap Couette flow geometry.

70 wt% glycerine, 28 wt% water, and 2wt% Carbopol 940. Carbopol 940 is a long-chain polymer which was chosen because it produces a highly shear-thinning, non-elastic fluid when mixed in solution (Gheissary and van den Brule, 1996). The initial concentration of the particle phase was $\phi_{\mathrm{B}} = 0.5$ and concentration measurements were taken using an NMR to image an axial slice of the geometry after a given number of rotations of the inner cylinder. The device length was much longer than the gap width and both ends were capped, leaving axial variation in concentration and flow negligible. The outer radius of the rotating inner cylinder was $R_i = 0.64$ cm and the inner radius of the stationary outer cylinder was $R_o = 2.38$ cm. The suspending fluid was characterized using a cone-and-plate viscometer. In Figure 28, the experimental viscosity measurements from Rao *et al* (2002) are plotted against a curve fit to the Carreau viscosity model given in Eq. (47). Rao *et al* (2002) chose fitting parameters of $\eta_o = 4 \times 10^5$ Poise for the zero-shear-rate viscosity, $\eta_\infty = 10$ Poise for the high-shear-rate viscosity, $\lambda_{TC} = 2150$ sec for the time constant, $n = 0.178$ for the power law exponent, and $a_c = 1.0$ for the transition exponent. The plot illustrates that these parameters provide a very good fit (solid line) to the experimental data. The one problem

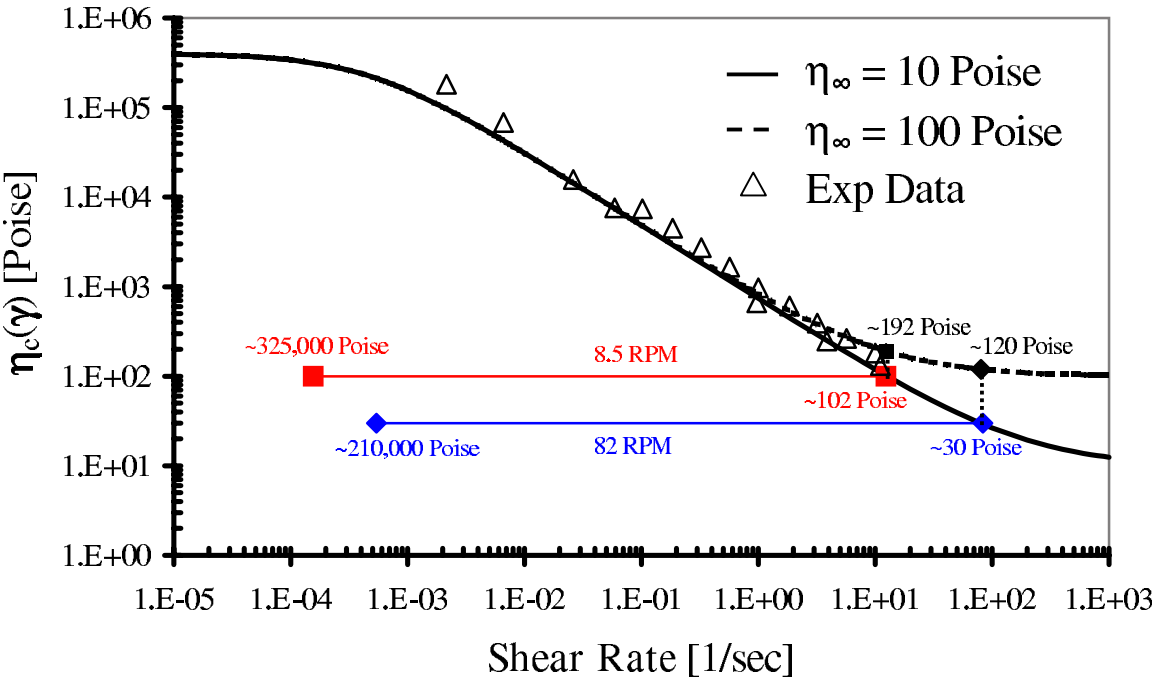

Figure 28: Comparison of the experimental viscosity data of Rao *et al* (2002) for a Carbopol 940 solution to a fit of the Carreau viscosity model given in Eq. (47). The line with square endpoints represents the predicted shear rate range in a wide-gap circular-Couette flow with a shear-thinning suspending fluid for an inner cylinder rotation rate of 8.5 RPM. The diamond endpoints represent the range for 82 RPM.

area occurs in the area of the high-shear-rate viscosity. The experimental data stops at a shear rate of $\dot{\gamma} = 10$ sec^{-1}, while the range of the shear-rate experienced for the inner cylinder rotation rate of 82 RPM exceeds this. To explore the effect that the high-shear-rate parameter has on migration we also look at cases where $\eta_\infty = 100$ Poise, represented by the dashed line in Figure 28.

Further cases beyond those matching the experimental data were modeled. This was done to allow the examination of the effects of varying bulk rate and particle size on migration and to explore the approach of the Newtonian and shear-thinning cases to what the model predicts should be an identical steady-state particle fraction profile.

4.3 Model Equations for a Wide-gap Circular Couette Flow

4.3.1 Flow field equations

For the flow field solution, we assumed no slip conditions at the wall, and a smooth variation in $\dot{\gamma}$ across the gap. In shear flow terms, the directions correspond as such: $(\theta, r, z) = (1,2,3)$

= (flow,gradient,vorticity) as explained in Section 4.1.

The flow conditions were limited by the assumption of no flow in the radial(r) or axial(z) directions, $\mathrm{u}_r = \mathrm{u}_z = 0$, and the assumption of no variation in the azmuth(θ) or axial(z) directions. This results in $\partial P/\partial\theta = 0$ and $\mathrm{u}_\theta = \mathrm{u}_\theta(r)$. These assumptions leave the θ-directed momentum equation as the only significant equation. After simplification and integration, this yields

$$\bar{\eta}_s E_{r\theta} = \frac{C_{\dot{\gamma}}}{r^2}, \tag{48}$$

where $C_{\dot{\gamma}}$ is a constant to be determined later. In addition, by definition $2\bar{\eta}_s E_{r\theta} \sim \bar{\eta}_s \dot{\gamma}$, resulting an expression for the shear-rate as a function of position in the gap

$$\dot{\gamma} = \frac{C_{\dot{\gamma}}}{\bar{\eta}_s r^2} \tag{49}$$

This equation for the shear rate is generally valid for both steady and unsteady solutions due to the nature of zero-Reynolds-number conditions. This results in a quasi-steady solution which changes on the time scale of the particle migration.

In order to solve for the constant, $C_{\dot{\gamma}}$, the form of the rate of strain, $E_{r\theta}$, is utilized. Substituting into Eq. (48), we get

$$\frac{\partial}{\partial r}\left(\frac{\mathrm{u}_\theta}{r}\right) = \frac{-C_{\dot{\gamma}}}{\bar{\eta}_s r^3}, \tag{50}$$

which is integrated across the Couette gap, applying boundary conditions of $\mathrm{u}_\theta(R_i) = \omega R_i$ at the inner cylinder and $\mathrm{u}_\theta(R_o) = 0$ at the outer cylinder. This results in an expression for $C_{\dot{\gamma}}$,

$$C_{\dot{\gamma}} = \frac{\omega}{\int_{R_i}^{R_o} \frac{\mathrm{d}r}{\bar{\eta}_s r^3}}, \tag{51}$$

which is a function of the inner cylinder rotation rate, ω, and current $\phi(r)$ profile. This equation can also be rearranged, with a substitution of the expression for $\dot{\gamma}$, to solve for $\mathrm{u}_\theta(r)$.

$$\mathrm{u}_\theta(r) = -r \int_{R_o}^{r} \frac{\dot{\gamma}}{r'} \mathrm{d}r'. \tag{52}$$

4.3.2 Particle migration equations

The particle migration flux is determined from the assumptions for a wide-gap Couette flow that particles migrate in the r-direction only. This results in the following expression for

the particle migration flux,

$$j_{\perp,r} = \frac{2}{9}a^2 \frac{f(\phi)}{\eta_c(\dot{\gamma})}[\nabla \cdot \Sigma_{\mathrm{P}}]_r, \tag{53}$$

where,

$$[\nabla \cdot \Sigma_{\mathrm{P}}]_r = \frac{1}{r}\frac{\partial}{\partial r}(r\Sigma_{\mathrm{P},rr}) - \frac{\Sigma_{\mathrm{P},\theta\theta}}{r} = \frac{\partial \Sigma_{\mathrm{P},rr}}{\partial r} - \frac{N_1}{r}, \tag{54}$$

with the first normal stress difference defined as, $N_1 = \Sigma_{11} - \Sigma_{22} = \Sigma_{\theta\theta} - \Sigma_{rr}$. Substituting the above expressions into Eq. (43) and noting that the convective term on the LHS drops out, we formulate an expression for the unsteady particle migration in a wide-gap circular Couette device,

$$\frac{\partial \phi}{\partial t} = -\frac{2a^2}{9}\frac{1}{r}\frac{\partial}{\partial r}\left\{ r\left[\frac{f(\phi)}{\eta_c(\dot{\gamma})}\left(\frac{\partial \Sigma_{\mathrm{P},rr}}{\partial r} - \frac{N_1}{r} \right) \right] \right\}. \tag{55}$$

The shear-thinning viscosity, $\eta_c(\dot{\gamma})$, remains within the differential due to the spatial variation of $\dot{\gamma}$. For the steady-state expression, we set $\partial\phi/\partial t = 0$ and use the fact that $j_{\perp,r} = 0$ at the boundaries to enforce no penetration of the particle phase into the walls. This leaves a steady-state solution of

$$\frac{\partial \Sigma_{\mathrm{P},rr}}{\partial r} - \frac{N_1}{r} = 0 \tag{56}$$

4.3.3 Numerical solution equations

The steady-state solution is determined from Eq. (56) by substituting in for the particle stress with the definition in Eq. (45). This definition results in $\Sigma_{\mathrm{P},rr} = -\bar{\eta}_n\dot{\gamma}\lambda_2$ and $N_1 = -\bar{\eta}_n\dot{\gamma}(1-\lambda_2)$ for the particle stress terms and

$$\frac{\partial(-\eta_c\eta_n\dot{\gamma})}{\partial r} = \frac{\eta_c\eta_n\dot{\gamma}}{r}\frac{(1-\lambda_2)}{\lambda_2}, \tag{57}$$

for the steady-state solution. The group of variables, $\eta_c\eta_n\dot{\gamma}$, occur on both sides of the equation and can be reduced by substituting for the shear rate with Eq. (49),

$$\eta_c\eta_n\dot{\gamma} = \frac{\eta_c\eta_n}{\eta_c\eta_s}\frac{C_{\dot{\gamma}}}{r^2}, \tag{58}$$

This results in η_c dropping out of the expression. The fact that the shear-thinning viscosity drops out of the equations is an interesting development because it results in the model predicting an identical steady-state $\phi(r)$ profile for both a Newtonian and non-Newtonian

suspending fluid, since the suspending fluid viscosity would drop out of the expression for a Newtonian fluid as well.

After the substitution for the shear-rate, we combine the ratio η_n/η_s into a single variable, $q(\phi)$. Then we rearrange Eq. (57) into an expression for q,

$$\frac{\partial q}{\partial r} = \frac{q}{r}\frac{(1+\lambda_2)}{\lambda_2}, \tag{59}$$

which is integrated to give

$$q(\phi) = A_1 r^{\frac{1+\lambda_2}{\lambda_2}}, \tag{60}$$

where A_1 is a constant. This equation is solved for $\phi(r)$ with a golden section search root finding routine in MATLAB. The constant, A_1, is determined by maintaining that the average particle volume fraction matches the initial bulk concentration, ϕ_{B}. A few important points to note about the steady-state solution are it does not depend on the rotation rate of the inner cylinder, the suspended particle size, or composition of the suspending fluid. In fact, it only appears to be dependent on λ_2 and ϕ_{B} for our model assumptions.

The unsteady solution is developed in a manner similar to the steady-state solution. Substituting for the particle stress terms and then for the shear-rate, Eq. (55) becomes

$$\frac{\partial \phi}{\partial t} = -\frac{2a^2}{9}\frac{C_{\dot{\gamma}}}{r}\frac{\partial}{\partial r}\left\{\frac{f(\phi)}{\eta_c(\dot{\gamma})}\left[-\frac{\lambda_2}{r}\frac{\partial q}{\partial r} + \frac{q}{r^2}(1+\lambda_2)\right]\right\}. \tag{61}$$

This equation was solved using a finite difference approximation with central differences in the r-direction and an explicit time step. The values of q, $f(\phi)$, and η_c are obtained using information from the previous time step. The RHS is then approximated with a central difference scheme and used to update the particle volume fraction value for the next time step.

$$\Delta\phi = -\frac{2C_{\dot{\gamma}}a^2}{9}\left[\frac{rj_{\perp,r}|_{i+1,t-1} - rj_{\perp,r}|_{i-1,t-1}}{r_i \Delta r}\right]\Delta t. \tag{62}$$

The boundary condition at the walls is taken to be

$$\mathbf{j}_\perp \cdot \mathbf{n}|_{wall} \sim j_{\perp,r} = 0. \tag{63}$$

Utilizing Eq. (59) and applying the chain rule, an expression for the gradient in particle volume fraction at the boundaries is obtained.

$$\frac{\partial \phi}{\partial r} = \frac{q}{\frac{\partial q}{\partial \phi}}\frac{1+\lambda_2}{r\lambda_2}. \tag{64}$$

The solutions to the unsteady state migration equations were obtain utilizing a finite difference code written in FORTRAN.

4.4 Results and Discussion

4.4.1 Comparison with experiments

The model matched the experimental results in a qualitative fashion, following all the major trends. Examining the data from Rao *et al* (2002) given in Figure 29(a) and Figure 30(a), we conclude that migration rate increases with inner cylinder rotation rate and that migration is more pronounced with the large particle size. Rotations of the inner cylinder will be used to characterize the overall strain imposed on the system and act as a measurement of "time", since this is roughly equivalent to the time non-dimensionalized by the rotation rate of the inner cylinder. Migration rate is measured by noting the value of r/R_o, where R_o is the radius of the outer cylinder, at the peak in the particle volume fraction concentration profile and the amount of strain (revolutions) to reach this condition. The larger the value of r/R_o the farther the particles have migrated away from the rotating inner cylinder. Therefore, the larger the value of r/R_o, the farther that migration effects have "penetrated" into this zone of increased resistance and the larger the peak in particle volume fraction the more initial resistance experienced at this point.

The model predictions are shown in Figure 29(a) and Figure 30(b,c). These predictions illustrate the same basic trends found in the experiments: an increase in migration with an increase rotation rate or an increase in particle size. In Figure 29, the increase in the penetration of the ϕ peak may be due to the increased amount of strain, 1600 revolutions for the 675 μm results as opposed to 1000 revolutions for the 100 μm case, but there is a distinct difference between the two curves in the experimental case. The 100 μm curve appears to be "flatter" than the 675 μm curve, which is not completely captured in the model. The model predicts a small peak, but does match the decrease in the penetration of this peak. For the case of increasing rotation rate in Figure 30, the model predictions match the increase in penetration of the ϕ peak with the higher rate of rotation. Using a Carreau model with a high-shear-rate viscosity of $\eta_\infty = 100$ Poise better matches the extent of this

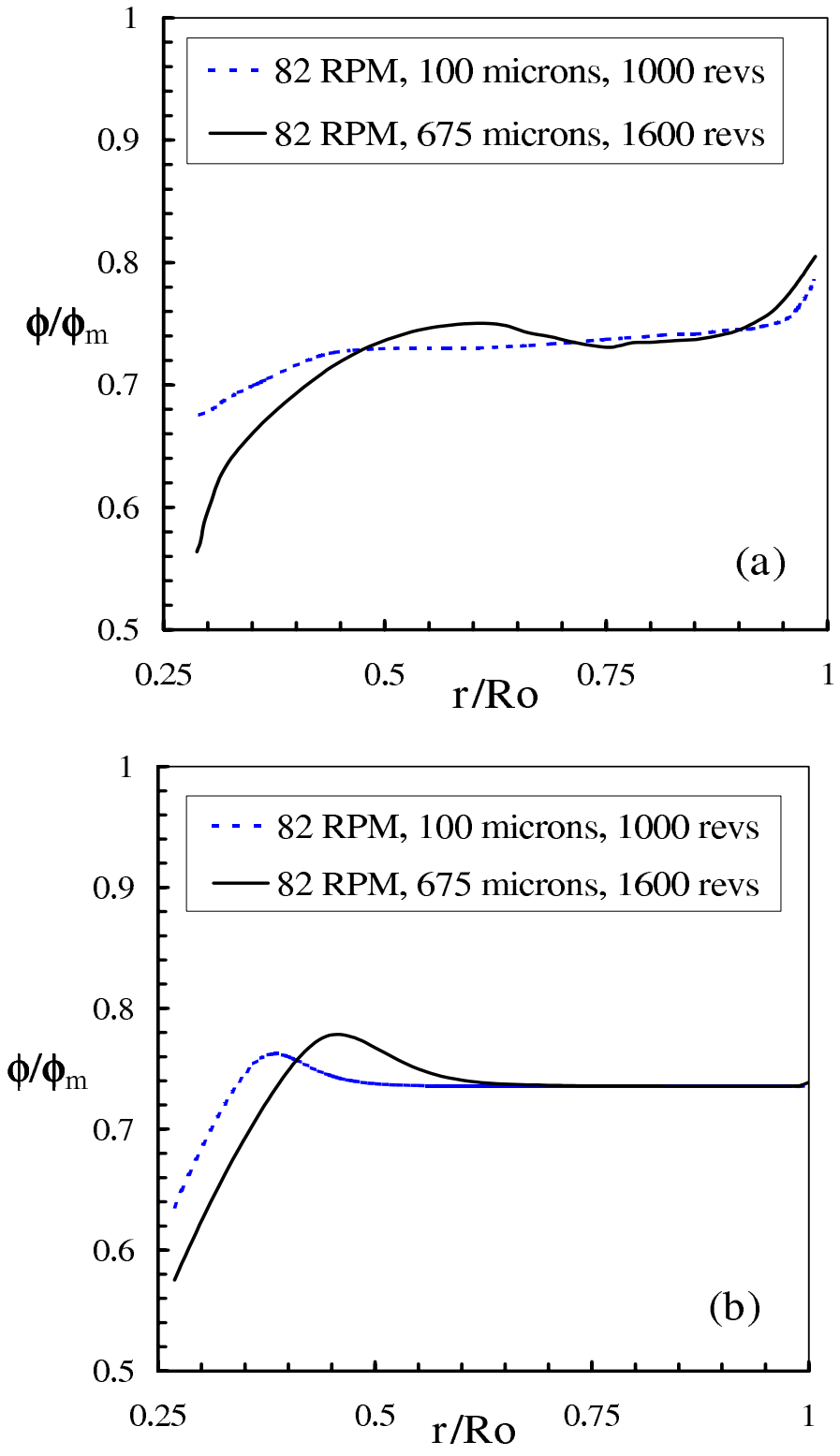

Figure 29: Comparison of the effect of the suspended particle size on the results for a circular-Couette device ($R_i = 0.64$ cm, $R_o = 2.38$ cm) with a shear-thinning suspending fluid (Carbopol 940 in glycerin/water) at a bulk concentration of $\phi_B = 0.5$ and inner cylinder rotation rate of 8.5 RPM for: (a) experimental results taken from Rao *et al* (2002); (b) model predictions with $\eta_\infty = 10$ Poise in the Carreau viscosity model.

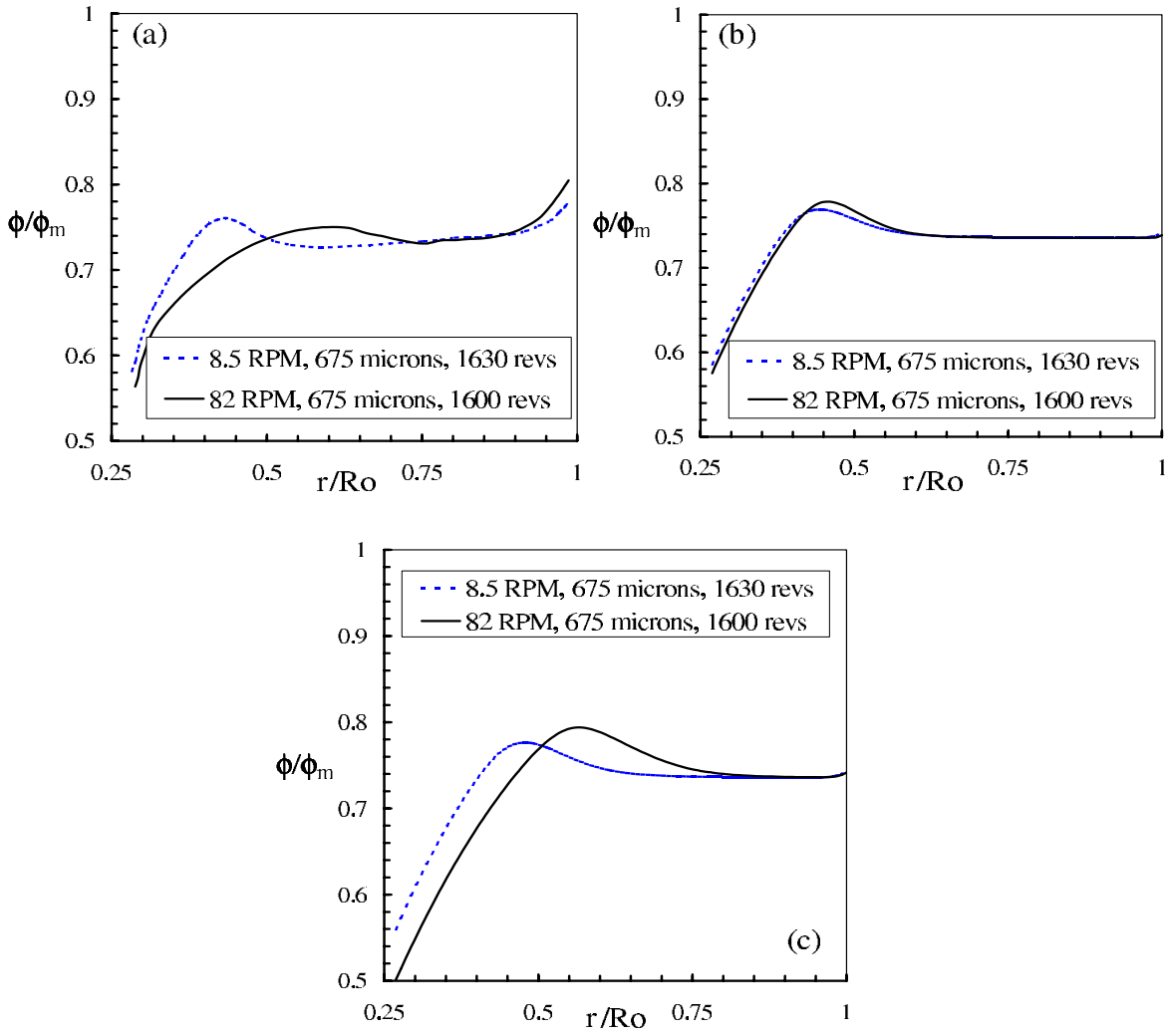

Figure 30: Comparison of the effect of the inner cylinder rotation rate on the results for a circular-Couette device ($R_i = 0.64$ cm, $R_o = 2.38$ cm) with a shear-thinning suspending fluid (Carbopol 940 in glycerin/water) at a bulk concentration of $\phi_B = 0.5$ and a suspended particle diameter of 675 μm for: (a) experimental results taken from Rao *et al* (2002); (b) model predictions with $\eta_\infty = 10$ Poise; (c) model predictions with $\eta_\infty = 100$ Poise.

Table 3: Quantitative comparison between the experimental results of Rao *et al* (2002) and the suspension flow model predictions ($\eta_\infty = 10, 100$ Poise) for the position of the ϕ peak and ϕ value at the inner cylinder with $\phi_B = 0.5$.

RATE (RPM)	SIZE (μm)		ϕ_{peak}	r/Ro_{peak}	$\phi_{inner\ cylindar}$
82	*100*	Experimental	0.730*	0.475*	0.675
		Model (10P)	0.762	0.385	0.651
		Model (100P)	0.763	0.452	0.596
8.5	*675*	Experimental	0.760	0.430	0.580
		Model (10P)	0.769	0.443	0.586
		Model (100P)	0.776	0.477	0.560
82	*675*	Experimental	0.750	0.605	0.560
		Model (10P)	0.778	0.460	0.575
		Model (100P)	0.794	0.568	0.501

***there was no defined peak, so the value was taken at the point the curve first levels off*

increase. The one thing the model did not match was the drop in the value of the ϕ peak for the higher rotation rate. The model, instead, predicted a slight increase.

Comparing the modeling and experimental results quantitatively in Figure 31 and Table 3, it is observed that the modeling and experimental data agree very well for the 8.5 RPM, 675 μm case with the lower η_∞ value, but deviate from the experimental measurements in the other two cases. For the higher rotation rate of 82 RPM, the model over-predicts the experimental value for the peak particle volume fraction by only 3% with $\eta_\infty = 10$ Poise and 5% with $\eta_\infty = 100$ Poise which is relatively good, but under-predicts the penetration of this peak into the Couette gap for both cases, with the higher value of η_∞ better predicting the penetration. The model predicts the position of the ϕ peak at an r/R_o value of 0.460 with $\eta_\infty = 10$ Poise and 0.568 with $\eta_\infty = 100$ Poise while experimental findings observe the peak at an r/R_o of 0.605. While the higher η_∞ better predicts the penetration of the ϕ peak for the higher rotation rate, it does appear to over-predict the dip in ϕ near the rotating inner cylinder. This leads to the conclusion that a better high-shear-rate set point for the Carreau viscosity model is somewhere between 10 and 100 Poise. Looking back at Figure 28, it is evident that the experimental data points fall between the two curves in the higher shear-rate zone. In addition, the model produces a better fit at the lower

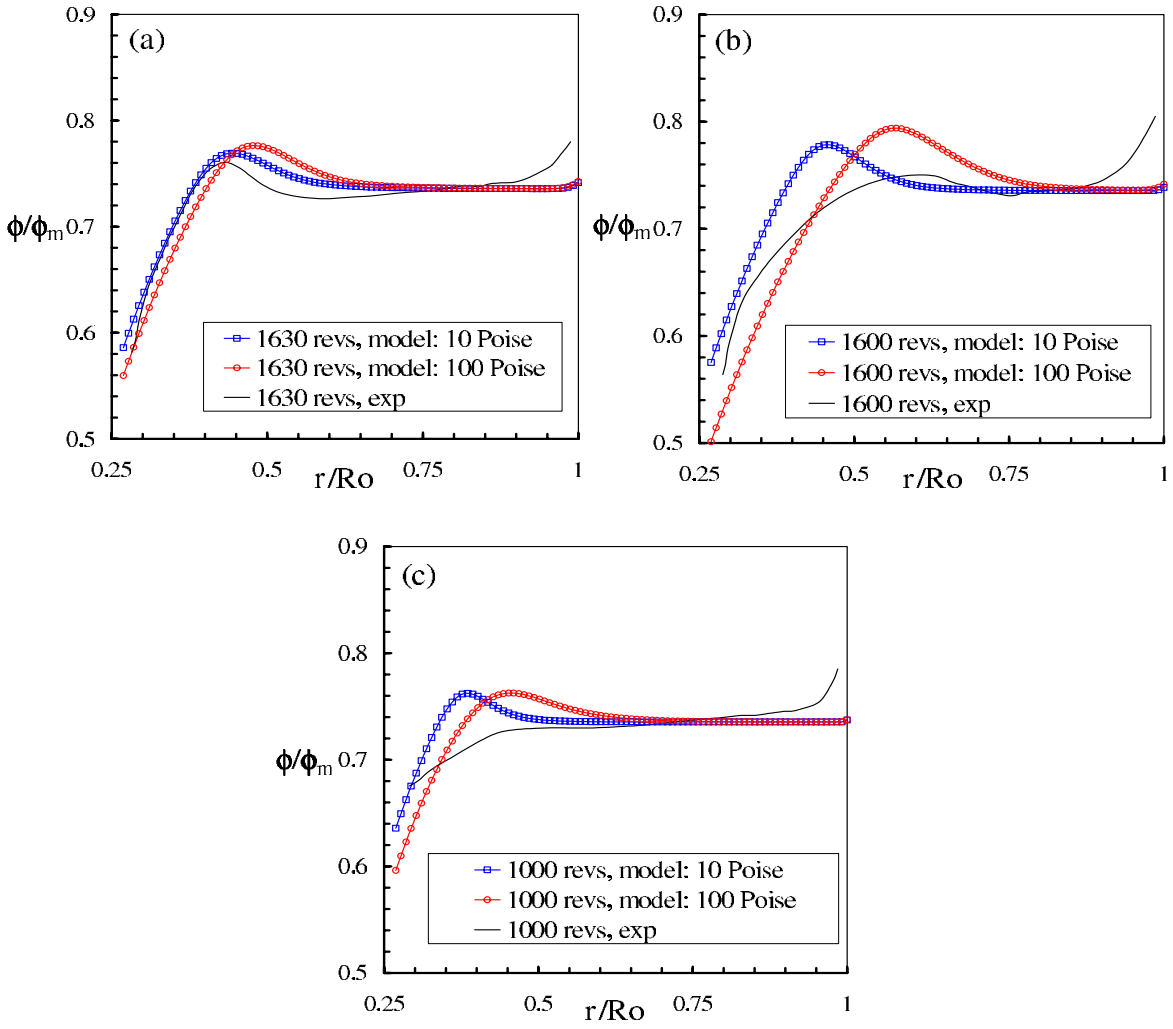

Figure 31: Comparison of the experimental results from Rao *et al* (2002) with suspension flow model predictions for a concentrated suspension ($\phi_B = 0.5$) of spherical particles in a circular-Couette device with a shear-thinning suspending fluid ($\eta_\infty = 10, 100$ Poise) for the cases of: (a) 8.5 RPM, 675 μm; (b) 82 RPM, 675 μm; (c) 82 RPM, 100 μm.

rotation rate with the lower η_∞ set point, where the two curves are closer together. When the shear-rate is increased for the higher rotation rate, the increase in the η_∞ set point is necessary to match the observed migration behavior.

In Figure 32, we consider model predictions with a Newtonian suspending fluid in comparison with the experimental observations with a shear-thinning suspending fluid. We set the Newtonian viscosity to the zero-shear-rate value used in the Carreau viscosity model, $\eta_o = 4 \times 10^5$ Poise. With the higher level of shear experience across the gap for the Newtonian case (Figure 33b), the migration occurs with a much lower level of strain. The plots in Figure 32 compare the Newtonian model predictions at 50 revolutions with the measured experimental $\phi(r)$ results at 50 - 1600 revolutions. While not matching the strain level or rate of migration, the Newtonian predictions do produce a similar profile in form. The Newtonian model seems to better predict the up-turn in concentration at the outer cylinder wall which was observed in the experiments and matched the form of the curves at 82 RPM, 675 μm quite well. It also produced a much "flatter" profile for the 82 RPM, 100 μm case, which was closer to the experimental observations.

4.4.2 Approach to steady-state

It was predicted by the model that the shear-thinning suspending fluid did not have any effect on the final steady-state particle volume fraction profile. This, as expected, holds for the numerical modeling results. The interesting aspect of this prediction is that the two cases approach this steady-state on drastically different time scales. Table 4 illustrates that for a Newtonian suspending fluid with an inner cylinder rotation rate of 10 RPM, the model predicts only about 11 hours to achieve the analytical steady-state $\phi(r)$ profile. For the shear-thinning case with $\eta_\infty = 10$ Poise at 10 RPM, the model predicts roughly *347 days* to reach steady-state. This leads to the conclusion that the experimental results only probed the very early stages of this phenomena and that much longer experimental runs are required to fully characterize the migration process with a shear-thinning suspending fluid.

This large difference between the predicted times to steady-state is due to the difference

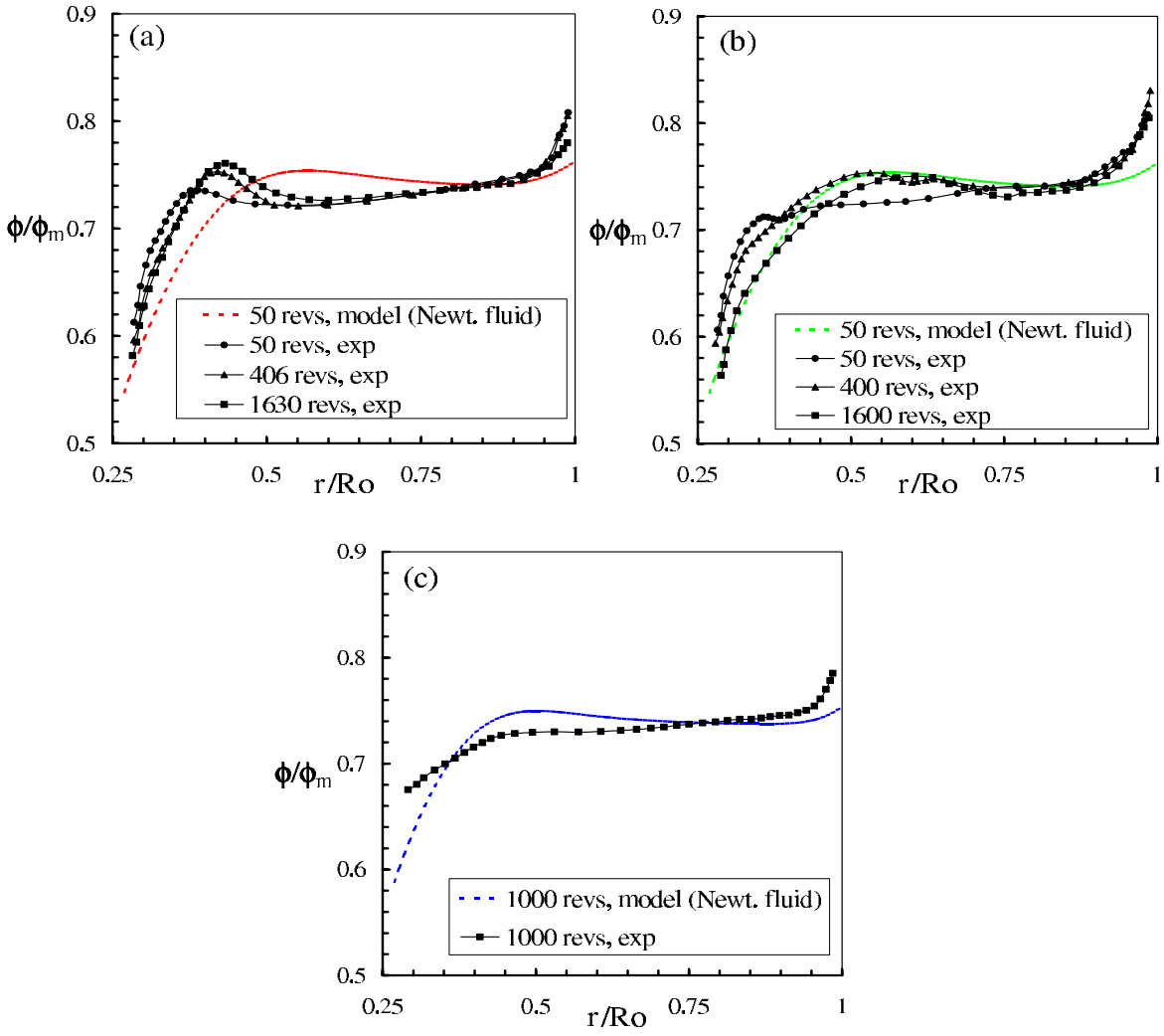

Figure 32: Comparison of the experimental results from Rao *et al* (2002) with suspension flow model predictions for a concentrated suspension ($\phi_{\rm B} = 0.5$) of spherical particles in a circular-Couette device with a Newtonian suspending fluid ($\eta_o = 4 \times 10^5$ Poise) for the cases of: (a) 8.5 RPM, 675 μm; (b) 82 RPM, 675 μm; (c) 82 RPM, 100 μm.

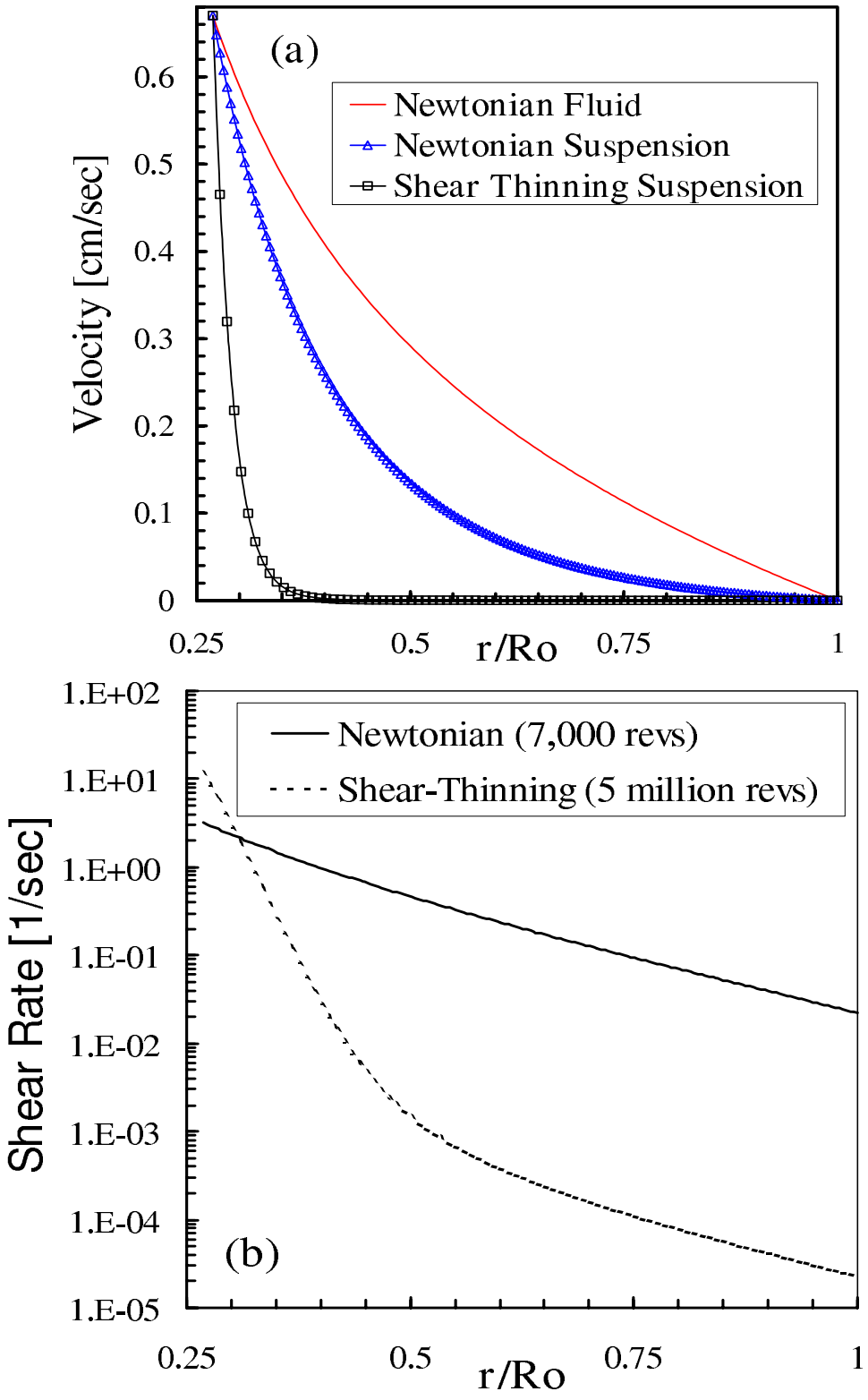

Figure 33: Comparison of modeling results for steady-state (a) velocity profiles and (b) shear-rate profiles across the gap of a circular-Couette device with an inner cylinder rotation rate of 10 RPM and a suspended particle diameter of 675 μm with an initial bulk concentration of $\phi_B = 0.5$ for the cases of a Newtonian suspending fluid (SS: 7000 rotations) with $\eta_o = 4 \times 10^5$ Poise and a shear-thinning suspending fluid (SS: 5 million rotations) with $\eta_\infty = 10$ Poise.

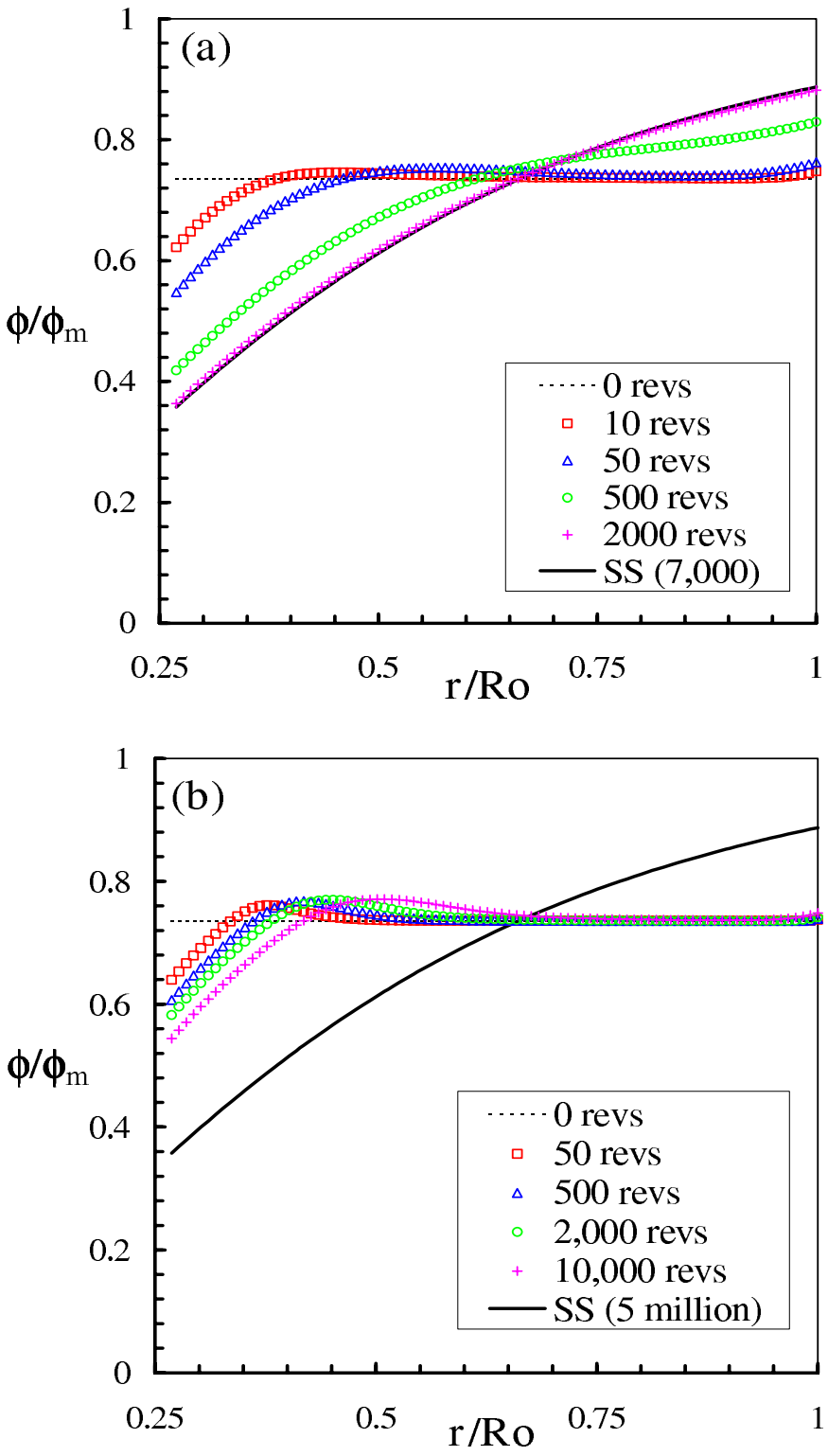

Figure 34: Comparison of modeling results for the evolution in time and strain of the $\phi(r)$ profile across the gap of a circular-Couette device with an inner cylinder rotation rate of 10 RPM and a suspended particle diameter of 675 μm with an initial bulk concentration of $\phi_B = 0.5$ for: (a) a Newtonian suspending fluid ($\eta_o = 4 \times 10^5$ Poise); (b) a shear-thinning suspending fluid ($\eta_\infty = 10$ Poise).

between the flow conditions. Figure 33 shows that while some movement was predicted in the fluid for the Newtonian case, the prediction for the shear-thinning case was practically quiescent everywhere except directly adjacent to the inner cylinder. This point is further illustrated in the plot of the predicted shear-rate profile across the gap. The predicted shear-rate in the Newtonian case only varies about two orders of magnitude across the gap while the predicted shear-thinning case varies about six orders of magnitude with the first five orders of magnitude of the drop occurring before the mid-point of the gap. This means that the time scale of particle migration was slowed down by roughly *five orders of magnitude* from the inner cylinder to the middle of the gap.

This drastic variation of the shear rate in the shear-thinning case causes slower overall particle migration. In the suspension flow model, the divergence of the particle stress drives the particle migration, $\mathbf{j}_\perp \sim \nabla \cdot \mathbf{\Sigma}_\mathrm{P}$. In the case of a Couette flow, the particle stress is directly proportional to the local shear rate, $\mathbf{\Sigma}_\mathrm{P} = -\bar{\eta_n}\dot{\gamma}$. Therefore, the particle migration is initially (when $\nabla\phi = 0$) driven by the gradient of the shear-rate. The rapid drop of the shear-rate in the inner half of the Couette gap is the result of a rapid migration near the inner cylinder which quickly slows to leave the peaks in $\phi(r)$ profiles observed in Figure 34 for the shear-thinning suspending fluid case. The peaks are due to the decrease in driving force resulting from the smaller shear-rate values. The Newtonian case was predicted to almost reach steady state by 2,000 revolutions while the shear-thinning case was predicted to remain far from steady state even at 10,000 revolutions. In fact, Figure 35 illustrates that it is predicted to take $O(10^7)$ rotations of the inner cylinder for the shear-thinning case to approach steady state.

4.5 Conclusions

The suspension flow model proved to be both flexible and robust in predicting at least the basic features of particle migration for a shear-thinning suspending fluid in a wide-gap circular Couette flow. The model captured the major trends of the experimental data in both inner cylinder rotation rate and suspended particle size. In addition, it illustrated a good quantitative agreement for the lower rotation rate, larger particle size results.

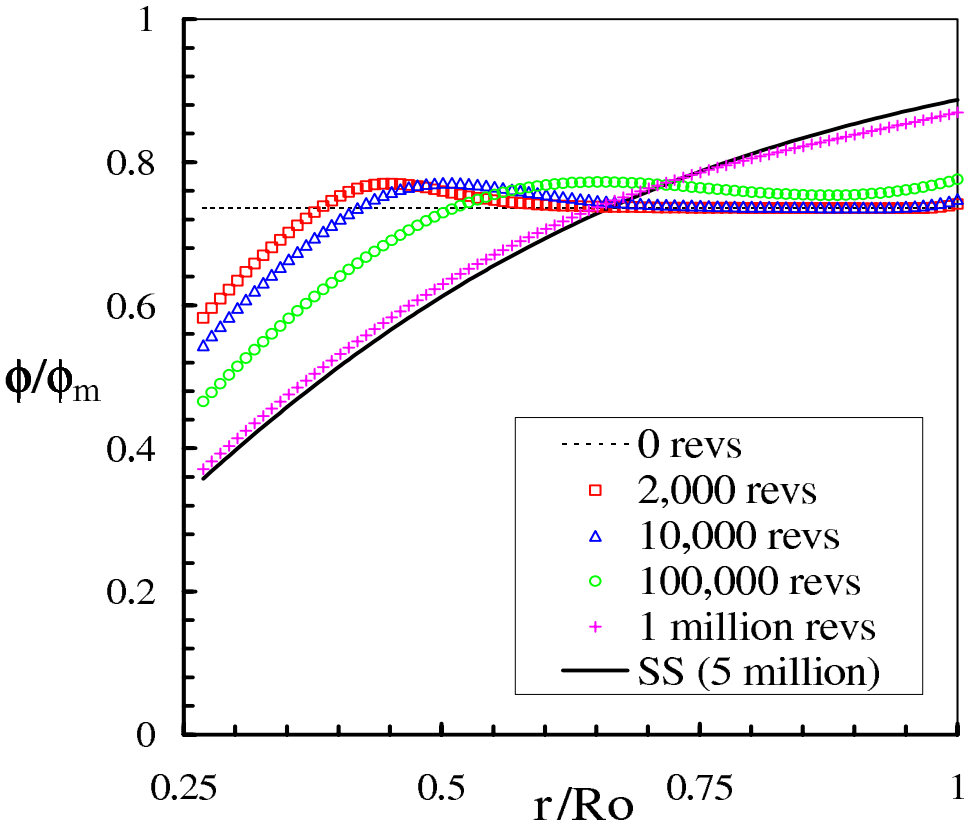

Figure 35: Modeling results for the approach to steady-state of the $\phi(r)$ profile across the gap of circular-Couette device with an inner cylinder rotation rate of 10 RPM and a suspended particle diameter of 675 μm at an initial bulk concentration of $\phi_B = 0.5$ with a shear-thinning suspending fluid ($\eta_\infty = 10$ Poise).

Table 4: Comparison of time predicted to achieve the analytical steady-state $\phi(r)$ profile from unsteady-state modeling results for a circular wide-gap Couette flow with 675 μm suspended particles, $\phi_B = 0.5$ and $\eta_\infty = 10$ Poise.

Rate (RPM)	Revolutions	Time [sec]	
Newtonian			
10	7,000	42,000	11.67 hours
100	7,000	4,200	1.17 hours
Shear-Thinning			
10	5 million	30 million	347 days
100	18 million	10.8 million	125 days

In our predictions, the only modification made to the basic suspension flow model proposed in Morris and Boulay (1999) and presented in Chapter 2 was a substitution of the Carreau viscosity model for the Newtonian viscosity. All other parameters matched those used for previous Newtonian suspending fluid studies. The only parameter variations studied was in the high-shear-rate set point for the Carreau viscosity model. This illustrates the flexibility of the model and possibilities for modification. By considering variation of the η_∞ value, we were able to illustrate that the model could be fit to the experimental observations with additional rheometric data on the suspending fluid in the relevant range of shear rates for the experimental conditions.

The major shortcomings in the modeling effort were in fully understanding the effects of the shear-thinning fluid on the particle migration. While the simple substitution of a shear-thinning viscosity law was able to produce remarkable good results, there were still some areas of concern. The over-prediction of the $\phi(r)$ profile peaks and under-prediction of the $\phi(r)$ profile near the wall are both concerns, especially when the Newtonian version of the model appeared to capture these features better, even though not under the proper amount of strain. This suggests that there should be some more thought and study on the interaction of the particles and polymer in a shear-thinning suspension. Specifically rheological measurements of the normal stress differences for both the suspension and suspending fluid alone would be particularly enlightening. These could lead to a reformulation and improvement of the normal stress and shear viscosities.

On the other hand, there is a possibility that the discrepancies may be due to the inability of the Carreau model to completely capture the behavior of the Carbopol 940 solution. In Gheissary and van den Brule (1996), they note that Carbopol suspensions form a gel structure which breaks up into smaller and smaller "blobs" of gel when the solution is put under shear. Whether a simple shear-thinning viscosity model can completely capture the consequences of this behavior is not clear. In addition, how "blobs" of gel effect the migration of the particle phase is another issue entirely.

The main point to note is that a suspension of particles in a shear-thinning suspending fluid is a complex system with many factors to consider. The fact that the model is able to

capture the main qualitative behavior and even approach a quantitative fit with a simple modification suggests that further progress may be made in this area of study by appropriate use of ideas applied to suspensions in Newtonian liquids. However, the model illustrates that the extreme variation in shear rate, and hence in time scale within a flow, must be considered in the design of an experiment. Other work in particle transport in shear-thinning liquids (Daugan *et al*, 2002a,b) shows that the flow history is important and thus thixotropy may play a role.

CHAPTER 5

COMPLEX GEOMETRY: FRAME INVARIANT RHEOLOGY

The primary goal of this work is to propose a framework to adapt shear-based rheological models for suspensions to general geometries. This is required due to the fact that the local flow kinematics in a general flow field are not necessarily simple shear. The flow can range from regions of solid-body rotation to areas of pure extension, with simple shear representing an equal balance between the two. As a test case for a general flow with varying local kinematics, we chose a sharp-edged contraction (or expansion) geometry. This case was chosen since it varies between simple shear in the regions upstream and downstream of the contractions to a region of nearly pure extensional flow at the mouth of the contraction. It has been illustrated that particle migration does occur in such a geometry, particulary an axisymmetric one (Iwamiya, Chow and Sinton, 1994; Altobelli, Givler and Fukushima, 1997; Moraczewski and Shapley, 2004). In fact, this migration has been shown to have a measurable impact on the flow field in this geometry (Iwamiya *et al*, 1994; Altobelli *et al*, 1997).

The development of constitutive stress laws to represent complex, multi-phase fluids has long standing roots in the polymer literature (Bird, Armstrong and Hassager, 1987) and the many experimental techniques developed for characterizing polymeric solutions can be extended to particulate suspensions. The key principle we explore here is that particle induced normal stresses drive particle phase migration. This makes suspension rheology especially influential in the particle distribution. By coupling the particle phase mass and momentum balances into a particle migration equation, it is illustrated that the change in particle volume fraction is driven by the divergence of the particle migration flux: $\partial\phi/\partial t \sim \nabla \cdot j_\perp$ where $j_\perp \sim \nabla \cdot \mathbf{\Sigma}_\mathrm{P}$, as illustrated in Chapter 2, Eq. (7). The particle phase stress is then defined by a rheological model based on the assumption of an anisotropic

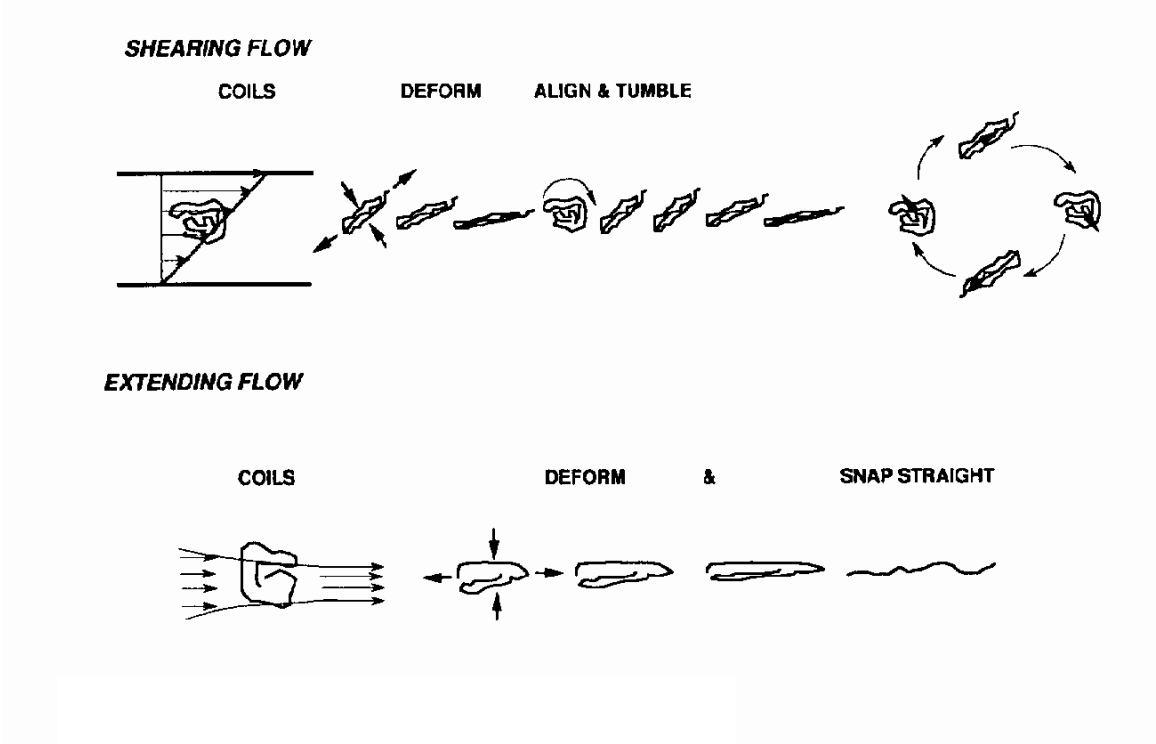

Figure 36: Polymer coils in shearing and extending flows. (taken from J. Rheol, Schunk and Scriven (1990), Figure 1)

particle phase normal stress (Morris and Boulay, 1999), as demonstrated in Chapter 2. The focus of this work is to determine a sufficient way to represent this anisotropic normal stress in general (non-shear) flow fields and to explore effect of spatial variations in the local kinematics on the particle stress.

Flow kinematics represent the local motion that a "particle" of fluid will undergo. Looking at Figure 36, taken from Schunk and Scriven (1990), the effect of local kinematics for shear and extensional flow are illustrated on an isolated polymer chain. In shearing flow, the flow both stretches the polymer chain and causes it to tumble. In extending flow, the polymer chain experiences stretching only. By analogy, for suspensions this difference in local flow behavior may result in altered particle interactions and possibly alters the particle phase stress behavior.

The model of Morris and Boulay (1999) was limited to flows where the local kinematics could be defined in terms of simple shear. Attempts have been made to adjust other continuum models to include anisotropic normal stresses in general flows (Fang *et al.*, 2002).

The solution proposed here involves representing the particle phase stress utilizing two additional parameters: ρ_k and $\mathbf{e}_i$. The kinematic ratio, ρ_k, is a measure of the relative strength of rotation versus extension locally in the flow. This gives a means to characterize the local kinematic state of the flow field. The eigenvectors of the rate of strain, $\mathbf{e}_i$, present a convenient reference frame in which to define the particle induced normal stresses. These can then be readily transformed into the coordinate system required for computation.

In this chapter, we explore how to set up a frame invariant rheological definition in Section 5.1 and how to apply this to forming a particle stress constitutive model for general geometry suspension flows in Section 5.2. In Section 5.3, we first look at predictions for particle migration utilizing the simplest form of the model, the isotropic normal stress. We explore variations in contraction geometry, flow direction (i.e. expansion flow) and compare to experimental results (Altobelli *et al*, 1997; Moraczewski and Shapley, 2004). We explore the effect of added model complexity in Section 5.4, by varying particle pressure with local kinematic conditions or by using an anisotropic normal stress to predict particle migration and flow fields for a two-dimensional, rectangular contraction flow. Finally, in Section 5.5 we wrap up the modeling results and present some conclusions.

5.1 Frame Invariant Rheology

To form a constitutive equation we require a frame of reference that is independent of the overall geometry/coordinate system boundaries and a function of local flow kinematics only. To do this, we base the constitutive model on a stationary rate of strain similar to Brunn and Ryssel (1997). This is done by defining the fundamental directions of the stress along the principal axes of the rate of strain and taking rotation measurements relative to the rotation of these axes. The principal axes of the rate of strain are defined as unit vectors, $\mathbf{e}_i$ ($i = 1$ or 2), along the directions corresponding to a diagonal rate of strain tensor, ($E_{ij} = 0$ for $i \neq j$). These correspond to the eigenvectors of the rate of strain tensor and form an orthogonal triad due to the symmetric nature of $\mathbf{E}$.

As a frame invariant measure of local shear strength, we use the shear rate, $\dot{\gamma}$, which is based off of the second invariant of the rate of strain ($\mathrm{II}_E = \mathbf{E} : \mathbf{E}$) and defined as

$\dot{\gamma} = \sqrt{2\mathbf{E} : \mathbf{E}}$. For a frame invariant measure of local rotation, we follow the work of Schunk and Scriven (1990) and later Ryssel and Brunn (1999a,b) where they described the idea of a relative rotation which they utilized to model flows of inelastic polymeric solutions in complex geometries. The relative rotation, ω_{rel}, is defined as the difference between the local angular velocity of a fluid element ($\omega/2$) and the local rotation of the axes of the rate of strain ($\mathbf{w}$),

$$\omega_{rel} = \frac{\omega}{2} - \mathbf{w}. \tag{65}$$

The local fluid rotation is one half of the local vorticity ($\omega = \nabla \times \mathbf{u}$), while the rotation of the axes of the rate of strain is defined:

$$\mathbf{w} \equiv \mathbf{e}_i \times [\frac{\partial \mathbf{e}_i}{\partial t} + \mathbf{u} \cdot \nabla \mathbf{e}_i]. \tag{66}$$

This formation sets the rotation relative to a stationary rate of strain and since each rotation quantity ($\omega/2$, $\mathbf{w}$) is calculated in the same Cartesian frame of reference, taking the difference produces a frame invariant measure of rotation.

5.1.1 Kinematic ratio

In general flow conditions, the local kinematics can vary spatially which leads to a non-uniform environment for the particle phase. These local kinematics control the particle stress which in turn drives the particle migration. To define a complete constitutive law, this variation should be taken into account. In previous attempts, only local shear strength was accounted for through the shear rate. A complete picture of the local kinematic conditions takes into account the local material deformation (shear rate), rotation and relaxation. Since the particles considered here are non-Brownian local material relaxation is not an issue, but local material rotation effects remain. To account for this, we introduce a fitting parameter based on both local deformation strength and rotation: the kinematic ratio, ρ_k. Through this kinematic ratio, we provide a more complete picture of the local kinematics that affect the particle interactions.

Following Schunk and Scriven (1990), the kinematic ratio can viewed as a ratio of the time scale of fluid deformation ($1/\dot{\gamma}$) to the time scale of fluid rotation ($2\pi/|\omega_{rel}|$). Dropping

the 2π results in the ratio, $\rho_k = |\omega_{rel}|/\dot{\gamma}$, which approaches zero in pure extension when the time scale of deformation dominates and infinity in solid body rotation when the time scale of fluid rotation dominates. In simple shear, the time scales of deformation and rotation are balanced resulting in a value of unity. This definition, though, creates problems due to the fact that it becomes unbounded as the shear rate approaches zero. To solve this problem, Ryssel and Brunn (1999a) suggest reformulating the parameter as:

$$\hat{\rho}_k = \frac{2\rho_k}{1+\rho_k} = \frac{2|\omega_{rel}|}{\dot{\gamma}+|\omega_{rel}|}. \tag{67}$$

This scales the ratio so that it approaches a value of two rather than infinity in the limit of solid body rotation and remains zero and one for pure extension and simple shear, respectively.

5.1.2 Compression-tension coordinates

To define the normal stress directions, we designate a "compression-tension" coordinate system. This corresponds to the principal axes of the rate of strain and represents the compression and extension axes of a local fluid element. The extension or "tension" direction is defined along the direction of the largest positive component of the diagonalized rate of strain. This diagonal definition corresponds to the eigenvectors of the rate of strain tensor, which in diagonal form has components E_{ii} corresponding to the eigenvalues. The compression direction is defined along the direction of the smallest or most negative diagonal component. This coordinate system depends only on the local kinematics of the flow field and not on the bulk flow geometry, resulting in a frame invariant coordinate system. In addition, since the eigenvectors form an orthogonal triad, it can be transformed into Cartesian coordinates by a simple rotation or frame.

Fang *et al* (2002) define a similar frame invariant coordinate system, which they use to define the principal direction of their flow-aligned tensor, similar to the tensor $\mathbf{Q}$ in Eq. (10) and later tensor $\mathbf{Q}_{ct}$ in Eq. (69) defined below. They use the eigenvectors of the rate of strain to determine the direction perpendicular to the flow plane (i.e. perpendicular to the compression-tension axes defined here). This direction corresponds to λ_3 in Eq. (10) and Eq. (69). They assume the other two directions are indistinguishable, and set direction-1 to

correspond to the tangent of the local flow streamlines (minus any influence of rigid body rotation) and direction-2 to be perpendicular to the streamline, in the plane of flow. This definition gives an adequate frame of reference and one particularly suited for the diffusive flux model (Phillips *et al*, 1992), which only correctly predicts particle migration across streamlines (or in the 2-direction) in its original form. But it has two major faults. First, it does not provide for a way to take into account any stress directionality in the plane of flow, since the 1, 2 directions are chosen arbitrarily to align with the local direction of the velocity vector. Second, the directions do not take into account local kinematic conditions. They accounts for the local direction of the flow, but not the local kinematic state of that flow, which has significant consequences on the local stress state of the system, as illustrated in Figure 36.

5.1.3 Three-dimensional kinematics

While not explored in this work, a three-dimensional kinematic description of a general flow field is possible though increasingly complex. For axisymmetric flows, the mode of local deformation can be uniaxial or biaxial extension. This ultimately affects the strength of compression the local particle fraction experiences. In uniaxial extension, there are two directions of compression while in biaxial extension there is only one. Since the effects of compression are the dominant source of stress in a particulate suspension, this can be a very important distinction for suspension stress calculations. This is accounted for by utilizing the geometric mean straining rate, defined as the third invariant of the rate of strain tensor, $\det|\mathbf{E}|$, as suggested in Schunk and Scriven (1990) and Brunn and Ryssel (1998). This parameter is positive in uniaxial extension flow and negative in biaxial extension flow.

In fully three-dimensional flows, the job is even more difficult and requires the definition of multiple relative rotations. Schunk and Scriven (1990) suggest using the rotation of the directions of maximum and minimum eigenvalues around the intermediate values. This corresponds to the compression-tension directions defined in three-dimensions. The second rotation comes from the precessional rotation of the third axis which can be visualized as the slow rotation of the axis of a spinning top.

5.2 Particle Stress Constitutive Model

To study the effects of the particle stress model on the migration of particles in complex geometries, we explore a series of constitutive models of varying complexity. We start with an isotropic approach, where the normal stress portion of $\mathbf{\Sigma}_{\mathrm{P}}$ can be viewed as an isotropic "pressure," with no directional dependence. In the isotropic framework, the normal stress term or suspension pressure depends only on particle phase concentration, ϕ, and local flow strength, $\dot{\gamma}$. In the next level of complexity, the suspension pressure depends on the ratio of local deformation and rotation through the reformulated kinematic ratio, $\hat{\rho}_k$, along with $\dot{\gamma}$ and ϕ as in the isotropic case. We call this the weighed-isotropic approach. In the final level of complexity, we define an anisotropic particle normal stress defined along the local compression-tension axes. This allows for particle induced normal stress differences which can lead to altered migration and flow behavior. The particle stress definitions are outlined in Table 5.

Table 5: Constitutive models for the particle stress.

Pure Isotropic:	$\mathbf{\Sigma}_{\mathrm{P}}^{NS} = \Pi^P = -\bar{\eta}_n \dot{\gamma} \underline{\underline{\delta}}$
Weighted Isotropic:	$\mathbf{\Sigma}_{\mathrm{P}}^{NS} = \Pi^P = -\bar{\eta}_n B(\hat{\rho}_k) \dot{\gamma} \underline{\underline{\delta}}$
Anisotropic:	$\mathbf{\Sigma}_{\mathrm{P}}^{NS} = [-\bar{\eta}_n \dot{\gamma} \mathsf{Q}_{ct}(\hat{\rho}_k)]_{xy}$

Constitutive Model: $\mathbf{\Sigma}_{\mathrm{P}} = \mathbf{\Sigma}_{\mathrm{P}}^{NS} + 2\bar{\eta}_p \mathbf{E}$

5.2.1 Weighted-isotropic constitutive model

In the weighted-isotropic approach, a dependence on the balance between local deformation and rotation is added through the addition of a kinematic weighting factor, $B(\hat{\rho}_k)$, to the particle pressure term. For the purely isotropic approach, the kinematic weighting factor is set to $B = 1$ for all values of $\hat{\rho}_k$. In the weighted-isotropic approach, the value of B is interpolated between two set points. We set $B = 1$ at simple shear conditions when $\hat{\rho}_k = 1$

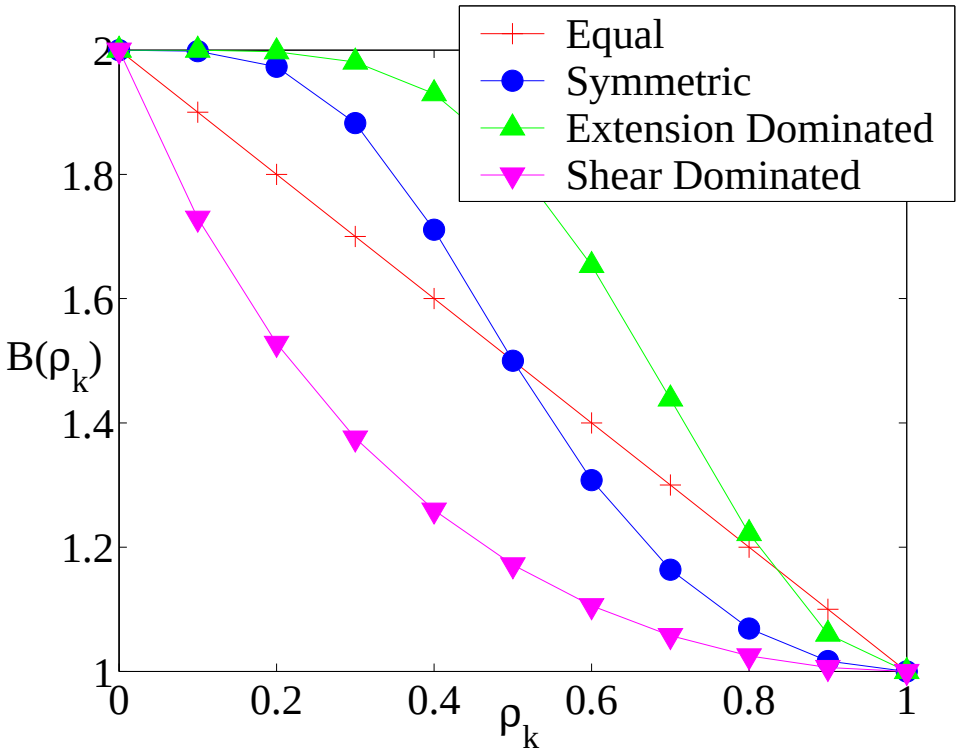

Figure 37: Plot of the kinematic weighing factor, $B(\hat{\rho}_k)$, used in the particle-pressure term as a function of $\hat{\rho}_k$ with $B_{ext} = 2$ for various interpolation functions.

and set B equal to an O(1) value which is greater than one at pure extension when $\hat{\rho}_k = 0$. A simulation study (Sami, 1997) suggests that the value is greater than unity by a factor which may be 2 or greater, but experimental evidence is unavailable. When $\hat{\rho}_k > 1$, there is no strong indication what the local particle stress behavior is, therefore we leave $B = 1$.

To interpolate between the set points of B, we utilize an arithmetic weighting relationship,

$$B(\hat{\rho}_k) = B_{sh} f(\hat{\rho}_k) + B_{ext}[1 - f(\hat{\rho}_k)], \tag{68}$$

where B_{sh} and B_{ext} equal the shear and extension set points and $f(\hat{\rho}_k)$ is an interpolation function. The interpolation function is chosen depending on what type of interpolation or fit is desired between the values. The results of the different interpolation functions suggested by Ryssel and Brunn (1999a) on $B(\hat{\rho}_k)$ with $B_{ext} = 2$ are shown in Figure 37. The function used for the equal linear fit was $f(\hat{\rho}_k) = \hat{\rho}_k$. The symmetric fit was achieved with, $f(\hat{\rho}_k) = \frac{2\sin(\hat{\rho}_k \pi/2)}{1+\sin(\hat{\rho}_k \pi/2)}$, where the interpolation favors the endpoints and moves rapidly through the

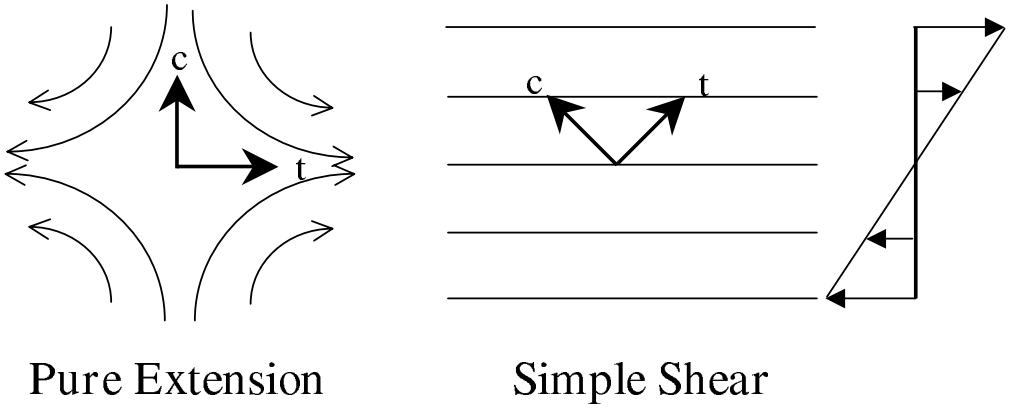

Figure 38: Sketch of the flow streamlines for a pure-extensional flow and a simple-shear flow relative to the compression-tension coordinate axes.

transition region. The final two fits, shear dominated [$f(\hat{\rho}_k) = \frac{3\sin^4(\hat{\rho}_k\pi/2)}{1+2\sin^4(\hat{\rho}_k\pi/2)}$] and extension dominated [$f(\hat{\rho}_k) = \sin^5(\hat{\rho}_k\pi/2)$,] both favor each endpoint accordingly. For the work here, we chose to emphasize the effect of the changing particle pressure and therefore used the extension dominated fit to emphasize its effect on the model. The other interpolation functions illustrate the fact that the model can be tuned for a more quantitative fit, if the data were available. In addition, as stated in Ryssel and Brunn (1999a, b) a geometric weighting relationship, $B(\hat{\rho}_k) = (B_{sh})^{f(\hat{\rho}_k)}(B_{ext})^{[1-f(\hat{\rho}_k)]}$, is also a possibility for an alternate fit.

5.2.2 Anisotropic constitutive model

The anisotropic model is set up in the compression-tension coordinates, as mentioned above. These provide a convenient frame of reference which does not depend on the geometry of the flow, instead only on the local kinematic state of the flow field, as illustrated in Figure 38 and later in Figure 55. Therefore the anisotropic particle stress definition is developed in a single form applicable to a range of flows and not limited to shear flows, as in Morris and Boulay (1999).

The new anisotropic tensor, $\mathbf{Q}_{ct}$, is defined as:

$$\mathbf{Q}_{ct} = \begin{pmatrix} B_t(\hat{\rho}_k) & N_{ct} & 0 \\ N_{ct} & B_c(\hat{\rho}_k) & 0 \\ 0 & 0 & \lambda_3 \end{pmatrix}. \tag{69}$$

The variables $B_t(\hat{\rho}_k)$ and $B_c(\hat{\rho}_k)$ represent functions that weight the normal stress in the tension and compression directions, while λ_3 produces a normal stress difference with the out-of-plane stress. As in the case of the weighted-isotropic model, these parameters are interpolated between set-points for simple shear ($\hat{\rho}_k = 1$) and pure extension ($\hat{\rho}_k = 0$). In simple shear we set $B_t = B_c = 1$ and in pure extension we set $B_t = 0$, $B_c = 2$. This imposes an extreme normal stress difference for pure extension, where all the stress is compressive. This is chosen to match analytical (Brady and Morris, 1997) and simulation data (Morris and Katyal, 2002) which predicts that particles tend to collect along the compression direction in a flow field which results in efficient momentum transport along this direction. The set point values are chosen to hold the dimensionless particle pressure, $(\Sigma^{NS}_{\mathrm{P},tt} + \Sigma^{NS}_{\mathrm{P},cc})/2\dot{\gamma}\eta_n$, at a value of one. The values of $B_t(\hat{\rho}_k)$ and $B_c(\hat{\rho}_k)$ are determined through interpolation utilizing an arithmetic weighing function with an extension weighted interpolation, as in the weighted-isotropic case above. For the case when $\hat{\rho}_k > 1$ the values of B_t, B_c are held at their simple shear values, as shown in Figure 39.

The variable N_{ct} is used to impose a first normal stress difference ($N_1 = \Sigma_{11} - \Sigma_{22}$) for simple shear conditions. This was found to be approximately $N_1 \approx -0.2\eta_n\dot{\gamma}$ in Morris and Boulay (1999) by fitting model predictions to experimental circular-Couette flow data (Phillips *et al*, 1992). The parameter N_{ct} is set to a constant value throughout the range of $\hat{\rho}_k$ and is only added to impose this slight normal stress difference at simple shear, if it is so desired.

5.3 Suspension Flow Modeling with an Isotropic Constitutive Law

In this section we look at model predictions with a purely isotropic (no $\hat{\rho}_k$ effects) constitutive model for a number of cases. We make comparisons to the experimental results of

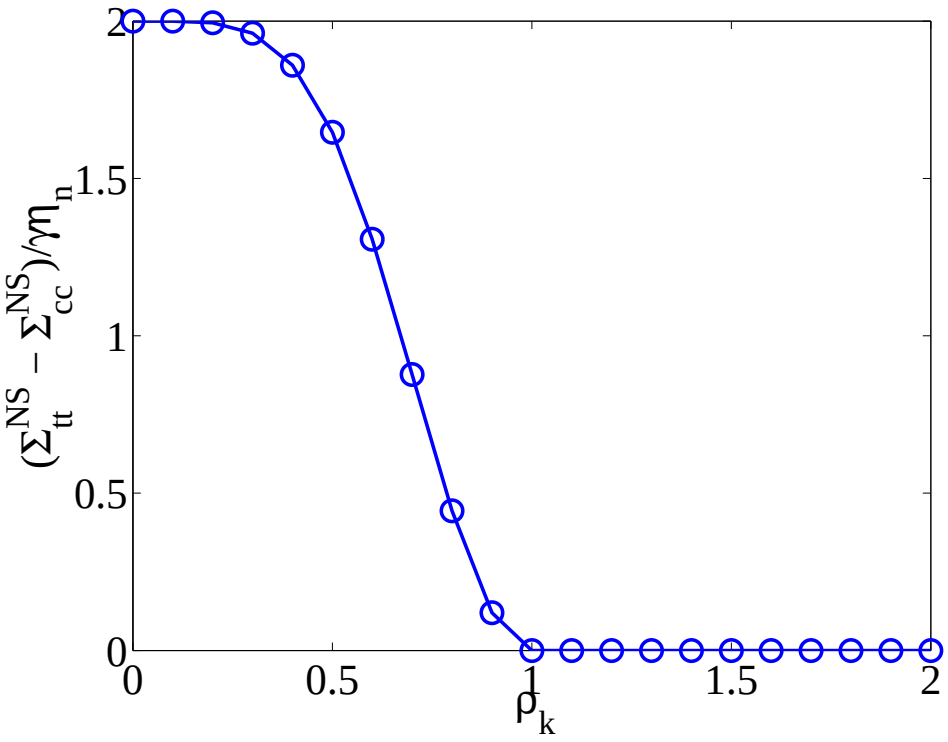

Figure 39: Plot of the normal-stress difference in compression-tension coordinates as function of $\hat{\rho}_k$ with $B_t = 0$, $B_c = 2$.

Altobelli *et al* (1997) and Moraczewski and Shapley(2004) for a 4:1:4 contraction-expansion geometry. For these cases, since the experimental results are somewhat rate dependent, we chose to use an $\alpha = 2$ for the sedimentation hindrance function, because this value matched the experimental axial development lengths of Hampton *et al* (1997) best in Chapter 3. For the rest of the model predictions for which comparable rate data is unavailable, $\alpha = 4$ was used because of better numerical stability. The $\alpha = 2$ produces steeper particle stress gradients (see Figure 2(b) in Chapter 2) at higher particle concentrations, which can cause problems for the particle migration solver and force smaller time steps. Since the value of α should have no effect on steady-state predictions and the other runs were for comparison purposes at assumed long-time conditions, an α of 4 was used to help with convergence issues. For the shear viscosity model (η_s), we chose to use the Morris and Boulay (1999) form, presented in Chapter 2, for all cases here.

The suspension conditions for the contraction-expansion runs were chosen to match experimental conditions, as will be explained below. For the rest of the runs, suspension

conditions of $\phi_{bulk} = 0.50$ ($\phi/\phi_{\rm m} = 0.735$, with an assumed value of $\phi_{\rm m} = 0.68$) and a particle size ratio of $L_s/a = 18$ were used. A high concentration was chosen since it enhances the effects of the model and leads to faster convergence rates for steady-state predictions (same as a larger particle size). Boundary conditions were set as illustrated in Figure 5 from Chapter 2, with particle boundary conditions the same as for the axially developing flows in Chapter 3. Particle flux in the direction normal to the boundary was set equal to zero at the walls, concentration was held constant at the inlet, and normal gradients were set equal to zero at the exit. At the centerline the normal flux and shear gradients were set equal to zero for a symmetry boundary condition. The grids used were the same as explained for the contraction runs in Chapter 2 and illustrated in Figure 6, with refinement at the contraction corners.

For the non-local stress contribution, since the scale of the shear-rate changes from the upstream to the downstream portion of the contraction, we chose to take a spatial average of the shear rate instead. The quantity $< \dot{\gamma} >_\epsilon$ represents a spatial average over a circular area of radius ϵ around the computation point of interest. The value of ϵ is calculated as $\epsilon = a/L_s$, which is the dimensionless particle size. This is roughly equivalent to setting the non-local stress parameter, $a_s(\epsilon)$, from chapter 3 equal to ϵ.

5.3.1 Piston-driven flow of a suspension in a 4:1:4 contraction/expansion

Altobelli *et al* (1997) studied the piston driven flow of a suspension through an abrupt contraction followed by an expansion. A schematic of the apparatus is shown in Figure 40. The apparatus consisted of tubing sections joined end-to-end to form the contraction-expansion geometry. The larger sections were 5.08 cm in inner diameter (ID) and the smaller section was 1.27 cm ID, corresponding to both a contraction and expansion ratio of $\beta = 4$. The center or neck section was 38 cm long, corresponding to approximately a length of $15R$, where R is the radius of the larger tube. For the experimental runs, the apparatus was filled with suspension to an approximate length of 30 cm upstream of the contraction and 4 cm downstream of the contraction, initially. The upstream length of 30 cm corresponds to about a length of $12R$. The upstream piston section was moved by a motor-driven push rod

at a rate of 0.0625 cm/s, which corresponds to mean velocity of 1 cm/sec in the smaller pipe section. The entire apparatus was placed inside an NMR magnet to allow measurement of the concentration and velocity.

The suspension consisted of a 50 vol% ($\phi/\phi_{\mathrm{m}} = 0.735$) concentration of neutrally-buoyant, suspended particles of sizes 675 μm and 100 μm, corresponding to $R/a = 75$ and 508, respectively. An NMR was used to take concentration and velocity measurements at various times during the travel of the piston, at both the contraction, expansion and along the narrow neck region. Quantitative particle volume fraction data is provided along the neck region after the upstream piston has travelled a distance of 12.5R. Also, NMR intensity plots are reported at various times during the movement of the piston (4R, 8R, 12R) at both the contraction and expansion.

To approximate this flow problem, we set up a domain as illustrated in Figure 41. Inlet conditions were set at a distance $6R$ upstream of the contraction. The ϕ profile was held at the initial bulk concentration of 0.50 and the velocity profile was set to a parabolic curve. The walls were set to no-slip, no particle penetration conditions as before and the outlet and centerline were set similar to the long-conduit flows. While the inlet/outlet conditions are not exactly in-line with the physical case, this set-up allows us to approximate the experimental conditions and to examine whether predictions agree with features of the observed behavior. We choose to only look at the larger of the two particle sizes which corresponds to $R/a = 75$. As will be seen later in Chapter 6, the parabolic profile is close to that observed away from the piston face in a piston driven flow. Assuming a constant ϕ profile at this distance is not necessarily a good approximation, but due to the size of the upstream channel and large R/a ratio, not much migration should occur in the upstream pipe. As for the drop in ϕ observed at the piston face, we assume that this is a highly localized phenomena and not likely to affect the results in the neck of the contraction-expansion to which we are comparing. This set-up provides a good approximation, that could only be improved by the addition of moving boundary conditions to simulate the movement of the piston face.

The contour and line plots in Figure 42 show that our results qualitatively match both

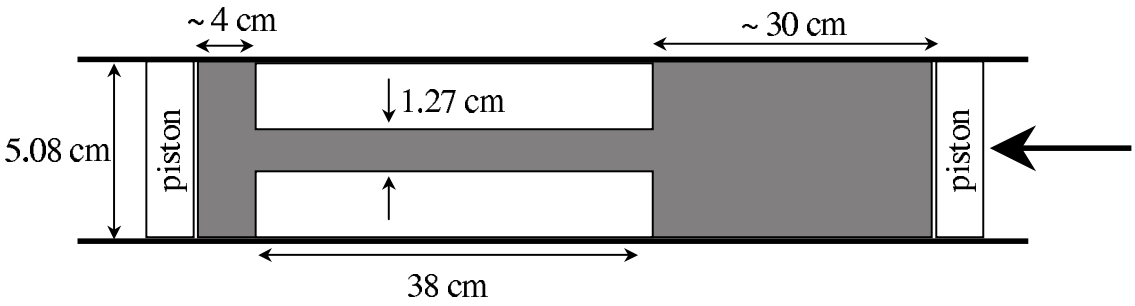

Figure 40: A sketch of the experimental flow apparatus used in Altobelli *et al* (1997) for an axisymmetric contraction/expansion geometry.

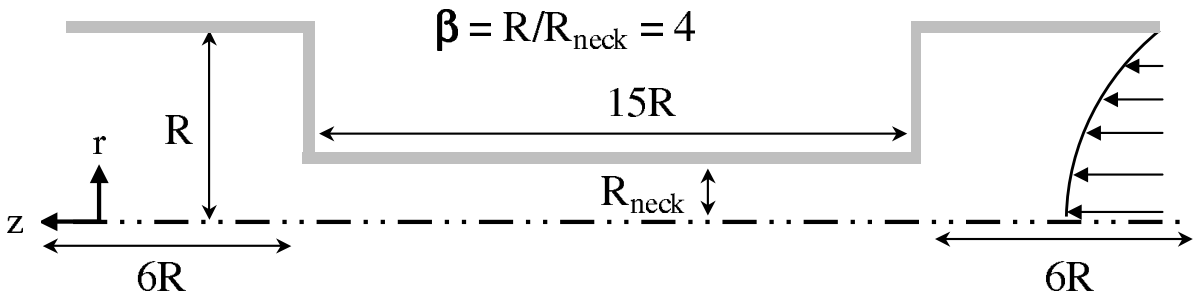

Figure 41: A sketch of the computational domain used to approximate the conditions of the Altobelli *et al* (1997) experiments.

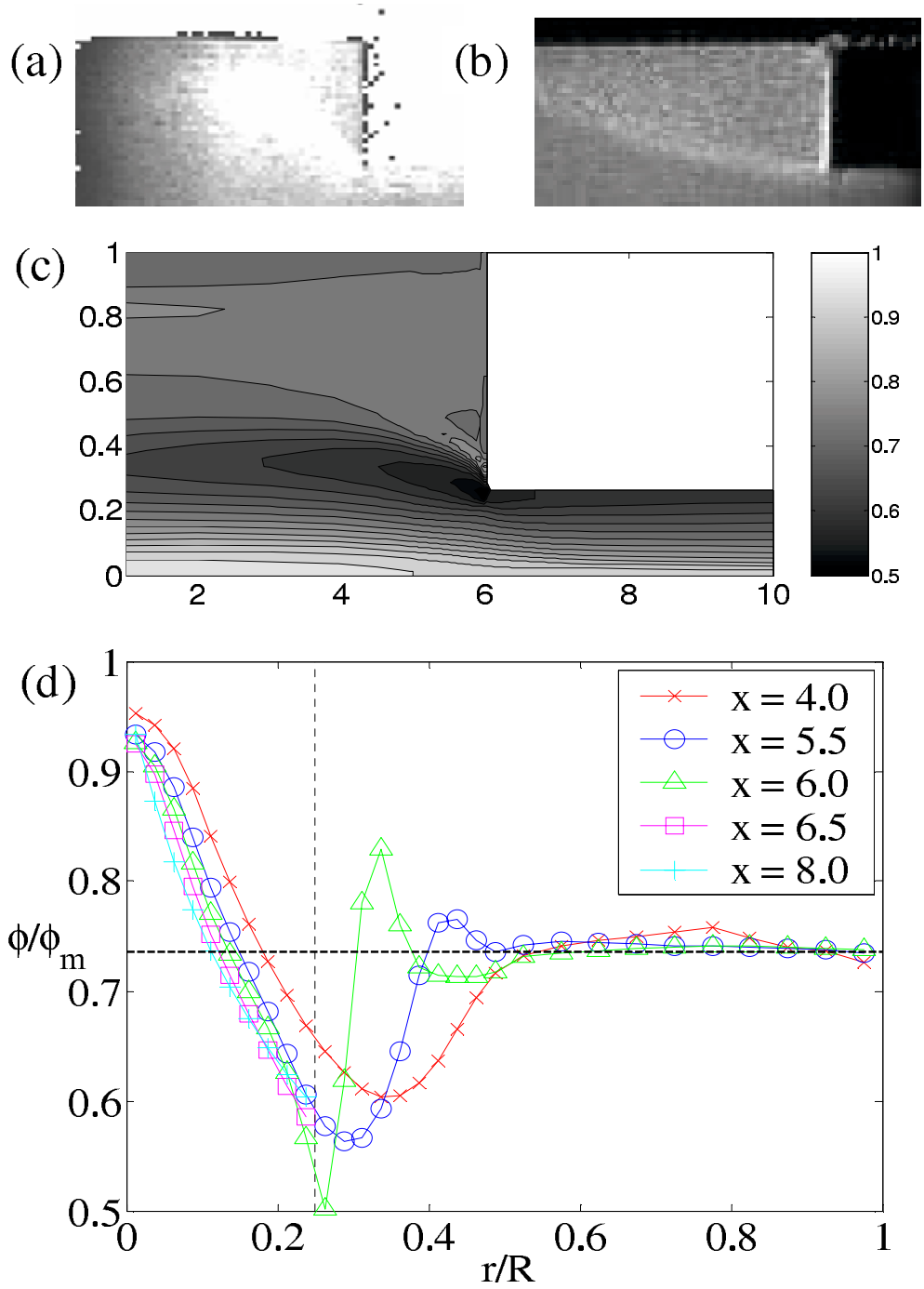

Figure 42: Particle volume fraction measurements and predictions for the expansion section (flow goes from right to left) of a $\beta_{cont} = \beta_{exp} = 4$ axisymmetric contraction-expansion geometry. Plot (a) is an NMR image taken from Altobelli *et al* (1997) after six diameters ($12R$) of piston travel. Plot (b) is an NMR image from Moraczewski and Shapley (2004), run at the same conditions as the Altobelli *et al* experiments. Plot (c) is a contour plot from a modeling run stopped at an equivalent of six diameters ($12R$) of piston travel and (d) is a plot of $\phi(r)/\phi_m$ profiles at various axial positions from the same run. In the NMR images, darker areas represent areas of higher particle concentration.

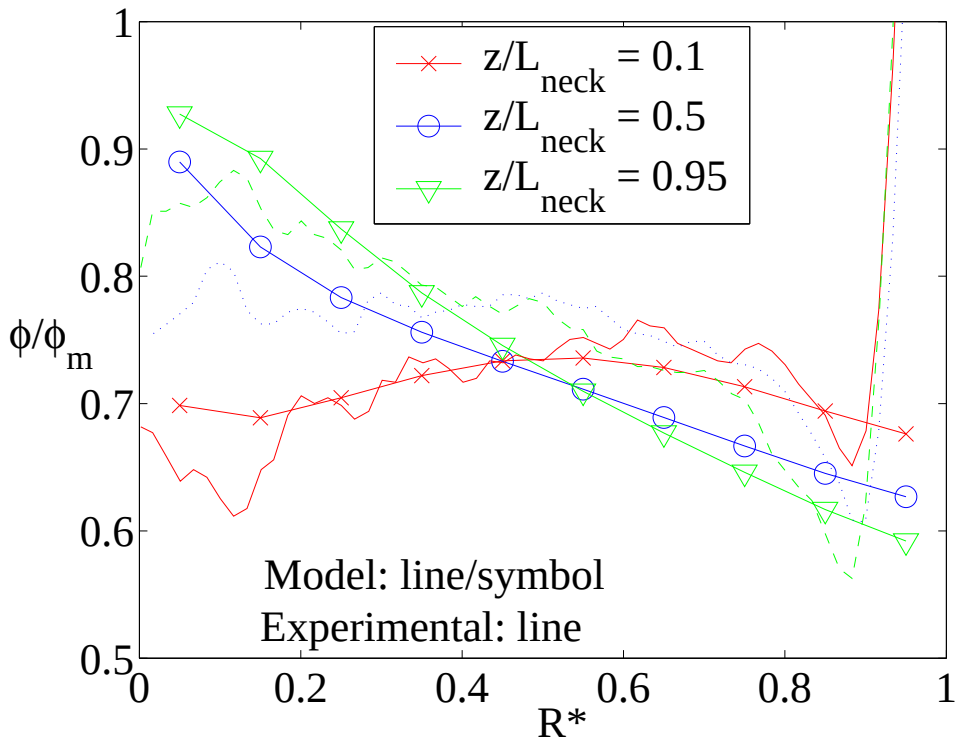

Figure 43: Comparison of model predictions with the experimental measurements of Altobelli *et al* (1997) for the development of the $\phi/\phi_{\rm m}$ profile in the neck region of a $\beta_{cont} = \beta_{exp} = 4$ contraction-expansion geometry. The experimental measurements were taken after the piston had travelled > 6 dia. $(12R)$, while the model predictions are at an approximate distance of 6 dia. $(12R)$ of piston travel. The radial coordinate is normalized by the radius of the neck region, $R^* = r/R_{neck}$, and the axial distance is normalized by the length of the neck region, L_{neck}.

experimental runs. The results presented are taken after the piston has moved 6 diameters $(12R)$ of axial length in the Altobelli *et al* (1997) experiments and the Moraczewski and Shapley (2004) results are an attempt to reproduce these results at the same experimental conditions. All three contour/intensity plots and the line plot show an area of particle depletion right at the sharp-edged corner which continues on downstream. The depleted area in Altobelli *et al* appears to be more pronounced, but with the current data a quantitative comparison cannot be made. In addition, both the model prediction and Moraczewski and Shapley results show that the majority of the particles remain in the center of the larger channel in a "jet"-like formation. Very little migration is observed into the corner, which remains close to the initial bulk concentration. This is strikingly different from the prediction for the contraction flow which will be illustrated below.

Figure 43 shows a quantitative comparison between model predictions and the experimental results of Altobelli *et al* along the neck region of the contraction-expansion. The two match qualitatively with the predictions matching the observed dip at the mouth of the contraction which the authors attributed to the dip in concentration at the piston face (since these results were taken after the piston had travelled > 6 dia. ($> 12R$) and was therefore nearly at the contraction opening or right on top of it depending on how much the geometry was initially filled). The main discrepancy is the sudden rise in concentration measured near the wall, which we have confirmed with the authors (Mondy, 2004) is due to an artifact of the experimental method rather than actual behavior.

5.3.2 Effect of contraction ratio on predicted results

In Figure 44, we present surface plots of the initial nonlocal shear rate fields for a $\beta = 2$ and $\beta = 4$ contraction along with contour and line plots of the final converged ($t = 500$) particle volume fraction profiles. The flow direction in the plots is from left to right. The $\beta = 4$ contraction shows an extreme increase in shear rate as the flow moves from the large to small section of the contraction, much more than for $\beta = 2$. As indicated on the plots, $< \dot{\gamma} >_\epsilon$ reaches a maximum value of 9.36 at the corner for $\beta = 2$ and a maximum value of 32.9 at the corner for $\beta = 4$. In actuality, the predicted value at the corner itself diverges and approaches infinity for both cases causing problems with the numerics. Fortunately, for our needs we only have to calculate it at the nodes adjacent to the actual corner point, since that is where the particle volume fraction field is stored and calculated (i.e. at the center of a computational cell).

The steady-state $\phi/\phi_{\rm m}$ profiles for the two contraction ratios show similar behavior in both cases. The smaller channel for the $\beta = 4$ contraction results in a longer dimensionless length, $[L_{small}/b]_{\beta=4} > [L_{small}/b]_{\beta=2}$, and therefore more axial evolution of the $\phi(y)$ profile, but both contractions show a similar build up of particles in the corner, right along the wall perpendicular to the flow direction. In the contraction-expansion results of Altobelli *et al* (1997), it is difficult to determine from the NMR images whether a build up in the corners took place on the contraction side. Despite the fact that the Altobelli *et al* data was for an

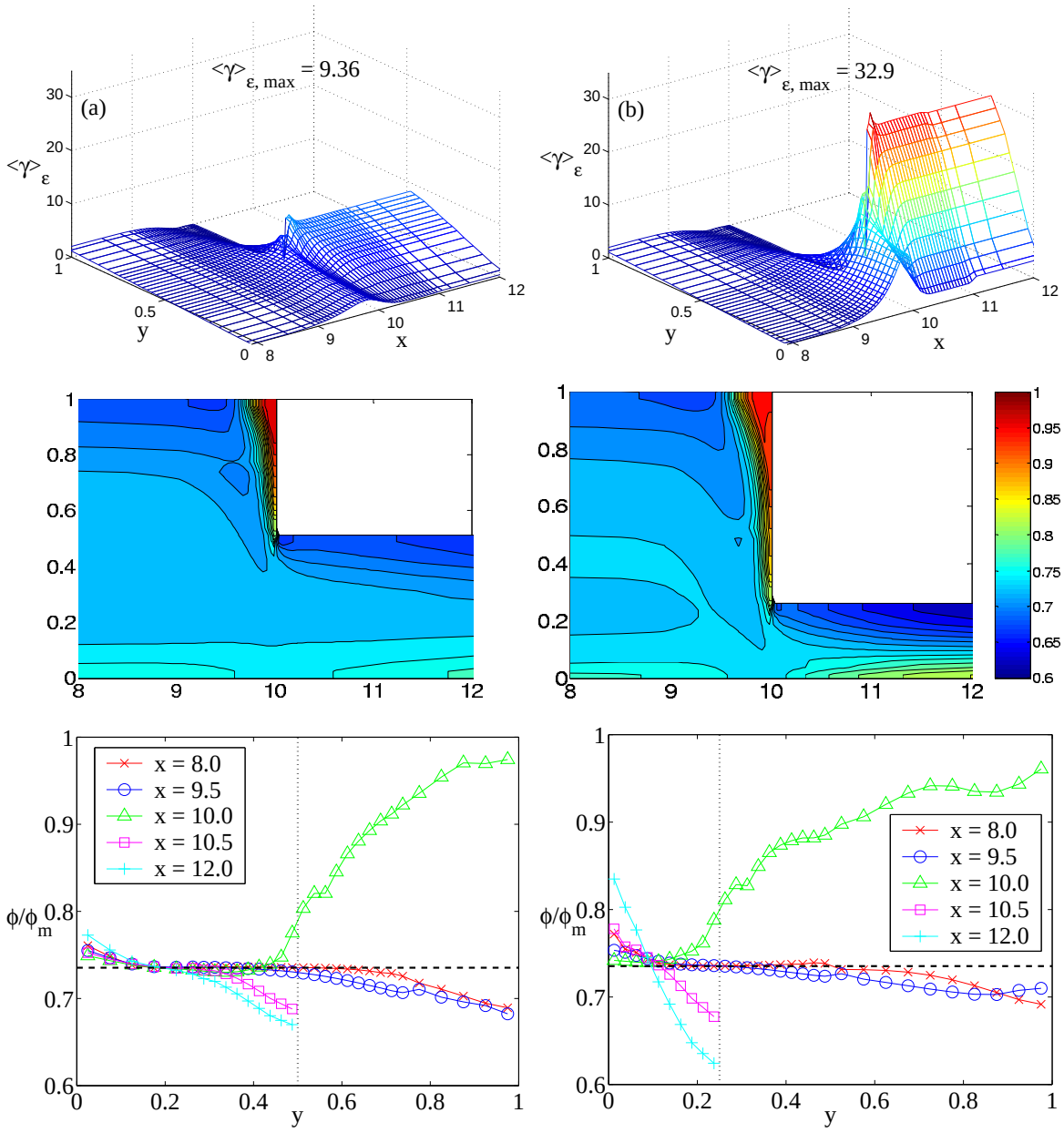

Figure 44: Comparison of isotropic model predictions for a contraction flow (flow from left to right) with a ratio: (a) $\beta = 2$, (b) $\beta = 4$. Top plots are the initial nonlocal shear-rate field. Underneath are the corresponding $\phi/\phi_{\rm m}$ plots at steady state. Model conditions: $\alpha = 4$, $[\phi/\phi_{\rm m}]_{bulk} = 0.735$, $\phi_{\rm m} = 0.68$, $B/a = 18$.

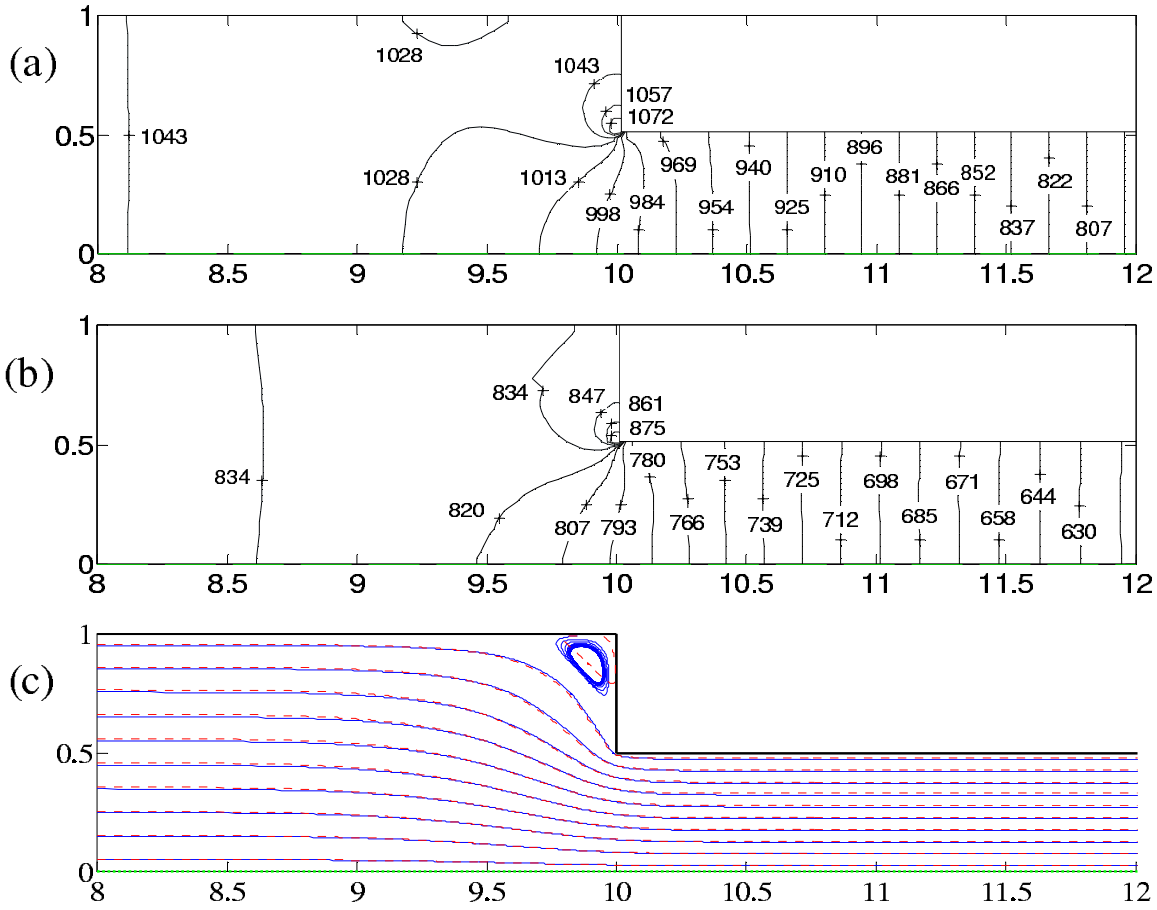

Figure 45: Isotropic model predictions for the pressure ($P^* = P/(\eta_o U_s/B)$) and flow fields for a $\beta = 2$ contraction flow (flow from left to right, $P = 0$ at $x = 20$). (a) Pressure at $t = 0$, (b) Pressure at $t = 500$, (c) Streamlines at $t = 0$ [solid], $t = 500$ [dashed]. Model conditions: $\alpha = 4$, $[\phi/\phi_{\rm m}]_{bulk} = 0.735$, $\phi_{\rm m} = 0.68$, $B/a = 18$.

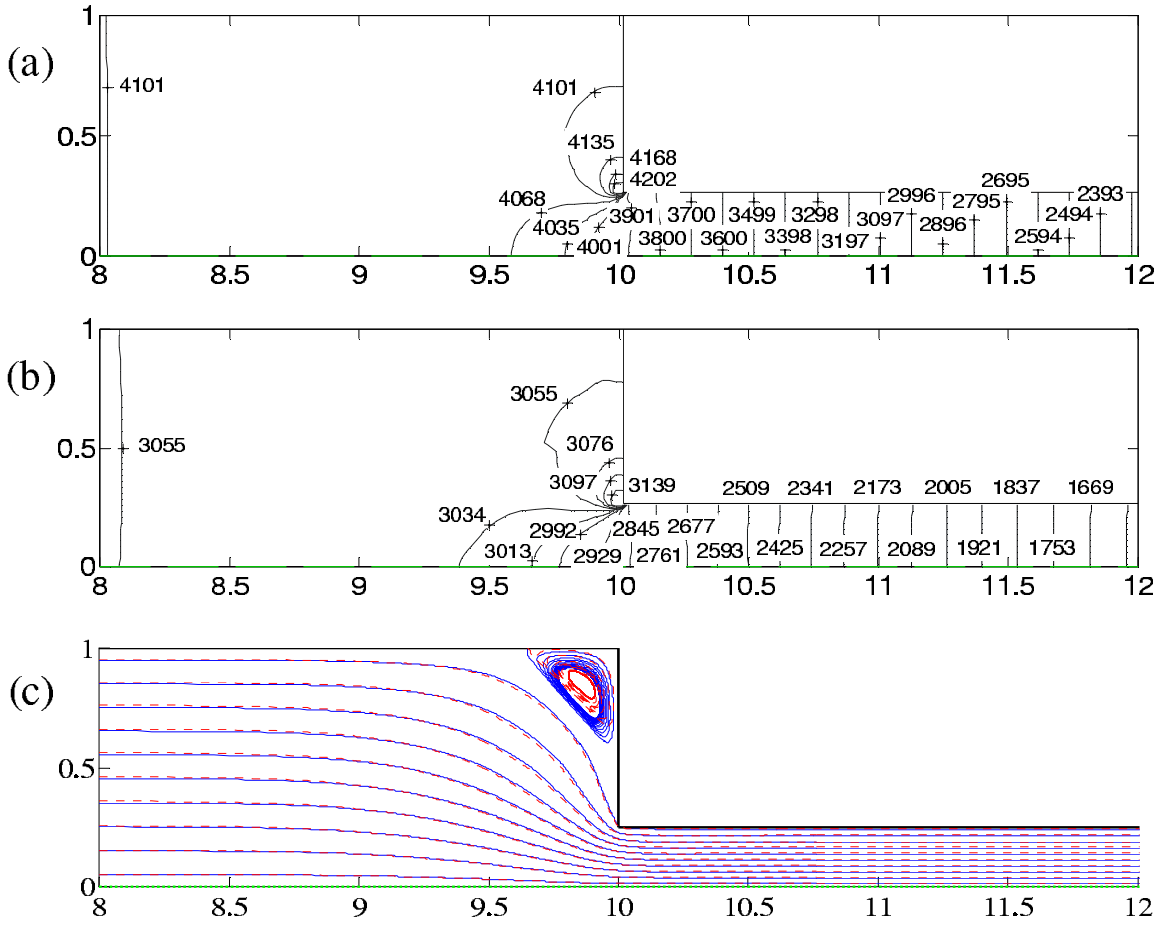

Figure 46: Isotropic model predictions for the pressure ($P^* = P/(\eta_o U_s/B)$) and flow fields for a $\beta = 4$ contraction flow (flow from left to right, $P = 0$ at $x = 15$). (a) Pressure at $t = 0$, (b) Pressure at $t = 500$, (c) Streamlines at $t = 0$ [solid], $t = 500$ [dashed]. Model conditions: $\alpha = 4$, $[\phi/\phi_{\rm m}]_{bulk} = 0.735$, $\phi_{\rm m} = 0.68$, $B/a = 18$.

axisymmetric geometry and the model predictions are for a rectangular geometry, the two should be qualitatively similar. There are two possible reasons that this build up was not obvious in the NMR images (since it is so extreme in the FVM predictions). First, as was seen in the data for the neck region in Figure 43, there were some issues of resolution near the wall. Second, they had not run their experiments very long, approximately equivalent to a piston movement of $12B$, where the steady-state results shown are equivalent to a piston movement of $250B$. Therefore, the experiments have not had enough time to achieve the amount of build up observed in the model predictions.

The effect of particle migration on the predicted pressure and flow fields is illustrated in Figure 45, Figure 46 and Table 6. The figures show contour plots of the pressure field near the corner region of the contraction for the $\beta = 2$ and $\beta = 4$ contractions and show a plot of the effect of migration on the flow streamlines near the corner. In these plots the flow is from left to right. The pressure contours illustrate a peak in pressure at the sharp-edge corner, but with little radial variation elsewhere. Overall, the pressure field shows a linear decrease in pressure with axial distance, with a larger rate of descent (or pressure drop) in the smaller channel. The contour plots and Table 6 show that the migration of the particle field results in a decrease in the required pressure to drive the flow field. The streamline plot shows that particle migration has some effect on the flow field near the contraction opening, but not much. The main effect is a decrease in the size of the flow vortex in the concave corner.

Figure 47(a,b) show unit vectors representing the direction of the particle migration flux, $\mathbf{j}_\perp$, for the $\beta = 4$ and $\beta = 2$ contraction flows at $t = 0$ before any particle migration has occurred (i.e. the entire domain is set equal to the initial bulk value of ϕ). The directions of the flux vectors are roughly the same for both cases, with particles being pushed away from the contraction opening and into the corner. There is also a general push away from the flow direction. When we look at the magnitudes of these vectors in Figure 48(a,b) we see there is a much greater push away from the contraction opening and high shear area at the sharp-edged corner in the $\beta = 4$ contraction case.

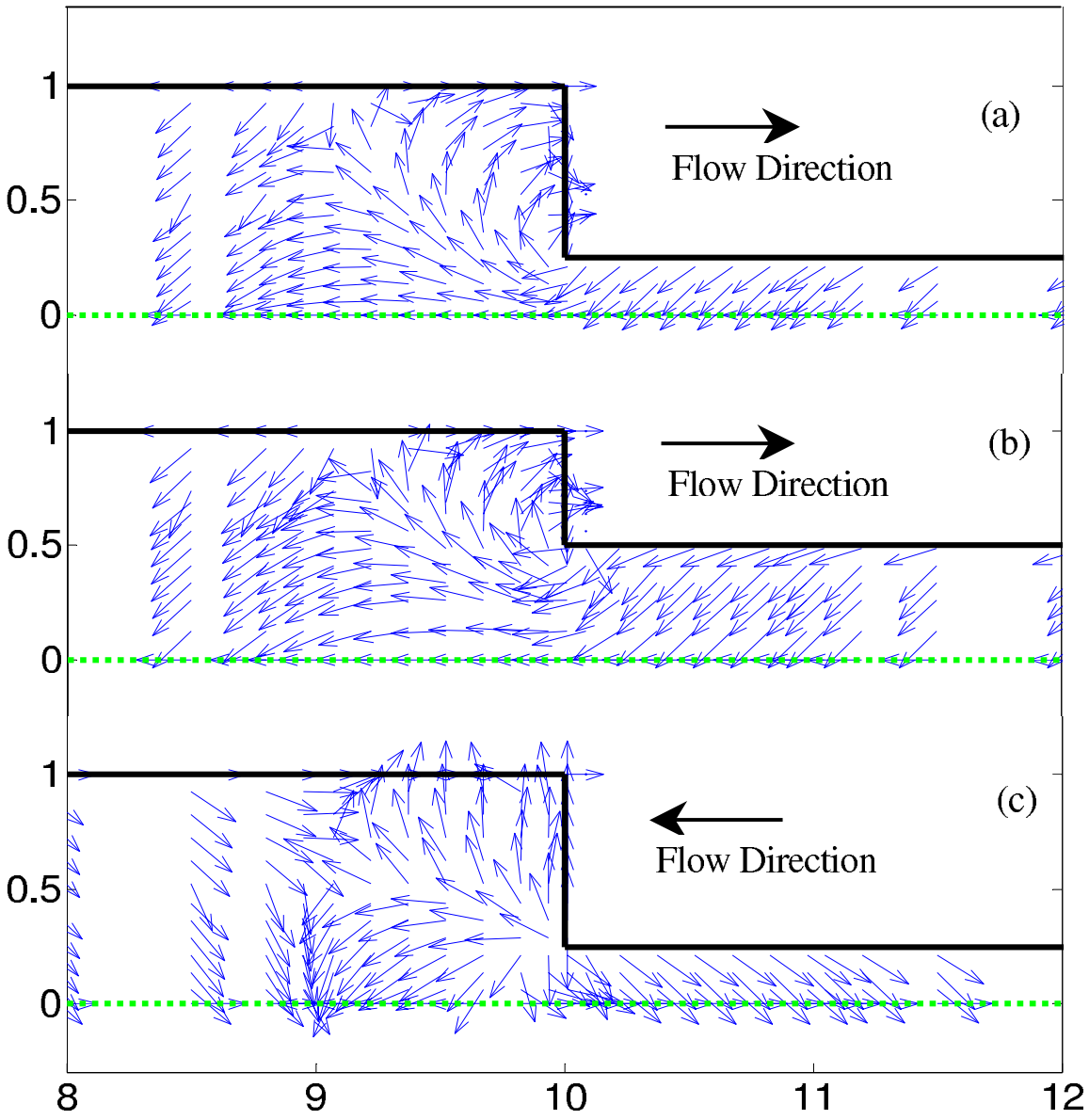

Figure 47: Comparison of unit vectors representing $\mathbf{j}_\perp$ for the isotropic model at $t = 0$. The vector magnitudes are given in Figure 48. (a) $\beta = 4$, contraction; (c) $\beta = 2$, contraction; (c) $\beta = 4$, expansion.

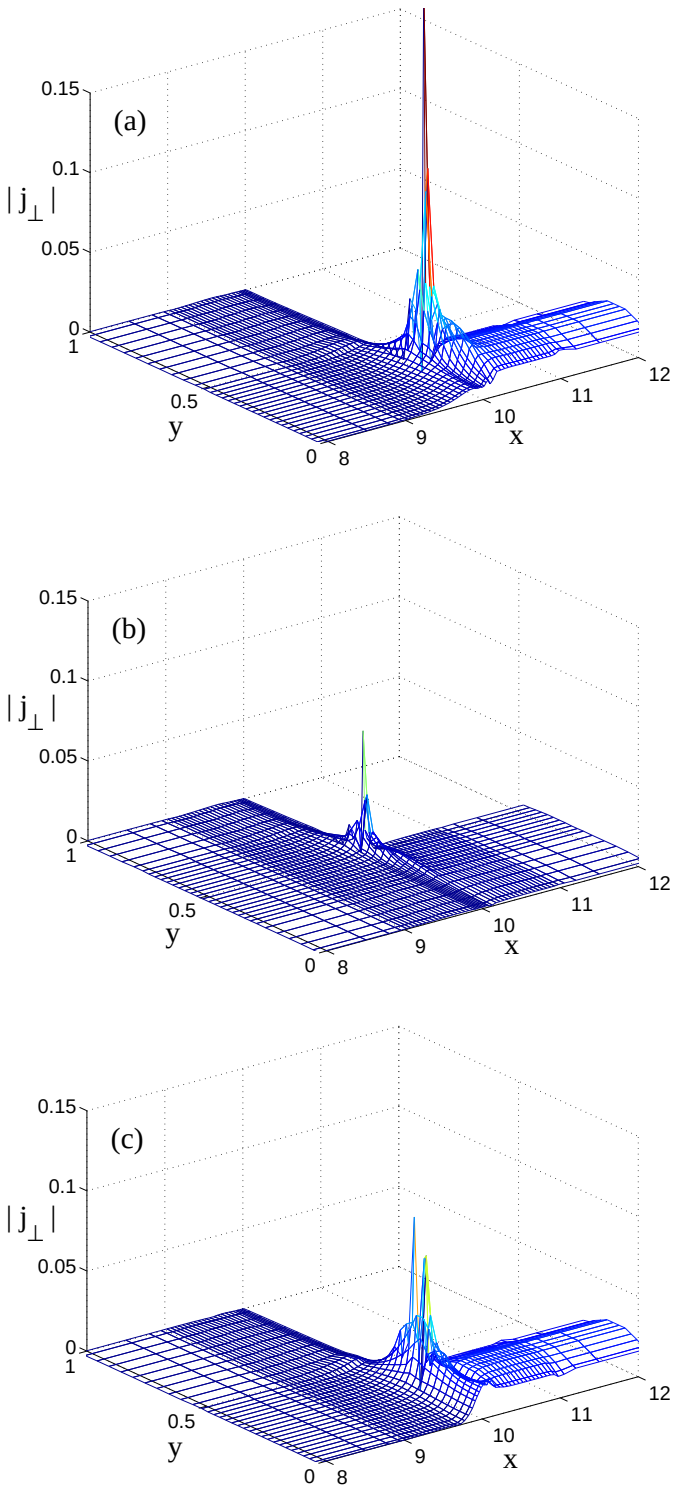

Figure 48: Comparison of the predicted magnitude of $\mathbf{j}_\perp$ for the isotropic model at $t = 0$. (a) $\beta = 4$, contraction; (c) $\beta = 2$, contraction; (c) $\beta = 4$, expansion. Note, for plot (a) the surface is off the scale, with a maximum value of 0.241.

Table 6: Predictions for the inlet pressure ($P^* = P/(\eta_o U_s/B)$) before and after particle migration has occurred. Model conditions: $\alpha = 4$, $[\phi/\phi_m]_{bulk} = 0.735$, $\phi_m = 0.68$, $B/a = 18$.

	Length		P* Inlet	
	Upstream	Downstram	t = 0	t = 500
Contraction, β = 2	10B	10B	1,149	940
Contraction, β = 4	10B	5B	4,204	3,152
Expansion, β = 4	10B	10B	8,349	5,709

5.3.3 Effect of flow direction on predicted results

Figure 49 shows the effect of the flow direction on the non-localized shear-rate at $t = 0$ and on the steady-state ϕ/ϕ_m predictions. For both cases the inlet was held at a constant ϕ/ϕ_m value, which results in different conditions at the contraction opening for both cases. For the expansion, the ϕ/ϕ_m was much closer to convergence than that going through the larger contraction channel. The $< \dot{\gamma} >_\epsilon$ conditions where nearly identical for both cases, but from Figure 47(a,c) and Figure 48(a,c), it is evident that the migration conditions were very different. In the expansion, the migration vectors went against the flow direction, just as in the contraction, but that was now in the opposite direction. This resulted in just a push away from the high shear region next to the sharp-edged corner, but not a push back into the concave corner section as in the contraction flow.

From the magnitude plots, it can be seen that the push away from the sharp-edged corner is not as strong as in the contraction flow, but the contour and line plots in Figure 49 show a much greater predicted dip in particle concentration by the sharp-edge corner than for the contraction, with the area just downstream of the sharp-edge corner almost completely free of particles. This resulted in an almost "jet"-like behavior as in the contraction-expansion flow, with most of the particles remaining in the center of the larger channel. The convex corner did not show the build up that the contraction flow results did, but remained close to the bulk concentration.

The predicted pressure field behavior for the expansion flow (Figure 50) showed a similar trend to the contraction flow, just with a dip in pressure near the corner, rather than a

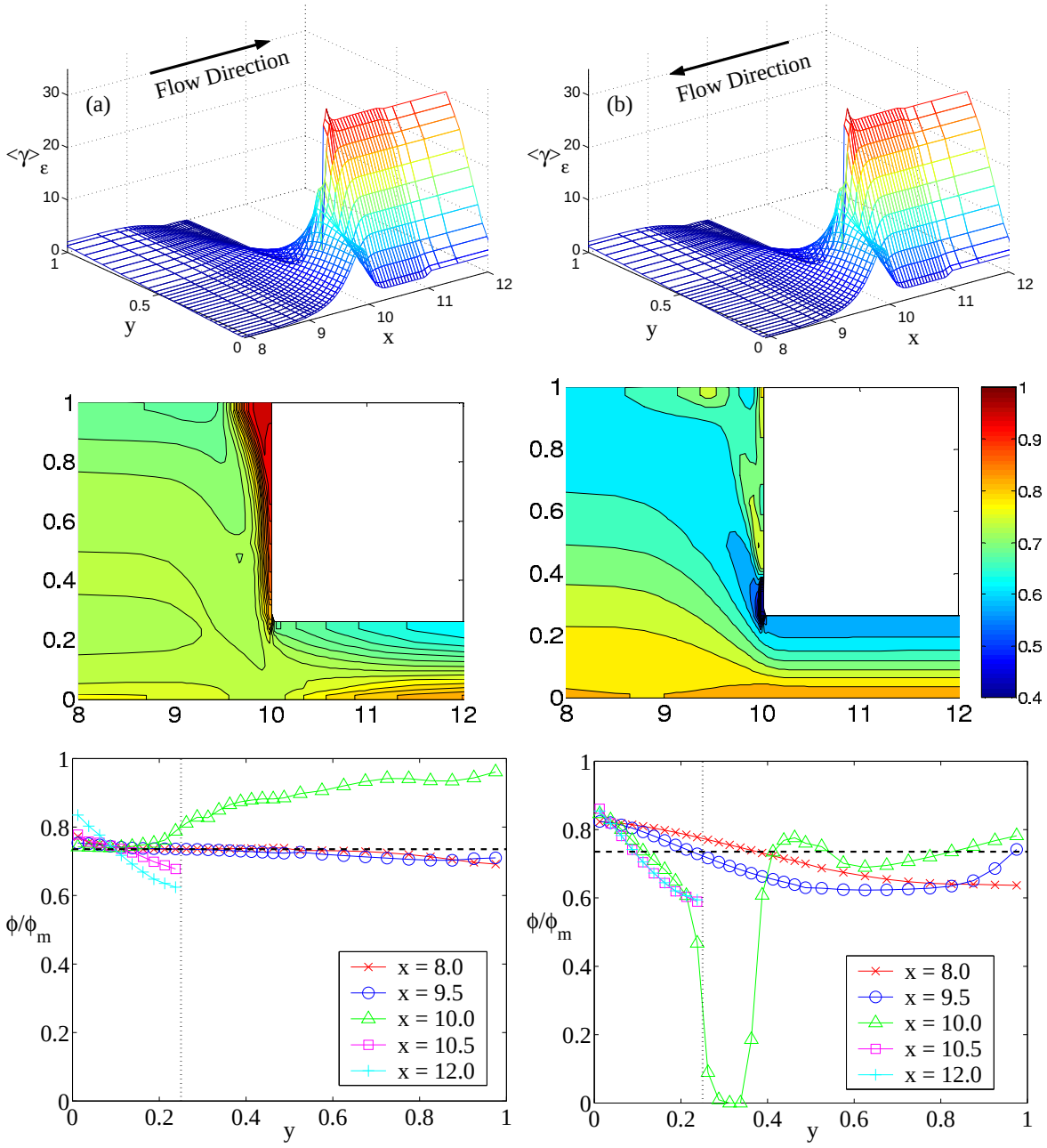

Figure 49: Comparison of isotropic model predictions for a: (a) $\beta = 4$, contraction; (b) $\beta = 4$, expansion. Top plots are the initial nonlocal shear rate field. Underneath are the corresponding $\phi/\phi_{\rm m}$ plots at steady-state. Model conditions: $\alpha = 4$, $[\phi/\phi_{\rm m}]_{bulk} = 0.735$, $\phi_{\rm m} = 0.68$, $B/a = 18$.

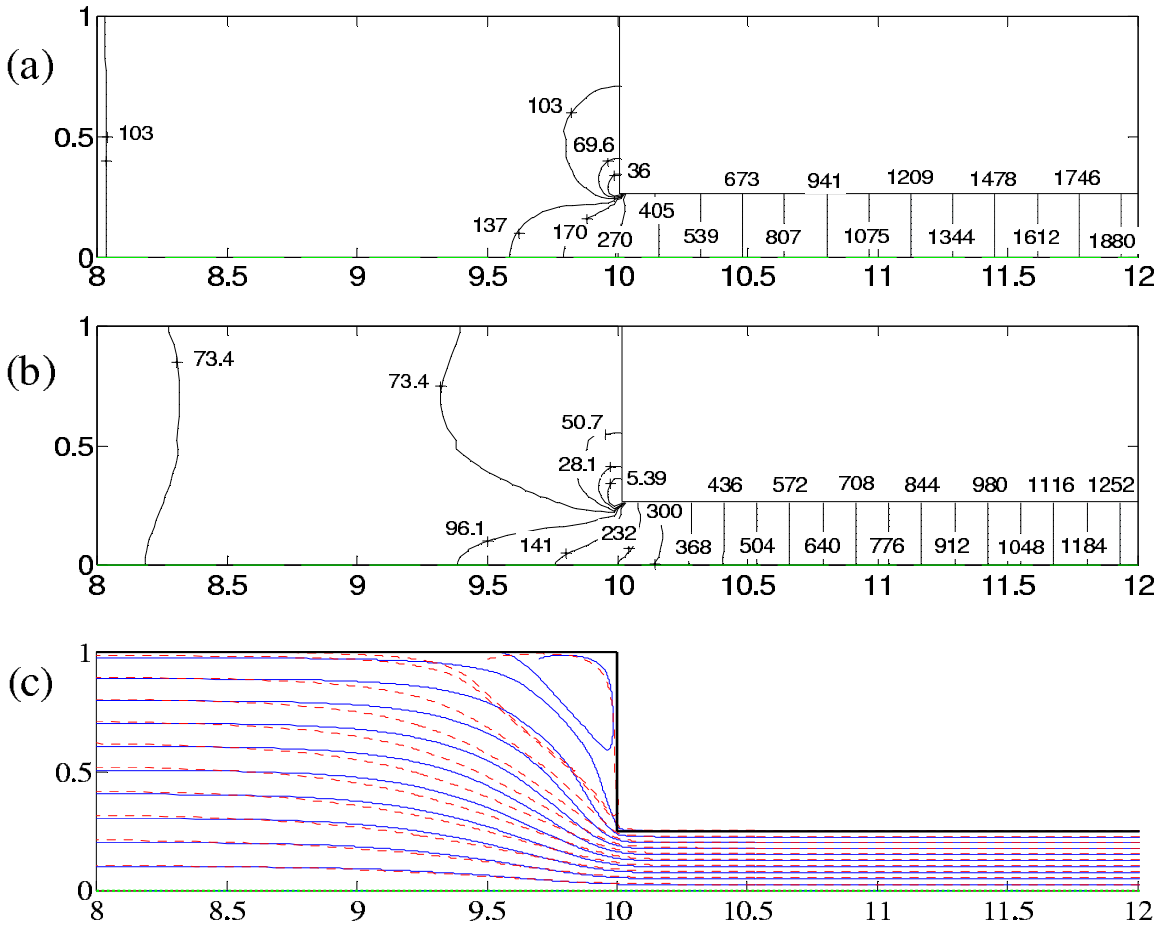

Figure 50: Isotropic model predictions for the pressure ($P^* = P/(\eta_o U_s/B)$) and flow fields for a $\beta = 4$ expansion flow (flow from right to left, $P = 0$ at $x = 0$). (a) Pressure at $t = 0$, (b) Pressure at $t = 500$, (c) Streamlines at $t = 0$ [solid], $t = 500$ [dashed]. Model conditions: $\alpha = 4$, $[\phi/\phi_{\rm m}]_{bulk} = 0.735$, $\phi_{\rm m} = 0.68$, $B/a = 18$.

peak. The same linear drop in pressure along the axial direction is evident, as it the overall drop in pressure needed to drive the flow after migration has occurred (Table 6). The model predicts a large increase in the recirculation zone in the corner after particle migration has occurred.

5.4 Effects of the Constitutive Law on Model Predictions

For our study of the constitutive model we chose to focus on the $\beta = 4$, planar contraction geometry. By looking at the planar geometry, we are able to focus on the in-plane stress effects without worrying about the effect of λ_3 on the equation. The $\beta = 4$ contraction was chosen due the extreme shear predicted in the neck region, which will amplify any difference between the model predictions.

Model conditions are the same as above with $\alpha = 4$, $\phi_{\mathrm{m}} = 0.68$ and a suspension of $\phi_{bulk} = 0.5$, $B/a = 18$. The grid from Chapter 2, Figure 6 was used with a 10B inlet, a 10B outlet and the same imposed boundary conditions.

5.4.1 Weighted-isotropic constitutive model predictions

The value of the normalized kinematic ratio ($\hat{\rho}_k$) in a $\beta = 4$ contraction is presented in Figure 51(c) for the region around the contraction opening at the initial state (constant particle field, Newtonian flow solution). For the majority of the domain (10B upstream:10B downstream) a value of $\hat{\rho}_k = 1$, corresponding to simple shear, was predicted. Figure 51(a,b) shows the magnitude of the shear rate and magnitude of the relative rotation which make up the kinematic ratio. From these plots it can be seen that the shear increases near the contraction opening to the point that $\hat{\rho}_k$ drops below one just upstream of the contraction opening in a region of extension-dominated flow. Right upstream and downstream of this region of extension-dominated flow, there are regions of higher relative rotation, ω_{rel}. This rotation is due to the change in flow type which causes a rotation of the local eigenvectors (as is evident in Figure 56). The same rise in $\hat{\rho}_k$ is evident along the boundary between the bulk flow and recirculation zone in the corner. This rise in the corner is then followed by a decrease, signifying another extension dominated region due to the separation of the streamlines where the secondary recirculation breaks away from the bulk flow into the

contraction opening. A region of high rotation is also seen at the sharp-edged corner.

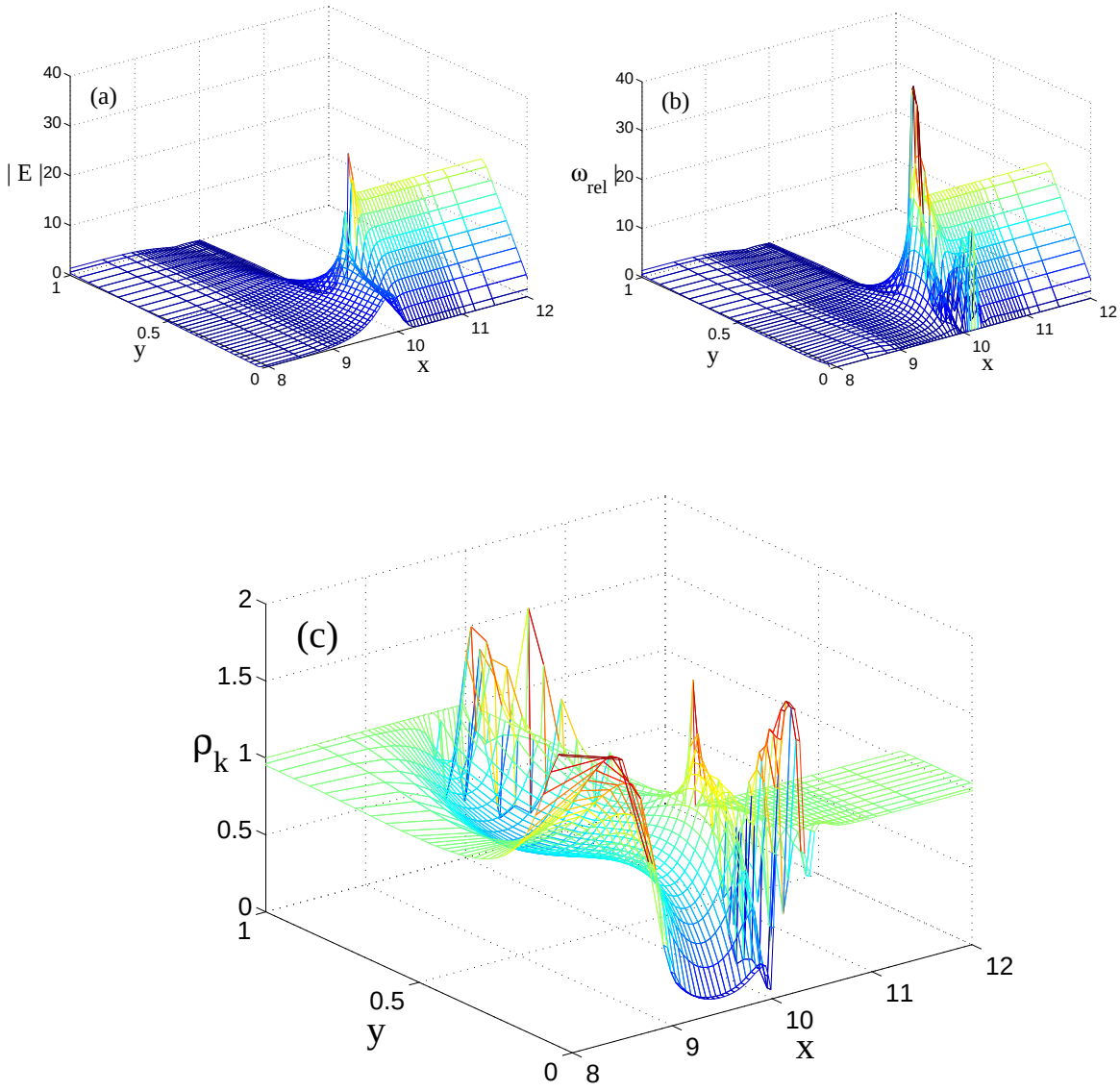

Figure 51: Plots of the: (a) magnitude of the rate of strain; (b) magnitude of the relative rotation; and (c) normalized kinematic ratio ($\hat{\rho}_k$), for a $\beta = 4$ contraction.

The effect of this variation in $\hat{\rho}_k$ on the particle pressure is illustrated in the surface plots (Figure 52) of the kinematic weighting function $B(\hat{\rho}_k)$ for set point values of $B_{ext} = 2$ and 5. Through most of the domain the value of $B(\hat{\rho}_k)$ remains at the simple shear value of one, except in the regions of high extension near the contraction opening. Here, the value of B increases, reaching the maximum value at the centerline just upstream of the contraction. Also there is an increase in the weighting function in the corner near the recirculation

zone. This is due to the extension generated by the separation of streamlines. The actual consequence of the kinematic weighting function on the suspension pressure is illustrated in Figure 53, when it is multiplied by the non-localized shear-rate. It is evident that despite the rise of B in the corners, there is little effect on the particle pressure due to the low shear-rate in this region. Also, an important point to note is that despite the appearance of oscillation in the value of $B(\hat{\rho}_k)$, it appears to be mainly limited to regions of low shear where it does not have a significant effect on the stability of the solution scheme.

The predicted results for the steady-state particle volume fraction profiles when using the weighed-isotropic particle stress model are presented in Figure 54. The only area of significant difference between the predictions for different B_{ext} is at the opening of the contraction. From Figure 54(d), we can conclude that the value of the extensional set point, B_{ext}, controls the predicted drop in particle volume fraction at the mouth of the contraction. There is some difference observed in the rise in ϕ/ϕ_{m} in the corner, but these values are fairly close. This illustrates that by varying particle pressure in areas of high extension, we can tune the model to predict the correct drop in particle volume fraction in such regions of a complex flow field.

5.4.2 Anisotropic constitutive model predictions

The behavior of the eigenvectors near the contraction opening for a $\beta = 4$ contraction is illustrated in Figure 56(a,b). Figure 56(a) is of unit vectors in the direction of the extension eigenvector, or of the tension direction in compression-tension coordinates, and Figure 56(b) is the angle that these unit vectors are rotated away from the x-axis, as illustrated Figure 55. The eigenvectors are calculated from the relationship:

$$\mathbf{E} \cdot \mathbf{e}_i = a_i \mathbf{e}_i, \tag{70}$$

where $\mathbf{E}$ is the rate of strain tensor and $\mathbf{e}_i$ is the eigenvector for eigenvalue, a_i, which was determined from the relationship $det|\mathbf{E} - a\underline{\underline{\delta}}| = 0$. These equations result in the following relationships for the rotation of the extension and compression eigenvectors away from the

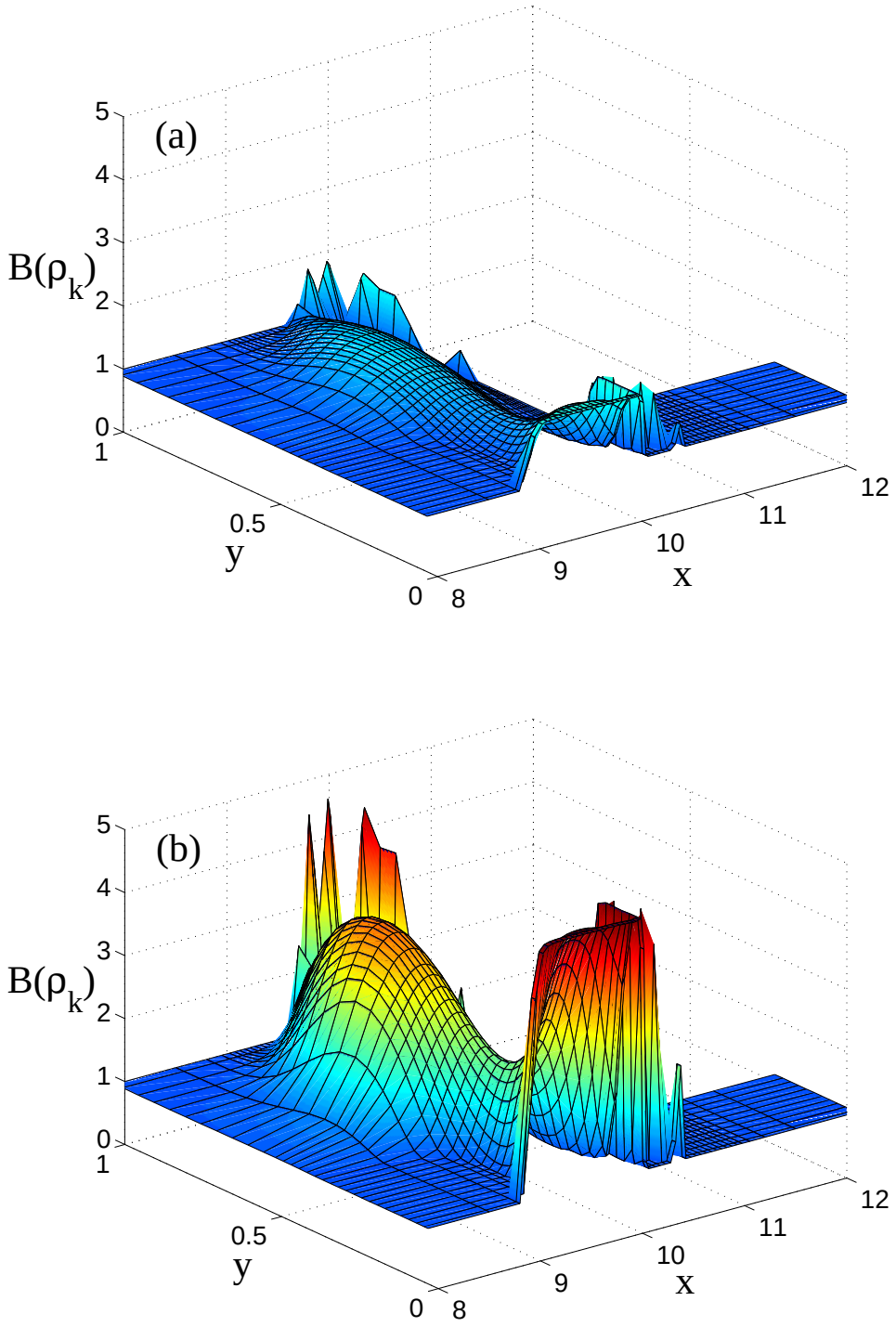

Figure 52: Plot of the kinematic weighting function, $B(\hat{\rho}_k)$, of the particle pressure for the weighted-isotropic particle stress model in a $\beta = 4$ contraction. (a) $B_{ext} = 2$, (b) $B_{ext} = 5$.

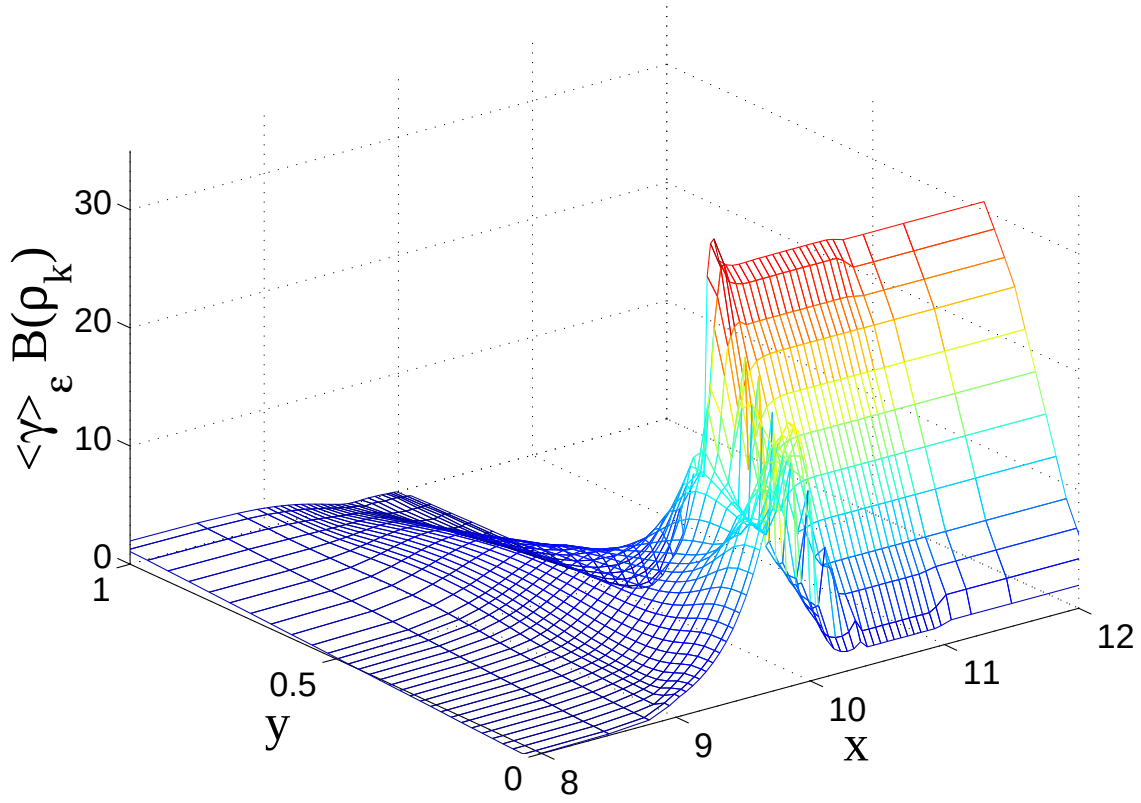

Figure 53: Plot of the product of the kinematic weighting function $B(\hat{\rho}_k)$ ($B_{ext} = 2$) with the nonlocal shear rate at initial conditions in a $\beta = 4$ contraction.

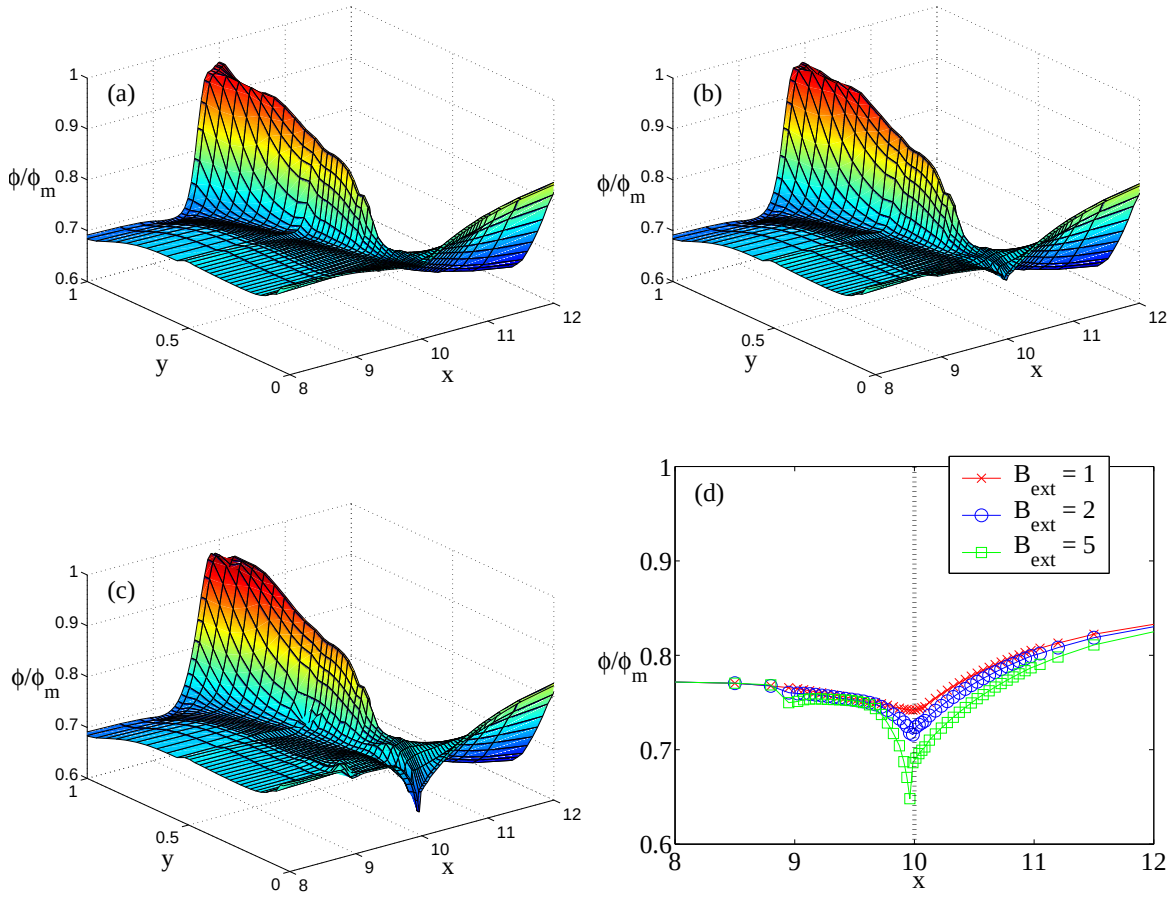

Figure 54: Surface plots of the predicted ϕ/ϕ_{m} profiles at steady-state ($t = 500$) for a $\beta = 4$ contraction using an isotropic-weighted constitutive law. (a) $B_{ext} = 1$, (b) $B_{ext} = 2$, (c) $B_{ext} = 5$. Plot (d) is $\phi/\phi_{\mathrm{m}}(x)$ at y = 0.

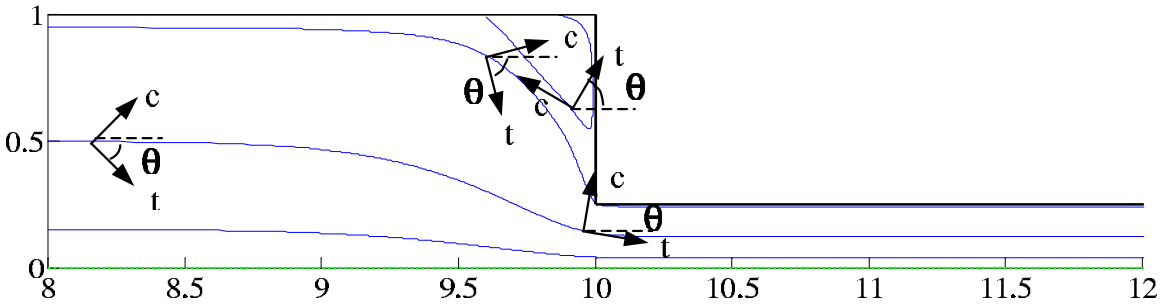

Figure 55: Sketch of the orientation of the compression-tension coordinates in a $\beta = 4$ contraction flow. The variable θ is the angle from the x-axis to the tension axis and defined in Eq. (71).

x-axis,

$$\theta_{ext} = tan^{-1}(\frac{a_{ext} - E_{xx}}{E_{xy}}), \tag{71}$$

$$\theta_{comp} = tan^{-1}(\frac{a_{comp} - E_{xx}}{E_{xy}}), \tag{72}$$

where a_{ext}, a_{comp} are the extension and compression eigenvalues as defined in Section 5.1.2. The use of tan^{-1} for the calculation limits the values of the rotation to $-90° \leq \theta \leq +90°$, even though for the definition of the compression-tension axis, the 180° equivalent would be just as valid. The main concern is to make sure that all the eigenvectors are calculated in a consistent manner to ensure that the calculation of the eigenvector rotation (Eq. (66)) used to determine ω_{rel} is valid.

For simple shear conditions the rotation of the extensional eigenvector, θ_{ext}, is ±45° from the flow direction. For an +x-directed channel flow, the rotation would be −45° above the plane of symmetry and +45° below. As can be seen in the vector plot of Figure 56 and sketch in Figure 55, the tension direction lines up with the x-axis as the flow approaches the contraction opening. Another point to note is that the direction of the extensional eigenvector abruptly changes signs (rotates 180°) in the corner due to the change in the orientation of shear (the flow near the wall is moving in the opposite direction) in the recirculation zone.

The predicted difference between the x-directed and y-directed particle normal stress (which we will call the geometric normal stress difference, $N_{xy} = (\Sigma^{NS}_{\mathrm{P},xx} - \Sigma^{NS}_{\mathrm{P},yy})/ < \dot{\gamma} >_{\epsilon} \eta_n$) for the initial flow field in a $\beta = 4$ contraction is shown in Figure 57. Figure 57(a) is with

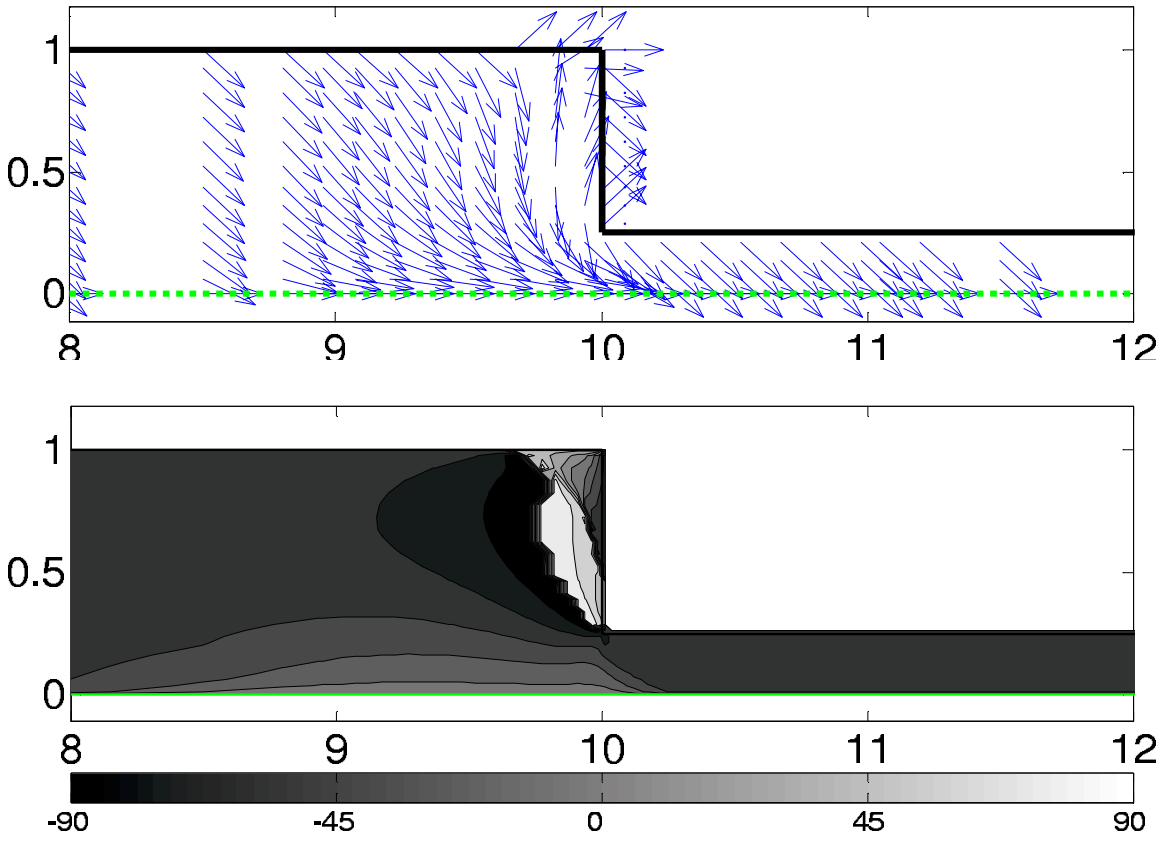

Figure 56: Vector plot of the extensional eigenvectors and a contour plot of the angle, θ_{ext}, that the eigenvectors make with the x-axis.

$N_{ct} = 0$ and Figure 57(b) is with $N_{ct} = 0.2$ (to predict a slight normal stress difference in simple shear). The plots have been rotated 180° from previous surface plots to give a better view of the corner and centerline. The main influence of the normal stress difference is again in the neck region of the contraction. For the stress values, compression is considered negative stress and tension positive stress. Therefore, with $N_{ct} = 0.2$ and the resulting prediction of $N_{xy} = -0.2$ in the simple shear regions of the flow corresponds to more compressive stress along the x-direction, since for the particle stress model, all stresses are predicted to be compressive, and therefor negative. With $N_{xy} < 0$, the x-directed particle normal stress is more negative than the y-directed, corresponding to a slight compression of the streamlines in the x-direction, with the opposite true when $N_{xy} > 0$.

From the surface plots in Figure 57, the model predicts $N_{xy} > 0$ in the region of the contraction opening with and area of $N_{xy} < 0$ along the wall perpendicular to the bulk flow. There are some oscillations in the stress difference near the wall and centerline, which is due to the calculation of the eigenvectors near the boundaries. These fluctuations oscillate throughout the migration solution, resulting in some added stability concerns, but eventually die out as a steady-state solution is approached.

The effect of this geometric normal stress difference on the streamlines of the flow solution is explored in Figure 58. Figure 58(a) shows the influence of the anisotropic model on the initial flow streamlines with $\phi_{\mathrm{B}} = 0.50$ and Figure 58(b) shows how this influence dies off as the bulk concentration is decreased. In Figure 58(a), it can be seen that the added y-directed compression (x-directed tension), pulls the streamline below the Newtonian predicted position, with the addition of $N_{ct} = 0.2$ amplifying this effect. The anisotropic normal stress also increases the size of the corner recirculation zone.

The driving force behind the alteration of the flow streamlines for the anisotropic model is explored in Figure 59, Figure 60, and Figure 61. Figure 59 and Figure 60 deal with anisotropic stress conditions at the initial uniform particle concentration with $B_t = 0$, $B_c = 2$ and $N_{ct} = 0, 0.2$, respectively. In both figures, plot (a) is a vector plot of the pressure gradient for the initial, isotropic, Newtonian flow field. This represents the driving force for the isotropic flow solution. In both figures, plot (b) is a vector plot of the particle

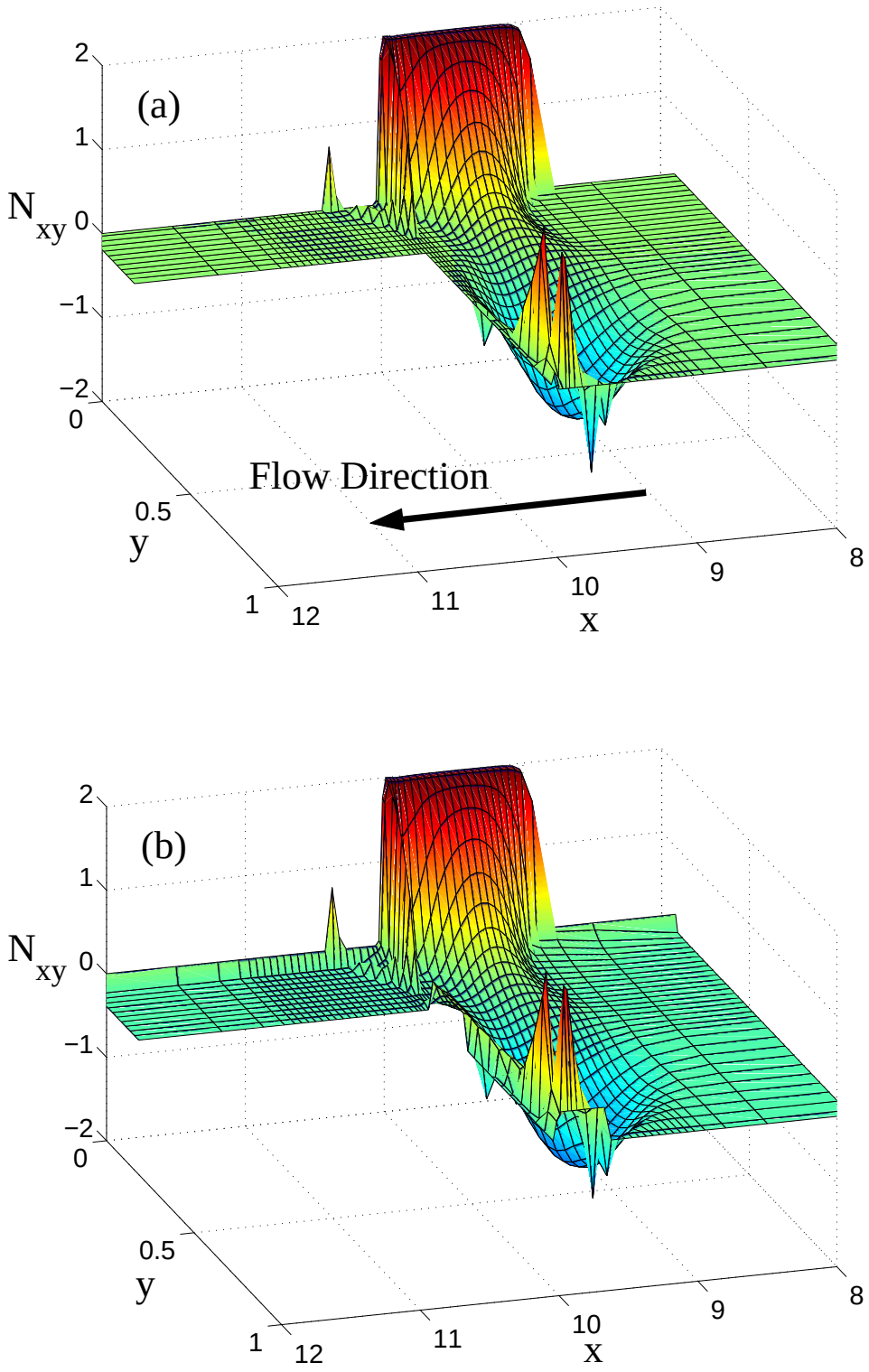

Figure 57: Plot of the geometric normal-stress difference, N_{xy}, in a $\beta = 4$ contraction flow. Model parameters are $Bc = 2$, $Be = 0$. (a) $N_{ct} = 0$, (b)$N_{ct} = 0.2$ (Note: the perspective is rotated 180 degrees from the previous surface plots.)

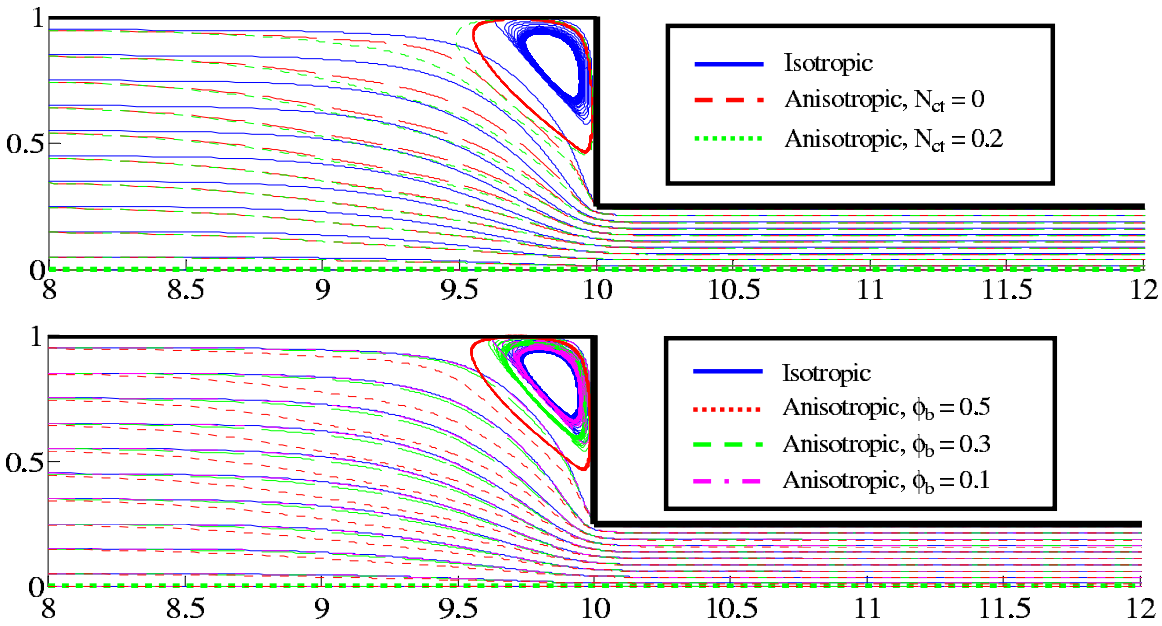

Figure 58: Comparison of the effect of the particle normal stress on the streamlines in a rectangular contraction ($\beta = 4$). The flow solutions are at the initial bulk concentration. The top plot is at $\phi_{\mathrm{B}} = 0.5$ while in the bottom plot holds $N_{ct} = 0$.

normal stress divergence, $\nabla \cdot \mathbf{\Sigma}_{\mathrm{P}}^{NS}$. This is calculated for a uniform particle concentration using the Newtonian velocity field. This term is treated as a source in the momentum equations for the determination of the altered streamlines in Figure 58. The effect of this added source is illustrated in the plot (c) of both figures, which is a difference between the pressure gradient and particle normal stress divergence. By taking the difference, we are able to illustrate the effect that the addition of the particle normal stress divergence has on the driving force of the flow field.

From the difference plots in Figure 59 and Figure 60, and the close up of the concave corner region in Figure 61, it is evident that the addition of the stress divergence alters the source field driving the bulk flow in a manner that compresses the streamlines toward the contraction opening. This also results in the increase in the size of the corner vortex region. As for the difference with the addition of $N_{ct} = 0.2$, it seems only to effect the magnitude of the change, with little difference between the direction of the difference vectors for the two cases.

The effect of the anisotropic model on steady-state particle volume fraction predictions

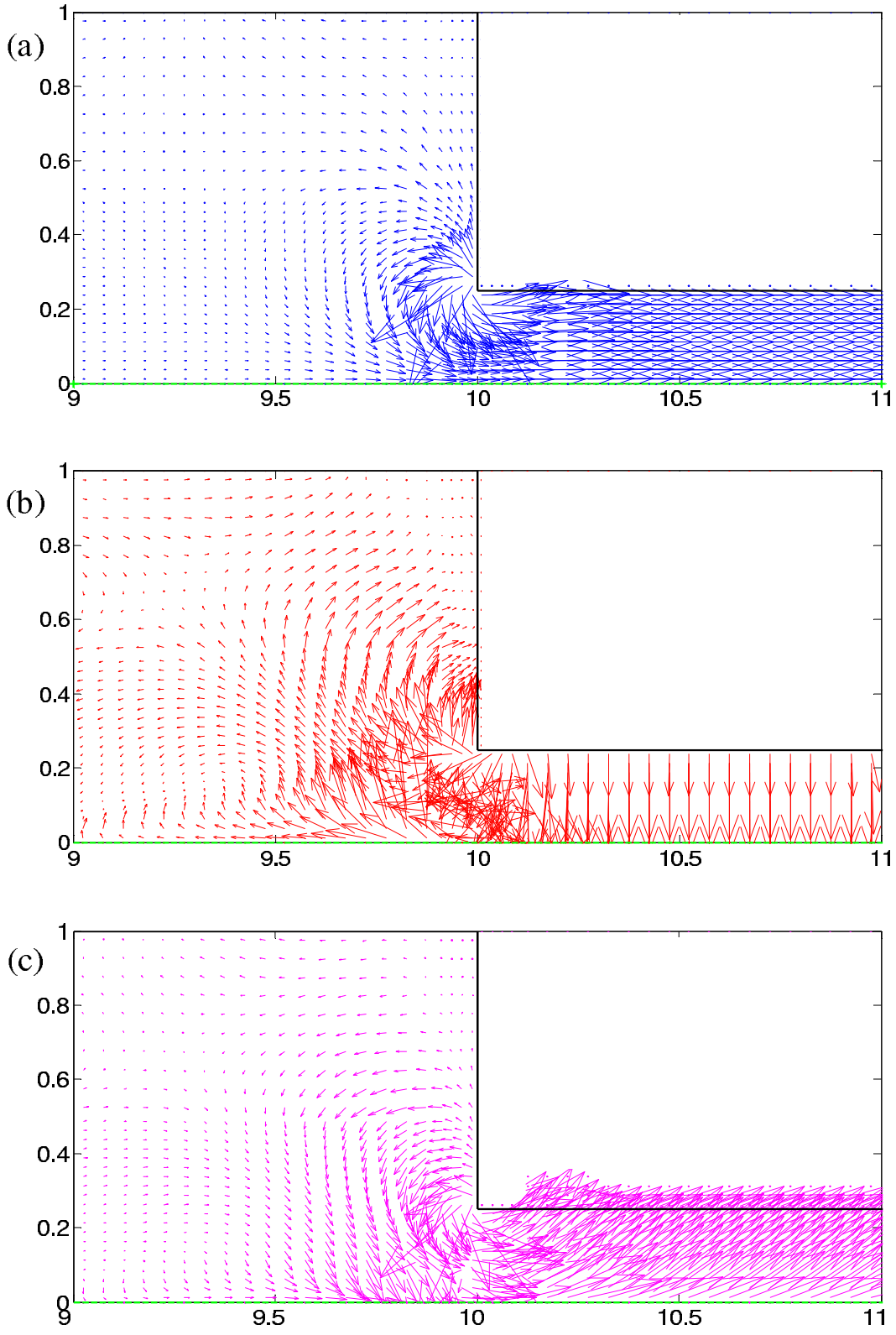

Figure 59: Vector plots of the pressure gradient for the initial Newtonian velocity field and particle normal stress divergence with an anisotropic model, $N_{ct} = 0$. (a) $-\nabla P$; (b) $\nabla \cdot \mathbf{\Sigma}_{\mathrm{P}}^{NS}$; (c) $-\nabla P - \nabla \cdot \mathbf{\Sigma}_{\mathrm{P}}^{NS}$.

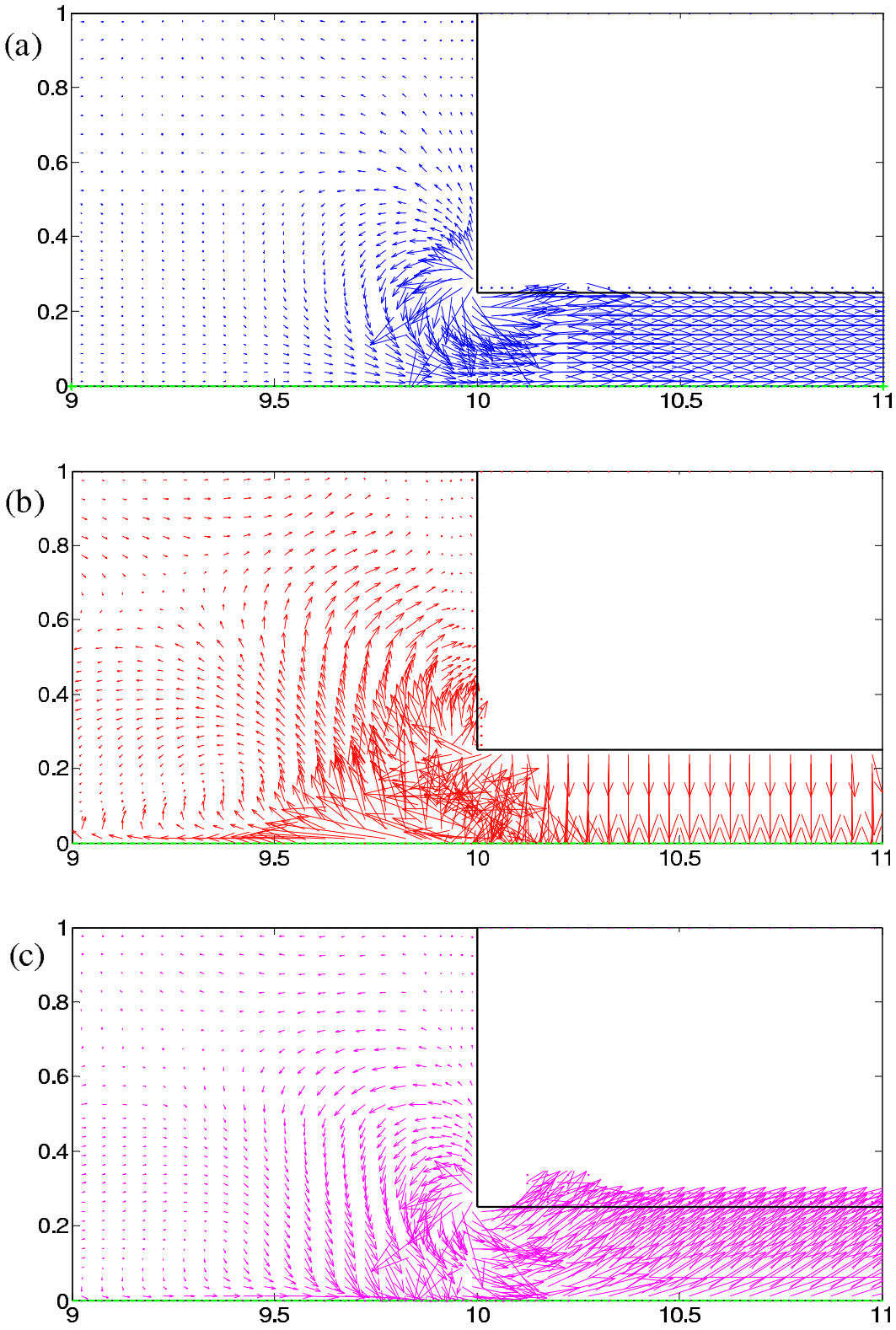

Figure 60: Vector plots of the pressure gradient for the initial Newtonian velocity field and particle normal stress divergence with an anisotropic model, $N_{ct} = 0.2$. (a) $-\nabla P$; (b) $\nabla \cdot \mathbf{\Sigma}_{\mathrm{P}}^{NS}$; (c) $-\nabla P - \nabla \cdot \mathbf{\Sigma}_{\mathrm{P}}^{NS}$.

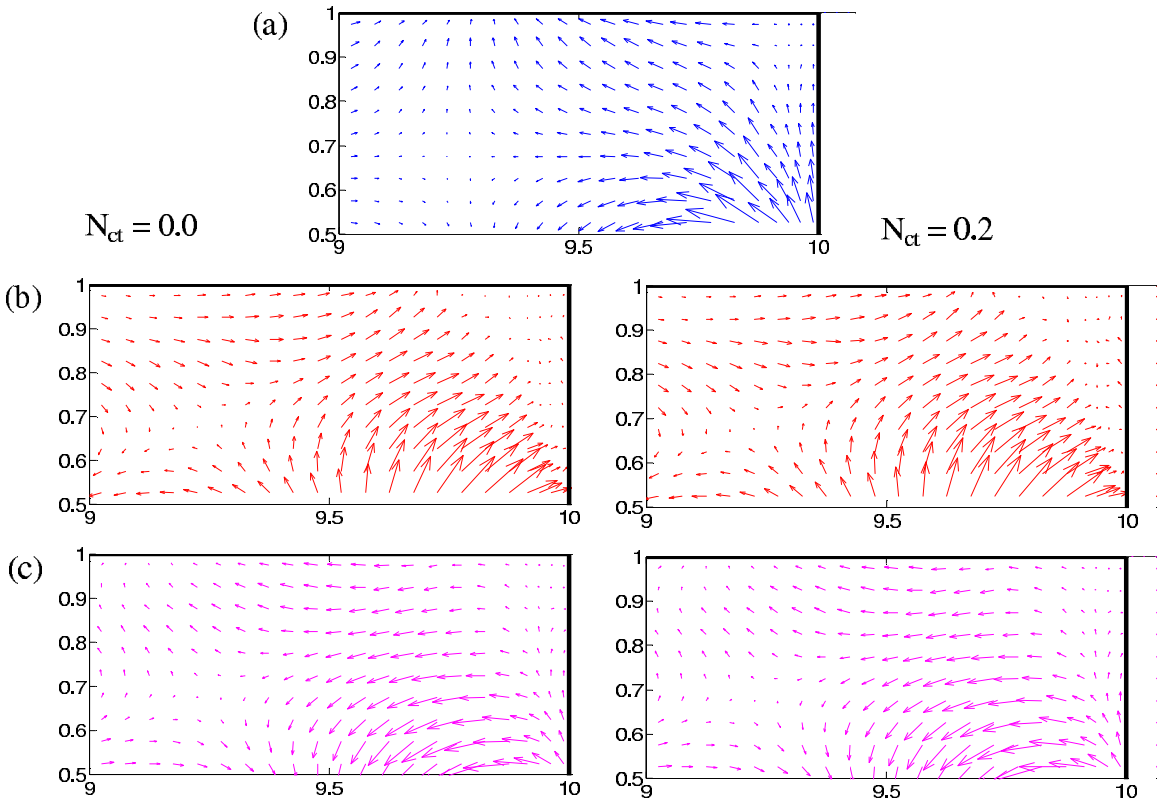

Figure 61: Close up of the corner region for vector plots of the Newtonian pressure gradient and particle normal-stress divergence with an anisotropic model. (a) $-\nabla P$; (b) $\nabla \cdot \mathbf{\Sigma}_{\mathrm{P}}^{NS}$; (c) $-\nabla P - \nabla \cdot \mathbf{\Sigma}_{\mathrm{P}}^{NS}$.

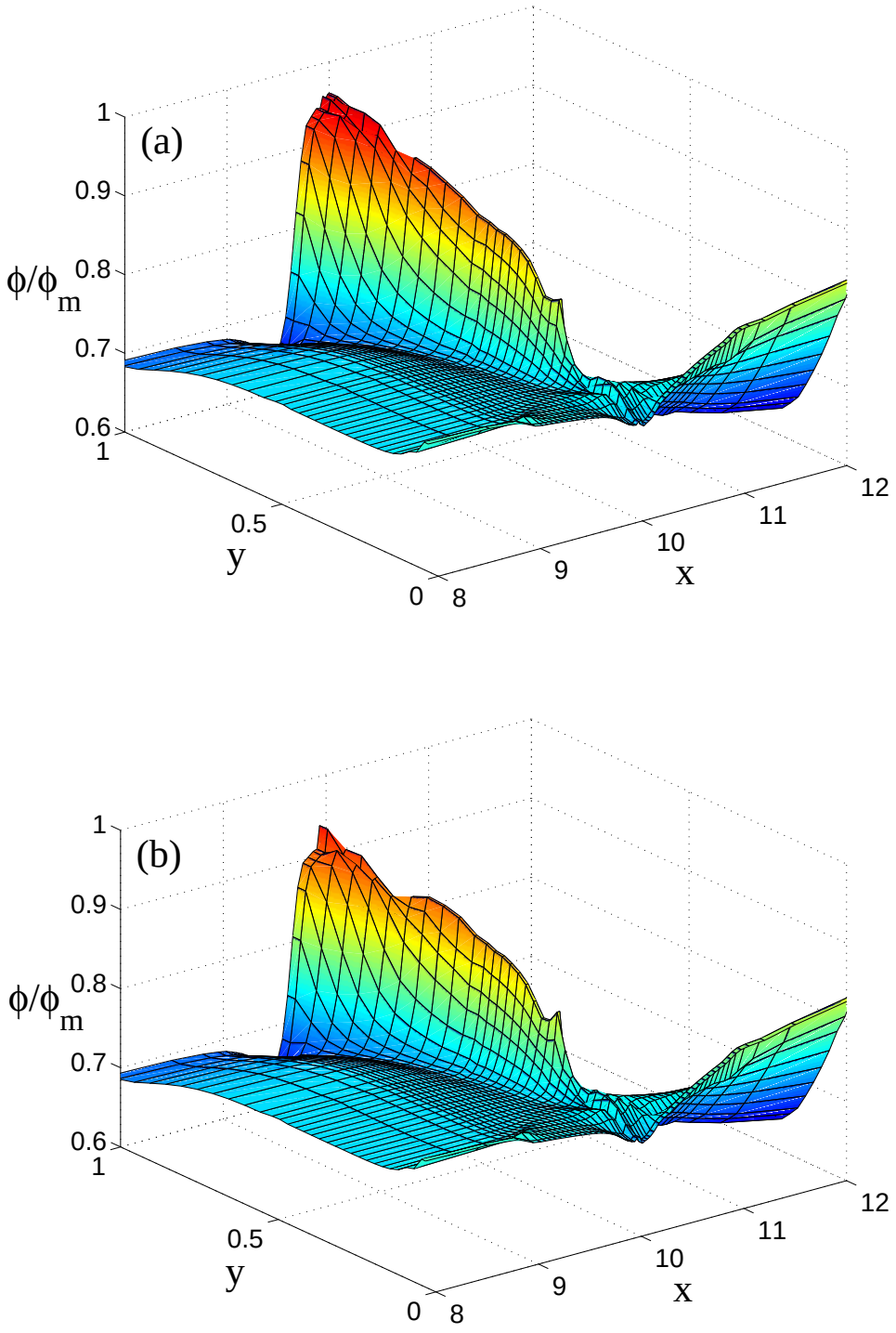

Figure 62: Surface plots of ϕ/ϕ_{m} at $t = 500$ for a $\beta = 4$ contraction solved with an anisotropic constitutive law: (a) $N_{ct} = 0$; (b) $N_{ct} = 0.2$.

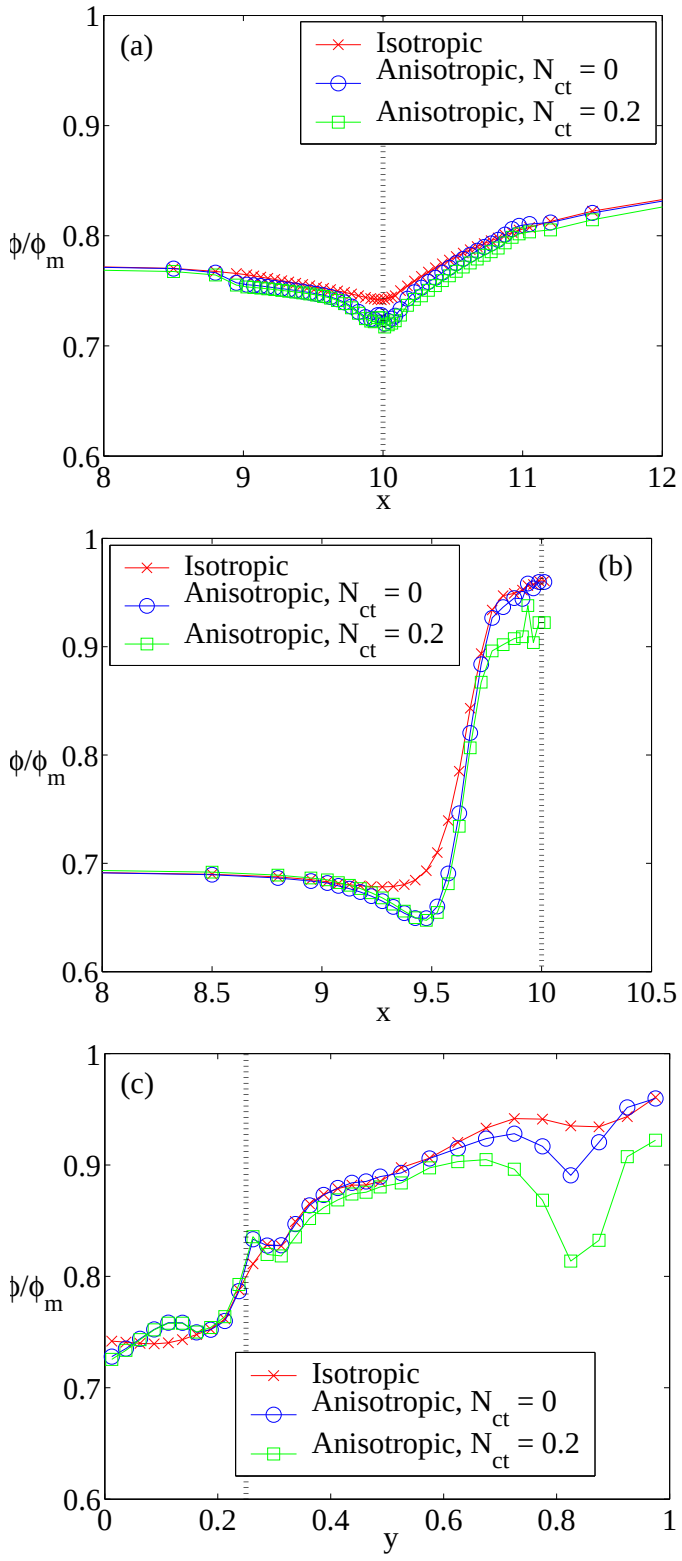

Figure 63: Plots of $\phi/\phi_{\rm m}$ at $t = 500$ for a $\beta = 4$ contraction comparing the predictions of an isotropic and anisotropic constitutive law: (a) $\phi(x)/\phi_{\rm m}$ at $y = 0$; (b) $\phi(x)/\phi_{\rm m}$ at $y = 1$; (c) $\phi(y)/\phi_{\rm m}$ at $x = 10$

is shown in Figure 62 and Figure 63. There is some difference between the predictions of the anisotropic and isotropic models in the mouth of the contraction, but not much. The anisotropic model predicts a slight drop in ϕ near the centerline and slight rise away from it, which is not predicted in the isotropic model. The anisotropic model also predicts a dip in ϕ right upstream of the convex corner. As for the effect of including an $N_{ct} = 0.2$ on the anisotropic model, the only significant effect seems to be in the amount of particles that accumulate in the convex corner region. The addition of $N_{ct} = 0.2$ appears to lower the amount of this accumulation which is most likely due to the increase in predicted vortex size.

5.5 Conclusions

In this chapter we illustrated how to adapt a rheological-based constitutive law developed for simple shear flows into a form which can be applied to general flow fields. The process involves modifying the particle phase stress constitutive law to take into account kinematic variations in the local flow field. By looking at the local balance in rotation to shear in the flow field, we characterized the kinematic state of the flow field and studied how such variations could effect the flow field or local composition of the suspension.

We chose to study the sharp-edged contraction flow as our initial test case due its varying local kinematics: pure extension at the contraction opening, simple shear upstream and downstream. First, looking at predictions for a purely isotropic model we explored how factors such as the contraction ratio or flow direction (contraction versus expansion) effected the model predictions. For the contraction flow (flow into the smaller channel), we found a build-up of particles along the contraction wall perpendicular to the flow direction, with the particle concentration approaching maximum packing in the corner. This was due to the fact that the particle migration flux pushed the particles away form the higher stress levels in the smaller channel. This resistance then allowed the particles to be swept up into the corner by bulk convective forces and deposited into the stagnant, recirculating flow in the corner. The amount of particle migration was found to be greater for the larger contraction ratio (large/small). In the expansion flow, the particle migration flux again

pushed the particles away from the higher stress in the smaller channel, but in this case the convective flux sweep the particles on downstream. This resulted in no build up in the corner region for the expansion flow.

For the isotropic constitutive law, we also compared predictions to an experimental contraction-expansion flow to which we achieved a qualitative match to the observed behavior. We matched an observed dip in the particle concentration at the mouth of the contraction and the lack of migration into the corner region for an expansion flow. In addition, we matched the increase in particle concentration in the center of the flow channel for the central region connecting the contraction and expansion.

To study the possible effect of complex flow conditions on particle migration, we looked at two alternate constitutive models. One in which the strength or magnitude of the isotropic particle normal stress increased in regions where the flow approached stronger extension flow conditions (such as at the entrance of the smaller channel in a contraction flow). Another in which we looked at the effect of an anisotropic particle normal stress, where the predicted particle normal stress was different for different local directions.

For the weighted-isotropic approach, we accounted for kinematic variations through the kinematic ratio ($\hat{\rho}_k$), a ratio of the local strength of rotation and to the local strength of shear. In this measure, an equal balance between rotation and shear is considered simple shear, while a rotationally dominated flow is considered solid body rotation and a shear dominated flow is considered pure extension. In our exploration, we found that by weighting the strength of the particle phase normal stress with local kinematics we could control particle concentration predictions at the entrance to the smaller channel in a contraction flow, an extensionally dominated region. The utility of this ability is a question that is still open, due to a lack of quantitative experimental evidence for this particular flow or any extensionally dominated complex flow field in general. What the work here enables is the ability to account for such behavior, if it proves to be significant, by utilizing a method which has been shown to work for polymeric flow field predictions.

For the anisotropic approach, we utilized a stress-based coordinate system to define the particle normal stress. The compression-tension coordinated proved a frame of reference

to define the relative magnitudes of our particle phase normal stresses in. We found that using an anisotropic stress law has a significant effect on the predicted flow field, especially on the size of the predicted stagnation or recirculation zone in a sharp-edged contraction flow. There was also an effect on the predicted particle field concentration that appeared to primarily result from the effect on the flow field. Again the validity of such an approach remains dependent on quantitative experimental evidence. This approach does provide, however, another tool for suspension flow modeling in complex flow fields. With further experimental evidence, it may prove to be significant or necessary for the accurate prediction of the flow fields or particle phase migration in a complex suspension flows.

The key to suspension flow study at this point lies with further experimental exploration augmented through the guidance of computational modeling. Computation modeling allows rapid exploration of multiple geometries and possibilities to help identify unique or interesting predicted behaviors. The identification of these possible behaviors can then provide a road-map to suggest which experiments would be the most interesting or significant to undertake. With further experimental study, the constitutive models developed here can be verified or deficiencies can be identified. Through this process, computational suspension flow modeling will be able to mature into a practical, valuable tool for use in many areas.

CHAPTER 6

COMPLEX GEOMETRY: APPLICATIONS

In this section, we explore the application of the solver-evolver code to a number of general, experimentally relevant flows. The object is to illustrate the utility of the solver-evolver code for comparison to experimental studies and its application to the design of processes involving suspension flow. In the past, a rigorously-based method to study the flow of two-phase, particulate suspensions through general geometries has not been available. There are a number of methods, as discussed in Chapter 1, using continuum approaches, but none that are immediately applicable to a broad range of complex flow conditions. The most general continuum models, such as the diffusive flux approach of Phillips et. al. (1992), tend to be oversimplified and cannot properly account for conditions such as anisotropic stress or varying local kinematics. Our method has been shown to work in the complex contraction-expansion environment, with some quantitative and qualitative matches to experimental data. In this chapter, we illustrate how this code is used in a general study. There is not a great deal of experimental data for the flows examined and thus modeling takes the lead. The predictions generated by the method allow us to explore the range of suspension issues which can be attacked with a continuum model implemented as a computational tool.

The solver-evolver method can be used for "computational suspension dynamics" (CSD) This means that we can explore a number of issues and features of a general flow, as can be done for Newtonian and non-Newtonian flows with a computational fluid dynamics (CFD) package. We explore the effect the suspended particles have on the streamlines and pressure conditions of the flow. We further consider how the evolution of the particle field changes these conditions and suggest what consequences this may have on design decisions or relevant pieces of complex processing equipment. In addition, the work allows one to predict the exit composition from processing flow geometries which may affect downstream processing conditions.

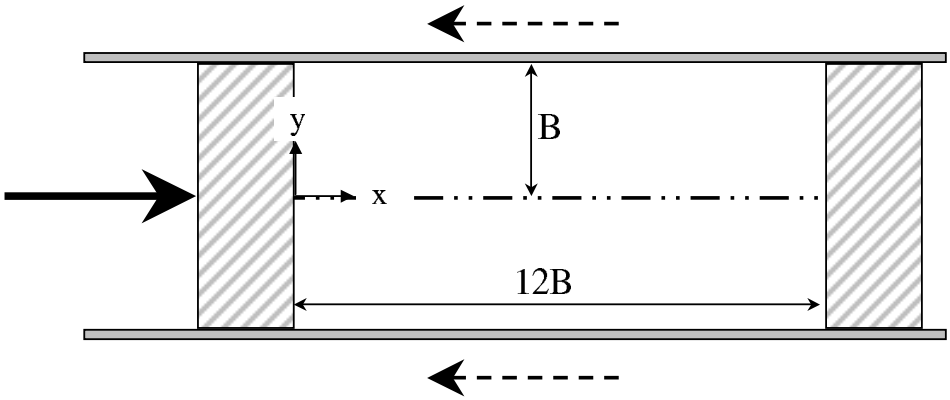

Figure 64: Sketch of the piston flow geometry.

We choose to explore the application of the solver-evolver code with an isotropic particle stress model for a rectangular piston-driven flow and a two-dimensional, rectangular, pressure-driven channel flow with an obstruction near the entrance. For both cases a value of $\alpha = 4$ was used for the sedimentation hindrance function and $\eta_s(\phi)$ was represented by the shear-viscosity model used in Morris and Boulay (1999). A shear-rate with an $O(\epsilon)$ nonlocal contribution, $< \dot{\gamma} >_\epsilon$, was used, as in Chapter 5. The nonlocal shear rate was determined by averaging the local shear-rate value over a circular area of radius ϵ around the computational point of interest, making this area comparable to the dimensionless particle size as $\epsilon = a/L_s$. For all cases, the entire domain was initially set to a bulk particle concentration of $\phi_{\rm B} = 0.50$. For scaling purposes, it is assumed $\phi_{\rm m} = 0.68$. The particle size chosen for both studies is $B/a = 16$, to match one set of the experimental conditions of Subia *et al* (1998) as explained in detail below.

6.1 Piston-driven suspension flow in a closed rectangular channel

We have modeled a piston-driven flow in a rectangular channel with both ends closed off by piston faces. This allowed a qualitative comparison with the experimental data of Subia *et al* (1998). In their work, they ran experiments for an axisymmetric piston-driven tube flow with a set-up similar to the one illustrated in Figure 64. The tube was filled with a particulate suspension and capped off at both ends. The downstream piston remained free

while the upstream piston was either: (1) fixed, while the tube walls were moved toward the fixed piston or (2) the walls were fixed while the upstream piston was driven forward. In both cases the moving surface was at a velocity of 0.0625 cm/s, corresponding to $Re \ll 1$ conditions.

The experimental apparatus was a circular pipe with an inner radius of 2.54 cm. The suspension consisted of neutrally-buoyant, spherical particles at an initial bulk concentration of 50 vol% with particle diameters of 678 μm and 3178 μm (corresponding respectively to $R/a = 75$ and 16). The initial volume of suspension in the tube corresponded to a length of 30 cm ($12R$) between the two piston surfaces. Measurements of the concentration were taken by placing the whole apparatus into the bore of an NMR magnet in order to take static images along the length of the domain after the piston/wall had travelled a given distance. Results were reported after 5 piston diameters ($10R$) of travel in the form of a radial average of ϕ at axial distances along the pipe length. From static NMR images, a liquid-rich region was observed next to the moving piston near the centerline. This result was also observed near the piston face in the experiments of Altobelli *et al* (1997).

We ran a 2-D numerical simulation of the above piston flow by setting the end walls stationary and moving the side walls. We assumed no-slip conditions at the walls for the velocity field and no penetration for the particle field, which corresponds to setting the migration flux normal to the wall equal to zero. The domain was discretized as illustrated in Figure 65. The grid was refined in the axial direction near the two end caps. This refinement corresponded to $dx = 0.1$ with $dx = 0.5$ throughout the rest of the domain. In the radial or cross-stream direction, the domain was refined around the centerline and near the walls. This corresponded to $dy = 0.05$ in the refined regions and $dy = 0.1$ through the rest of the domain.

6.1.1 Results and discussion

The flow solution is shown in Figure 66 for the rectangular piston-driven flow before any particle migration has occurred (i.e. constant viscosity conditions). The streamlines form

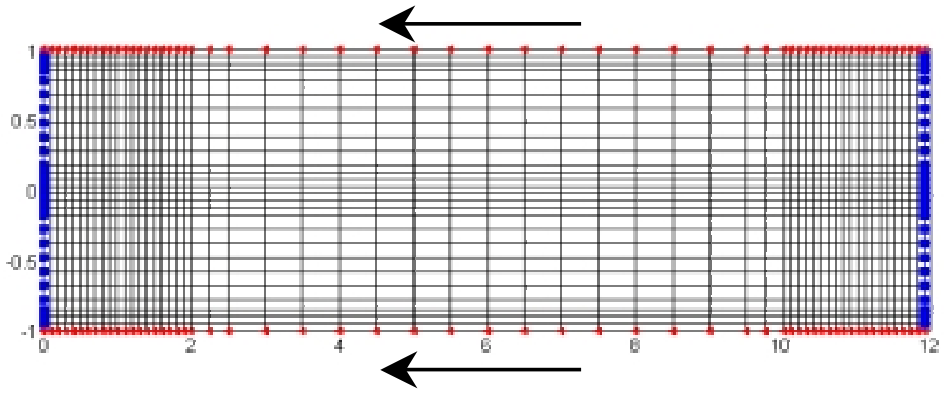

Figure 65: Computation grid used for the piston-flow geometry.

a bulk recirculation, with a sharp bend at the corners by the piston faces. If the end-caps were moving and side walls fixed, this would be a bulk recirculation relative to that forward movement. The evolution of the particle volume fraction due to migration is given in Figure 67 after 5, 10, and 15 diameters ($10B$, $20B$, $30B$) of piston travel. The model predicts migration away from the side walls and toward the center of the channel. This qualitatively matches the NMR images in Subia *et al* (1998), as does the decrease in particle concentration near the upstream piston and increase near the downstream piston. As stated before, the decrease near the upstream piston was also observed in the piston driven contraction-expansion flow of Altobelli *et al* (1997).

In Figure 68, a plot of $< \phi/\phi_{\mathrm{m}} >$ (averaged over the cross-sectional area) along the axial length of the domain is given for 5, 10 and 15 piston diameters ($10B$, $20B$, $30B$) of travel. In addition, experimental measurements from Subia *et al* for an axisymmetric flow after 5 diameters of piston travel are included. While not a quantitative match (considering the differences between planar and axisymmetric conditions), they do display the same qualitative behavior with the dip near the upstream piston and rise at the downstream one. The main quantitative difference between the rectangular and axisymmetric cases is the increased particle migration observed in the axisymmetric piston flow as opposed to the migration predicted for the rectangular piston flow.

The key question is why does this drop/rise in particle concentrations at the two piston

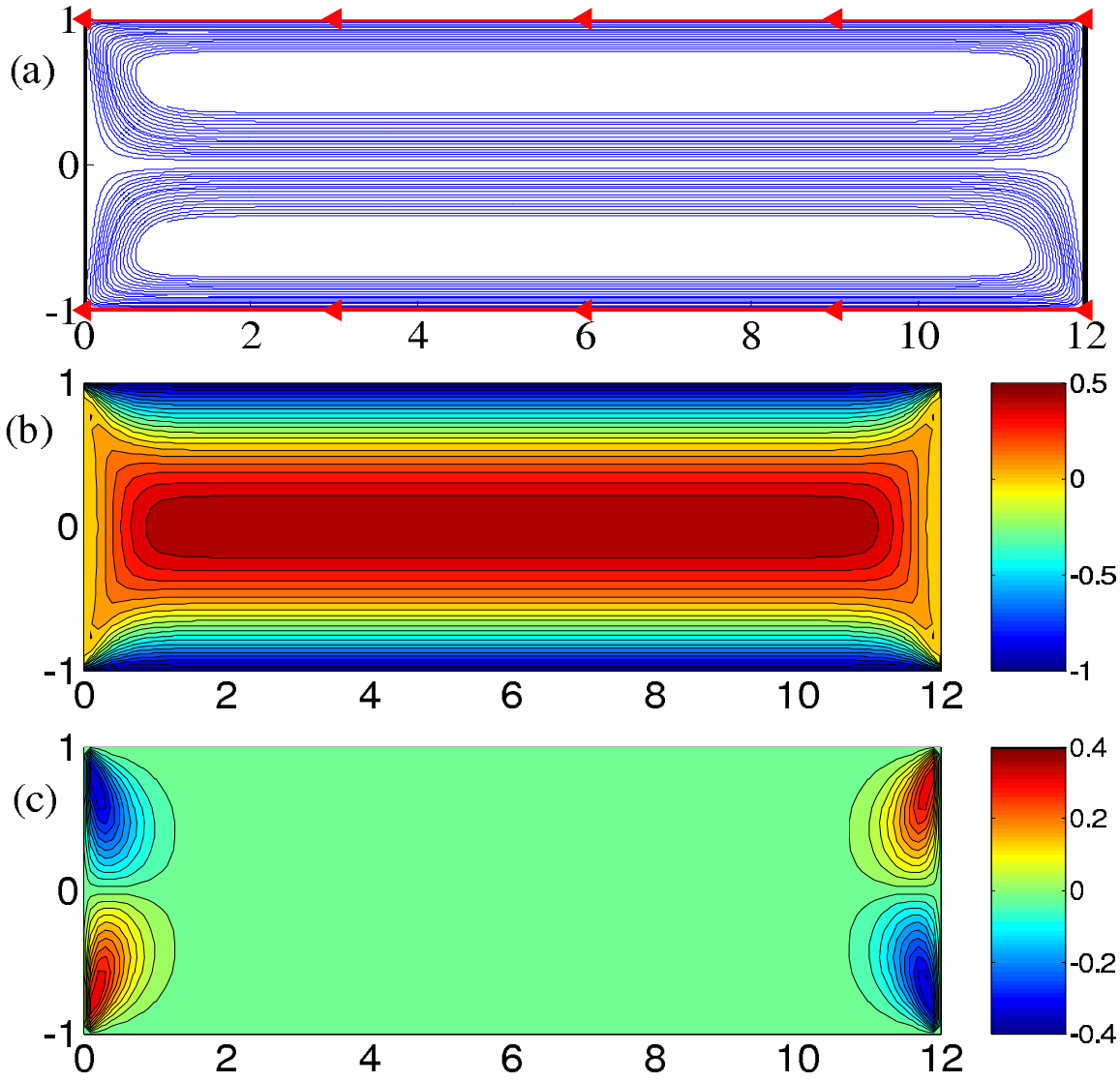

Figure 66: Initial flow solution (unform particle concentration) for a rectangular piston-driven flow with suspension conditions of $B/a = 16$, $[\phi/\phi_{\mathrm{m}}]_{bulk} = 0.735$. (a) streamlines; (b) axial velocity; (c) cross-stream velocity.

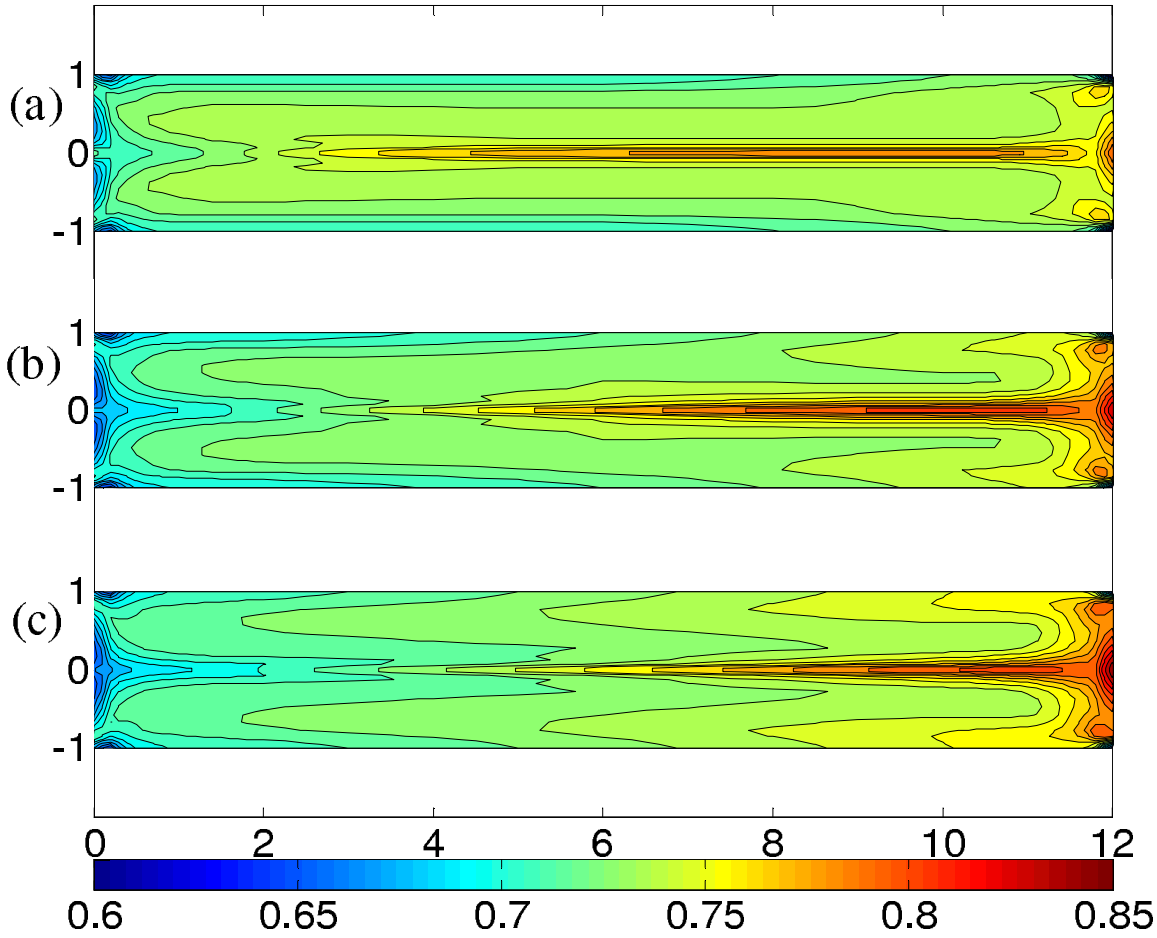

Figure 67: Plots of the evolution of ϕ/ϕ_{m} for suspension conditions of $B/a = 16$, $[\phi/\phi_{\mathrm{m}}]_{bulk} = 0.735$ after the piston has travelled: (a) 5 diameters ($10B$); (b) 10 diameters ($20B$); (c) 15 diameters ($30B$).

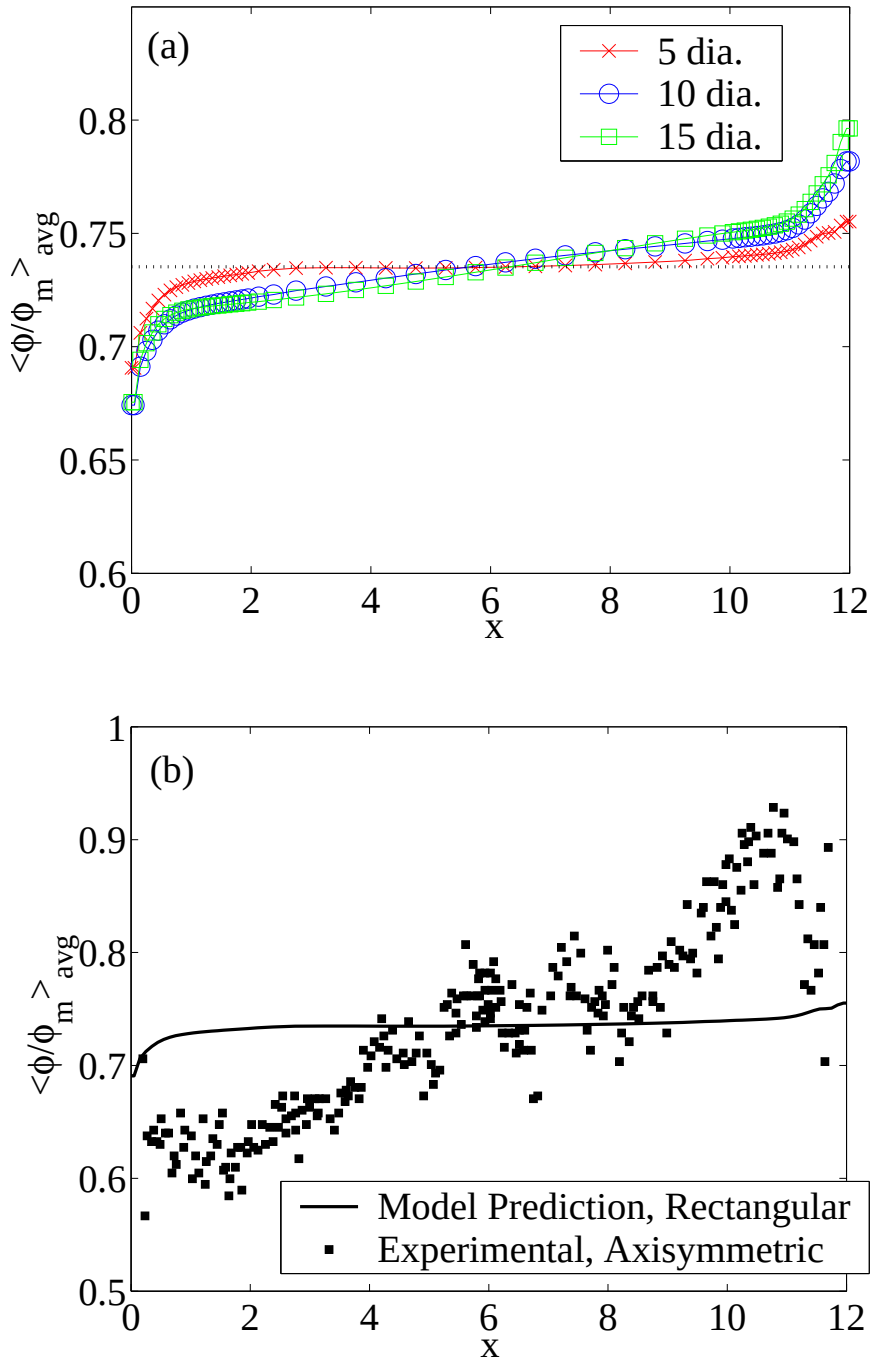

Figure 68: Plots of (a) model predictions for the area averaged value of $\phi/\phi_{\rm m}$ for suspension conditions of $B/a = 16$, $[\phi/\phi_{\rm m}]_{bulk} = 0.735$ along the axial length of a rectangular piston flow. Plot (b) is a comparison of the model prediction after 5 diameters of piston travel with the experimental results of Subia *et al* (1998) for an axisymmetric piston flow at the same conditions.

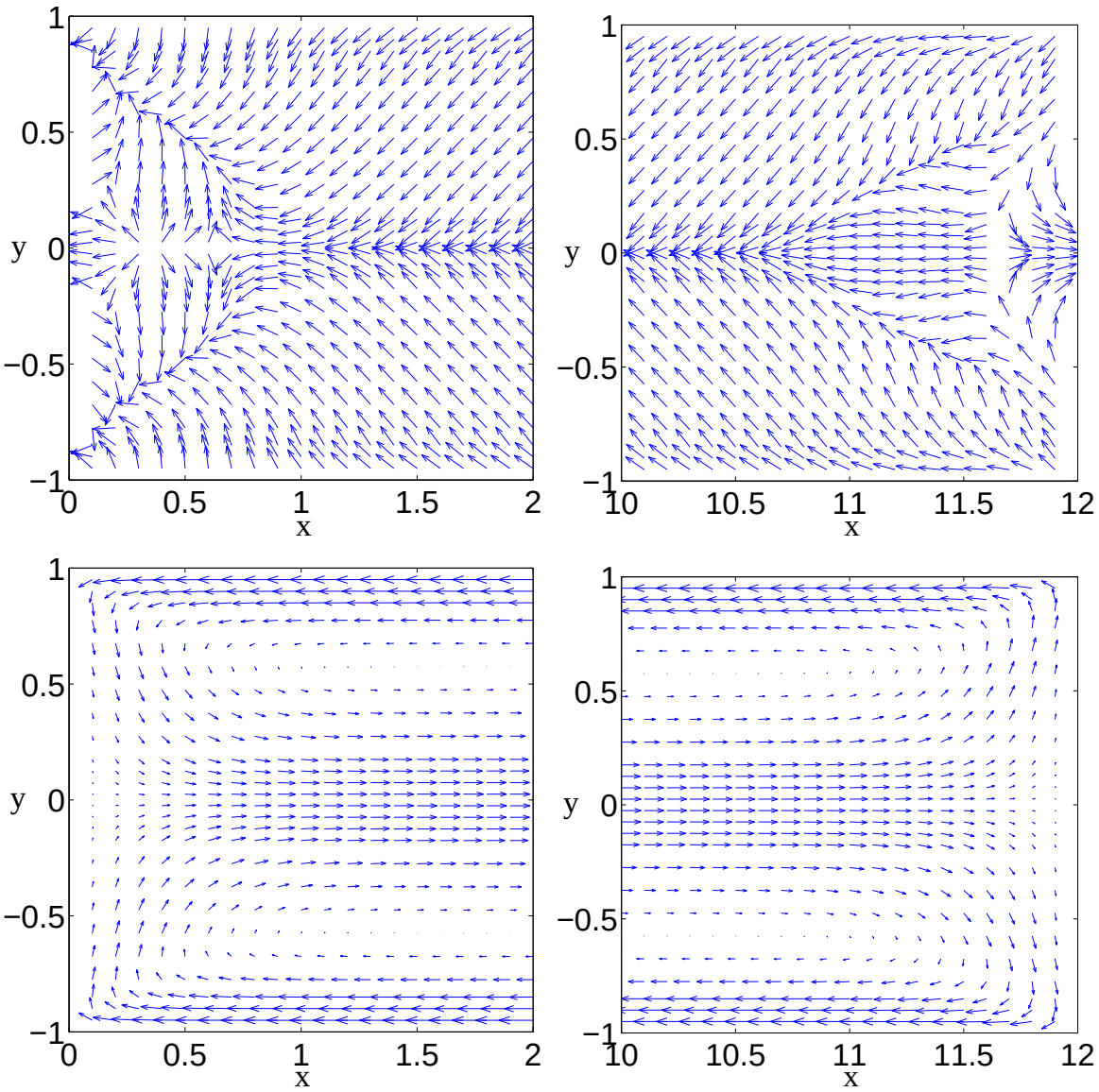

Figure 69: Plots of the direction of the particle migration flux, $\mathbf{j}_\perp$, (unit vectors) and the direction of the flow at the upstream and downstream piston faces.

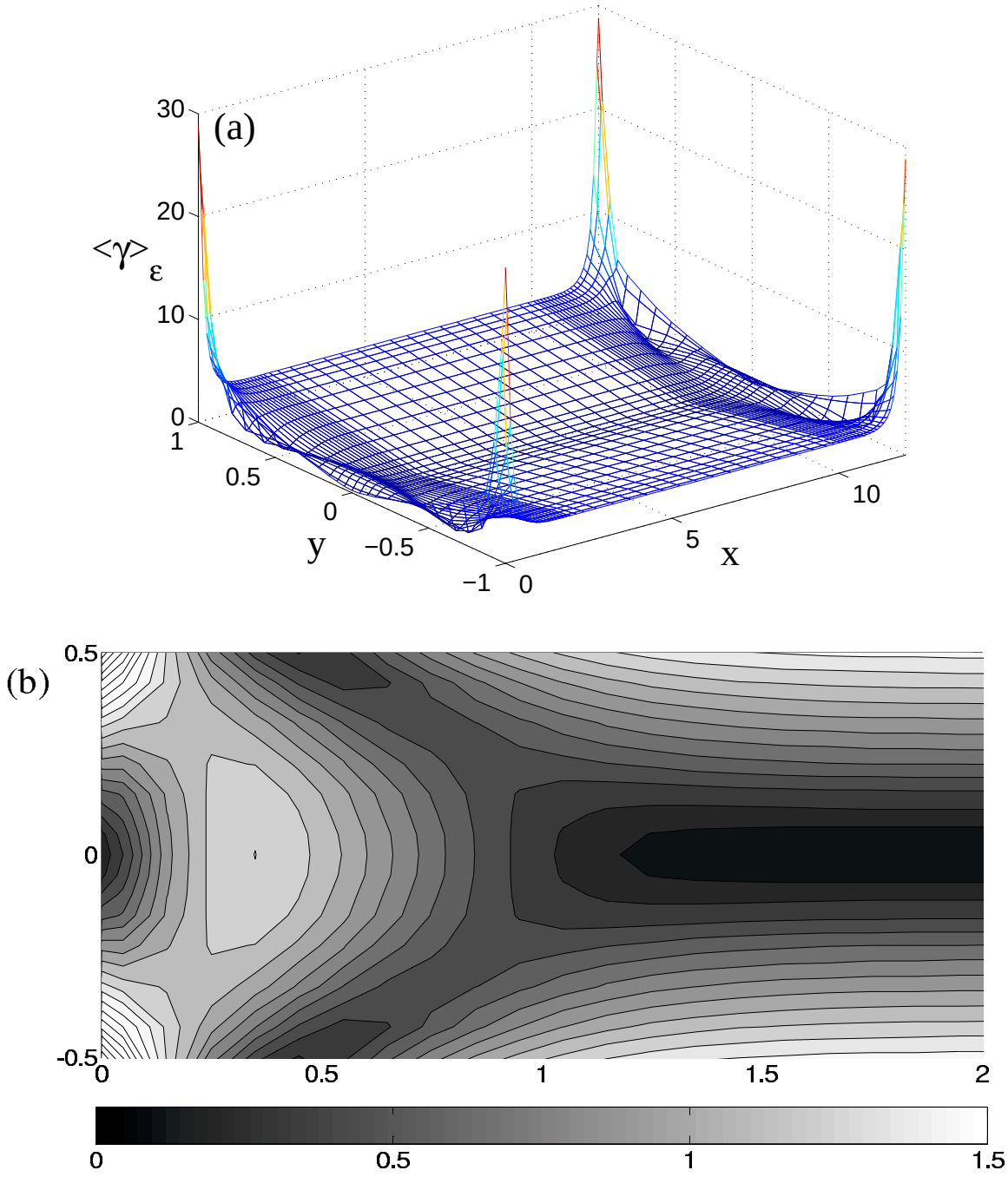

Figure 70: Plots of the nonlocal shear rate at the initial, uniform particle concentration conditions. (a) Surface plot of $< \dot{\gamma} >_\epsilon$ over the entire domain; (b) Close up of $< \dot{\gamma} >_\epsilon$ contours at the center ($-0.5 < y < 0.5$) of the channel next to the upstream piston ($0 < x < 2$).

surfaces occur. Looking at the plot of the particle migration flux vectors (set to unit size) at the initial conditions (i.e. before particle migration has begun), in Figure 69(a,b), it can be noted that the vectors are similar at each end-cap, except for their opposition to the bulk flow, given in Figure 69(c,d). It is this opposition of the particle migration flux to the bulk flow which causes the difference in migration behavior at the two faces. At the upstream face, since the flow is coming from the side walls toward the centerline, the particle migration flux slightly opposes this resulting in a depletion in particles at the centerline. The opposite holds true at the downstream piston, where particle migration opposes the flow toward the outer wall from the center which causes the slow build up of particles at this piston face. The surface and contour plots of the nonlocal shear rate in Figure 70 illustrates the driving force behind the particle migration flux, with particles migrating "downhill" away from peaks in $< \dot{\gamma} >_{\epsilon}$. The plot shows a very large shear-rate in the corners, which leads to a depletion in particles in these regions. In addition, there is an increase in shear rate right next to the piston surfaces but not right on them. This predicted "hump," illustrated in the close-up contour plot of the upstream piston, further drives the depletion/build up at the surfaces, since the "hump" will add resistance to the particle migration toward/away from the upstream/downstream piston surfaces.

6.2 Pressure-driven suspension flow in a rectangular channel with an obstruction near the entrance

The problem domain for studying a pressure-driven, two-dimensional, rectangular channel flow with an obstruction near the entrance is illustrated in Figure 71. We look at cases where the obstruction is square in shape with each side equal to the channel half-width (B). The center of the obstruction is placed a length 10B from the entrance and the domain is initially set to a bulk particle fraction of 0.50 everywhere. The inlet is held at this bulk value throughout the run and the velocity field is set to a unidirectional parabolic inlet condition. The distance beyond the obstruction is set to a length of 100B to look at the effect that the obstruction has on the axial development of the $\phi(y)$ field. At the outlet all normal gradients are set equal to zero while the pressure is set to zero in order to provide

a reference value. All solid surfaces are assumed to be no-slip, with no particle penetration ($\mathbf{j}_\perp \cdot \mathbf{n} = 0$).

We explore two separate cases, one where the obstruction is placed at the center of the channel ($b_1/b_2 = 1$). This corresponds to two gaps that are a quarter of the width of the channel, $B/b_1 = B/b_2 = 2$. In the second case, the obstruction is placed off-center by a distance of $B/4$ ($b_1/b_2 = 1/3$), corresponding to a narrow gap ratio of $B/b_1 = 4$ and wide-gap ratio of $B/b_2 = 4/3$.

The domain is discretized as illustrated in Figure 72 for the off-centered obstruction ($b_1/b_2 = 1/3$). The grid spacing in the axial direction is refined near the obstruction to a value of $dx = 0.1$, with $dx = 1.0$ through the bulk of the domain. The grid is also refined in the cross-stream direction near the corner of the obstruction on the wide-side and throughout the entire region of the narrow gap. The refined step size is $dy = 0.05$, with $dy = 0.1$ throughout the rest of the region.

6.2.1 Results and discussion

The streamlines for the centered ($b_1/b_2 = 1$) and off-centered ($b_1/b_2 = 1/3$) obstruction are shown in Figure 73. For the off-centered obstruction, the majority of flow passes through the larger opening, as is illustrated in the plots of the nonlocal shear rate in Figure 74. The majority of shear takes place near the wall of the larger opening, corresponding to a stronger flow field through this gap. For the centered-obstruction case, it can be seen that the flow and stress fields are symmetric.

The migration of the particle field shown in Figure 75, shows a build up of particles on the upstream side of the obstruction in both cases with a depletion on the downstream side, as would be expected. For the off-centered obstruction ($b_1/b_2 = 1/3$), there is a sharp peak in ϕ/ϕ_m in the center of the small gap, but this quickly dissipates as the suspension leaves the gap. An interesting prediction to note is a zone of depleted particle concentration that forms near the wall downstream of the obstruction. This depleted zone does not continue downstream though, but remains local to the obstruction. Instead the bulk flow sweeps past it and returns the ϕ value near the wall to a higher concentration until the migration

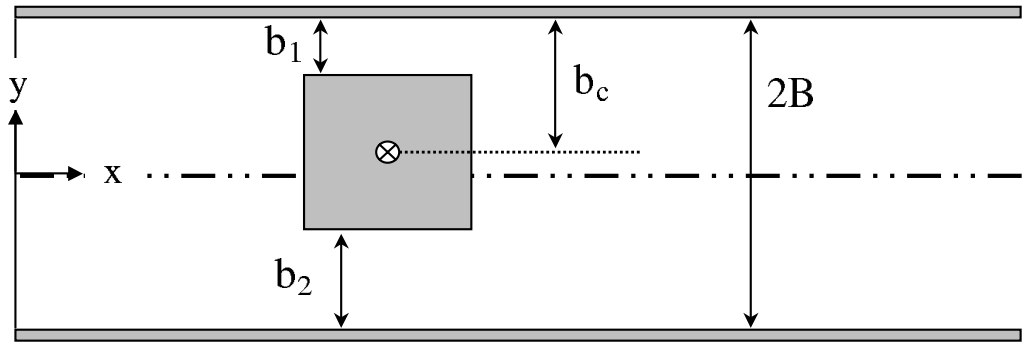

Figure 71: Sketch of a channel with an obstruction.

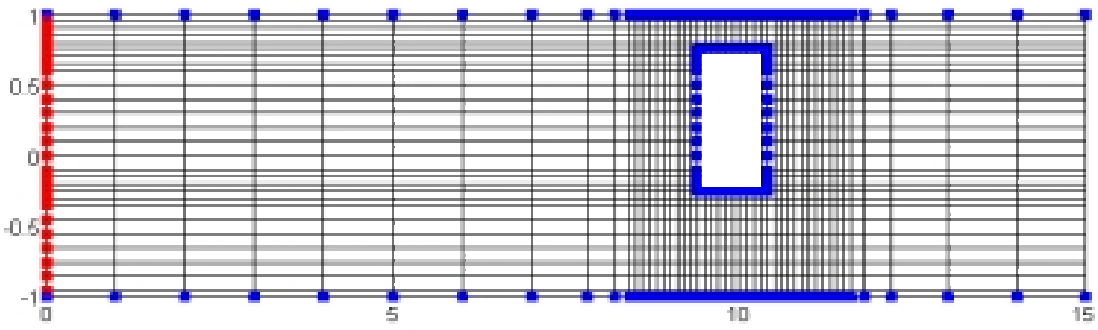

Figure 72: Computational grid for a two-dimensional, rectangular channel with an obstruction, $b_1/b_2 = 1/3$.

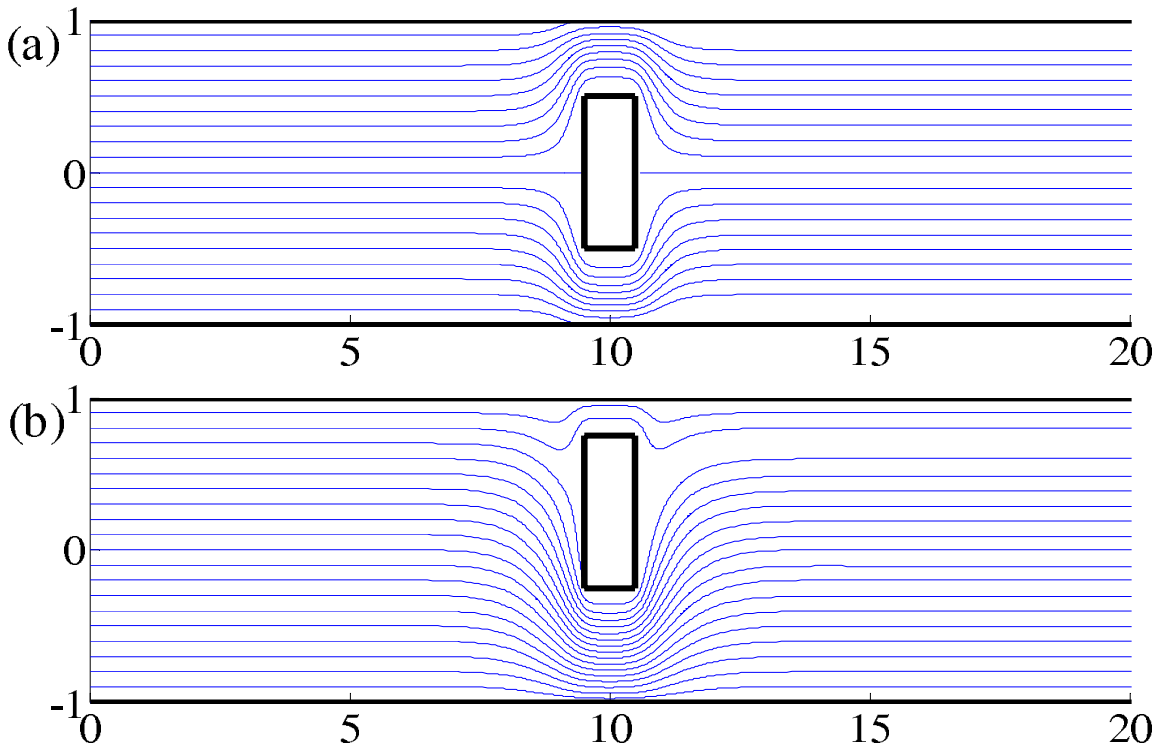

Figure 73: Streamline plots for a channel flow with an obstruction located: (a) center ($b_1/b_2 = 1$); (b) off-center ($b_1/b_2 = 1/3$).

approaches the typical pattern for a channel flow, with a depletion of particles near the wall and an increase of particles at the centerline, as is illustrated in Figure 76.

In the full domain contour plots of ϕ/ϕ_{m} in Figure 76, the particle migration pattern quickly resumes that of an unobstructed channel, with most of the effects of the obstruction on particle migration remaining close to the obstruction. In the line plots of Figure 77 and Figure 78, this is further illustrated. The migration appears to resume the typical pattern of the axial development of the $\phi(y)$ profile for a channel flow by about a length of $5B$ ($x = 15$) downstream from the center of the obstruction. In Figure 78(b), it is evident that by about a distance of $45B$ ($x = 55$) downstream from the center of the obstruction the migration has completely resumed the pattern of the unobstructed channel flow. In this plot, one may note that the three predicted solutions do not appear to match at the centerline of the flow. This is due to grid spacing differences between the $b_1/b_2 = 1$ and $b_1/b_2 = 1/3$ obstruction runs. In the meshing scheme for the off-centered obstruction, no computational node was placed on the $y = 0$ centerline, which resulted in differences in the averaged shear-rate in

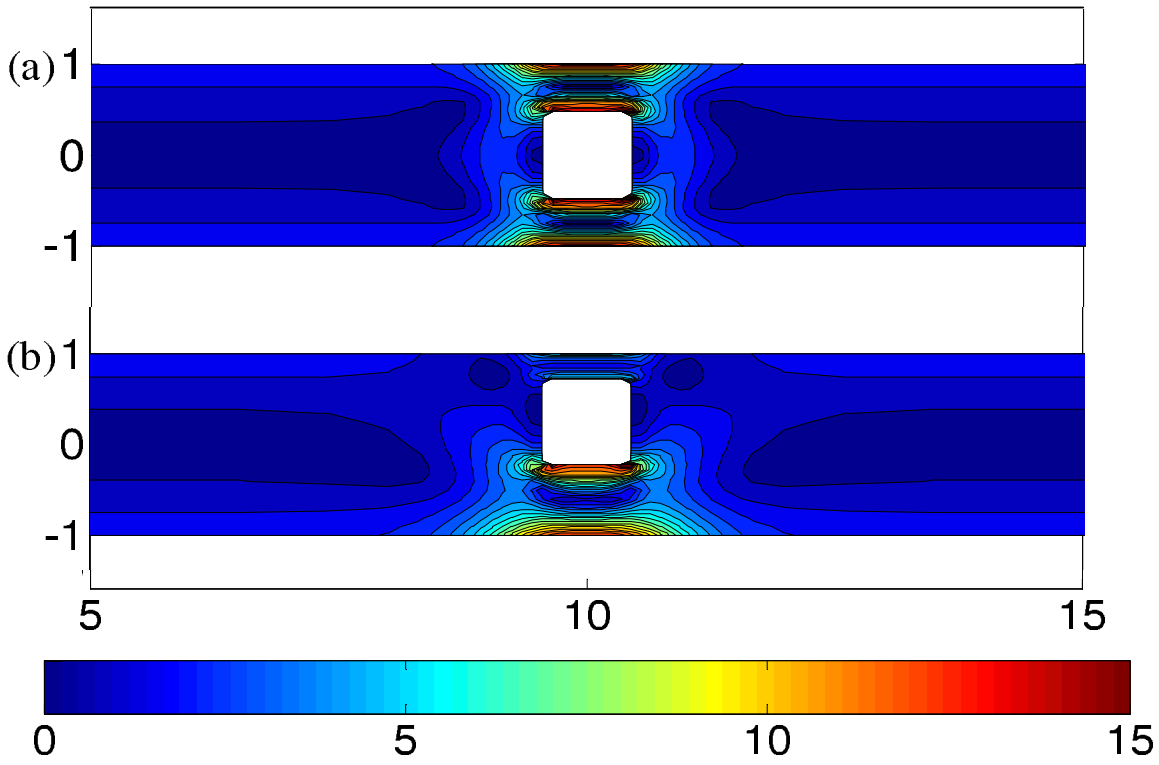

Figure 74: Plots of the nonlocal shear rate for a channel flow with an obstruction located: (a) center ($b_1/b_2 = 1$); (b) off-center ($b_1/b_2 = 1/3$).

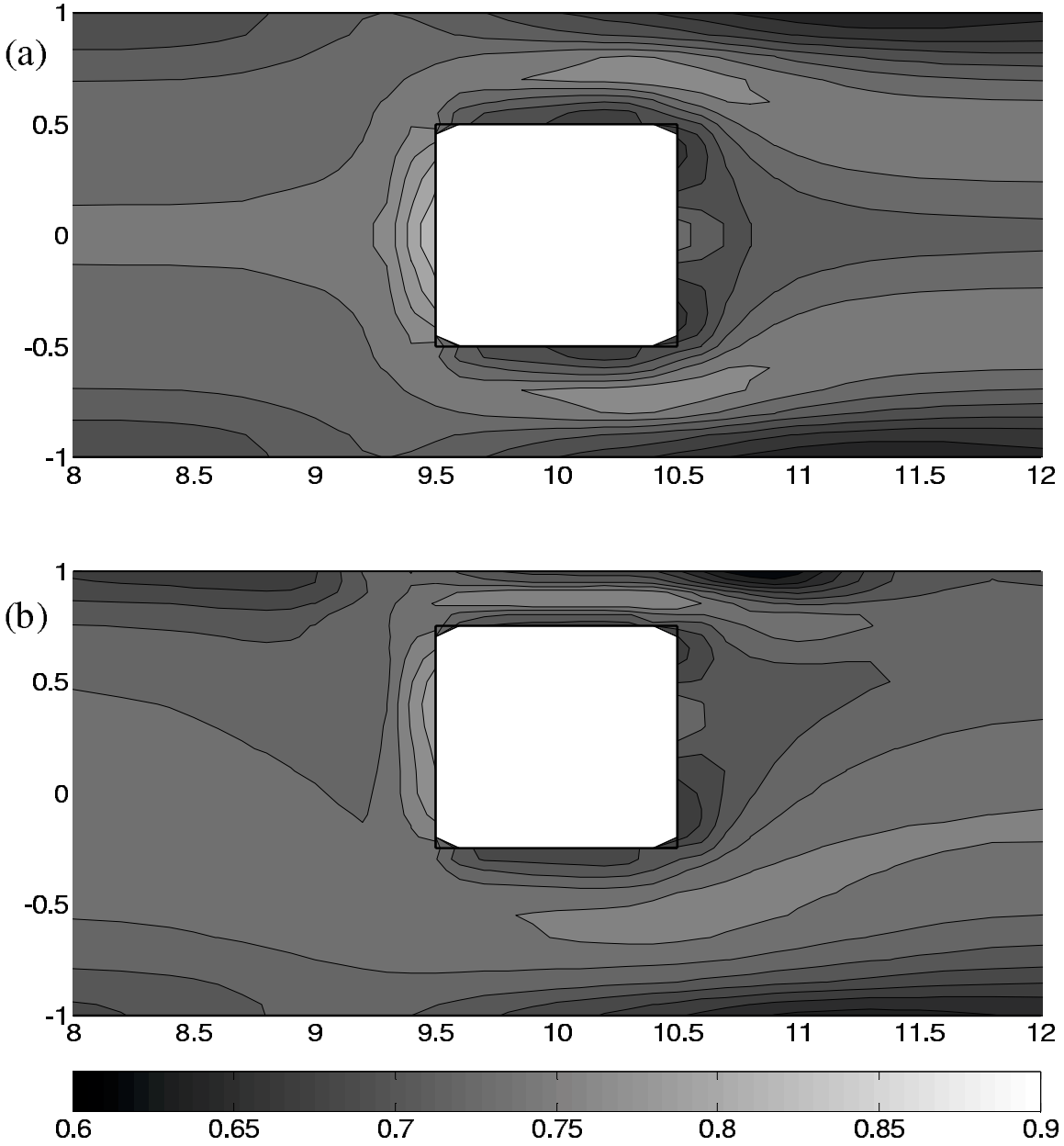

Figure 75: Plots of ϕ/ϕ_{m} at steady-state for: (a) centered obstruction ($b_1/b_2 = 1$); (b) off-centered obstruction ($b_1/b_2 = 1/3$).

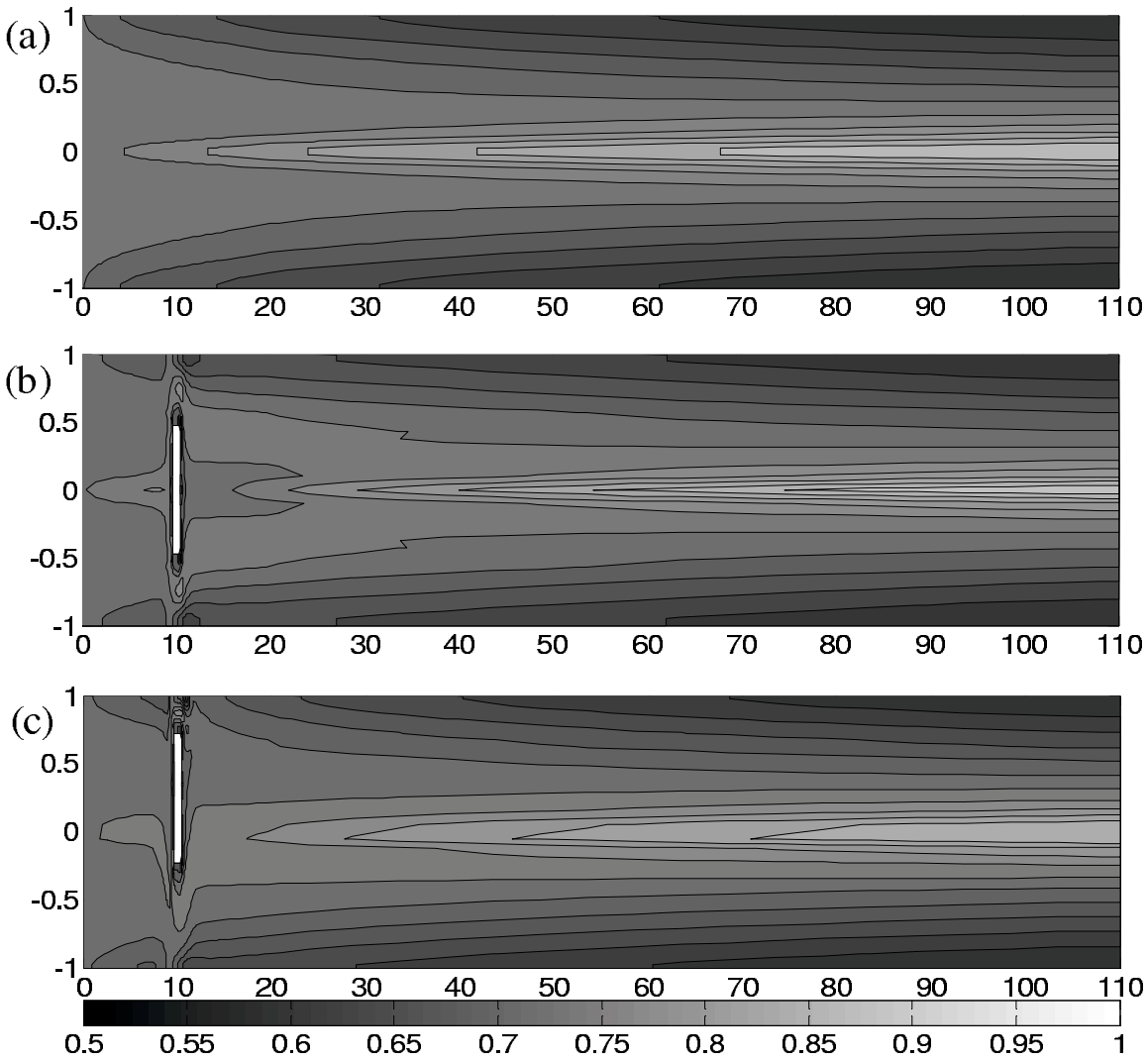

Figure 76: Plots of ϕ/ϕ_{m} at steady-state for: (a) no obstruction; (b) centered obstruction ($b_1/b_2 = 1$); (c) off-centered obstruction ($b_1/b_2 = 1/3$).

this region. A final point to note is that the off-centered obstruction appeared to have less effect on the migration and resulted in a quicker recovery to unobstructed conditions.

The values of the predicted inlet pressure conditions before and after particle migration are presented in Table 7. The data shows that the unobstructed channel required the least amount of pressure to drive the flow field. The off-centered obstruction requires a higher inlet pressure with the centered obstruction requiring the highest. For all cases the particle migration resulted in a lower predicted inlet pressure.

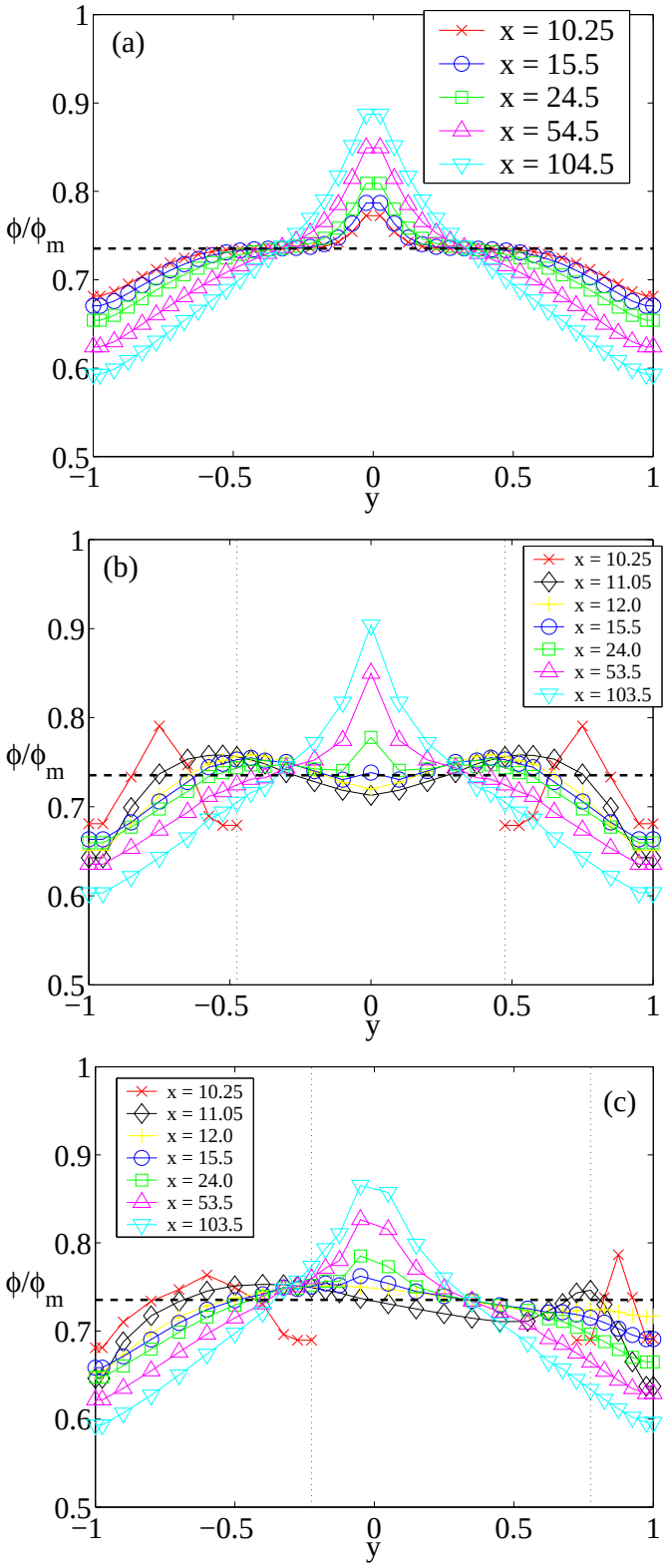

Figure 77: Plots of $\phi(y)/\phi_{\rm m}$ at various points downstream of the obstruction (square obstruction, $1B$ side length, centered at $x = 10B$) for: (a) un-obstructed channel; (b) centered obstruction ($b_1/b_2 = 1$) in a channel; (c) off-centered obstruction ($b_1/b_2 = 1/3$) in a channel.

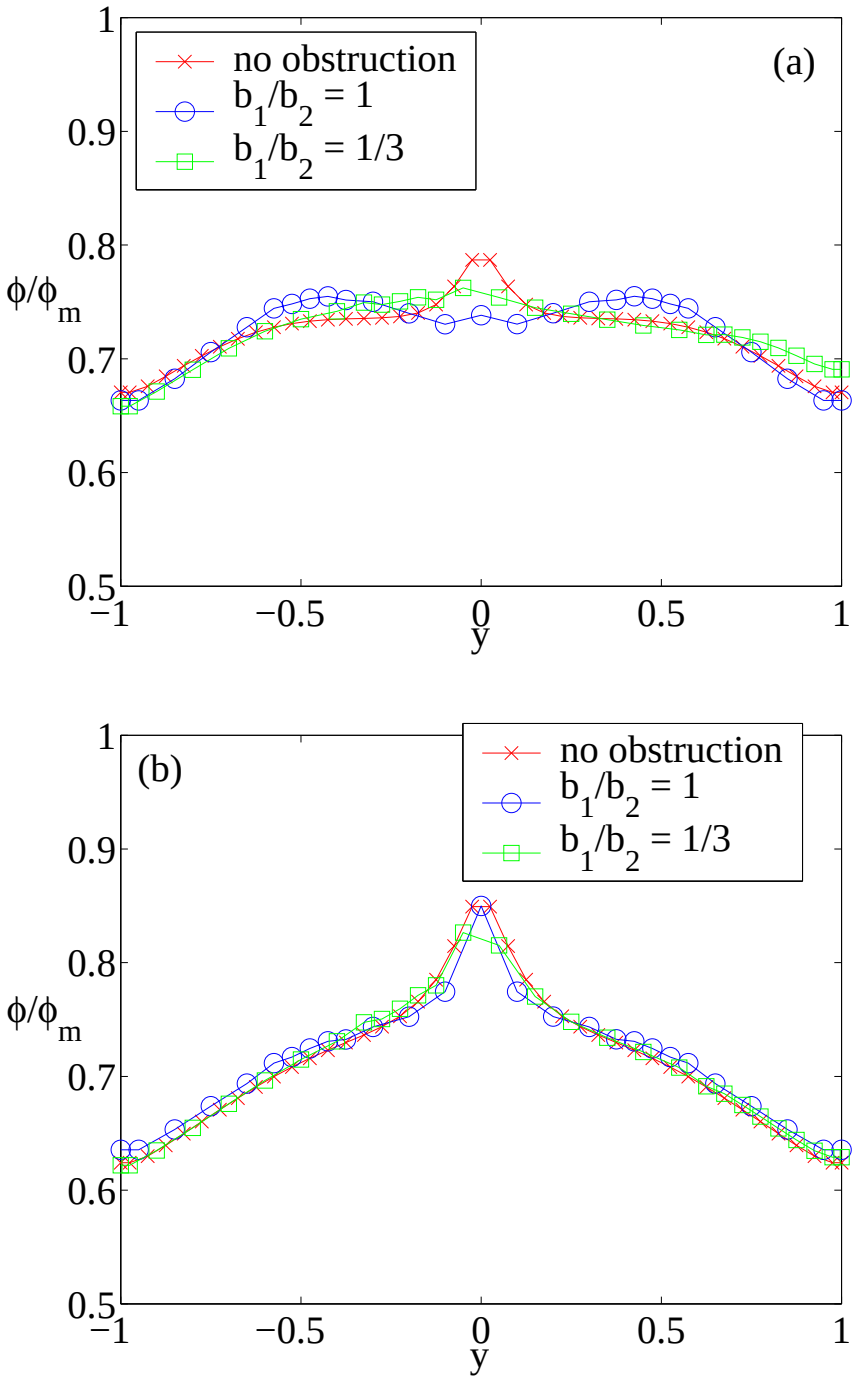

Figure 78: Comparison of $\phi(y)/\phi_{\mathrm{m}}$ at (a) $x = 15.5B$, (b) $x \sim 55B$, for a rectangular channel flow of length $110B$ with no obstruction to a rectangular channel flow with a square obstruction $10B$ downstream from the inlet with b_1/b_2 ratios of 1 and 1/3.

Table 7: Predictions for the inlet pressure, $P^* = P/(\eta_o U_s/B)$, before and after particle migration has occurred. The reported position of the obstruction is the distance from the inlet of the channel to the center of the obstruction. Model conditions: $\alpha = 4$, $[\phi/\phi_m]_{bulk} = 0.735$, $\phi_m = 0.68$, $B/a = 18$.

	Obstruction		P* Inlet	
Length	Dist. Inlet	b_1/b_2	t = 0	t = 500
110B	---	---	1,405	1,057
110B	10B	1.00	1,965	1,591
110B	10B	0.33	1,769	1,405

6.3 Conclusions

We used the solver-evolver code for CSD, specifically to study suspension flow behavior in a closed piston-driven channel flow and a pressure-driven channel flow with an obstruction near the entrance. These represent just a sample of the flows which can be studied with a computational tool able to predict particle migration and bulk suspension flow in general geometries. While only predictions for the basic isotropic particle stress have been considered, these illustrate the type of information available from this modeling approach and the model can be generalized to include stress anisotropy, if so desired.

For the piston-driven flow, the model predictions provide the basis for accumulation of particles at the downstream piston face and depletion at the upstream piston face. By showing how the predicted particle migration flux vectors oppose the recirculation of the bulk flow in Figure 69, a possible mechanism for this nonintuitive experimental observation (Subia *et al*, 1998; Altobelli *et al*, 1997) is revealed. Furthermore, model predictions of the shear rate in Figure 70 illustrate an unusual pattern of shear next to the upstream piston which further supports the prediction and observation of this behavior. For the channel flow with an obstruction, the differences between identical centered and off-centered obstructions are explored. It is found that the off-centered obstruction causes less disruption in the flow field and the axial development of the particle concentration profile. The off-centered obstruction also results in less of an increase in the inlet pressure than the centered obstruction, when compared to an un-obstructed channel flow. The data can be used to

predict how far downstream the effect of the obstruction is relevant on the particle phase composition or bulk flow field.

In this study, the solver-evolver was able to provide some insight into two general flows. This use of "computational suspension dynamics" or CSD is one that can be developed in the future with the addition of further experimental data for suspension flows in complex geometries. As more data becomes available for validation purposes, the model can be fully explored and verified or revised for a wider range of conditions, including those requiring anisotropic stress relationship or kinematic weighting of the model parameters to properly predict the experimental observations. With further verification, the model can be extended to completely general flow conditions and possibly packaged as part of a enhanced CFD solver.

CHAPTER 7

FUTURE DIRECTIONS

This work set up a framework to guide the study of suspension flows through the use of numerical modeling. We built a numerical tool which can be used to model suspension flows in general geometries. This was done by implementing a general geometry flow solver which could take into account spatially varying viscosity. The particle migration solution was then coupled to this flow solver through an iterative approach. This approach involved solving for the flow field at a give particle volume fraction field and then using the new flow field to update the particle volume fraction field through the particle migration equation. This allows the migration solution to be used with other, more powerful computational fluid dynamics (CFD) solvers, if the need arises.

The key to formulating a "general" geometry particle migration solution was in the set-up of the particle stress constitutive model. Previous to this work, most suspension flow models were tested in and limited to simple shear flows. In this work, we illustrated some of the critical parameters to forming a frame invariant particle stress constitutive model. Exploring parameters dealing with the local kinematics of a general flow field, such as the kinematic ratio ($\hat{\rho}_k$) which is a measure of the balance of local rotation to shear, we illustrated a systematic way to extend a model proposed for simple shear suspension flows to general geometry conditions.

Now that a general suspension flow model has been developed, the next greatest need in the area of suspension flow study is further experimental work. If data were available for a wider range of suspension flow conditions, the solver-evolver tool could be used to greatly increase the understanding of the phenomena of shear-induced phase segregation in solid-liquid suspension flows. With each new flow studied, the assumptions of the model could be tested and verified or disqualified. This would allow the formation of an appropriate scope for the application of the suspension flow model.

This work resulted in the development of a frame invariant normal stress based rheological model for the study of concentrated particulate suspension flows. Here we have explored how this fits into the current state of suspension flow research by first exploring the relationship between experiment, simulation and rheology in Section 7.1. Next, we look at how the solver-evolver computational tool can be used effectively in the study of suspension flows in Section 7.2. Finally, we look at ways that additional capabilities can be added to the suspension flow model in Section 7.3 and wrap up the discussion with some conclusions in Section 7.4.

7.1 Experiment, Simulation and Rheology

The use of experiment, simulation, rheology and continuum models forms the core of suspension flow research. While we have looked extensively at the use of continuum-based particle migration models, how this fits in with the other three is extremely important.

Experimental work represents the much needed look into "reality" that is needed for any modeling approach. Verification of the model predictions with real world data brings confidence that the modeling approach is appropriate and that the assumptions used are valid. While experimental work is important, it is not the only means to provide model verification or gain insight into suspension flow behavior. Simulation and rheology also provide key tools for this process.

Simulation represents a numerical "experiment." The suspension is studied by rigorously tracking individual particles and using first principles to predict the effect of a bulk flow field on their relative positions, as well a their effect on each other. One such method is Stokesian dynamics, outlined in a paper by Brady and Bossis (1988). Simulations present key information that is not easily accessible in a real-world experiment. They allow access to stress data, particle correlation functions and large-scale structure formation. This data can help provide insight into the form that a constitutive model should take on and had a major part in the formation of the constitutive model used here (Nott and Brady, 1994; Morris and Boulay, 1999).

Rheology, which is also an experimental approach, is more diagnostic in nature rather

than an exploration of new territory. Rheology contains a tool-set of basic, well defined flow fields used to extract data to quantify the behavior of a complex fluid. It has been used extensively in the study of polymeric suspensions and other non-Newtonian fluids. Rheological flows measure key modeling constants and parameters that make up most non-Newtonian constitutive laws. In the same manner that the viscosity must be measured to model the flow of a Newtonian fluid, for a non-Newtonian fluid there are a set of parameters that must be known. These include things such as the $\dot{\gamma}$ dependence of the viscosity or the existence of directionally dependent or anisotropic normal stresses.

Anisotropic normal stresses result in a difference between the stress in different directions and is behind some of the more unusual behaviors observed for non-Newtonian fluids. The terms N_1, N_2 represent the normal stress differences observed in a simple shear flow. N_1 is the difference between the stress in the flow direction and stress in the gradient direction with the directions defined as in Chapter 2. N_2 is the difference between the stress in the gradient and vorticity directions. Rheological flows provide a means to capture the $\dot{\gamma}$ dependence of these term, as well as the ϕ dependence for a suspension flow.

For extensionally dominated or "shear-free" flows, there are usually separate sets of experiments used to measure suspension flow behavior. In addition, there are separate sets of parameters to quantify. This is because traditionally there have been two separate sets of constitutive models for the two flow regimes, shear and shear-free. In our work, we must take advantage of both "end-points" on the spectrum and rely on local kinematic measurements to interpolate between the two.

Rheology therefore provides a very power tool in suspension flow study. It helps to provide suspension dependent parameters that can be measured under controlled conditions and then used to model more complex phenomena. While suspension rheology has proved to be problematic, there are some newer techniques such as the parallel-ring geometry (Kolli, Pollauf and Gadala-Maria, 2002) which have helped to get over the difficulties and shed light into this area.

7.2 Using the Solver-Evolver

With the support of experimental study, rheological observation and simulation results, continuum modeling is a very power tool for the study of suspension flows. With a properly verified modeling approach and constitutive relationship, new flows can be studied and current results can be extrapolated out to provide insight into potential flow configurations for experimental devices or point out shortcomings in current flow configurations. The solver-evolver provides the ground work for such a computational tool. With the finite-volume method (FVM) used to discretize the governing equations and the coupled flow-migration solution, this tool proves to be flexible to a number of geometries and conditions. Furthermore, the migrator portion can even be split off and used with other another flow solver, including current commercial applications.

For a commercial application to be compatible there are only a few basic requirements that would need to be in place. The commercial flow solver must allow a systematic iterative solution such as the solver-evolver approach. This means that the commercial solver must allow an outside or custom set of equations to update critical fluid parameters between each time step or steady-state solution. The flow field would also have to allow the use of user-defined, spatially varying viscosity functions, along with user-defined source terms. All-in-all, for any flow solver capable of handling current non-Newtonian constitutive laws for polymer solutions, these requirements should be relatively standard.

In itself, the solver-evolver provides a ready-made suspension flow solver for anyone with a copy of MATLAB and a basic knowledge of how to use it. Beyond this, it provides a foundation and starting point for the development of a viable commercial application or plug-in to a commercial CFD solver.

7.3 Extending the Particle Stress Constitutive Model

The key aspect of the suspension flow model is that it is stress based. This means that any modification to the assumptions and requirements of the model will first involve measuring the stress of this new "type" of suspension on a basic rheometer and seeing how the viscosity and normal stress differences (N_1, N_2) are effected by changes in the shear-rate ($\dot{\gamma}$) and

particle volume fraction (ϕ). After exploring basic shear-flow behavior, tests need to be run for shear-free (extension) flow conditions. This allows the determination if the model is fundamentally able to handle the new "type" of suspension with a minor modification in the form of the viscosity model or if a more fundamental modification must be made. By basing the suspension modeling approach on a particle stress constitutive model which can be changed, the suspension flow equations can be altered to fit the needs of the "type" of suspension to be modeled. Here we explain strategies for altering the solver-evolver and particle stress model to attempt to take into account and model new "types" of suspensions.

Basic initial issues involve heavy/light particles, Brownian particles, electrically charged particles, and finite-Reynolds-number flows. The ability to account for a mismatch between particle density and suspending fluid density is in place, as can be seen in Chapter 2, Eq. (2) and Eq. (7). The next step would be to verify that this portion of the code works and matches some basic experimental data. As for Brownian particles, this has been done in Frank *et al* (2003) to model the channel flow of Brownian suspensions. To add this ability to the current suspension flow model, the normal stress portion ($\mathbf{\Sigma}_{\mathrm{P}}^{NS}$) from the constitutive particle stress model given in Chapter 2, Eq. (9) would have to be altered,

$$\Sigma_{\mathrm{P},ii}^{NS} = \frac{a^B(\phi)}{2/9Pe} + \frac{\eta_o \dot{\gamma}}{\frac{1}{\mathrm{A}\eta_b(\phi)Pe\mathsf{Q}_{ii}^B} + \frac{1}{\eta_n(\phi)\mathsf{Q}_{ii}}}. \tag{73}$$

In this expression, Pe is the Peclét number which is a measure of the balance between Brownian and shear forces. For non-Brownian particles, where $Pe \to \infty$, this expression would simply to the previous definition of the particle phase normal stress, $\Sigma_{\mathrm{P},ii}^{NS} = \eta_n \dot{\gamma} \mathsf{Q}_{ii}$. The term $a^B(\phi)$ is the particle volume fraction dependence of the isotropic Brownian stress, $\eta_b(\phi)$ is the ϕ dependence of the anisotropic Brownian stress, Q_{ii}^B takes into account the degree of anisotropy of the Brownian stress and A controls the transition between low to high Peclét number conditions.

Charged particles were addressed in von Pfeil *et al* (2003) with the addition of an electric-field induced particle stress term. This term was,

$$\mathbf{\Sigma}_{\mathrm{P}}^{elec} = \varepsilon_o[(\varepsilon(\phi, a_1) - \varepsilon_f)\mathbf{E}^{elec}\mathbf{E}^{elec} - \frac{1}{2}(\varepsilon(\phi, a_1) - \varepsilon_f + a_2)E^2\underline{\underline{\delta}}], \tag{74}$$

where ε_o is the permittivity of free space, $\varepsilon(\phi, a_1)$ is the suspension dielectric constant, ε_f is

the dielectric constant of the suspending fluid, a_1 and a_2 are electrostriction coefficients of the suspension, and $\mathbf{E}^{elec}$, E characterize the applied electric field. This addition allowed von Pfeil *et al* to study the stability of particle banding in simple shear flow of electrorheological suspensions.

Adding the ability to handle finite-Reynolds-number (or inertia) flow conditions is just a matter of adding back in the convective terms to the flow solution, which were removed with the assumption of zero-Reynolds-number flow conditions. The applicability of the flow solver to the solution of finite-Reynolds-number flows would need to be verified with literature and experimental data. As for the effect of finite-Reynolds-number conditions on the particle stress or constitutive behavior, this was addressed in the work of Mikulencak and Morris (2004). A further look into inertial influences, especially those involving turbulence, may be beyond the scope of the model at this point or may just involve coupling the migrator to a turbulent flow solver and observing how the predictions match up to experiments. Some turbulent suspension flow work has been done (Matas, Morris and Guazzelli, 2003), but is still in the early stages.

Other major issues include deformable particles, particle clumping, and non-spherical suspended particles. These issues involve complex phenomena, which require careful consideration to address. The first issue of deformable particles will most likely need to be resolved with basic rheological measurement and determination of how this affects $\eta_s = \eta_s(\dot{\gamma}, \phi)$ and $\eta_n = \eta_n(\dot{\gamma}, \phi)$ relationships. The next issue of particle clumping or the formation of large scale structures presents a much more tricky problem, since this is a continuum based modeling approach. If the structures approach the size scale of the geometry of the flow solution, the continuum modeling approach will eventually break down. If they remain well below this level, they could possibly be taken into account for by adjusting the value of the particle size scale, a. It could be simply set to a larger value to represent the size of an average clump. It could also be done more intelligently by setting $a = a(\dot{\gamma}, \phi)$, if some information is available on the mechanism of clumping or the observed parameter range of clumping behavior.

The problem of non-spherical particle shapes, such as an oblong shape, results in the

question of how does the orientation of the particles themselves effect the stress law. This can lead to two possible adjustments. First, how this effects the stress law needs to be determined through rheometric measurements, including "history" effects. If history effects such as lining up along streamlines are observed, then an orientation parameter may need to be added to the constitutive law to take into account these effects. The orientation parameter acts as an approximation of the configuration of the particle and the amount of resistance that they place on the bulk flow. Also some consideration might need to be taken on how different flow types could affect these suspensions in general flow fields. Local kinematics should have an effect on how particles will orient themselves to on another. This kinetic dependence could eliminate the necessity for a history or orientation parameter, since $\hat{\rho}_k$ would track the kinematic history of the particles.

7.4 Conclusions

The suspension flow model developed in this work represents a solid starting point for further suspension flow research. The solver-evolver is a rigorous computational tool which can be applied to general geometry suspension flow solutions on its own or coupled to more powerful commercial CFD packages.

The suspension flow model illustrates different strategies and methods for modeling general flow-field conditions and waits only for further experimental work to verify which method works best to match real-world behavior. Also, the suspension flow model is not limited to the assumptions used in this work, but can be applied to a wide number of types of suspensions. Here we have suggested ways to adjust the model to handle such complex behavior as particle clumping, deformable particles and non-spherical particle shapes. In addition, we have pointed out previous work in the literature where variations of the suspension flow model have been used for Brownian particles and electrically charged particles in an applied electric or magnetic field.

We believe that this work has set a solid foundation for future suspension flow study and has added further insight in using a frame invariant formulation for the particle stress constitutive law, in order to allow a fundamental basis for its use in general geometry

suspension flow solutions.

APPENDIX A

SOLVER-EVOLVER CODE: MATLAB M-FILES

If you are interesting in getting a copy of the Solver-Evolver m-files used for this work please contact Ryan Miller at `t_ryno76@hotmail.com` with SOLVER-EVOLVER in the subject line. (Note: if you do not put SOLVER-EVOLVER in the subject line, the message will most likely be deleted)

REFERENCES

Abbott, J. R., Tetlow, N., Graham, A. L., Altobelli, S. A., Fukushima, E., Mondy, L. A., and Stephens, T. S., "Experimental observations of particle migration in concentrated suspensions: Coutate flow," *J. Rheol.*, vol. 35, no. 5, pp. 773 – 795, 1991.

Altobelli, S. A., Fukushima, E., and Mondy, L. A., "Nuclear magnetic resonance imaging of particle migration in suspensions undergoing extrusion," *J. Rheol.*, vol. 41, no. 5, pp. 1105 – 1115, 1997.

Altobelli, S. A., Givler, R. C., and Fukushima, E., "Velocity and concentration measurements of suspensions by nuclear magnetic resonance imaging," *J. Rheol.*, vol. 35, no. 5, pp. 721 – 734, 1991.

Bao, W., "An economical finite element approximation of generalized Newtonian flows," *Comput. Methods Appl. Mech. Engrg.*, vol. 191, pp. 3637 – 3648, 2002.

Batchelor, G. K., "The effect of Brownian motion on the bulk stress in a suspension of spherical particles," *J. Fluid Mech.*, vol. 83, no. 1, pp. 97 – 117, 1977.

Batchelor, G. K. and Green, J. T., "The determination of the bulk stress in a suspension of spherical particles to the order c^2," *J. Fluid. Mech*, vol. 56, no. 3, pp. 401 – 427, 1972.

Bird, R. B., Armstrong, R. C., and Hassager, O., *Dynamics of Polymeric Liquids*, vol. 1. Wiley & Sons, 2nd ed., 1987.

Brady, J. F. and Bossis, G., "Stokesian dynamics," in *Annual Review of Fluid Mechanics* (Lumley, J. L., Dyke, M. V., and Reed, H. L., eds.), vol. 20, pp. 111–157, Palo Alto, CA: Annual Reviews, 1988.

Brady, J. F. and Morris, J. F., "Microstructure of strongly sheared suspensions and its impact on rheology and diffusion," *J. Fluid Mech.*, vol. 348, pp. 103 – 139, 1997.

Brady, J. F., Phillips, R. J., Lester, J. C., and Bossis, G., "Dynamic simulation of hydrodynamically interacting suspensions," *J. Fluid Mech.*, vol. 195, pp. 257–280, 1988.

Brunn, P. O. and Ryssel, E., "The ω - **D** fluid: general theory with special emphasis on stationary two dimensional flows," *Continuum Mech. and Thermodynamics*, vol. 9, pp. 73–82, 1997.

Brunn, P. O. and Ryssel, E., "Steady non-swirling axisymmetric flows: flow classification and rheological consequences," *Continuum Mech. and Thermodynamics*, vol. 10, pp. 349–357, 1998.

Chapman, B. K., *Shear-induced migration phenomena in concentrated suspensions*. Ph.D. thesis, University of Notre Dame, 1990.

Chow, A. W., Iwayima, J. H., Sinton, S. W., and Leighton, D. T., "Particle migration of non-Brownian, concentrated suspensions in a truncated cone-and-plate." Society of Rheology Meeting, Sacramento, CA, 1995.

Chow, A. W., Sinton, S. W., Kwamiya, J. H., and Stephens, T. S., "Shear-induced migration in Coutate and parallel-plate viscometers: NMR imaging and stress measurements," *Phys. Fluids A*, vol. 6, pp. 2561 – 2676, 1994.

Christiansen, E. B., Kelsey, S. J., and Carter, T. R., "Laminar tube flow through an abrupt contraction," *AIChE J.*, vol. 18, no. 2, pp. 372 – 380, 1972.

Daugan, S., Talini, L., Herzhaft, B., and Allain, C., "Aggregation of particles settling in shear-thinning fluids, part 1. two-particle aggregation," *Eur. Phys. J. E*, vol. 7, pp. 73 – 81, 2002.

Daugan, S., Talini, L., Herzhaft, B., and Allain, C., "Aggregation of particles settling in shear-thinning fluids, part 2.three-particle aggregation," *Eur. Phys. J. E*, vol. 9, pp. 55 – 62, 2002.

Dratler, D. I. and Schowalter, W. R., "Dynamic simulation of suspensions of non-Brownian hard spheres," *J. Fluid Mech.*, vol. 325, pp. 53 – 77, 1996.

Drew, D. A. and Lahey, R. T., "Analytical modeling of multiphase flow," in *Particulate Two-Phase Flows* (Roco, M. C., ed.), Boston: Butterworth-Heinemann, 1993.

Fang, Z., Mammoli, A. A., Brady, J. F., Ingber, M. S., Mondy, L. A., and Graham, A. L., "Flow-aligned tensor models for suspension flows," *Int. J. Multiphase Flow*, vol. 28, pp. 137–166, 2002.

Ferziger, J. H. and Perić, M., *Computational Methods for Fluid Dynamics*. New York: Springer, 3rd ed., 2002.

Frank, M., Anderson, D., Weeks, E. R., and Morris, J. F., "Particle migration in pressure-driven flow of a Brownian suspension," *J. Fluid Mech.*, vol. 493, pp. 363 – 378, 2003.

Gadala-Maria, F., *The rheology of concentrated suspensions*. Ph.D. thesis, Stanford University, 1979.

Gheissary, G. and van den Brule, B. H. A. A., "Unexpected phenomena observed in particle settling in non-Newtonian media," *J. Non-Newtonian Fluid Mech.*, vol. 67, pp. 1 – 18, 1996.

Hampton, R. E., Mammoli, A. A., Graham, A. L., Tetlow, N., and Altobelli, S. A., "Migration of particles undergoing pressure-driven flow in a circular conduit," *J. Rheol.*, vol. 41, no. 3, pp. 621–640, 1997.

Han, M., Kim, C., Kim, M., and Lee, S., "Particle migration in tube flow of suspensions," *J. Rheol.*, vol. 43, no. 5, pp. 1157 – 1174, 1999.

Husband, D. M., "Continuous processing of composite solid propellants," *Chem. Eng. Prog.*, vol. 85, pp. 55 – 61, 1989.

Iwamiya, J. H., Chow, A. W., and Sinton, S. W., "NMR flow imaging of Newtonian liquids and a concentrated suspension through an axisymmetric sudden contraction," *Rheol. Acta*, vol. 33, pp. 267 – 282, 1994.

Kelsey, S. J., *Isothermal and non-isothermal, laminar, Newtonian and non-Newtonian entrance region flow.* Ph.D. thesis, University of Utah, Salt Lake City, 1971.

Koh, C. J., Hookham, P., and Leal, L. G., "An experimental investigation of concentrated suspension flows in a rectangular channel," *J. Fluid Mech.*, vol. 266, pp. 1 – 32, 1994.

Kolli, V. G., Pollauf, E. J., and Gadala-Maria, F., "Transient normal stress response in a concentrated suspension of spherical particles," *J. Rheol.*, vol. 46, no. 1, pp. 321 – 334, 2002.

Krieger, I. M., "Rheology of monodisperse latices," *Adv. Colloid Interface Sci.*, vol. 3, pp. 111–136, 1972.

Laun, H. M., "Normal stresses in extremely shear thickening polymer dispersions," *J. Non-Newtonian Fluid Mech.*, vol. 54, pp. 87 – 108, 1994.

Leighton, D. and Acrivos, A., "The shear-induced migration of particles in concentrated suspensions," *J. Fluid Mech.*, vol. 181, pp. 415–439, 1987.

Lyon, M. K. and Leal, L. G., "An experimental study of the motion of concentrated suspensions in two-dimensional channel flow. part 1. monodisperse systems," *J. Fluid Mech.*, vol. 363, pp. 25–56, 1998.

Lyon, M. K. and Leal, L. G., "An experimental study of the motion of concentrated suspensions in two-dimensional channel flow. part 2. bidisperse systems," *J. Fluid Mech.*, vol. 363, pp. 57–77, 1998.

Matas, J. P., Morris, J. F., and Guazzelli, E., "Transition to turbulence in particulate pipe flow," *Phys. Rev. Lett.*, vol. 90, 2003. article number 014501.

MathWorks, *Using MATLAB: Version 6*, ch. 15: Sparse Matrices. The MathWorks, Inc, 2002.

Mikulencak, D. R. and Morris, J. F., "Stationary shear flow around fixed and free bodies at finite reynolds number," *J. Fluid Mech.*, vol. 520, pp. 215 – 242, 2004.

Miller, R. M. and Morris, J. F., "Frame invariant suspension flow modeling in a sharp-edged, sudden contraction flow utilizing a finite volume method." *to be submitted* to J. Fluid Mech., 2004.

Mills, P. and Snabre, P., "Rheology and structure of concentrated suspension of hard spheres. shear induced particle migration," *J. Phys. II*, vol. 5, pp. 1597–1608, 1995.

Mompean, G., "On predicting abrupt contraction flows with differential and algebraic viscoelastic models," *Computers & Fluids*, vol. 31, pp. 935 – 956, 2002.

Mondy, L. A., "*personal communication.*" Sandia National Laboratories, 2004.

Mondy, L. A., Graham, A. L., and Gottlieb, M., "Microrheological observations on the onset of non-Newtonian behavior in suspensions." 10th International Congress on Rheology, Sydney, 1988.

Moraczewski, T. and Shapley, N. C., "*personal communication*." Columbia University, Dept. Chem. Eng., 2004.

Morris, J. F. and Brady, J. F., "Pressure-driven flow of a suspension: Buoyancy effects," *Int. J. Multiphase Flow*, vol. 24, no. 1, pp. 105–130, 1998.

Morris, J. F. and Katyal, B., "Microstructure from simulated Brownian suspension flows at large shear rate," *Phys. of Fluids*, vol. 14, no. 6, pp. 1920 – 1937, 2002.

Morris, J. F. and Boulay, F., "Curvilinear flows of noncolloidal suspensions: The role of normal stresses," *J. Rheol.*, vol. 43, no. 5, pp. 1213–1237, 1999.

Mutsuddy, B. C. and Ford, R. G., *Ceramic Injection Molding*. Chapman & Hall, 1995.

Nott, P. R. and Brady, J. F., "Pressure-driven flow of suspensions: Simulation and theory," *J. Fluid Mech.*, vol. 275, pp. 157–199, 1994.

Parsi, F. and Gadala-Maria, F., "Fore-and-aft asymmetry in a concentrated suspension of solid spheres," *J. Rheol.*, vol. 31, no. 8, pp. 725 – 732, 1987.

Patankar, S. V., *Numerical heat transfer and fluid flow*. Series in computational methods in mechanics and thermal sciences, New York: McGraw-Hill, 1980.

Phillips, R. J., Armstrong, R. C., Brown, R. A., Graham, A., and Abbott, J. R., "A constitutive model for concentrated suspensions that accounts for shear-induced particle migration," *Phys. Fluids A*, vol. 4, pp. 30–40, 1992.

Phung, T. N., Brady, J. F., and Bossis, G., "Stokesian dynamics simulation of Brownian suspensions," *J. Fluid Mech.*, vol. 313, pp. 181–207, 1996.

Rao, R. R., Mondy, L. A., Baer, T. A., Altobelli, S. A., and Stephens, T. S., "NMR measurements and simulations of particle migration in non-Newtonian fluids," *Chem. Eng. Comm.*, vol. 189, no. 1, pp. 1–22, 2002.

Richardson, J. F. and Zaki, W. N., "Sedimentation and fluidization: Part I," *Trans. Inst. Chem. Eng.*, vol. 32, pp. 35–47, 1954.

Russel, W. B., Saville, D. A., and Schowalter, W. R., *Colloidal Dispersions*. Cambridge University Press, 1989.

Ryssel, E. and Brunn, P. O., "Comparison of a quasi-Newtonian fluid with a viscoelastic fluid in planar contraction flow," *J. Non-Newt. Fluid Mech.*, vol. 86, pp. 309–335, 1999.

Ryssel, E. and Brunn, P. O., "Flow of a quasi-Newtonian fluid through a planar contraction," *J. Non-Newt. Fluid Mech.*, vol. 85, pp. 11–27, 1999.

Sami, S., "Stokesian dynamics simulation of extensional flow of Brownian suspensions," m.S. thesis, California Institute of Technology, 1997.

Schunk, P. R. and Scriven, L. E., "Constitutive equation for modeling mixed extension and shear in polymer solution processing," *J. Rheol.*, vol. 34, no. 7, pp. 1085–1119, 1990.

Seshadri, V. and Sutera, S. P., "Apparent viscosity of coarse, concentrated suspensions in tube flow," *Trans. Soc. Rheol.*, vol. 14, pp. 351 – 373, 1970.

Singh, A. and Nott, P. R., "Normal stresses and microstructure in bounded sheared suspensions via Stokesian dynamics simulations," *J. Fluid Mech.*, vol. 412, pp. 279 – 301, 2000.

Singh, A. and Nott, P. R., "Experimental measurements of the normal stresses in sheared Stokesian suspensions," *J. Fluid Mech.*, vol. 490, pp. 293 – 320, 2003.

Subia, S. R., Ingber, M. S., Mondy, L. A., Altobelli, S. A., and Graham, A. L., "Modelling of concentrated suspensions using a continuum constitutive equation," *J. Fluid Mech.*, vol. 373, pp. 193–219, 1998.

von Pfeil, K., Graham, M. D., Klingenberg, D. J., and Morris, J. F., "Structure evolution in electrorheological and magnetorheological suspensions from a continuum perspective," *J. App. Physics*, vol. 93, no. 9, pp. 5769 – 5779, 2003.

Zarraga, I. E., Hill, D. A., and Leighton, D. T., "The characterization of the total stress of concentrated suspensions of noncolloidal spheres in Newtonian fluids," *J. Rheol.*, vol. 42, no. 2, pp. 185 – 220, 2000.

Zhang, K. and Acrivos, A., "Viscous resuspension in fully developed laminar pipe flows," *Int. J. Multiphase Flow*, vol. 20, pp. 579 – 591, 1994.